Deformation of Tian Shan from Coseismic to Million-year Timescales

by

Siyu Wang
A Dissertation Submitted in Partial Fulfillment of the
Requirements for the Degree of

DOCTOR OF PHILOSOPHY

in the School of Earth and Ocean Sciences

University of Victoria

Deformation of Tian Shan from Coseismic to Million-year Timescales

by

Siyu Wang

Supervisory Committee

Dr. Ruohong Jiao, Supervisor
(School of Earth and Ocean Sciences)

Dr. Edwin Nissen, Co-supervisor
(School of Earth and Ocean Sciences)

Dr. Lucinda Leonard, Departmental Member
(School of Earth and Ocean Sciences)

Dr. Randall Scharien, Outside Member
(Department of Geography)

ABSTRACT

Intracontinental deformation is often driven by tectonic forces associated with distant plate collisions. The late Cenozoic deformation of Tian Shan is accommodated by both thrust faults bounded the mountain range and strike-slip motion within the mountain. Earthquake hazards and deformation mechanics in the far-field active regions of the Tian Shan are generally poorly quantified due to slow strain accumulation, poor data coverage, and incomplete historical earthquake records. This dissertation aims to gain a better understanding of the kinematics of deformation in this far-field intracontinental mountain belt.

I use multidisciplinary techniques to investigate the late Cenozoic deformation of the Tian Shan across different time scales ranging from coseismic to postseismic and interseismic to million-year scales. I start with an earthquake that occurred in the Kepingtag fold-and-thrust belt in southwestern Tian Shan, a seismically active region and a clear example of basinward migration of deformation. I use Interferometric Synthetic Aperture Radar to measure coseismic deformation, combined with teleseismic waveform modelling and calibrated relocation of the mainshock. The results reveal a fault plane situated on the décollement at the base of the folded sedimentary cover and a prevalence of seismicity at basement depths throughout the Kepingtag belt and its foreland, indicating rheological controls on earthquake depths. Then, I apply both coseismic modelling and postseismic time series analysis to study another earthquake that happened along the northern Chinese Tian Shan front, adjacent to the Southern Junggar Fold-and-thrust Belt. The findings indicate that the coseismic rupture on a shallow dipping fault plane triggers postseismic deformation that is farther north beneath the anticline. In the third part of this dissertation, I use low-temperature thermochronology, including apatite fission track and apatite U-Th/He dating systems, to model the thermal history of samples collected from the previously overlooked region in the northern Tian Shan. Inverse modelling of over 1000 published and new thermochronological data from the Tian Shan, Pamir, and northeastern Tibetan Plateau, suggests accelerated exhumation during 15–10 Ma, which represents an acceleration of strike-slip motion.

The dissertation concludes by integrating results across various timescales to discuss deformation styles throughout the region's tectonic evolution. This study also demonstrates that integrating techniques across multiple timescales effectively quantifies the evolution of active faulting and deformation in the Tian Shan.

Contents

List of Tables

List of Figures

ACKNOWLEDGEMENTS

I would like to begin by thanking my supervisors, Ruohong Jiao and Edwin Nissen, for guiding me over the past five years. Ruohong, thank you for your assistance during fieldwork, your help in solving many technical problems, and your constant encouragement. Ed, thank you for being both a mentor and a friend. Your expertise and knowledge have been invaluable during this research, and you have built a supportive research group that has been a pleasure to be a part of.

I am especially grateful to Professor John Elliott and Professor Tim Wright for hosting my visit to the University of Leeds and supervising my third project on InSAR time series analysis. Our weekly group meetings have been a tremendous source of inspiration. I feel fortunate to have worked with such a world-leading group in InSAR. Thanks to Mitacs Globalink Research Award for providing me the opportunity to conduct three months of research in the UK.

Many people have helped me throughout this journey. A special thank goes to Dr. Léa Pousse-Beltran for her patient and detailed instruction on InSAR coseismic modelling. Your example plotting scripts of the Generic Mapping Tool (GMT) have been invaluable in helping me get started and become a proficient GMT user now. Thanks also to Dr. Eric Bergman for helping me relocate the Jiashi earthquake sequence and Professor Tim Craig for helping me with the teleseismic body waveform modelling, which contributes to essential parts of Chapter 2.

I would also like to acknowledge the financial support from Professor Huiping Zhang for the field trip expense and thermochronology lab work. Dr. Jiawei Zhang, thank you for your help with my sample handling. Dr. Jianzhang Pang and Dr. Ying Wang are thanked for their precise work in thermochronological dating and careful experiments during the COVID-19 pandemic when I was unable to travel to Beijing. The fieldwork support from Jiawei is also warmly appreciated.

I have made many amazing friends at the University of Leeds. Qi Ou, thank you for your dedicated help with time series data processing; I could not have achieved such complete and convincing results without your assistance. Thank you, Dr. Milan Lazecký and Dr. Yasser Maghsoudi, for helping me with the LiCSAR and LiCSBAS data processing, without which this work would have been impossible. Yuan Gao and Jin Fang, thank you for always being timely and doing your best with my technical questions. Dr. Jack McGrath, thanks for sharing the Python scripts for fitting pre- and post-seismic linear velocities with me. Muhammet Nergizci and many other students in the office at Priestley 7.28, as well as members of other groups at the School of Earth and Environment, are thanked for providing a warm and welcoming atmosphere during my time at a new university and in a new country.

Thank you to everyone in the SEOS B311 office, our coffee and dinner times are fond memories. Élyse, thank you for generously introducing me to the world of Sentinel-1, sharing interferogram processing scripts, and offering job-hunting suggestions. Grace, thank you for always being energetic and encouraging, which motivated me a lot.

I have been supported through scholarships from the China Scholarship Council, as well as donor awards from the Charles S. Humphrey Graduate Student Award and David McGillivray Scholarship in Science, which are sincerely appreciated.

I am grateful to have a warm and supportive family. To my mom, Xuelian Su, and my dad, Qianming Wang, thank you for your unwavering financial, emotional, and physical support throughout this process.

Finally, my most heartfelt thanks go to my partner, Yijie, who has been incredibly supportive over these years, helping me with emotional and scientific problems. I cannot imagine having gone through this without you.

Chapter 1

Introduction

Starting in the Eocene, the convergence between the Indian subcontinent and Eurasia has resulted in extensive crust shortening and thickening, giving rise to the world's highest mountain ranges: the Himalaya, Karakoram, Pamir, and Tian Shan (Argand, 1922). Among these, the Tian Shan (sometimes spelled as Tien Shan or Tianshan) stands out as one of the largest active intracontinental mountain belts. Located ∼1300 km north of the Himalayan thrust front (Figure 1.1), the Tian Shan extends east-west for ∼2,500 km through western China, Kazakhstan, and Kyrgyzstan, forming a major part of the southern Central Asian Orogenic Belt (CAOB).

The geological evolution of the Tian Shan has been marked by several significant tectonic events. An ancestral range was initially formed during the Paleozoic, and then reactivated as the modern Tian Shan in the late Cenozoic as a result of the India-Eurasia collision. This led to both the uplift of the Tian Shan itself and the development of the Tarim and Junggar foreland basins, along with associated fold-and-thrust belts, on the southern and northern margins of the mountain ranges (Molnar and Tapponnier, 1975; Tapponnier and Molnar, 1979). While the India-Eurasia collision began as early as in the Paleocene-Eocene, substantial uplift of the Tian Shan started during the Oligocene and Miocene (Molnar and Tapponnier, 1975; Tapponnier and Molnar, 1979; Windley et al., 1990; Avouac et al., 1993a; Hendrix et al., 1994; Yin et al., 1998; De Grave et al., 2007). Therefore, there is a notable time lag between the collision at the Himalayan margin to the south and the deformation of the Tian Shan in the north. Understanding the present-day uplift pattern and exhumation history of the Tian Shan is thus crucial for understanding how deformation propagates from the collision zone to the distant interior of the continent.

This dissertation aims to provide a comprehensive, multidisciplinary analysis of

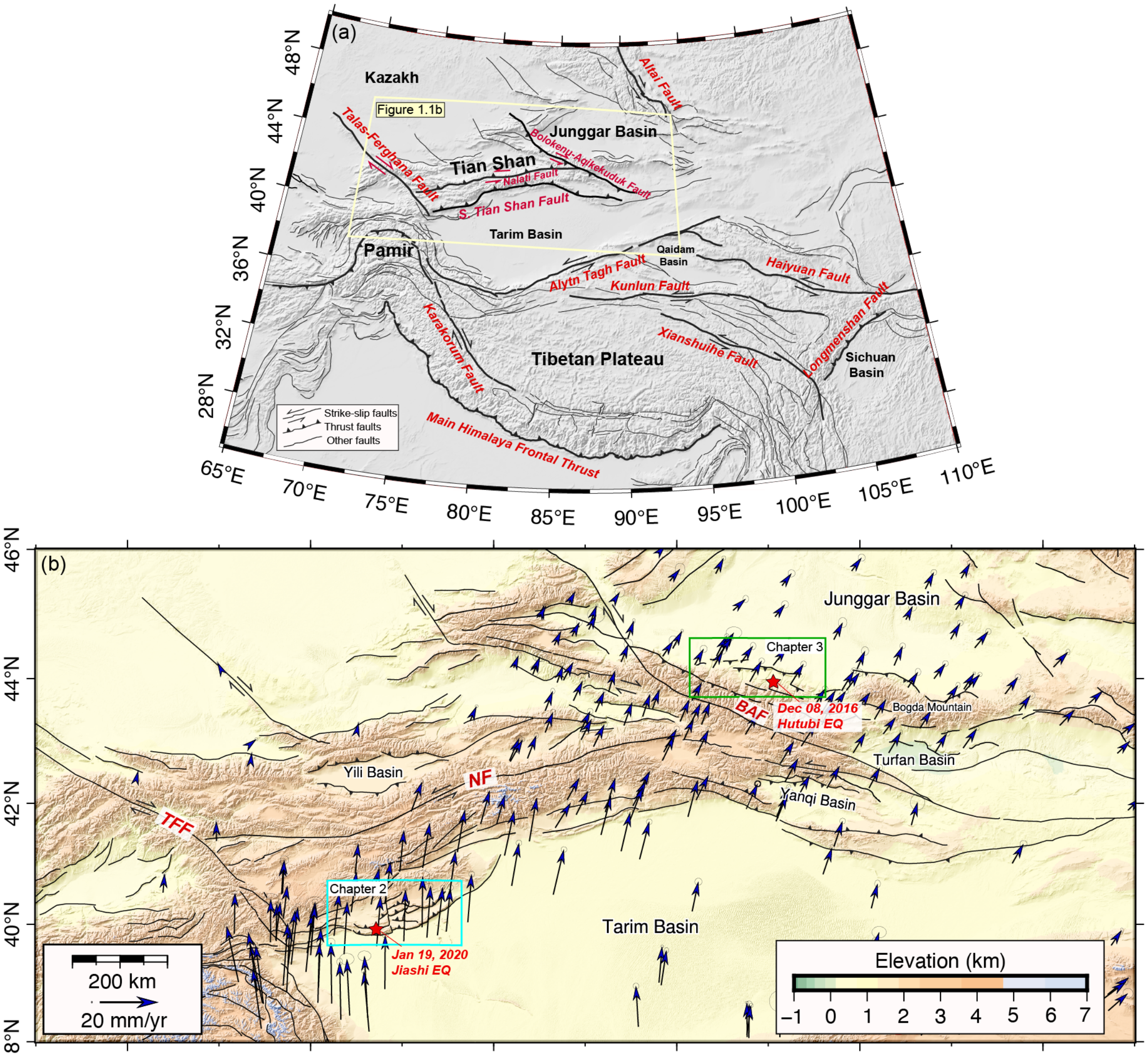

Figure 1.1: Tectonic map of the Tian Shan and its surrounding area with major structures. (b) Topography and active faults of the Tian Shan mountain. The cyan rectangle in the southwestern Tian Shan marks the study area discussed in Chapter 2, with the red star indicating the relocated epicentre of the January 19, 2020 Jiashi mainshock. The green rectangle in the northern Tian Shan represents the study area of Chapter 3, with the red star marking the epicentre of the December 08, 2016 Hutubi mainshock. Active faults are from Styron and Pagani (2020). GPS velocities relative to stable Eurasia are from Wang et al. (2020a)

the late Cenozoic deformation and earthquake hazards of the Tian Shan. I incorporate Interferometric Synthetic Aperture Radar (InSAR) surface deformation mapping and fault slip modelling to gain precise insights into the geometry and depths of two notable earthquakes along the two margins of the Tian Shan: one located in the Kepingtag fold-and-thrust belt on the southern side, and the other beneath the Southern Junggar Fold-and-thrust Belt on the northern side. In the Southern Junggar Fold-and-thrust Belt in addition to the coseismic deformation, I also conduct an InSAR time series analysis to examine postseismic and interseismic deformation, helping illuminate relations between the seismic cycle and fold growth. Finally, I utilize new and published low-temperature thermochronological data to reconstruct the cooling history and understand the long-term exhumation process of the entire Tian Shan and adjacent regions over geological time scales.

In the rest of Chapter 1, I introduce the tectonic, geologic, and climatic settings of the Tian Shan, providing a foundational understanding of the region's context. I then review the current applications of satellite radar interferometry in earthquake studies, highlighting the advancements and methodologies relevant to this research. Following this, I discuss the motivations behind this dissertation and outline the significance of the expected contributions of this study. Finally, I summarise the results from the subsequent three chapters, offering a preview of the key findings and their implications.

1.1 Tectonic and geological settings of Tian Shan

As one of the highest and most rapidly deforming intracontinental mountain belts in Central Asia, the Tian Shan mountains have experienced a complex history of geological evolution. Geological, paleomagnetic, and paleofloral data suggest that multiple island arcs and Precambrian microcontinents, rifted from the Gondwana and/or Siberia, amalgamated during the Paleozoic (e.g. Şengör et al., 1993; Windley et al., 2007). Following the accretion of continental blocks and arc-type terranes from the late Carboniferous to early Permian, the ancestral Tian Shan underwent major exhumation, relief building, and the formation of intermontane basins along major strike-slip faults (Allen et al., 1993; Dumitru et al., 2001; Jolivet et al., 2010; Carroll et al., 1995). During the Mesozoic, the Tian Shan experienced tectonic stability from the Triassic to the late Jurassic, followed by active deformation from the late Jurassic to early Cretaceous (Hendrix et al., 1992; De Grave et al., 2007). An exception to this stability is found in the southern Junggar Basin and northern Tarim Basin, where extensive lower to middle Jurassic strata unconformably overlie intensively deformed Paleozoic rocks, indicating significant exhumation during this period. Subsequent tectonic quiescence during the late Mesozoic to Paleogene led to the development of flat depositional landscapes with limited detrital input into the basins surrounding the range (Allen et al., 1991; Bullen et al., 2003; Windley et al., 1990). The Tian Shan was then reactivated in the late Oligocene as a consequence of the indentation of India into Eurasia and accommodated up to 200 km of cumulative Cenozoic shortening (Tapponnier and Molnar, 1979; Windley et al., 1990). A magnetostratigraphic study from the northern Tarim Basin indicates substantial thrusting, based on the facies transition from lacustrine to braided-fluvial deposits between 24 Ma and 21 Ma (Sobel, 1999). Fission track thermochronology data, collected from the northern Tian Shan and along the Du-Ku Highway across the significant topographic relief of the north and south flanks of the Tian Shan, suggest that a 3 to 5-km-thick crust has been exhumed in the past $\sim$ 24 Ma (Hendrix et al., 1994; Dumitru et al., 2001). High levels of seismicity, coupled with GPS measurements and evidence from surface faulting and folding all attest to ongoing, rapid deformation across the Tian Shan (Ghose et al., 1998; Zubovich et al., 2010).

1.2 Cenozoic kinematic deformation pattern

Intracontinental deformation, unlike mountain building at plate margins, typically involves widespread deformation across numerous faults. The Tian Shan mountain is a typical example, comprising several E-W trending Paleozoic ranges separated by parallel faults and intermontane basins filled with syntectonic Cenozoic deposits (e.g. Avouac et al., 1993a; Campbell et al., 2013; Burtman, 1975).

The overall crustal deformation pattern in the Tian Shan is primary oblique shortening with a maximum principal stress direction oriented NNE. This shortening is not only accommodated by E-W range-front thrust faulting, but also facilitated by deformation on E-W sinistral faults and NW-SE trending dextral faults that cut across the mountain ranges (e.g., Buslov et al., 2003).

Holocene and late Pleistocene thrust faults are commonly found within the basin interiors, located kilometres to tens of kilometres away from surface faults and folds that delineate the range-basin margins (e.g., Thompson et al., 2002; Wang et al., 2020b). The Bolokenu-Aqikekuduk Fault, also known as the Dzhungarian Fault, stretches ∼1000 km along the northern margin of the central Tian Shan, marking the boundary between the northern and central Tian Shan (Figure 1.1). This fault extends from southwest Kazakhstan eastward to the Turfan Basin in China. It obliquely cuts the western part of the northern Tian Shan mountain at an angle of 30°–40°, and eastwards the angle gradually decreases, to 10°–20° near the Turfan Basin. The large-scale dextral slip ductile shearing along this structure likely resulted from the collision of the Siberian continental plate with the northern margin of the Tarim plate during the late Carboniferous period (Shu et al., 1999; Laurent-Charvet et al., 2003). The late Quaternary right-lateral slip rate of the western segment of the fault, measured from displaced alluvial fans, is estimated to be between 2.2 and 5 mm/yr (Shen et al., 2011; Campbell et al., 2013).

The central Tian Shan and southern Tian Shan are separated by a major structure, which is referred to as the Nikolaev Line in Kyrgyzstan and the Nalati Fault in northwest China (Gao et al., 2009). For simplicity, we will refer to this structure as the Nalati Fault throughout this dissertation. The presence of widely exposed Paleozoic magmatic rocks around the Nalati Range indicates the northward subduction of the Paleo-Tianshan Ocean (Gao et al., 2009). The Nalati Fault merges with the Bolokenu-Aqikekuduk Fault at its eastern end. The late Quaternary left-lateral slip rate is ∼0.36 mm/yr with a vertical slip rate of ∼0.15 mm/yr (Wu et al., 2014).

The western Tian Shan is transected by the Talas-Fergana Fault zone, a late Paleozoic to Mesozoic structure that has been reactivated as a NW-SE trending dextral strike-slip fault, extending ∼800 km. The Talas-Fergana Fault is of great significance for understanding the hinterland kinematics of the India-Eurasia collision. Within the Tian Shan interior, the Talas-Fergana Fault exhibits a right-lateral slip rate of ∼10–14 mm/yr (Burtman et al., 1996; Korjenkov et al., 2010). Bande et al. (2017b) identified a rapid exhumation event of Talas-Fergana Fault around 25 Ma. This event aligns with a simultaneous pulse of cooling and thrust belt propagation in the southern Tian Shan, suggesting that both regions experienced coeval and rapid exhumation, and the strike-slip motion on the fault enables the counterclockwise rotation of the Fergana Basin. Modern GPS data surrounding the basin corroborates that the Ferghana Valley rotates at a rate of -0.73°±0.08°/Myr relative to Eurasia (Zubovich et al., 2010).

The Tarim Basin is bounded by the left-lateral Alytn Tagh Fault to the south. Its initial uplift began in the late Eocene to Oligocene (Yin and Harrison, 2000), with rapid uplift starting in the middle Miocene, and started evolving into a lithospheric-scale strike-slip shear zone by the early Miocene (Yue et al., 2004). Geologic evidence indicates a clockwise rotation of 7°±2.5° for the Tarim Basin since the onset deformation of Tian Shan in the early Miocene (Avouac et al., 1993b).

These evidence and observations have confirmed significant strike-slip motion within the Tian Shan mountains. Understanding the prevalent strike-slip faulting in the Tian Shan, along with its relationship to crustal shortening and earthquake hazards, is crucial for comprehending the dynamics of intracontinental convergence.

1.3 Climate

Surface uplift is the difference between rock uplift and exhumation (England and Molnar, 1990). Understanding the Cenozoic climate in Central Asia provides key insights into the underlying controls on surface uplift. The climate of Cenozoic has been characterized by a transition from a warm and humid climate to the current arid and semi-arid conditions. These changes have been driven by a combination of global climatic trends and regional tectonic events.

Throughout the Cenozoic, climate fluctuations have strongly impacted the diversification, dispersal, and extinction of various floras and faunas worldwide. High-resolution deep-sea oxygen ($\delta^{18}O$) and carbon ($\delta^{13}C$) isotope records are principal means of reconstructing global and regional climate change on a variety of geologic time-scales (Raymo and Ruddiman, 1992). Oxygen and carbon isotopes in foraminifera and plant fossils show a pronounced cooling of Earth's surface since the beginning of the Cenozoic (Shackleton, 1975). Major climatic events include warming periods such as the Paleocene-Eocene Thermal Maximum (PETM) and the early Eocene Climatic Optimum (EECO), followed by cooling events during the Eocene-Oligocene Transition (EOT)(Zachos et al., 2001; McInerney and Wing, 2011). The Miocene epoch saw further climatic fluctuations, with intervals of warming and cooling. The middle Miocene Climatic Optimum (MMCO) was a period of relative warmth, with mid-latitude temperatures about 6°C higher than present(Flower and Kennett, 1994). Another phase of cooling began, at least at high latitudes, in the middle Miocene time (16-14 Ma)(Savin et al., 1975; Shackleton, 1975).

Regionally, Central Asia experienced significant changes during the Cenozoic. Sedimentary records and climate models have shown that the primary influences are due to (1) the uplift of the Tibetan Plateau, which affects the intensity of the monsoon and global climate change (Harris, 2006; Li et al., 2018; Graham et al., 2005); (2)

the retreat of the Paratethys epicontinental sea associated with the India-Eurasia collision (Ramstein et al., 1997; Abels et al., 2011), and (3) global cooling (Dupont-Nivet et al., 2007; Fang et al., 2015). Caves et al. (2015) reconstructed the spatial distribution of oxygen isotopes $\delta^{18}O$ in precipitation since the early Eocene using a compilation of sedimentary samples. Their results suggest that the spatial distribution of paleo-precipitation $\delta^{18}O$ has remained remarkably consistent over time, implying the progressive uplift of the Tibetan Plateau has had little impact on the Central Asian climate (Caves et al., 2015). As a result, the mid-latitude westerlies have played an important role in delivering moisture to Central Asia throughout the Cenozoic and have been the dominant moisture source since at least the early Eocene.

On the other hand, modelling and geological evidence support the conclusion that Asian inland aridity was enhanced during the Eocene (Bosboom et al., 2014) and this aridification is attributed to topographic changes, particularly the early uplift of the central Tibetan Plateau, and global cooling induced by decreased atmospheric CO_2 concentration(Ruddiman and Kutzbach, 1991; Harris, 2006; Li et al., 2018).

During the Oligocene, the global climate began a cooling trend that was associated with the development of the Antarctic ice sheet and a reduction in atmospheric CO_2 levels. In Central Asia, these changes led to the gradual onset of aridification. Magnetostratigraphy and cyclostratigraphy demonstrate that global climate cooling must be recognized as a major contributor to the Asian palaeoenvironment (Dupont-Nivet et al., 2007). The monsoon-dominant climate formed near the Oligocene/Miocene boundary in East China and Central Asia (Sun and Wang, 2005; Wang, 1990; Zhang et al., 2007b).

From the Pliocene to the Pleistocene, the climate in Central Asia was characterized by continued aridification and the development of modern desert and steppe landscapes. During the Pleistocene, glacial advances in the Tian Shan mountains significantly influenced the regional climate by modifying precipitation patterns and creating periglacial environments. The Last Glacial Maximum (LGM) saw extensive glaciation in the Tian Shan, with glaciers covering large portions of the mountain range and contributing to cooler and drier conditions in the surrounding lowlands (Koppes et al., 2008). The Quaternary glacial-interglacial cycles had profound impacts on the regional climate, vegetation, and hydrology.

The modern climate in Central Asia is characterized by a predominantly arid and semi-arid climate, with significant seasonal and interannual variability. Central Asia is beyond the reach of the Indian summer Monsoon. The dominant weather patterns include summer orographic thunderstorms, mid-latitude westerlies bringing cyclonic disturbances in the spring and fall, and winter thermal high-pressure systems that may act to divert storms along tracks south of the Himalaya (Zhang et al., 2007b). The Tian Shan continues to play a crucial role in modulating the regional climate by acting as a barrier to moist air masses, resulting in varied precipitation patterns across the region, especially the southern and northern regions. The ongoing impacts of global climate change, including rising temperatures and changing precipitation regimes, pose significant challenges for water resources and ecosystems in this arid region (Koppes et al., 2008).

1.4 Low-temperature thermochronology

Exhumation of rock is the unroofing history of deeply buried rocks being brought to the surface. This process is primarily driven by two mechanisms: tectonic forces and climatic influences. Tectonic forces contribute indirectly to erosion by uplifting rocks, which are then subject to removal by surface processes. Climatic influences, such as increased precipitation, enhance these surface processes by accelerating weathering and erosion (Ring et al., 1999). Thermochronology provides a way to reconstruct the cooling history of minerals, thereby allowing us to infer the timing and rate of rock exhumation (Figure 1.2). The basic principle of thermochronology is the temperature-dependent retention of radiogenic daughter products within minerals. The concept closure temperature (T_c) was proposed by Dodson (1973), which is a very useful reference point representing the temperature below which a mineral begins to retain daughter products of radioactive decay, depending on the cooling rate. The cooling age, therefore, reflects the time since the mineral cooled below its closure temperature.

This dissertation focuses on two low-temperature thermochronometric systems: apatite fission track (AFT) and apatite (U-Th)/He (AHe) methods. These systems are sensitive to temperatures as low as 40°C, depending on the cooling rate, chemical composition, and mineral grain size (Wolf et al., 1998; Farley, 2000). This make them particularly sensitive to near-surface cooling and perturbations linked to exhumation processes, typically from depths of about one to four kilometres through the upper crust. The fundamental principle behind both AFT and AHe methods lies in the radioactive decay of ^{238}U, which occurs through two ways: physical radiation damage resulting in fission tracks, and the emission of α particles, producing ^{4}He and other daughter particles.

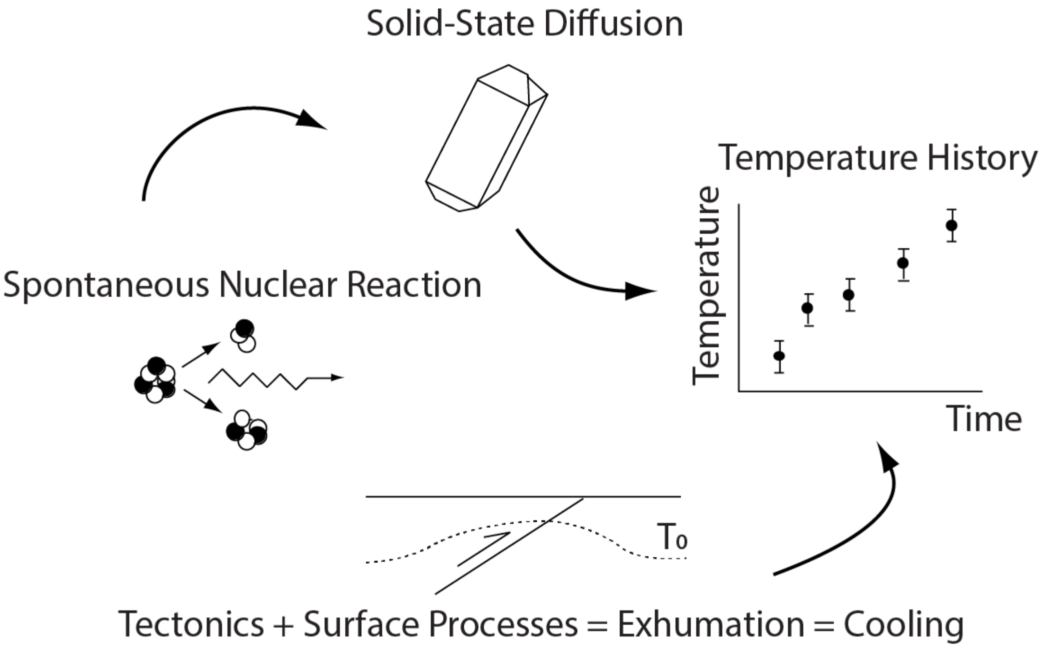

Figure 1.2: Schematic representation of the processes influencing thermal history reconstruction in low-temperature thermochronology adapted from (Braun et al., 2006). The figure illustrates the interplay between spontaneous nuclear reactions (resulting in the production of isotopic decay products), solid-state diffusion (whereby these decay products migrate within the crystal lattice), and exhumation driven by tectonics and surface processes. These factors shape the cooling history of rocks, which is recorded in the temperature-time path shown in the upper right graph.

Fission track thermochronology relies on the analysis of damage zones, or tracks in the crystal lattice caused by the spontaneous fission of ^{235}U. These fission tracks form at a rate directly proportional to the concentration of uranium in the mineral, and they initially exhibit similar lengths of ~11 μm in zircon and ~16 μm in apatite (Green et al., 1989; Donelick et al., 2005; Reiners and Brandon, 2006). Over time, the lengths of fission tracks will shorten due to thermal annealing, with earlier-formed tracks being more affected than later-formed ones due to their longer exposure to higher temperatures and more time to anneal. The distribution of fission track lengths thus can be used to assess the amount of annealing that a sample has experienced (Ketcham et al., 1999). By combining this information with thermochronological age, one can model possible cooling pathways and estimate the magnitude of exhumation. The Partial Annealing Zone (PAZ) for apatite, where tracks progressively shorten, is between ~60°C and 110°C. At temperatures below about 60°C, track shortening is negligible, whereas at temperature above 110°C, tracks anneal rapidly (Green et al., 1989). Assuming a geothermal gradient of about 20–30°C/km (Hendrix et al., 1994), this is equivalent to exhumation up through a depth window of about 2–6 km beneath the Earth's surface.

The (U-Th)/He technique is based on the alpha decay of isotopes from ^{235}U, ^{238}U, ^{232}Th, ^{147}Sm to ^{4}He. The Partial Retention Zone (PRZ) is defined by temperatures where ^{4}He is partially retained within the mineral crystal. In apatite, ^{4}He is completely expelled from apatite at temperature above ~75°C and nearly fully retained in apatite at temperature below ~40°C (Wolf et al., 1998). The cooling age can thus be calculated by measuring the concentrations of ^{4}He and the parent isotopes. The ratio of helium to parent isotopes provides information about the time elapsed since the mineral cooled below its closure temperature. This data is then used to reconstruct thermal histories and estimate exhumation rates. Due to its low closure temperature, the (U-Th)/He system, especially in apatite, is often used to complement the thermal history information obtained from AFT data to provide information about the cooling history of rocks.

Periods of slow cooling followed by rapid cooling preserve a break in slope in the time-temperature cooling history. Such cooling is commonly a result of uplift and exhumation of rock units during large-scale deformation in the upper crust and so may be used to constrain the timing, magnitude, and location of the deformation.

1.5 InSAR remote sensing technique

Interferometric Synthetic Aperture Radar (InSAR) is a powerful geodetic technique for measuring topography and detecting changes of Earth's surface with large spatial coverage and high resolution (Zubker and Goldstein, 1986; Massonnet and Feigl, 1998; Gabriel et al., 1989; Bürgmann et al., 2000). One of the key advantages of this method is its ability to acquire images under various weather conditions, both day and night (Hanssen, 2001).

SAR images are generated by a radar system that transmits microwave pulses and then records the echoes reflected back from the Earth's surface. The phase of the radar signal at each point on the ground is determined by the distance between the radar antenna and the surface. When a second radar observation is made from nearly the same location but at a different time, the phase difference between the two observations can be calculated. This phase difference, or interferometric phase, encodes the relative changes in distance between the radar and the ground, which can be attributed to surface deformation (Figure 1.3a). The interferogram is constructed by forming the complex cross-product of two SAR images acquired at different times. However, the phase of the radar echoes is recorded modulo 2π, meaning it is "wrapped" and only represents values between 0 and 2π (Figure 1.3b). To obtain meaningful and unique measurements of surface displacement, the wrapped phase must be converted into a continuous "unwrapped" phase, a process known as phase unwrapping (Rosen et al., 2000) (Figure 1.3b).

Numerous spaceborne SAR systems operated by various countries routinely collect data at different radar wavelengths, e.g., L-band Japanese Earth Resources Satellite (JERS-1) and Japanese Advanced Land Observation Satellite (ALOS), C-band European Remote Sensing Satellite (ERS), European Environmental Satellite (Envisat), Sentinel-1, and Canadian Radar Satellite RADARSAT, as well as X-band Italian COSMO-SkyMed constellation and TerraSAR-X, enabling diverse applications across geoscience disciplines, including the monitoring of earthquakes, volcanoes, land subsidence or uplift, landslides, glaciers, and hydrology change (e.g., Wright et al., 2004; Massonnet and Sigmundsson, 2000; Colesanti and Wasowski, 2006; Amelung et al., 1999; Rignot and Kanagaratnam, 2006). Among these systems, the Sentinel-1 mission, launched by the European Space Agency (ESA), operates at a wavelength of 5.6 cm in the C-band, providing valuable data for topographic and deformation studies (Torres et al., 2012). The mission consists of two satellites: Sentinel-1A, launched on

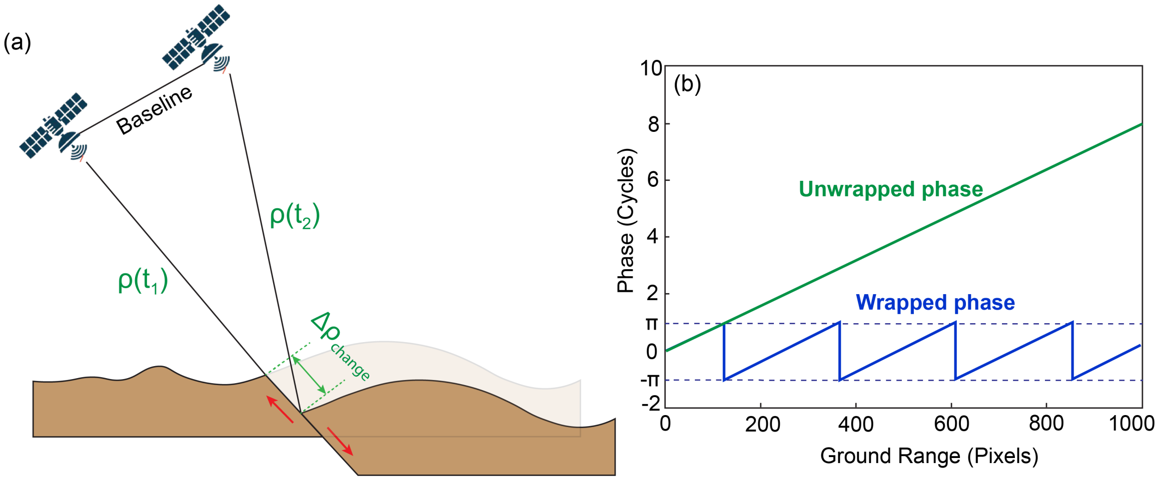

Figure 1.3: (a) Schematic representation of InSAR showing the geometry of satellite observations. Two SAR images are acquired at different times,t_1 and t_2, from slightly different positions. Baseline is the distance between the two satellites. The radar measures the distance, $\rho(t_1)$ and $\rho(t_2)$, to the Earth's surface at each observation. Changes in distance ($\Delta\rho_{\text{change}}$) between observations can indicate surface subsidence. (b) The concept of phase unwrapping in InSAR modified from Osmanoğlu et al. (2016). The wrapped phase (blue) is constrained between -π and +π, while the unwrapped phase (green) provides a continuous measurement of surface displacement, overcoming the 2π ambiguity.

April 3, 2014, and Sentinel-1B, launched on April 25, 2016. These satellites orbit 180° apart, enabling a revisit time of just six days for consistent Earth observation. However, Sentinel-1B has been unable to deliver radar data since December 23, 2021, due to an anomaly in the instrument electronics power supply from the satellite platform (Torres et al., 2017). The satellites primarily operate in Interferometric Wide (IW) mode, which covers a 250 km swath and provides systematic coverage of the Earth's landmasses and coastal waters. In this dissertation, Sentinel-1 data were utilized to conduct detailed analyses of surface deformation and related geophysical processes.

When a series of SAR images is available over a specific area, they can be combined into a series of interferograms to detect small amplitude, long duration displacement over time, resulting in multi-temporal InSAR. Time-series InSAR method estimates the spatial-temporal evolution of deformation over large areas by incorporating information from multiple SAR interferograms. Compared with traditional differential InSAR, it can mitigate the uncorrelated phase noise such as atmospheric propagation delay, thus reduce errors in deformation estimates (Casu et al., 2006). Current algorithms for multi-temporal InSAR can be broadly classified into two categories. The first is the Persistent Scatterer (PS) InSAR method, which focuses on pixels with consistent scattering properties over time and consistent viewing geometry (e.g., Ferretti et al., 2001; Hooper et al., 2007). The second is the Small Baseline (SB) approach (e.g., Berardino et al., 2002; Schmidt and Bürgmann, 2003), which uses redundant interferograms with perpendicular baseline and temporal baseline values below a threshold to limit the effects of geometric decorrelation. In the PS method, all interferograms are formed relative to a single master image, whereas the SB approach utilizes multi-master interferograms and directly investigates distributed scatters. Although there are many frameworks for time-series InSAR processing, e.g. Interferometric Point Target Analysis (IPTA) (Werner et al., 2003), Looking into Continents from Space with Small Baseline Subset (LiCSBAS) (Morishita et al., 2020), Permanent Scatterer InSAR (PSInSA) (Ferretti et al., 2001), Persistent Scatterer Pairs (PSP) (Costantini et al., 2008), Stanford Method for Persistent Scatterers (StaMPS) (Hooper et al., 2004, 2012), Small Baseline Subset (SBAS) (Berardino et al., 2002), SqueeSAR (Ferretti et al., 2011). Despite the differences in these methodologies, they share common basic principles and similar major processing steps, including image co-registration, spatial baseline estimation, interferograms generation, atmospheric delay correction, phase unwrapping, and inverting for mean line-of-sight velocity.

1.6 Using InSAR to analyze seismic cycle

Most earthquakes are caused by a sudden slip along a fault. Faults are relatively planar fractures in the Earth's crust along which the rocks on either side move in different directions (Figure 1.4a). However, rocks do not slide freely past each other but are instead locked for long periods by friction. Over decades to millennia, strain builds up within the rocks (Figure 1.4b). Eventually, the strain surpasses the frictional forces preventing slip, causing the fault to rupture (Figure 1.4c). At this point, rocks on either side of the fault slide rapidly to release the accumulated strain, resulting in an earthquake (Savage, 1983; Thatcher, 1975). After an earthquake, all three deformation mechanisms may exist and operate in different spaces and times (Figure 1.4).

The concept of the seismic "cycle" refers to the repeated rupture of a specific segment of a fault(Reid, 1910). This cycle can be divided into three phases: interseismic slip, co-seismic slip, and postseismic slip. However, the timing of earthquakes is irregular and influenced by various geological factors. Given the long-term nature of the timescale, historical and instrumental seismic records provide only a brief snapshot of the present-day deformation field within a short period. Traditional methods of measuring interseismic strain, such as ground-based geodetic surveys and the Global Positioning System (GPS), have been complemented by advanced remote sensing techniques. Among these, Interferometric Synthetic Aperture Radar (InSAR) has emerged as a powerful tool due to its high spatial resolution and ability to cover large areas. As earthquakes result from the long-term accumulation of strain in the crust, there are two ways to analyze seismic hazards using geodetic methods: (1) measuring the coseismic deformation during earthquakes; and (2) investigating the long-term time series of accumulated crustal displacement.

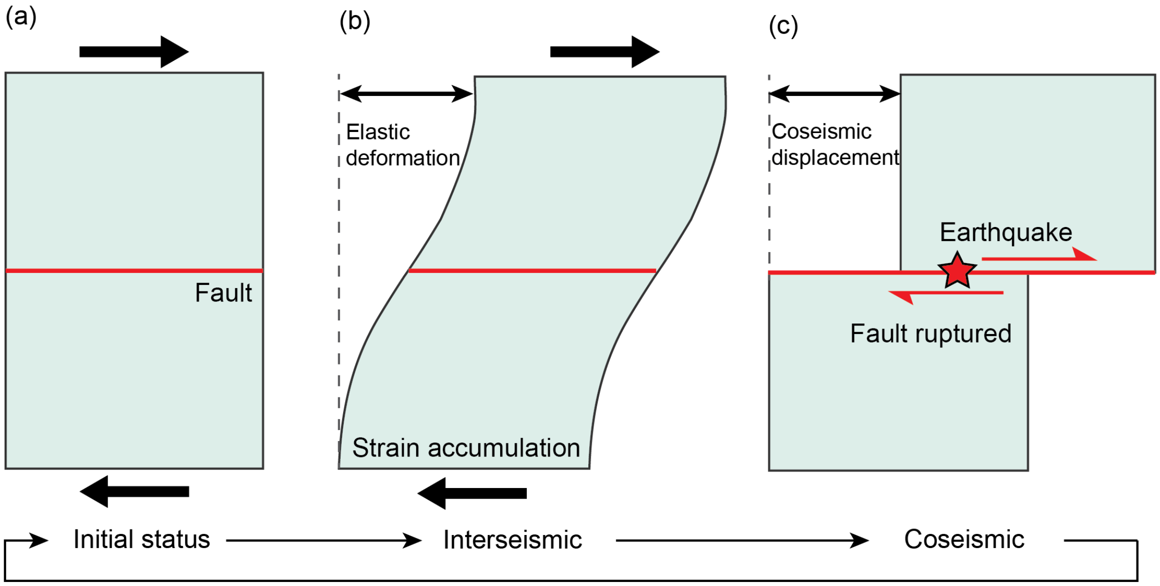

Figure 1.4: Schematic diagram of the earthquake cycle based on Reid (1910)'s elastic rebound model, adapted from Wright (2002). (a) Initial stage of the cycle, however, there is no specific time for the initial deformation time. (b) Interseismic period, during which faults are locked while plates continue to move. (c) Coseismic, where the fault slips abruptly, releasing energy in the earthquake.

1.6.1 Interseismic

The interseismic phase is the period of slow accumulation of elastic strain that coincides with the frictional locking of a fault between earthquakes (Reid, 1910). This period can last for decades to centuries. Quantifying interseismic strain accumulation provides insights into the stress loading on faults, the potential size of future earthquakes, and the overall mechanics of the earthquake cycle.

Radar signals can penetrate clouds and operate day and night, allowing for continuous monitoring regardless of weather conditions (Rosen et al., 2000; Bürgmann et al., 2000). Multi-temporal InSAR has been used to estimate interseismic strain accumulation along faults to identify aseismic deformation transients between two earthquakes. For instance, Fialko (2006) utilized InSAR to measure strain accumulation along the southern San Andreas Fault, revealing significant interseismic deformation approaching the end of the interseismic phase of the earthquake cycle. In the subduction zone, Béjar-Pizarro et al. (2013) showed that North Chile subduction zone is currently accumulating significant elastic shortening that is likely to rebound in a future tsunamigenic megathrust earthquake breaking the whole seismogenic zone. In the seismically active Himalayan region, InSAR has been employed to monitor interseismic strain along the Main Himalayan Thrust. Elliott et al. (2016) have contributed to understanding the strain accumulation in the Himalayas to demonstrate Himalayan topography may largely occur during the ongoing postseismic phase.

Different from faults that remain locked throughout the entire thickness of the seismogenic zone during the interseismic period, another process observed is steady fault creep, characterized by the continuous slip along a fault without the buildup of significant strain (Bürgmann et al., 2000). This phenomenon indicates minimal or absent frictional forces locking the fault. Near-surface creep can be readily detected as sharp offsets in interferograms (e.g., Bürgmann et al., 1998).

1.6.2 Coseismic

The sudden release of accumulated strain along a fault marks the coseismic phase. Since the pioneering use of InSAR to map the surface displacement caused by the 1992 M_w 7.3 Landers earthquake (Massonnet et al., 1993), this space geodetic technique has become standard for measuring coseismic deformation of shallow (<20 km) continental earthquakes (e.g., Funning et al., 2005; Jónsson et al., 2002; Nissen et al., 2007; Pousse-Beltran et al., 2020). By comparing radar images of the Earth's surface taken before and after an earthquake, InSAR can generate detailed maps of coseismic deformation.

Using interferograms that cover the rupture area, parameters such as fault geometry (including strike, dip, rake), depth, slip amount, location, and slip distribution at depth can be inverted using elastic dislocation theory to match the observed surface displacement fields (Okada, 1985). However, moderate to large earthquakes are often accompanied by many foreshocks and aftershocks within a short timeframe, ranging from several minutes to days (Helmstetter and Sornette, 2003). These seismic events can significantly contribute to the total slip pattern observed in the InSAR coseismic deformation field. The limited temporal resolution of InSAR, with revisit times of 6, 12, or even 24 days for Sentinel-1 data, poses a challenge in distinguishing between displacements caused by the mainshock and those from foreshocks and aftershocks. Conventional InSAR coseismic modelling often overlooks these sequences, potentially leading to overestimating coseismic slip. This overestimation can skew our understanding of earthquake mechanics, including seismic triggering processes and hazard assessments. In such cases, seismological methods are essential to provide a more robust fault mechanism solution.

1.6.3 Postseismic

The postseismic period, occurring minutes to years after an earthquake, is when the crust and fault both adjust to the state of crustal stress modified by the earthquake. Postseismic deformation reflects aseismic adjustments within the fault zone and bulk deformation of the surrounding area in response to the applied stresses, offering insights into the inelastic behaviour of the Earth's crust. Unlike the abrupt coseismic deformation, postseismic deformation typically follows a logarithmic or exponential decay over time and involves various mechanisms such as afterslip (Bürgmann et al., 2002; Freed, 2007), viscoelastic relaxation (Freed and Lin, 2001), and poroelastic rebound (Peltzer et al., 1996). Postseismic deformation has been extensively monitored using InSAR, highlighting the importance of afterslip and viscoelastic relaxation in the earthquake cycle (Biggs et al., 2007).

Afterslip is the continued slip along the fault plane after the mainshock. Marone et al. (1991) described how shallow afterslip in a velocity-strengthening region, such as near-surface creep, can occur following an earthquake. It usually occurs at depths adjacent to the rupture zone and can be effectively captured by InSAR (e.g., Ryder et al., 2007; Biggs et al., 2009; Daout et al., 2019). Viscoelastic relaxation involves the flow of the lower crust and upper mantle in response to the stress changes induced by the earthquake. This process usually has a longer decay time, often spanning years to decades. Similar to afterslip, viscoelastic relaxation following a large earthquake can result in postseismic motion observable by satellite geodesy, but will have a longer wavelength of deformation. Jackson et al. (2006) utilized InSAR time series data to investigate the deformation following two earthquakes in southwest Iceland, finding that viscoelastic models of a strong lower crust and a weak upper mantle could explain the magnitude and pattern of the deformation, whereas afterslip models alone were not compatible with the observations. These results suggest that afterslip may not play as significant a role in young and immature fault zones. Poroelastic rebound, resulting from the equilibration of the pore fluid pressure, has also been detected with InSAR, as demonstrated after the 1992 Landers earthquake (Peltzer et al., 1996).

1.7 Motivation

The Tian Shan serves as one of the best examples of intracontinental orogeny. The relative significance of interseismic, coseismic, and postseismic deformation in modifying geological structures and topography in regions of continental shortening remains uncertain. Historical earthquake records often do not cover the full recurrence intervals for individual faults. Therefore, utilizing data sources with different temporal and spatial coverage provides a valuable opportunity to enhance seismic hazard assessments.

Moreover, the prevalent strike-slip faulting within the Tian Shan and their geological relationship to the crustal shortening and earthquake hazards are important for understanding the dynamics of the intracontinental convergence. Dating and quantifying the magnitudes and rates of exhumation of crustal basement rocks in Tian Shan could provide quantitative constraints on the deformation processes. This dissertation endeavours to address these knowledge gaps, thereby enhancing our understanding of how seismic activity is related to the long-term geological evolution and how Tian Shan is accommodating the India-Eurasia collision.

1.8 Organization

For each of the chapters below, I also give a short summary of the main focus.

Chapter 1 reviews the geological history of Tian Shan, the motivation, and the research goals of this dissertation followed by an overview of the structure of the dissertation.

Chapter 2 examines the fault geometry associated with the 2020 M_w 6.0 Jiashi earthquake that occurred in the Kepingtag fold-and-thrust belt of southwestern Tian Shan by InSAR and seismology. This chapter investigates how coseismic deformation is accommodated in a structural setting characterized by thin-skinned, northward-dipping thrust sheets that detach in an Upper Cambrian décollement. The findings indicate significant structural control on the rupture extent, with the narrow and elongated slip pattern possibly due to an abrupt change in the dip angle where the Kepingtag thrust intersects the décollement.

Chapter 3 delves into the fault properties associated with the 2016 M_w 6.0 Hutubi earthquake in the northern Tian Shan foreland. This earthquake occurred in another typical fold-and-thrust belt developed along the mountain range. In this chapter, I use both coseismic interferograms and 5 years of InSAR data to perform small baseline time series analysis, which reveals a significant and intriguing pattern of fold growth following the earthquake. This study provides valuable insights into the postseismic deformation that controls the evolution of fold-and-thrust belts. The results indicate not only the immediate impact of the earthquake but also the longer-term geological adjustments in the region. This work contributes to a deeper understanding of the dynamic processes shaping the northern Tian Shan foreland.

Chapter 4 presents new thermochronological data and modelled time-temperature histories from the northern Tian Shan. Additionally, I have compiled and analyzed more than 1000 published apatite fission track (AFT) data and apatite (U-Th)/He (AHe) data from the Tian Shan, Pamir, and northern Tibet to reconstruct the exhumation rate history. The data and models are thoroughly discussed and interpreted. Our new AFT and AHe data from the northern Tian Shan near the western Bolokenu-Aqikekuduk Fault (BAF) indicate a significant increase in exhumation during the Miocene, with a total magnitude of ∼2 km during the late Cenozoic. This aligns with uplift rates extrapolated from the late Quaternary, suggesting the reactivation of the Paleozoic fault during the Miocene.

The timing of this rapid strike-slip deformation matches other major changes around the Tarim Basin, such as the expansion of the northeastern Tibetan Plateau and the northward advance of the Pamir. This implies that the current deformation pattern around the Tarim Basin was established by the Miocene. The clockwise rotation of the Tarim block plays an important role in accommodating and transferring the stress from the far-field collision zone.

Chapter 5 concludes the dissertation by summarising the key research outcomes and proposing directions and remaining open questions for future studies.

Within this dissertation, Chapter 2, Chapter 3, and Chapter 4 are written as individual papers intended for publication in scientific journals, incorporating the standard components of an abstract, introduction, background, methodology, results, discussion, and conclusion. As of the submission date, Chapter 2 has been published in the journal *Geophysical Journal International*. Chapter 4 was accepted by the journal *Lithosphere* on July 30, 2024, and is currently in press. Chapter 3 has been finalized and is currently under revision by my co-authors.

Chapter 2

Structural controls on coseismic rupture revealed by the 2020 M_w 6.0 Jiashi earthquake (Kepingtag belt, SW Tian Shan)

Article information

Siyu Wang[1*], Edwin Nissen[1], Léa Pousse-Beltran[1,2], Timothy J. Craig[3], Ruohong Jiao[1], and Eric A. Bergman[4]

[1] School of Earth and Ocean Sciences, University of Victoria, Victoria, BC, Canada
[2] Institut des Sciences de la Terre, Université Grenoble Alpes, Grenoble, France
[3] School of Earth and Environment, COMET, Institute of Geophysics and Tectonics, University of Leeds, Leeds, UK
[4] Global Seismological Services, Golden, CO, USA

Status: Published
Citation: Wang, S., Nissen, E., Pousse-Beltran, L., Craig, T. J., Jiao, R., & Bergman, E. A. (2022). Structural controls on coseismic rupture revealed by the 2020 M w 6.0 Jiashi earthquake (Kepingtag belt, SW Tian Shan, China). Geophysical Journal International, 230(3), 1895-1910. doi: 10.1093/gji/ggac159.
Corresponding author: Siyu Wang (siyuwang@uvic.ca)

Abstract

The Kepingtag (Kalpin) fold-and-thrust belt of the southern Chinese Tian Shan is characterized by active shortening and intense seismic activity. Geological cross-sections and seismic reflection profiles suggest thin-skinned, northward-dipping thrust sheets detached in an Upper Cambrian décollement. The January 19 2020 M_w 6.0 Jiashi earthquake provides an opportunity to investigate how coseismic deformation is accommodated in this structural setting. Coseismic surface deformation resolved with Sentinel-1 Interferometric Synthetic Aperture Radar (InSAR) is centered on the back limb of the frontal Kepingtag anticline. Elastic dislocation modelling suggests that the causative fault is located at ∼7 km depth and dips ∼7° northward, consistent with the inferred position of the décollement. Our calibrated relocation of the mainshock hypocentre is consistent with eastward, unilateral rupture of this fault. The narrow slip pattern (length ∼37 km but width only ∼9 km) implies that there is a strong structural or lithological control on the rupture extent, with up-dip slip propagation possibly halted by an abrupt change in dip angle where the Kepingtag thrust is inferred to branch off the décollement. A depth discrepancy between mainshock slip constrained by InSAR and teleseismic waveform modelling (∼7 km) and well-relocated aftershocks (∼10–20 km) may suggest that faults within sediments above the décollement exhibit velocity-strengthening friction.

2.1 Introduction

Late Cenozoic crustal deformation in central Asia is dominated by reverse and strike-slip faulting and folding within and around the margins of the Tian Shan mountains. Geodetic data indicate that ∼6–9 mm/yr of the present-day shortening occurs across the Chinese Tian Shan between the northwestern Tarim Basin and southern Kyrgyzstan (Reigber et al., 2001; Wang et al., 2020a). The Kepingtag (Kalpin) fold-and-thrust belt has developed along part of the southern margin of this range (Figure 2.1). This actively deforming belt is one of the most earthquake-prone regions of the Tian Shan and of China. In recent years, this intense seismicity has attracted much interest in the deformation style, rate and other characteristics of the Kepingtag belt (Allen et al., 1999; Zhou and Xu, 2000; Zhang et al., 2008; Yang et al., 2002, 2006; Ran et al., 2006). Furthermore, it is one of the few parts of Tian Shan where deformation can be seen stepping into the surrounding foreland, with emergent thrust sheets predominantly vergent toward the Tarim basin in the south. Therefore, the deformation of the Kepingtag belt can also inform how the mountain ranges of southern Tian Shan grow through time.

Fold-and-thrust belts pose distinct challenges for seismic hazard assessment since much of the active faulting is buried. This is exemplified by iconic earthquakes such as the 1978 M_s 7.4 Tabas, Iran earthquake (Walker et al., 2003) and the 1987 M_w 5.9 Whittier and 1994 M_w 6.7 Northridge, California earthquakes (e.g., Davis et al., 1989; Jones et al., 1994), each characterized by shallow folding and blind faulting without accompanying surface rupture. There are many other examples of large earthquakes that ruptured faults that were not previously mapped, and where historical and instrumental records were too short to have revealed the associated seismic hazard beforehand. Furthermore, fold-and-thrust belts contain a wide range of fault structures including décollements and ramp-and-flat thrusts, and it is often not clear which of these host large earthquakes and which creep aseismically (e.g., Copley, 2014; Ainscoe et al., 2017; Mallick et al., 2021). It is also important to consider how subsurface structure and stratigraphy may influence rupture extents, and thus potential earthquake magnitudes (e.g., Elliott et al., 2011; Nissen et al., 2011).

On January 19 2020 at 13:27:56 UTC, a M_w 6.0 earthquake struck near Jiashi in the western Kepingtag belt (∼39.83°N, 77.21°E) (Figure 2.1), causing intense ground shaking and damage to hundreds of buildings. A regional seismic network recorded 1,639 aftershocks as of February 11 2020 (Ran et al., 2020), with the largest (M_b 5.1) occurring ∼1 hour after the mainshock. This sequence provides an opportunity to investigate patterns of seismicity and deformation in this region. Routine teleseismic moment tensor solutions for the mainshock from the U.S. Geological Survey (USGS) and the Global Centroid Moment Tensor project (GCMT) implicate thrust or reverse faulting, but exhibit discrepancies of tens of degrees in strike, dip, and rake and of several kilometres in centroid depth and location. This makes it difficult to associate the earthquake with specific faulting or characterize its tectonic implications without further investigation (Engdahl et al., 2006; Weston et al., 2011; Wimpenny and Scott Watson, 2020).

Interferometric Synthetic Aperture Radar (InSAR) observations and modelling can provide more precise constraints on fault geometries and depth extents of large, shallow continental earthquakes (e.g., Elliott et al., 2016). Furthermore, growing compilations of seismic phase arrival times can help relocate earthquake hypocentres

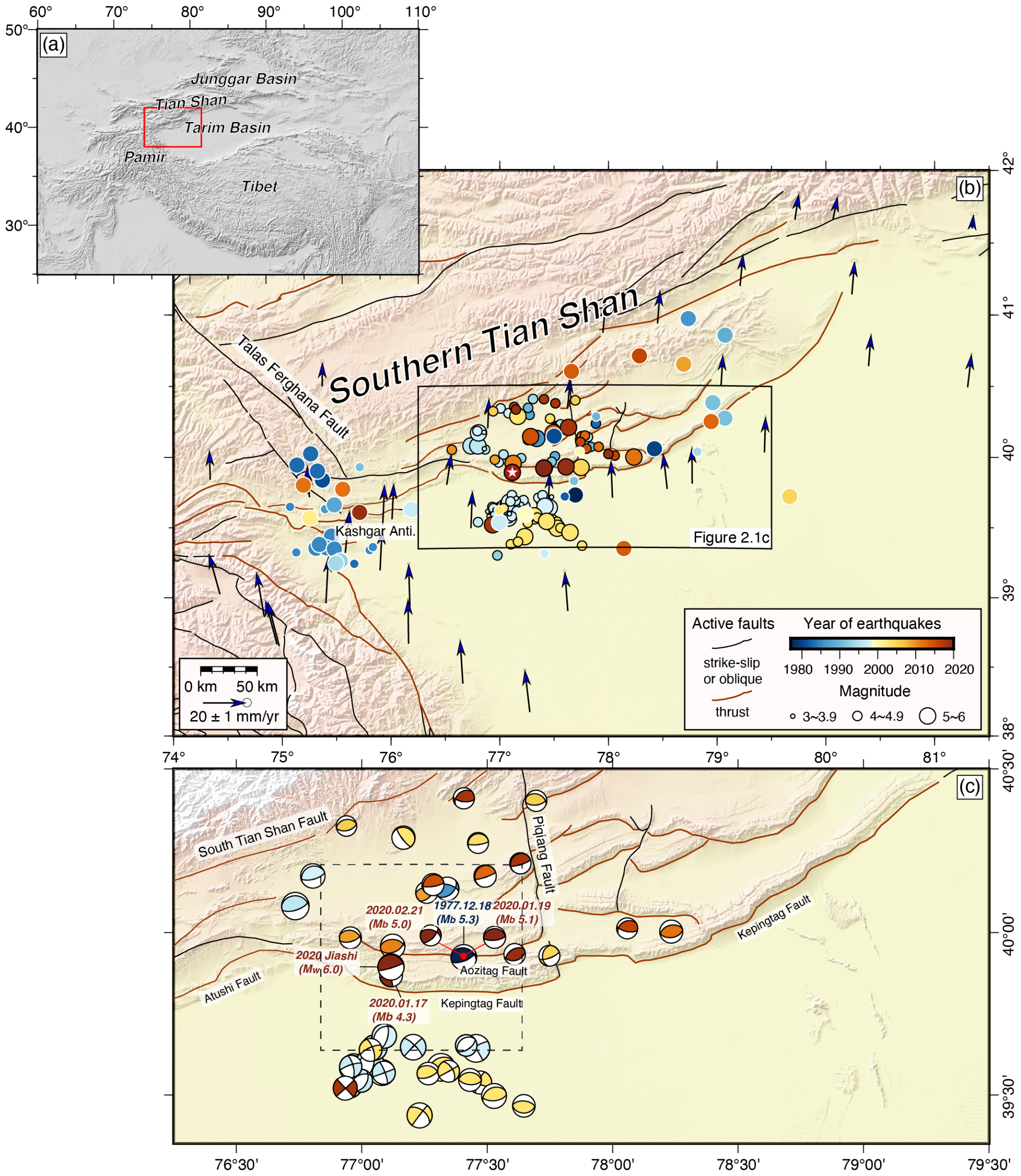

Figure 2.1: Tectonics and seismicity of the study area. (a) Shaded relief of the Himalayan orogeny with the location of panel (b) outlined in red. (b) Tectonic map of the southern Tian Shan. Instrumental seismicity is scaled by magnitude and coloured by year from 1977.12.18 to 2020.02.21. Our own relocated epicentres are shown with black outlines, while those from the United States Geological Survey (USGS) have white outlines. The white star is the relocated epicentre of the 2020 January 19 Jiashi mainshock. Active faults are from the online database provided by the Institute of Geology, China Earthquake Administration (http://www.neotectonics.cn/arcgis/apps/webappviewer) and Global Navigation Satellite Systems (GNSS) velocities relative to stable Eurasia are from Wang et al. (2020a) with 95% confidence ellipses. (c) Topography, active faults, and earthquakes of the Kepingtag fold-and-thrust belt. Focal mechanisms are from teleseismic body-waveform modelling studies or the Global Centroid Moment Tensor (CGMT) catalogue (see Table 2.1 for details). They are plotted at our relocated epicentres, coloured by year and scaled by magnitude. The black dashed box shows the location of Figure 2.2.

more accurately which, in conjunction with InSAR slip models, can provide additional information on rupture directivity (e.g., Pousse-Beltran et al., 2020). In this paper, we map the surface deformation of the 2020 Jiashi earthquake using the Sentinel-1 InSAR imagery and characterize its subsurface fault geometry and slip distribution using elastic dislocation modelling. We provide an independent check on its mechanism and centroid depth using teleseismic body waveform modelling and pinpoint its hypocentre using a calibrated, multi-event relocation. We relate some striking features of the surface deformation and slip model to the subsurface structure of the Kepingtag belt. Our multi-event relocation also allows us to reassess earlier instrumental earthquakes in this region. These new results are used to reevaluate the active tectonics and seismic hazards of the Kepingtag belt.

Table 2.1: Earthquake source parameters in the Kepingtag belt and its foreland. Relocated hypocentres are from this study. The focal depth (FD) is followed by a superscript letter describing how it was calibrated: d = teleseismic depth phases, l = local-distance readings, n = near-source station readings, and c = cluster default depths. Focal mechanisms are taken from *(1)* Fan et al. (1994), *(2)* Sloan et al. (2011), *(3)* Ghose et al. (1998), *(4)* the Global Centroid Moment Tensor (GCMT) catalogue, and *(5)* this study. The centroid depth (CD) is also given a superscript letter that describes whether it was obtained by modelling (t) teleseismic body-waveforms, (d) teleseismic depth phases, (r) regional waveforms, or (i) = InSAR surface displacements. Where only a less reliable GCMT centroid depth is available, we mark the solution with an asterisk.

		Relocated hypocentre			*Focal mechanism*					
Date	Time	Long.	Lat.	FD (km)	CD (km)	Strike	Dip	Rake	M_w	Ref.
1977.12.18	16:47	77.4065	39.9236	22^d	7^t	74	51	79	5.8	*1*
1986.04.25	16:12	77.3404	40.1340	13^d	15*	283	60	125	5.4	*4*
1996.03.19	15:00	76.7353	40.0810	13^l	34^t	234	16	87	6.0	*2*
1996.03.20	00:14	76.8644	40.0562	17^l	6^r	268	20	76	4.5	*3*
1996.03.22	08:26	76.7983	40.0816	15^l	6^r	260	18	78	5.2	*3*
1996.04.02	02:28	77.5587	40.2328	10^l	16^r	242	59	128	4.1	*3*
1997.01.21	01:48	77.2050	39.6475	11^l	12^t	317	85	177	5.4	*2*
1997.01.29	08:20	76.9678	39.5923	12^l	33*	04	83	132	5.2	*4*
1997.03.01	06:04	76.9532	39.5288	14^l	14^d	180	80	−173	5.6	*2,4*
1997.04.05	23:36	76.9622	39.5832	12^l	18^t	177	64	−139	5.4	*2*

Continued on next page

		Relocated hypocentre			*Focal mechanism*					
Date	Time	Long.	Lat.	FD (km)	CD (km)	Strike	Dip	Rake	M_w	Ref.
1997.04.06	04:36	77.0809	39.5694	12^l	17^t	246	41	−74	5.8	*2*
1997.04.06	12:58	77.0324	39.6105	17^l	13^t	210	38	−74	5.1	*2*
1997.04.11	05:34	77.0326	39.6023	15^n	20^t	226	42	−79	6.0	*2*
1997.04.12	21:09	77.0039	39.5334	14^n	16^t	239	27	−74	5.1	*2*
1997.04.15	18:19	77.0506	39.6461	14^n	18^t	177	64	−139	5.7	*2*
1997.06.24	09:24	76.9562	39.5877	16^n	34*	345	72	−167	5.1	*4*
1997.10.17	17:35	77.0875	39.5686	25^d	33*	177	64	−139	5.3	*4*
1998.03.19	13:51	76.8048	40.1732	15^l	15^d	243	5	79	5.6	*2,4*
1998.08.02	04:40	77.0897	39.6817	10^d	15^t	173	40	−140	5.5	*2*
1998.08.03	15:15	77.0905	39.6527	15^l	29^r	253	10	129	4.6	*2*
1998.08.27	09:03	77.4554	39.6437	16^l	15^t	57	80	1	6.3	*2*
1998.09.03	06:43	77.4162	39.6528	25^d	10^r	179	59	178	4.8	*2*
1998.10.31	16:09	77.2469	39.6081	19^l	14^r	152	74	−164	4.6	*2*
2003.01.04	11:07	77.0350	39.6389	14^l	33*	245	73	−20	5.2	*4*
2003.02.24	02:03	77.3157	39.5852	19^l	5^t	280	17	115	6.2	*2*
2003.02.24	21:18	77.2653	39.5663	12^l	15*	289	33	126	5.2	*4*
2003.02.25	03:52	77.4717	39.5385	8^l	15*	239	33	62	5.3	*4*
2003.03.12	04:47	77.5273	39.4969	8^l	7^d	245	33	73	5.7	*2,4*
2003.03.15	22:59	77.3459	39.5733	9^l	15*	330	57	178	5.0	*4*
2003.03.30	23:15	77.4315	39.5462	17^l	10^t	287	27	117	5.2	*2*
2003.05.04	15:44	77.2305	39.4369	9^l	15*	308	53	179	5.8	*4*
2003.06.04	16:28	77.6458	39.4665	10^l	10^d	274	54	92	5.2	*2,4*
2003.09.26	23:35	77.1664	40.2902	30^d	15*	290	13	58	5.3	*4*
2004.10.07	16:14	77.4633	40.2740	12^l	17*	245	14	72	4.8	*4*
2005.03.24	07:37	77.7478	39.9288	11^d	30*	187	35	32	4.8	*4*
2006.06.08	11:34	77.6951	40.4025	6^d	30*	290	35	113	4.8	*4*
2006.09.06	07:51	76.9389	40.3257	15^l	32*	258	37	91	4.7	*4*
2009.04.22	09:26	77.2583	40.1229	11^d	16*	264	50	124	5.0	*4*
2009.10.16	02:56	76.9545	39.9836	15^d	19*	284	32	116	5.0	*4*
2011.08.11	10:06	77.1232	39.9575	19^d	12*	272	42	109	5.6	*4*
2012.08.11	09:34	78.2335	40.0027	15^d	12*	255	43	84	5.3	*4*

Continued on next page

		Relocated hypocentre			*Focal mechanism*					
Date	Time	Long.	Lat.	FD (km)	CD (km)	Strike	Dip	Rake	M_w	Ref.
2013.03.11	03:01	77.4916	40.1729	9^d	12*	210	11	50	5.2	*4*
2015.01.10	06:50	77.2838	40.1469	14^c	15*	227	17	57	5.1	*4*
2016.07.09	16:36	78.0578	40.0128	14^c	12*	240	32	53	4.8	*4*
2018.04.12	10:41	77.4068	40.4104	17^l	22*	231	36	50	4.9	*4*
2018.09.03	21:52	76.9341	39.5211	14^c	15*	317	89	178	5.5	*4*
2018.11.03	21:36	77.6323	40.2120	14^c	12*	225	12	63	4.9	*4*
2019.01.06	16:22	77.6093	39.9331	6^d	12*	238	50	79	4.9	*4*
2020.01.17	16:05	77.1167	39.8682	12^d	21*	261	86	−178	5.3	*4*
2020.01.19	13:27	77.1161	39.8944	11^d	7^i	279	7	115	6.0	*5*
2020.01.19	14:23	77.4089	39.9236	14^c	18*	268	22	95	5.1	*4*
2020.02.21	15:39	77.4059	39.9232	14^c	14*	287	46	143	4.8	*4*

2.2 Tectonic Setting

The Tian Shan in Central Asia originally formed in the Paleozoic, and most of the present topography of the mountain ranges resulted from Cenozoic reactivation as a result of the India-Eurasia collision (Windley et al., 1990; Hendrix et al., 1992; Avouac et al., 1993a; Burchfiel et al., 1999). Over time, the deformation has propagated outward into the Tarim and Junggar basins, where along certain parts of the Tian Shan margins, intense folding and faulting have created sets of narrow ridges. The Kepingtag fold-and-thrust belt, located along the arid southern margin of the Chinese Tian Shan, offers one of the clearest examples of this basinward migration of active deformation (Figure 2.1b).

2.2.1 Geology of the Kepingtag belt

About 200 km long by 50 km wide and trending WSW–ENE, the Kepingtag belt consists of fault-related folds associated with a series of south-verging, imbricated thrust stacks (Allen et al., 1999). Folded strata are composed of Cambrian–Ordovician Qiulitag group limestones, Middle Ordovician Saergan group limestone and dolomite, Silurian Kepingtag group sandstone, Devonian sandstone, Carboniferous Kangkelin group sandstone, lower Permian limestone, and Paleogene–Neogene Wuqia group sandstone and conglomerate (Chen et al., 2006a; Yang et al., 2010). The thickness of the upper Paleozoic strata in the Kepingtag belt increases from about 2 km in the south to greater than 4 km in the north (Yin et al., 1998). There is a major angular unconformity between the Paleozoic strata and the Cenozoic foreland basin deposits, with the near absence of Mesozoic sedimentary rocks implying significant Paleozoic crustal shortening.

The thick Paleozoic sequence of mainly Upper Cambrian to Permian strata is exposed in a series of parallel anticlines (Xinjiang Bureau of Geology and Mineral Resources, 1993). The hanging wall cut-offs of the imbricate thrusts have been eroded away. This thrust system is interpreted as thin-skinned, with fault-propagation folds detached in Upper Cambrian limestones along a décollement at ∼6–10 km depth according to seismic reflection profiles and balanced geological cross-sections (Allen et al., 1999; Yin et al., 1998; Nishidai and Berry, 1990; Yang et al., 2010). The left-lateral Piqiang fault (Figure 2.1) has developed perpendicular to the Kepingtag belt, dividing it into two (western and eastern) segments. Interpretations of satellite imagery and balanced cross-sections suggest that the thin-skinned imbricate thrusting and folding has accommodated crustal shortening strains of 20–28% between the main Tian Shan and Tarim block, equivalent to ∼35 km across the western segment and ∼22 km across the eastern segment (Allen et al., 1999; Yin et al., 1998).

2.2.2 Seismicity of the Kepingtag belt and its foreland

Active crustal shortening and thickening of the southern Tian Shan are manifest in frequent reverse faulting earthquakes that cluster around the margins of the high topography with nodal planes oriented approximately parallel to the range (Ghose et al., 1998; Xu et al., 2006; Sloan et al., 2011). The Kepingtag belt and its adjacent foreland are amongst the most seismically active parts of the Tian Shan, with thirty-six earthquakes of M_w 5.0–6.3 since the late 1970s (Figure 2.1b and Table 2.1). The 1902 M_w 7.7 Atushi (Kashgar) earthquake, located ∼150 km west of our study area, hints that much larger earthquakes may be possible (Kulikova and Krüger, 2017). Within the Kepingtag belt, instrumental seismicity is concentrated west of the Piqiang fault and the available focal mechanisms indicate a predominance of thrust and reverse faulting. Assuming that northward-dipping nodal planes represent faulting, dip angles range from ∼5°–60° with an average of around 30°. Only a few of these events have reliable centroid depths from detailed waveform modelling, mostly in the range 6–16 km, consistent with faulting within the lower sedimentary cover and the underlying basement (Fan et al., 1994; Ghose et al., 1998; Sloan et al., 2011). Sloan et al. (2011) placed a single outlier event at 34 km depth, within the middle-to-lower crust, but noted that its relatively complex waveforms could potentially be explained by a compound (multi-event) source mechanism at a much shallower depth.

Between 1997 and 1998, thirteen earthquakes of M_w 5.0–6.3 struck the foreland south of the Kepingtag belt. These included the destructive January-October 1997 Jiashi earthquake swarm, which caused 21 fatalities (Zhang et al., 1999). This sequence involved a mix of strike-slip and normal faulting with well-resolved centroid depths of ∼12–20 km (Sloan et al., 2011), as well as some smaller, deeper earthquakes located by a temporary regional network but without reliable focal mechanisms (Xu et al., 2006). The mechanisms and depths are challenging to interpret but may reflect flexural rebound of the Tarim basin under loading from the Tian Shan (Sloan et al., 2011). On February 24 2003, the M_w 6.2 Bachu-Jiashi earthquake struck the same area, resulting in 261 reported fatalities. In contrast with the 1997 swarm, the 2003 earthquake involved northward-dipping thrust faulting with a much shallower centroid depth of ∼5–7 km, interpreted to represent southward propagation of the Kepingtag belt into the Tarim basin (Sloan et al., 2011). It also produced an abundant aftershock sequence that was apparently concentrated in the middle crust between ∼15–25 km (Huang et al., 2006). Following the 2003 Bachu-Jiashi sequence, the Kepingtag belt and its foreland entered a relatively quiescent period of seismic activity, with no earthquake of magnitude 6 or above until the January 19 2020 event.

The 2020 Jiashi sequence occurred within the frontal, western Kepingtag belt. The sequence was recorded by thirteen permanent stations at ∼30–170 km distance and by two local stations ∼20 km SW and NW of the mainshock epicentre, which were deployed by the Xinjiang Earthquake Administration 4 and 18 hours after the mainshock, respectively. These regional recordings have been used as the basis of three previous seismological studies of the sequence, summarized below (Ran et al., 2020; Yao et al., 2021a; He et al., 2021). The M_w 6.0 mainshock was preceded by two days of foreshock activity involving ∼N–S-oriented left-lateral strike-slip faulting. The mainshock itself ruptured an ∼E–W-oriented thrust or reverse fault, though there is disagreement amongst available seismological and geodetic models on its geometry and depth, which will be discussed further in light of our own results in Section 2.4. The mainshock was followed by an energetic aftershock sequence of several hundred events that lasted at least three months. Double-difference relocated seismicity forms a ‘T’ shaped pattern in map view, with the mainshock located at the bottom of the ‘T’ and aftershocks extending ∼20 km northward to the junction of the ‘T’, and from there, ∼20 km east and west for a total length of ∼40 km, with the greatest concentration of events along the western branch (Ran et al., 2020; Yao et al., 2021a; He et al., 2021). The double differencing also shows that the aftershocks are concentrated at depths of 10–20 km (Figures A.12 and A.13).

2.3 Methods

2.3.1 InSAR measurements and modelling

We used InSAR to measure surface deformation in the January 19 2020 earthquake, and elastic dislocation modelling to estimate the fault geometry and slip distribution. The raw data are from the European Space Agency’s C-band Sentinel-1A satellite, with wavelength ∼5.6 cm. Two ascending tracks (056A and 129A) and one descending track (034D) capture the Jiashi mainshock. Three, 12 day coseismic interferograms (January 11–23, January 16–28 and January 10-22 2020) were processed using GAMMA software (Werner et al., 2000) and multi-looked to four looks in range and twenty in azimuth to achieve a ∼30 m × 30 m pixel resolution. The topographic phase contribution was removed using the 30 m-resolution Shuttle Radar Topographic Mission Digital Elevation Model, which was also used to geocode the interferograms. The two ascending-track interferograms were unwrapped using the branch-cut algorithm (Goldstein et al., 1988) while the noisier, descending-track interferogram was unwrapped using the Minimum Cost Flow algorithm.

The interferograms exhibit excellent coherence, reflecting the dry desert conditions and sparse vegetation of the southwestern Tian Shan. Coseismic surface deformation is easily distinguished in all three interferograms as a double fringe ellipse elongated in an E-W orientation (Figure 2.2a, d, g). The southern lobe is focused on the Kepingtag anticline and exhibits up to ∼7.5 cm of line-of-sight (LOS) displacement toward the satellite, and the northern lobe is centered along the Aozitag anticline and contains up to ∼5 cm of displacement away from the satellite (Figure 2.7a–c). The similarity of the fringe patterns in ascending and descending interferograms implies that the largest contribution to the observed LOS deformation is from uplift/subsidence rather than E/W lateral displacement, consistent with predominantly dip-slip faulting. We also observe some localized deformation along the southern Kepingtag rangefront its proximal foreland basin. The short wavelengths, and absence of shallow aftershocks in this area, hint that this deformation is caused by secondary effects such as landsliding or liquefaction, and/or subsidence from agricultural activity (e.g. through aquifer drawdown).

After downsampling the LOS displacements using a quadtree algorithm to concentrate sampling in regions with high phase variance (Jónsson et al., 2002), we employed a routine, two-step inversion strategy to estimate the causative fault parameters (e.g. Wright et al., 1999, 2004; Funning et al., 2005; Elliott et al., 2013, 2015; Ainscoe et al., 2017; Pousse-Beltran et al., 2020). In the first step, we inverted the downsampled data to solve for the optimal strike, dip, rake, slip, length, and top and bottom depths of a rectangular, uniform slip model fault plane buried within an elastic half-space; we also jointly solved for nuisance parameters (a static shift and linear ramp in LOS displacement for each interferogram to account for their different unwrapping reference points, satellite orbital errors, and long-wavelength lateral variations in tropospheric delay) and weighted the single descending interferogram equal to the two ascending interferograms. We used Okada's expressions (Okada, 1985) to relate model fault slip

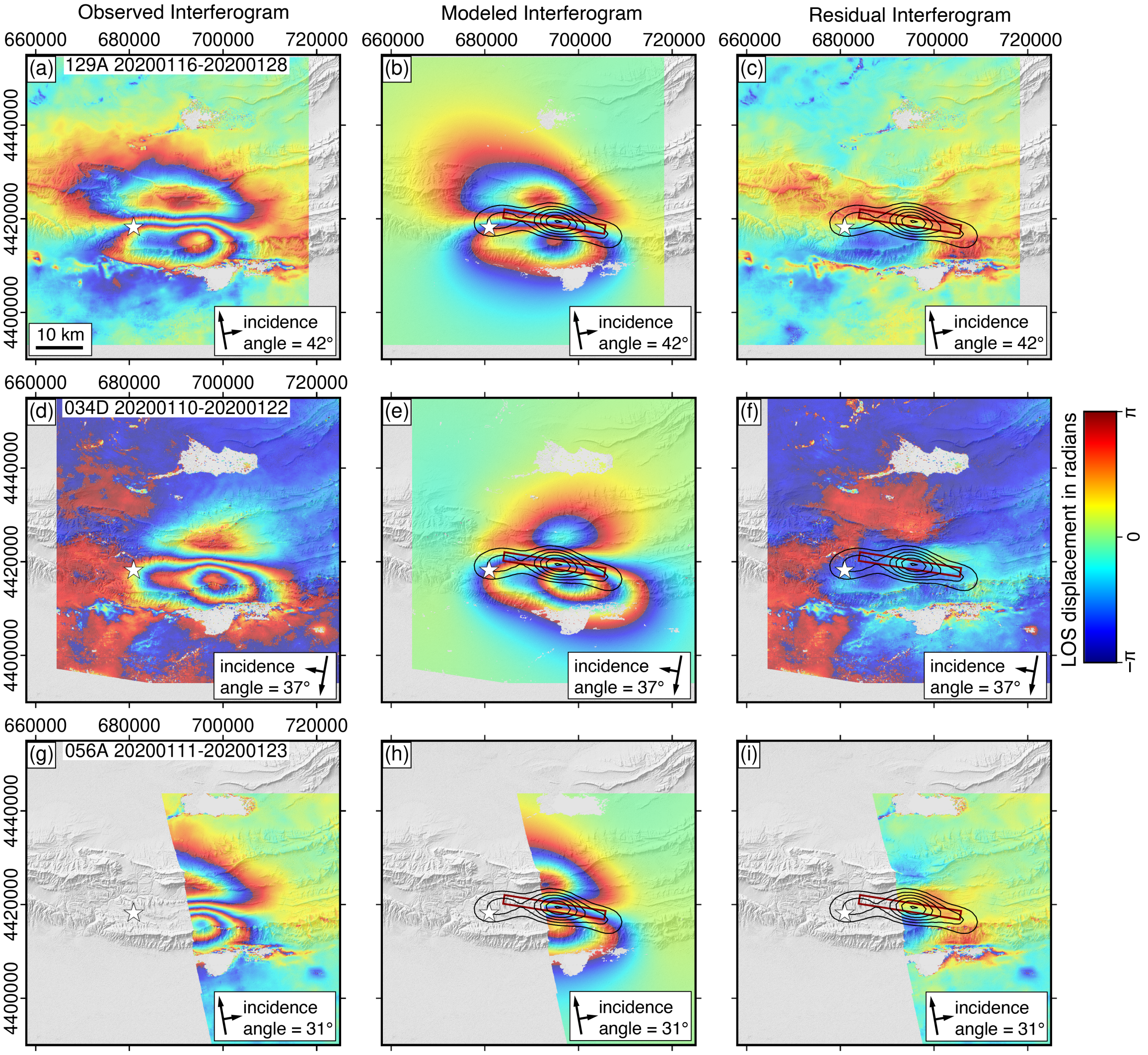

Figure 2.2: (Left column) Observed, (center) distributed slip model and (right) residual interferograms of the 2020 Jiashi mainshock rupture. Modelling was performed using unwrapped LOS displacements, but here we plot the original, wrapped (filtered) interferograms since these show more clearly the shape of the deformation field. The coordinates are in UTM 43N. Color cycles of blue through yellow to red indicate motion away from the satellite and one color cycle (2π radians) represents a half radar wavelength (2.8 cm) of LOS displacement. The satellite track azimuths and LOS direction with local angle of incidence are indicated by the longer and shorter black arrows, respectively. The white star indicates the relocated mainshock epicentre. In the central and right-hand panels, ten-centimeter model slip contours are shown in black and the outline of the uniform slip model fault plane is marked in dark red.

to deformation of the free surface, applied a non-linear, downhill Powell's algorithm (Press et al., 1992) to obtain the minimum misfit parameters, and ran 500 Monte Carlo restarts with random starting parameters to sample the parameter space fully and avoid local minima (Wright et al., 1999). Without firm constraints on how rheological properties vary with depth locally, we assumed an elastic half-space with standard Lamé parameters (λ and μ) of 3.2×10^{10} Pa. We anticipate that this assumption only moderately impacts the retrieved fault parameters; for example, tests of layered and half-space elastic structures for a similar magnitude, buried earthquake in Tibet showed differences of <1° in fault strike and dip, ∼6° in rake, 0.2–0.5 km in fault length, top and bottom depths, and center coordinates, and 5–8% in slip and moment (Bie et al., 2014). We also assumed a flat free surface, which is appropriate given the limited (<1 km) relief across the study area and is not expected to impact the retrieved fault parameters significantly (Li and Barnhart, 2020). Finding a trade-off between slip and fault width — which is common for buried earthquakes (e.g. Funning et al., 2005; Elliott et al., 2013) — we obtained the initial fault geometry by fixing slip to 1.0 m. Inversions performed with 0.5 m, 1.5 m and 2.0 m show that this choice makes no significant difference to the resulting fault geometry, with variations of <1° in the resulting model fault strike, dip and rake, and <0.5 km in fault length and fault center point latitude, longitude and depth (Table A.1).

In the second step, we estimated the slip distribution by extending the uniform slip model fault plane along strike and up- and down-dip, dividing it into 1 km × 1 km sub-fault patches, and solving for slip on each patch (with rake fixed to the uniform slip solution) using a Laplacian operator to vary smoothing (Wright et al., 2004; Funning et al., 2005) and a non-negative least squares algorithm to ensure positive slip (Bro and De Jong, 1997). We solved for the best-fitting slip model and nuisance parameters, m, using the equation,

$$\begin{pmatrix} \mathbf{G} \\ \kappa\nabla^2 \end{pmatrix} \mathbf{m} = \begin{pmatrix} \mathbf{d} \\ 0 \end{pmatrix}$$

where G is the matrix of Green's functions (LOS displacements calculated at downsampled data locations using the formulation of Okada (1985) for 1 m of slip on each fault patch), ∇^2 is the finite difference approximation of the Laplacian operator which acts to smooth the distribution of slip, κ is a scalar smoothing factor which determines the relative importance of the smoothing operator, and d contains the downsampled LOS displacements. We settled upon a preferred smoothing factor that represents a compromise between decreasing the fault slip roughness to prevent unrealistic, oscillating slip distributions, while minimizing the resulting increase in misfit (Wright et al., 2004). The resulting model still included a few outlier slip patches that lay several kilometres up-dip from the main slip distribution, which we consider spurious and exclude from our final, reported results, that were used to generate the forward model and residual interferograms shown in Figure 2.2.

Given the structural complexity of the Kepingtag belt, we also investigated whether the Jiashi earthquake may have involved non-planar rupture geometries by inverting the InSAR displacements for two uniform slip model fault planes (e.g., Pousse-Beltran et al., 2020). We explored a range of listric and anti-listric configurations by matching the top depth of a deeper model fault to the bottom depth of a shallower model fault, and allowing their dips to vary independently and up to angles as steep as 32.5°. Though the large number of free parameters in these two-fault models makes it challenging to explore fully this parameter space, none of the two-fault configurations that we tested produced a realistic geometry that improved upon the misfit of the simple, single-fault model. This leads us to favour involvement of a single, planar fault.

We did not have access to GNSS data that could potentially constrain our slip model further, though we know of six stations within ∼100 km of the mainshock that may have exhibited coseismic offsets (Figure 2.1; Wang et al. (2020a)).

2.3.2 Calibrated hypocentre relocations

We relocated hypocentres of the January 19 2020 Jiashi mainshock and its principal foreshock (m_b 4.3) and two largest aftershocks (m_b 5.1 and 5.0) using teleseismic, regional and local seismic phase arrival times. Thirty-seven well-recorded background events starting from 2003 were also relocated, providing the repeated phase observations at common stations and the improved azimuthal coverage at local distances needed to calibrate the cluster, by which we mean minimizing hypocentral biases from unknown Earth structure and reliably quantifying their uncertainties (Bergman et al., 2022). We adopt the Hypocentroidal Decomposition relocation approach of Jordan and Sverdrup (1981) which separates the relocation into two distinct inverse problems, each reliant on customized phase arrival time data. We solve first for the relative locations of each hypocentre with respect to the reference hypocentroid (defined as the arithmetic mean of all individual event hypocentres within the cluster) using arrival data at all distances, allowing us to capitalize upon the abundance of teleseismic phase picks available for larger events in the cluster. We then solve for the absolute location of the hypocentre using only locally recorded, direct *Pg* and *Sg* phases, which are impacted least by unknown Earth structure. This enables us to update the absolute hypocentre coordinates of every event in the cluster. In other, comparably instrumented regions, direct calibrations (ones that utilize local seismic data to solve for the hypocentroid) have resolved epicentres to within ∼1–2 km (at 90% confidence) and focal depths to within ∼5 km (Karasözen et al., 2019), improving substantially on the uncertainties of routine catalogues such as the USGS and GCMT (Engdahl et al., 2006). Juxtaposing calibrated epicentres with InSAR-derived slip models can distinguish bilateral from unilateral rupture propagation (e.g., Gaudreau et al., 2019; Pousse-Beltran et al., 2020) and help resolve ambiguities in subsurface fault geometry, which are otherwise commonplace for buried earthquakes (e.g., Roustaei et al., 2010; Copley et al., 2015; Elliott et al., 2015; Karasözen et al., 2018).

The cluster was relocated and calibrated in the *Mloc* program (Walker et al., 2011; Karasözen et al., 2016; Bergman et al., 2022) using a customized travel-time model (Table A.2) comprising a 3-layered crust of thickness 50 km — consistent with several previous estimates of regional Moho depths (Gao et al. (2013) and references therein) — over the upper mantle portion of the global 1D model ak135 (Kennett et al., 1995). For the best-recorded events, we estimated focal depths using local arrival times; for others, we relied upon teleseismic depth phases or simply fixed the focal depth to a representative cluster default of 14 km (Figure A.1). We estimated the hypocentroid using epicentral distances of up to 2°, for which there is excellent azimuthal coverage (Figure A.2); average residual travel times for phases used in this direct calibration are 0.0 sec for *Pg* and 0.1 sec for *Sg* (Figure A.3). Observed phase arrivals and theoretical travel times for distances of up to 4°, 15° (for shear phases), and 30° are shown in Supplementary Figures A.4, A.5, and A.6.

Our results were then combined with an earlier *Mloc* relocation cluster focused on the 1997 Jiashi earthquake swarm and the 2003 Bachu-Jiashi earthquake in the foreland south of the Kepingtag belt (Bergman et al., 2022). The earlier cluster adopted the same relocation procedure and the same regional velocity structure for the crust and upper mantle as this study. The earlier cluster is available through the Global Catalog of Calibrated Earthquake Locations (GCCEL) database (Bergman et al., 2022) and figures in the main paper incorporate both relocated datasets.

2.3.3 Teleseismic body waveform inversion

Finally, we used teleseismic body waveform modelling to provide additional constraints on the mainshock source depth and mechanism, complementing those from InSAR analysis. Modelling of both seismological and geodetic data is important when there are disagreements in the depth of faulting, as is the case for the Jiashi earthquake (see Section 2.4). Centroid depths obtained from waveform modelling can also help clarify whether fault slip resolved by InSAR models occurred coseismically or through afterslip (Nissen et al., 2014).

We followed the approach of Heimann et al. (2018), and inverted vertical and transverse component data from stations between 3,300 km and 9,900 km from the reported earthquake location (Supplementary Figure A.7). Waveforms were filtered between 0.01 and 1 Hz, and we used a window starting 15 seconds before, and ending 25 seconds after, the principle phase (P for vertical component waveforms, S for transverse component waveforms). Synthetic seismograms were generated using the velocity structure determined in our calibrated relocation (Section 2.3.2 and Supplementary Table A.2). The source-time function is constrained to be a variable-duration half-sinusoid — appropriate for an earthquake of this size, and for the frequencies used in our inversions. Observed data and synthetics were aligned using cross correlation. The Bayesian approach outlined in Heimann et al. (2018) allows for the full sampling of the parameter space available in source depth, latitude, longitude, magnitude, and mechanism (Supplementary Figures A.8 and A.9). Misfits between observed and synthetic waveforms are plotted in Supplementary Figures A.10 and A.11.

2.4 Results

Our best-fitting InSAR uniform slip model fault strikes 279°, dips 7° N, has a slight right-lateral component (rake 115°), and is ∼22 km long by ∼2 km wide, centered at 7 km depth (Table 2.2). To further test model sensitivity to centroid depth, we ran the inversion by prescribing different (fixed) top and bottom depths while allowing other parameters to vary freely. We also undertook similar tests of model sensitivity to dipping angle and fault width (aspect ratio). There is a fairly steep increase in misfit at fault center depths shallower or deeper than the minimum misfit value of 7 km (Figure 2.3). For the equivalent dip sensitivity test, we find low misfits for dip angles of 5–10°, but abrupt increases in root mean square error outside of this range

Table 2.2: Source parameters of the 2020 Jiashi mainshock inferred from our model and other sources. The longitude and latitude listed for our InSAR-derived models (first two rows) represent the surface projection of the model slip plane; our relocated epicentre is 77.117° E and 39.894° N. The other InSAR studies parameterize the fault location differently. Depths are given as the top, middle (or centroid) and bottom depths of the slip plane in that order. L and W are length and width, respectively. Yu et al. (2020) prefer their listric, two fault model with a deeper, flatter segment fixed at 2° dip and a shallower, steeper ramp at 52°. Yao et al. (2021b) used uniform slip of 0.32 m in their InSAR-derived model, which may account for their much larger model fault plane.

Source	Long.°	Lat.°	Strike°	Dip°	Rake°	Depth (km)	L/W (km)	Moment (Nm)	M_w
This study, uniform slip	77.28	39.90	279	7°	115	7.0/7.1/7.2	22/2	1.31×10^{18}	6.0
This study, distributed slip	77.17	39.42	279	7	115	6.3/7.0/7.6	37/9	1.75×10^{18}	6.0
USGS body-wave	77.11	39.84	262	9	105	–/4/–	–	1.493×10^{18}	6.1
USGS W-phase	77.11	39.84	221	20	72	–/19.5/–	–	1.387×10^{18}	6.0
CGMT	77.19	39.80	196	38	31	–/11/–	–	1.39×10^{18}	6.0
Yu et al. (2020), 1 fault	77.30	39.91	275	9	111	–/6.3/–	–	–	6.1
Yu et al. (2020), 2 faults	77.30	39.90	275	2/52	111	–/4.15/–	–	–	6.1
Yao et al. (2021b)	77.86	39.31	269	20	92	4/5/6	58/30	2.29×10^{18}	6.2
He et al. (2021)	77.45	39.79	276	10.2	109	5/7.3/9.6	50/26	$– \times 10^{18}$	6.08

(Figure 2.4a). For the fault width test, we find that extending the fault plane up- and down-dip leads to larger misfits, particularly when the aspect ratio (length to width) is forced from the minimum misfit value of ∼12 to below ∼6. This shows that the highly-elongated model rupture area is real (Figure 2.4b).

Compared to the uniform slip model, our preferred distributed slip model is longer at ∼37 km and wider at ∼9 km, but remains centered at ∼7 km depth (Figure 2.5). The slip distribution is characteristically narrow, with an aspect ratio (length to width) of around 4. The peak slip is ∼0.5 m and the model moment is $\sim 1.75 \times 10^{18}$ N. The resultant forward model interferogram matches the observed surface deformation closely, with less than one residual fringe and a root mean square residual of ∼0.25 cm (Figure 2.2c, f, i), which is substantially lower than that of the uniform slip model (∼0.35 cm). The close agreement between observed and forward model coseismic fringe patterns implies that the more localized deformation along the Kepingtag range front had negligible impact on our modelling.

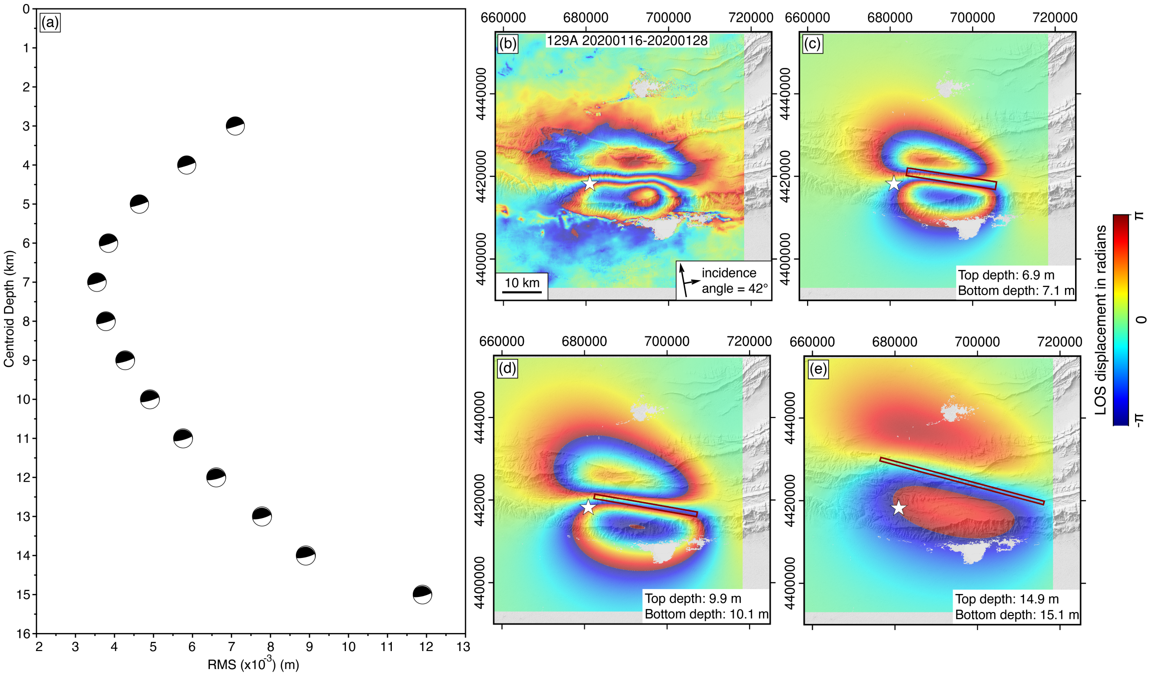

Figure 2.3: (a) Fault center depth sensitivity tests of our InSAR uniform slip fault models for the 2020 Jiashi mainshock. Each focal mechanism shows the minimum-misfit model solution for a fixed center depth, with all other parameters kept free in each inversion. The x-axis is root mean square error (RMS) in meters; the y axis shows 1 km increments of fixed center depth. (b) Observed ascending track interferogram (same as in Fig. 2.2a). (c) Preferred uniform slip model interferogram, with its (free) center depth of 7 km. (d) A forward model interferogram with center depth fixed to 10 km. The forward model used the same uniform slip parameters as in (c) except for the top and bottom depth and the surface projection coordinates. (e) Same as (d) but with a centroid depth of 15 km. The coordinates are in UTM 43N.

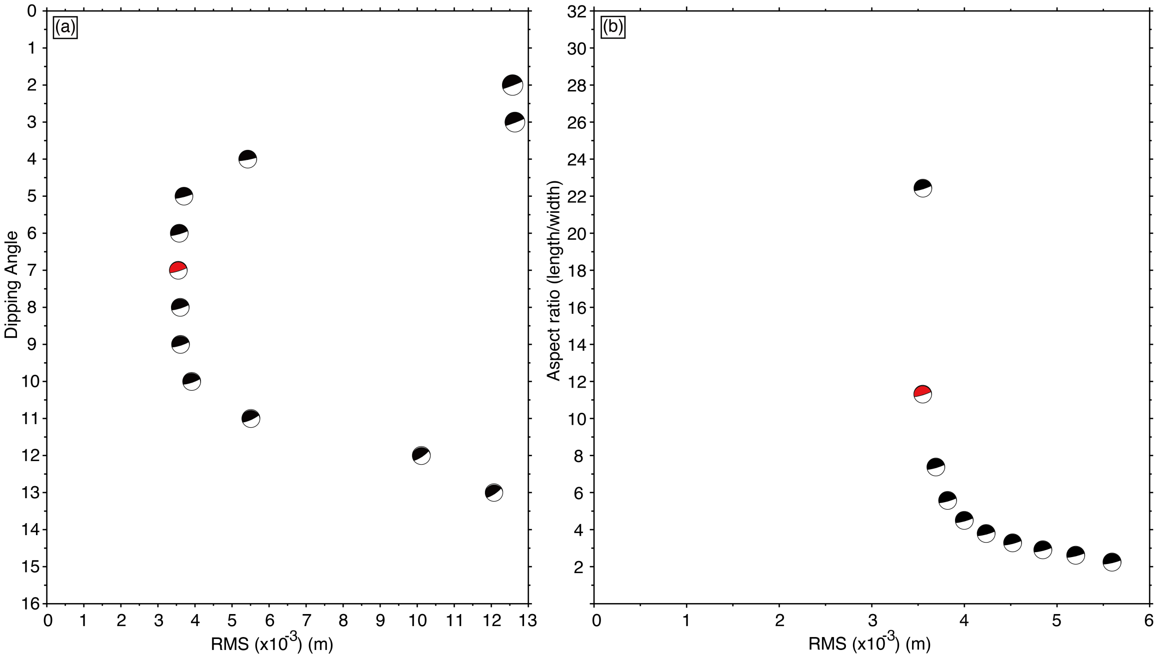

Figure 2.4: (a) Fault dip sensitivity tests of our InSAR uniform slip fault models for the 2020 Jiashi mainshock. Each focal mechanism shows the minimum-misfit model solution for a fixed dip angle, with all other parameters kept free in each inversion. The x-axis is root mean square error (RMS) in meters; the y axis shows 1° increments of fixed dip. The one with red compression part indicates the optimal uniform slip model. (b) Fault plane width sensitivity tests. Each focal mechanism shows the minimum-misfit model solution for a fixed fault width (obtained by fixing the centroid depth and dip to the minimum misfit values and extending the fault plane up- and down-dip at 1 kilometer increments). All other parameters, including slip and fault length, are allowed to vary and the results are plotted according to the aspect ratio of length to width. The red focal mechanism indicates the optimal uniform slip model.

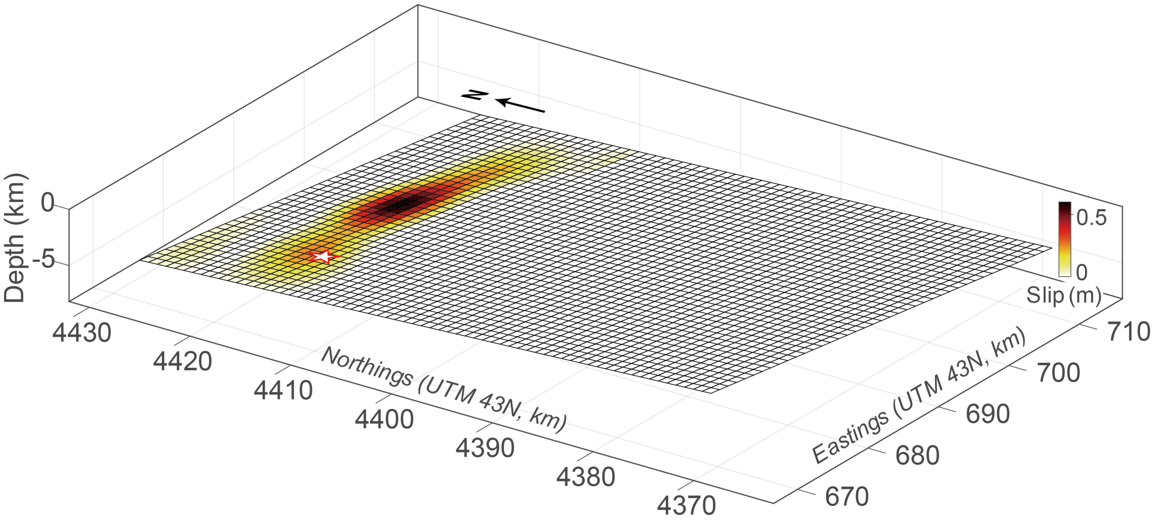

Figure 2.5: The perspective view of the coseismic slip distribution. The fault plane dips to north shallowly. Significant slip occurs over the depth range 6.5–7.4 km. The red star marks the relocated epicentre near the western end of the deformation field for the 2020 Jiashi earthquake.

Our InSAR model fault plane is 10° different in strike and 17° different in rake from the N-dipping nodal plane of the USGS body-wave moment tensor, and there are even larger discrepancies in strike and rake with the USGS W-Phase and GCMT solutions (Table 2.2). However, of the four mechanisms the InSAR model strike is most closely aligned with ∼E–W trends in local faulting, geological structure and topography. Furthermore, the shallow-dipping nodal planes of the USGS and GCMT models are poorly constrained by teleseismic data and liable to be affected by a strong trade-off between strike and rake (e.g. Beckers and Lay, 1995). Our distributed slip model is 17–26% larger in moment than the three available seismological catalogue solutions.

Four other InSAR-derived fault models are also available for comparison (Table 2.2). Our model is closest to that of He et al. (2021) and to the single fault solution of Yu et al. (2020); the three models agree to within 4° in strike and dip, to within 6° in rake, and to within 1 km in centroid depth. Yu et al.'s preferred, two-fault model is strongly listric, with slip apportioned between a deep, gentle (2°) décollement and a much steeper (52°) ramp. However, we prefer the single-fault solution, as the two-fault models we tested using different configurations of listric and antilistric faults could not yield smaller misfits. Our model is ∼2 km deeper and significantly shorter and narrower than a uniform slip model by Yao et al. (2021b). However, they do not provide model or residual interferograms, so there is no easy way to assess the accuracy of their model.

Our relocated mainshock hypocentre lies beneath the northern limb of Kepingtag anticline, which is located ∼6.6 km NNW from one inferred by Ran et al. (2020) using local data. However, our epicentre is somewhat closer to the InSAR-derived slip distribution patch, lying at its far western end. Both our model and Ran et al. (2020)'s show that the Jiashi earthquake is strongly unilateral, rupturing from west to east (Supplementary Figure A.12). Our relocated epicentre of the January 17, 2020 m_b 4.3 foreshock lies ∼3 km SE from the mainshock, and the two largest aftershocks (m_b 5.1 and 5.0) lie near the eastern end of the mainshock model slip patch (Figure 2.1c).

We show the results of our seismological inversions in Figure 2.6 and synthetic waveforms for all stations used in the inversion in Supplementary Figures A.10 and A.11. A probability density function (PDF) of centroid depth results from an inversion with all parameters free shows both the mean and the best-fit solution at just under 10 km (Figure 2.6a). Using teleseismic data offers good constraints on the mechanism only near the center of the focal sphere, where the pierce-points of teleseismic body waves cluster. As such, the mechanism, and particularly the shallowly dipping nodal plane are poorly constrained (inset mechanism, Figure 2.6a). Consequently, we repeated the inversion using double couple nodal planes fixed to match the InSAR-determined fault plane (Figure 2.6b). This pushes the PDF slightly deeper, with a mean depth at 11 km, but with a best-fit solution still at 10 km, and makes only a marginal difference to the overall misfit values. We also show the PDF for the seismologically-determined magnitude in Figure 2.6c, which matches well with the inferred magnitude of the geodetic signal. The model source time function duration of 8–10 seconds is rather long for a M_w 6.0 thrust earthquake (e.g. Bayasgalan et al., 2005; Nissen et al., 2007; Elliott et al., 2015) and supports our inference of unilateral rupture of a ∼22–37 km fault assuming typical propagation speeds of 1.5–4 km/s (Chounet et al., 2018).

In order to illustrate the constraints that the teleseismic data offer on the centroid depth, we show a set of six example waveforms (three vertical components, three transverse components) and best-fit synthetics calculated using three fixed centroid depths in Figure 2.6d. The middle row shows waveforms calculated at 10 km centroid depth, which is the best fit seismological solution, while the upper row shows waveforms with the depth fixed to match the geodetic results at 7 km, and the lower row shows waveforms with the depth fixed to match the centre of the regionally-determine aftershock distribution at 15 km. We discuss these waveform misfits further in the following section.

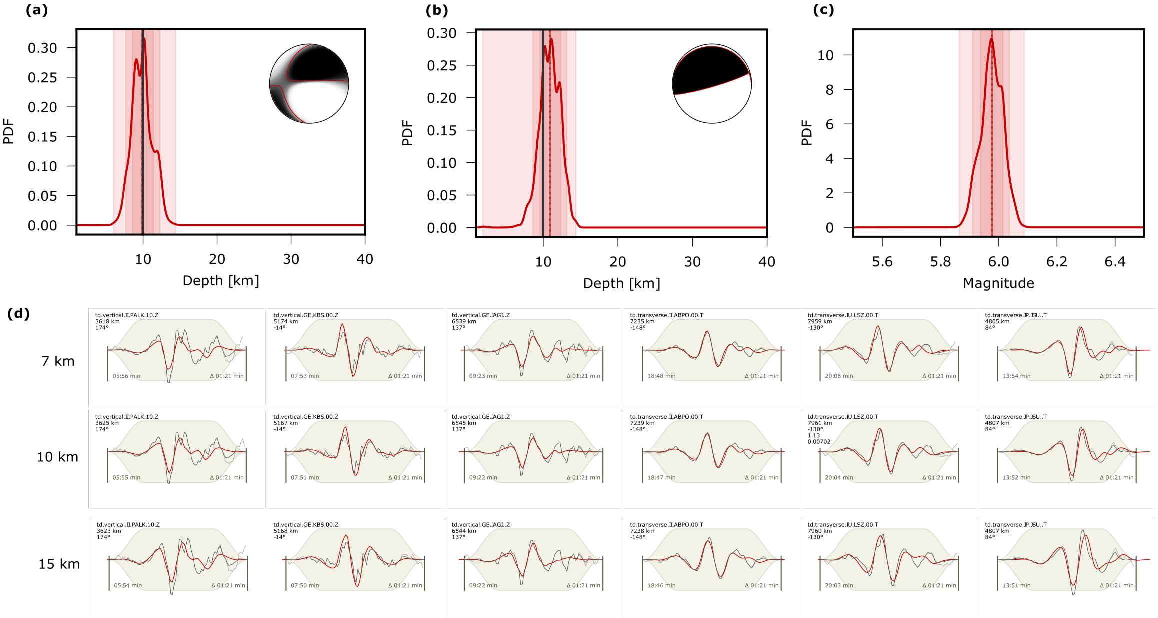

Figure 2.6: Seismological processing results for the 2020 Jiashi mainshock. (a) Probability-density function for depth, for an inversion with all parameters free. Inset mechanism shows the mechanism probability density function (greys) and the best-fit solution (red). (b) Probability-density function for depth, for an inversion with the mechanism constrained to be a double couple matching the InSAR-derived fault plane. (c) Probability-density function for moment, for an inversion with the mechanism constrained to match the InSAR-derived fault plane. (d) Example waveforms for 6 stations (three vertical component, three transverse component). Black traces show the observed data, red line shows the best-fitting inversion result. Text on each waveform indicates the station and component, epicentral distance, and azimuth. Each row of waveforms show synthetics calculated at 7, 10, and 15 km respectively, as discussed in the text.

2.5 Discussion

2.5.1 Depth discrepancy between the Jiashi mainshock and aftershocks

Our InSAR-derived model suggests that the Jiashi mainshock ruptured along the décollement at the base of the sedimentary cover, with a centroid depth of ∼7 km. From the high-quality locally-recorded and double-difference relocated aftershock data, aftershocks cluster along E–W and NNW–SSE trends, with the former matching the ∼40 km length and orientation of our slip model (Supplementary Figures A.12 and A.13) (Ran et al., 2020; Yao et al., 2021a; He et al., 2021). However, locally-recorded aftershocks concentrate at 10–20 km depth, well below the depth of mainshock slip resolved by InSAR inversion. We consider two possible explanations for this apparent discrepancy.

The first possible explanation is that the surface deformation captured with InSAR may reflect aseismic afterslip along the décollement, above an earthquake buried within the underlying basement (at the depth of the aftershock concentration) and itself invisible to InSAR. We tested this possibility by forward modelling the interferograms based upon a M_w 6.0 thrust earthquake with the same geometry as our preferred uniform slip model fault but centered at depths of 10 km and 15 km, more consistent with the aftershock seismicity (Figure 2.3c, d). These forward model interferograms match poorly with the observed InSAR data, with noticeably more far-field deformation and a broader spacing of fringes between the southern and northern lobes. However, the fact that this surface deformation remains distinguishable leads us to rule out the possibility that coseismic slip is too deep to be resolved with InSAR.

The second possible explanation is that the InSAR captures mainshock slip but those well-located aftershocks are vertically separated from the mainshock within the underlying basement, perhaps concentrated within a lobe of positive Coulomb stress change expected below the base of a thrust or reverse fault (e.g. Lin and Stein, 2004; Zhou et al., 2019). He et al. (2021) showed that double-difference relocated aftershocks concentrate along two steep planes within the basement; they then used Coulomb stress calculations to estimate the kinematics of these faults most consistent with static stress triggering by the shallower mainshock. This implies that the basement aftershocks involved N–S-oriented sinistral and steep, S-dipping reverse faulting. However, this does not explain the absence of shallow aftershocks within positive

Coulomb stress lobes expected above the top mainshock fault edge. This might reflect an effect on the stress field from the stress-free boundary of the Earth's surface, that the faults within the sediments above the décollement may exhibit velocity-strengthening friction, favouring aseismic creep over seismic slip (Karasözen et al., 2016), or that the seismic network is insensitive to shallow events due to its average station spacing of ∼30 km. Local seismic networks are able to constrain the focal depth most accurately only if *Pg* and *Sg* phases are recorded at epicentral distances of less than ∼1–2 times of focal depths and the average station spacing is also less than ∼1–2 times of focal depths (Gomberg et al., 1990). Therefore, the apparent absence of shallow events may be an artefact, as the stations with average spacing of ∼30 km cannot record aftershocks shallower than 15 km depth.

We agree with the explanation favored by He et al. (2021) that the mainshock and aftershocks are vertically separated, as our teleseismic waveform inversion reinforces that the geodetically-imaged signal is indeed coseismic. The waveform misfit differences between depths of 10 km and 7 km are minimal (Figure 2.6d). However, synthetics are notably too broad at all six of the stations shown when the depth is increased to 15 km. Due to the cross-correlation based alignment, synthetics are typically aligned on the dominant peak to minimise misfit. However, at 15 km depth, this leads to the peaks to either side being too far out from the main peak due to the increase separation between direct and depth phases. Thus, we conclude that the seismological data are consistent with the deformation signal detected using InSAR, but are notably shallower than the aftershocks located using regional seismology.

Mainshock–aftershock depth discrepancies are not uncommon and several other earthquake sequences also exhibit similar characteristics. The 2000 M_w 6.6 Torrori (Japan), 2003 M_w 6.6 Bam (Iran), 2008 M_w 7.9 Wenchuan (China), 2009 M_w 5.9 Karonga (Malawi), 2011 M_w 5.9 Simav (Turkey), and 2014 M_w 6.1 South Napa (California) earthquakes all exhibited shallower mainshock slip, resolved mostly using geodesy, with deeper aftershock distributions, resolved using seismology (Semmane et al., 2005; Jackson et al., 2006; Tong et al., 2010; Wei et al., 2015; Karasözen et al., 2016; Gaherty et al., 2019). Similar patterns were also observed in M_w ∼6 earthquakes and aftershock sequences at Qeshm (2005) and Fin (2006) in the Zagros Simply Folded Belt, Iran (Nissen et al., 2010; Roustaei et al., 2010). These are especially analogous to the Jiashi sequence, as the Zagros mainshocks were centered within a thick sedimentary cover, with aftershock microseismicity vertically separated within the underlying basement (Nissen et al., 2014). Finally, we recollect that the

February 24, 2003 M_w 6.2 Jiashi earthquake in the foreland basin south of the Kepingtag was centered at ∼5–7 km depth, but exhibited aftershocks at ∼15–25 km depth (Huang et al., 2006; Sloan et al., 2011).

2.5.2 Structural interpretation of the 2020 Jiashi rupture

Coseismic uplift in the 2020 M_w 6.0 Jiashi earthquake resolved by InSAR is centered along the back limb of the Kepingtag anticline (Figure 2.7a–d). Seismic reflection profiles and balanced geological cross-sections depict this as a fault-propagation fold, with Paleozoic-Mesozoic sediments thrust over Cenozoic strata along the moderately northward-dipping Kepingtag fault, which branches off a décollement with an estimated depth of ∼5–10 km (Yin et al., 1998; Allen et al., 1999; Yang et al., 2010, 2002). Projecting our slip model onto a modified geological cross-section suggests that the 2020 earthquake ruptured the décollement where it intersects with the base of the Kepingtag thrust fault (Figure 2.7e).

A striking feature of our distributed slip model is its elongate shape, with a length-to-width aspect ratio of greater than 4 (Figure 2.5). This indicates that the earthquake was able to propagate readily along strike, but was prevented from doing so up- and down-dip. We consider two potential causes of this pattern. One possibility is that the stratigraphic configuration could have determined where slip was able to propagate, with rupture restricted to competent rocks such as the lowermost Cambrian limestone. A similar explanation was proposed by Elliott et al. (2015) for the elongate slip distribution (length-to-width ratio ∼3) of the 2013 M_w 6.2 Khaki-Shonbe earthquake in the Zagros fold-and-thrust belt, where Infracambrian Hormuz evaporites and Cretaceous Kazhdumi mudstones were inferred to have controlled the bottom and top of the rupture, respectively. Length-to-width ratios of ∼3–4 inferred for the 2006 Fin and 2019 Khalili earthquakes (both M_w 5.7) suggest that this may be a common feature of Zagros ruptures (Roustaei et al., 2010; Jamalreyhani et al., 2021). Another possible mechanism could be due to structural complexities in the fault geometry. This was discussed by Elliott et al. (2011) for the 2008 and 2009 Qaidam M_w 6.3 earthquakes, whose vertical segregation resulted from disruption of the rupture plane by a cross-cutting, conjugate reverse fault. In the 2020 Jiashi event, we suggest that the abrupt change in dip angle between the sub-horizontal décollement and the much steeper Kepingtag fault may have provided a barrier to rupture. Our testing of listric fault geometries is in good agreement with the inference

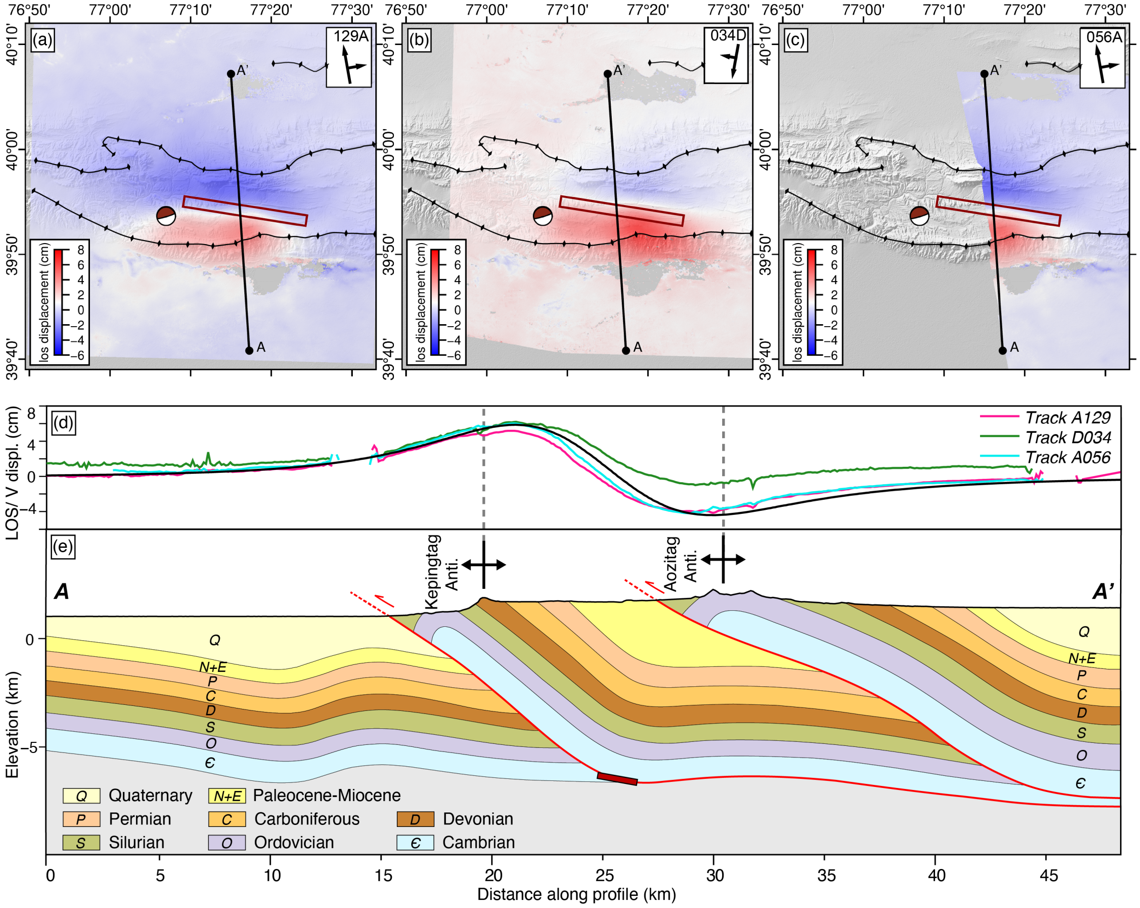

Figure 2.7: Coseismic LOS displacements in the 2020 Jiashi earthquake from unwrapped interferograms on tracks (a) 129A, (b) 034D and (c) 056A. Black lines with ticks show the traces of the Aozitang (north) and Kepingtag (south) fold axes. The dark red rectangle is the uniform slip model fault plane, centered at ∼7 km depth. (d) LOS displacement profiles and vertical displacement profile (track A129 in pink, D034 in green, A056 in cyan, and vertical displacement in black) along profile A-A' in (a), (b) and (c). Maximum LOS displacements are ∼7.5 cm toward the satellite and ∼4 cm away from the satellite. Vertical displacement field is predicted by our best-fitting, InSAR-derived distributed slip model. (e) Geological cross-section along the profile A-A' is interpreted from seismic reflection profiles (Yang et al., 2010). The surface topography is extracted from the 30 m resolution SRTM DEM. The dark red rectangle indicates the uniform slip model fault plane.

that there was minimal slip on the steeper fault. Although the current data does not allow us to distinguish between the two mechanisms, there is a clear structural or lithological control on the extent of coseismic slip during the main shock.

2.5.3 Regional distribution of seismicity and seismic hazard

The Pamir and Tian Shan jointly accommodate a crustal shortening of 20–25 mm/yr, nearly half of the total India-Eurasia convergence rate (Abdrakhmatov et al., 1996; Zubovich et al., 2010). The southwestern margin of the Tian Shan is characterized by frequent seismicity, mostly with thrust faulting and strike-slip mechanisms. Here, we use our own calibrated earthquake relocations together with previous waveform modelling studies to assess the finer-scale distribution of seismicity across this region.

From the calibrated earthquake relocations, it is apparent that seismicity is not concentrated along the frontal Kepingtag belt, but is distributed throughout the fold-and-thrust belt as well as the adjacent foreland to the south. The shallow events occur to the north of the frontal Kepingtag anticline as well as in the foreland to the south. This pattern indicates that all stacks of the thrust sheets may be simultaneously capable of generating earthquakes, even as one of them might be most favourable at a particular time due to a variable stress state and the history of previous earthquakes. This inference is also supported by geomorphological and geochronological data (Yang et al., 2006) and suggests that seismic hazard is high across the region, rather than being focused along the range front.

Moreover, the seismic hazard in the Kepingtag region is not only restricted to faulting along the décollement but also within the folded cover rocks and the piedmont area. Reliable earthquake centroid and focal depths — from teleseismic or regional waveform modelling (Fan et al., 1994; Ghose et al., 1998; Sloan et al., 2011) and our own calibrated hypocentral relocations — are concentrated at depths shallower than 25 km, except for two isolated events at 29–35 km (Figure 2.8). The 1997 Jiashi earthquake swarm and the 2003 Bachu-Jiashi sequence all occurred on blind faults in the piedmont area ∼50 km south of the Kepingtag frontal thrust. The largest events between 1997 and 1998 (M_w 5.7, 5.9, 6.0 and 6.3) represented activity on normal faulting or left-lateral strike-slip faulting at mid-crustal depths of ∼12–20 km, while the 2003 events involved much shallower thrust faulting (Sloan et al., 2011). Within the Kepingtag fold-and-thrust belt, most of the reliable centroid depths are greater than 10 km, indicating faulting within the basement is below the décollement.

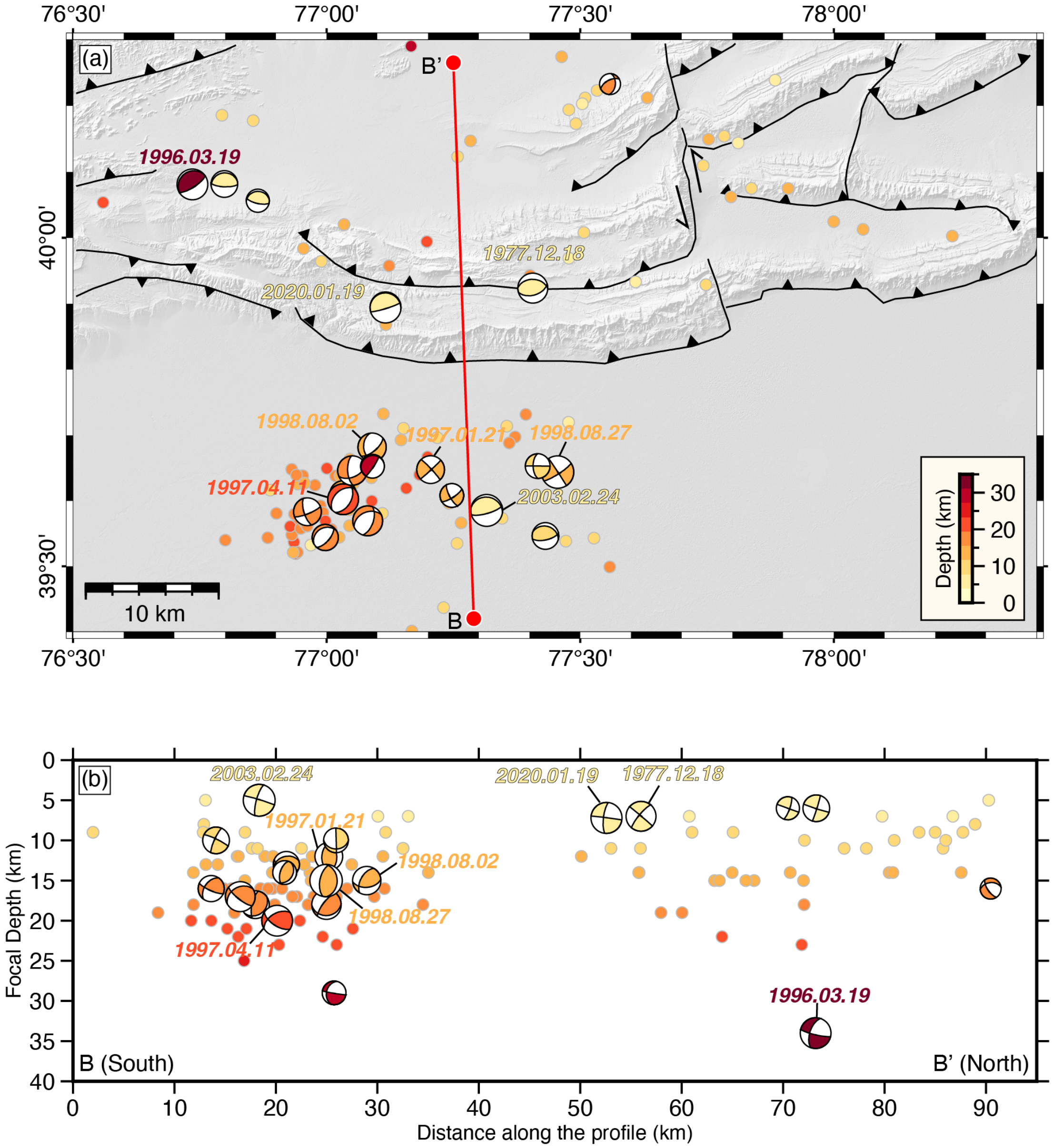

Figure 2.8: Calibrated relocated earthquakes from 1977–2020 in the Jiashi area, coloured according to the best available estimate of depth. Focal mechanisms determined by teleseismic and regional waveform modelling, including some from the GCMT catalogue. The depths of focal mechanisms with black outlines are determined by teleseismic and regional waveform modelling and depth phases, while those with grey outlines are our own calibrated focal depths (see Table 2.1 for full details). Other moderate relocated earthquakes without focal mechanisms are shown as dots.

Though usually depicted as a ‘thin-skinned’ fold-and-thrust belt, the Kepingtag basement clearly accommodates shortening by reverse faulting, and should therefore be considered as an important source of seismic hazard.

2.6 Conclusion

We use InSAR data to characterize the coseismic surface deformation and model the fault geometry and slip distribution of the January 19 2020 M_w 6.0 Jiashi earthquake. Modelled coseismic uplift is centered on the back limb of the Kepingtag anticline, consistent with previous structural models that depict this as a fault-propagation fold. Our best-fit model fault plane dips $\sim$7° northward at depth of $\sim$7 km, placing it on or close to the mapped décollement at the base of the folded sedimentary cover. This depth is consistent with teleseismic body-waveforms, confirming that the slip modelled with InSAR occurred coseismically. The small ($\sim$1/4) width to length ratio of our model slip distribution hints at structural and/or lithological controls on slip propagation; for example, rupture may have been prevented from advancing up-dip by the abrupt change of dip angle between the sub-horizontal décollement and the much steeper Kepingtag thrust. Published seismological studies show that aftershocks cluster within underlying basement rocks at $\sim$10–20 km depth, vertically separated from the mainshock slip. Our own relocated background seismicity also shows a prevalence of seismicity at basement depths throughout the Kepingtag belt and its foreland, hinting at rheological controls on the depths at which earthquakes occur.

Chapter 3

InSAR observations of shallow afterslip-driven fold growth triggered by the deep 2016 M_w 6.0 Hutubi earthquake

Article information

Siyu Wang[1*], Edwin Nissen[1], Qi Ou[2], John Elliott[2], Léa Pousse-Beltran[3], and Ruohong Jiao[1]

[1] School of Earth and Ocean Sciences, University of Victoria, Victoria, BC, Canada
[2] School of Earth and Environment, COMET, Institute of Geophysics and Tectonics, University of Leeds, Leeds, UK
[3] Institut des Sciences de la Terre, Université Grenoble Alpes, Grenoble, France
Status: Under revision with co-authors.
Corresponding author: Siyu Wang (siyuwang@uvic.ca)

Abstract

The relationship between individual earthquakes and long-term topographic growth remains unclear. Interferometric Synthetic Aperture Radar (InSAR) observations from arid fold-and-thrust settings provide opportunities to examine the spatial and temporal relationships between long-term geological structures and individual seismic events. This study focuses on the 2016 M_w 6.0 Hutubi earthquake beneath the northern flank of the Tian Shan, and the nearby Tugulu Anticline, part of the Southern Junggar Fold-and-thrust Belt (SJFB) in the adjacent foreland. We use InSAR to determine the fault parameters and coseismic slip distribution of the Hutubi earthquake, and build a 5-year InSAR time series to analyze the postseismic deformation. Our results show that the earthquake ruptured a south-dipping fault plane at a depth of ∼14 km. The time series analysis indicates that there is no obvious postseismic deformation around the epicentre. However, farther north, the Tugulu Anticline exhibits accelerated deformation immediately after the earthquake, then decaying over time. This implies that a deep earthquake triggered an increased creep rate on a shallower thrust fault beneath the anticline, located ∼25 kilometres horizontally from the epicentre. Accelerated creep may act as a mechanism to relieve stress gradually, but it can also transfer stress to adjacent faults, potentially increasing the seismic hazards in nearby regions.

3.1 Introduction

The limitations inherent to tectonic geomorphology, including the scarcity of observations at relevant timescales, make it challenging to infer relationships between Earth's surface deformation and the long-term growth of topography and geological structure. Observations of modern earthquakes in fold-and-thrust belt settings show that long-term fold growth may be controlled primarily by repeated earthquakes. For example, the 1983 M_w 6.5 Coalinga earthquake in California elastically folded the top few kilometres of the crust (Stein and King, 1984). However, not all surface deformation associated with blind reverse faults can be attributed directly to slip along the fault during seismic events (Yue et al., 2005; Ainscoe et al., 2017; Johnson, 2018; Elliott et al., 2016). By comparing coseismic and postseismic surface deformation with indicators of active deformation preserved in the geomorphology, it is possible to infer what deformation, at what time in the seismic cycle, produced these features.

Previous studies have used geodetic measurements to investigate the relationship between buried thrusting and the growth and evolution of surface folding (Fielding et al., 2004; Nissen et al., 2007; Daout et al., 2019). A key question therefore is how such deformation relates to the long-term uplift and crustal shortening seen in the geological record.

Propagation of faults and folds in the foreland basins of the Tian Shan mountains is an important process accommodating Cenozoic crustal shortening and mountain building in central Asia. The southward-dipping Northern Tian Shan Fault marks the major boundary between the Tian Shan and the foreland Junggar Basin (Figure 3.1). To its north, the Southern Junggar Fold-and-thrust Belt (SJFB) is composed of three approximately east-west striking subparallel fold-and-thrust zones with en-échelon right steps, with the gently dipping thrust faults merging with the steeper Northern Tian Shan Fault at depth (Deng et al., 1996). There are two detachment surfaces at depths of $\sim$ 7 km and $\sim$ 16 km beneath the foreland area (Wang et al., 2004). The thrust fault converging with the detachment surface at 16 km depth was inferred as the source of the December 22, 1906 M 7-8 Manas earthquake (Avouac et al., 1993a; Deng et al., 1996; Stockmeyer et al., 2014) (Figure 3.1). Several kinematic fault-related models have been developed to quantitatively describe the relationship between surface folding and fault activity in this area (Guan et al., 2016; Stockmeyer et al., 2017; Qiu et al., 2019). However, due to the structural complexity, accurate evaluation of seismic potential is still challenging if solely relying on traditional geologic methods.

On December 8, 2016, at 05:15:04 UTC (local time 13:15:04), a M_w 6.0 earthquake struck Hutubi county in Xinjiang province, northwestern China (Figure 3.1). The epicentre is located at the northern Tian Shan range front, approximately 30 km south of the Tugulu Anticline, which locally marks the northern deformation front of the SJFB. The reported focal mechanism from the United States Geological Survey (USGS) indicates one nodal plane striking 80° and dipping 19° southwards, and the other striking 269° and dipping 71° northwards, with rake angles indicating mostly reverse slip. There is some debate over which of these nodal planes represents the fault. Lu et al. (2018) interpreted seismic reflection data to propose that the earthquake ruptured a south-dipping reverse fault. In contrast, Yang et al. (2019) and Wang et al. (2019) suggested a steeply north-dipping back thrust based on InSAR coseismic deformation modelling and the distribution of aftershocks. This discrepancy in interpretations highlights the complexity of the fault structures in this region

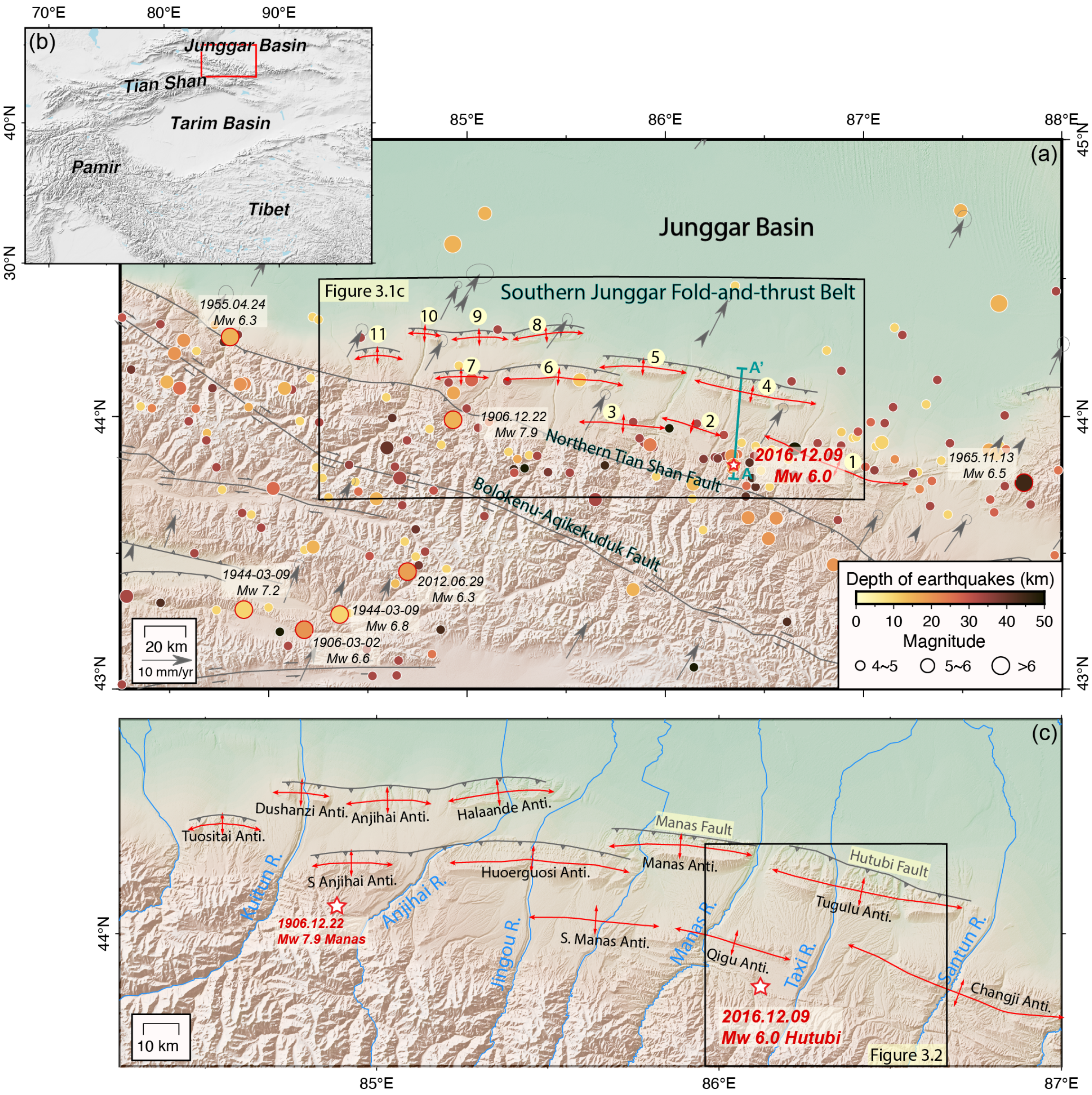

Figure 3.1: (a) Tectonic map of the northern Tian Shan range front and adjacent foreland. Instrumental seismicity from 1906.12.22 to 2024.02.01 is scaled by magnitude and coloured by depth. Active faults are adapted from the dataset compiled by Li et al. (2021b). GNSS velocities relative to stable Eurasia are from Wang et al. (2020a) with 95% confidence ellipses. A-A' marks the seismic reflection profile from Lu et al. (2018). Labels 1-11 mark anticlines of the Southern Junggar Fold-and-thrust Belt I: (1) Changji Anticline, (2) Qigu Anticline, (3) South Manas Anticline; Zone II: (4) Tugulu Anticline, (5) Manas Anticline, (6) Huoerguosi Anticline, (7) South Anjihai Anticline; Zone III: (8) Halaande Anticline, (9) Anjihai Anticline, (10) Dushanzi Anticline, (11) Tuositai Anticline. (b)Regional tectonics map of Tian Shan and its adjacent regions. (c) Enlarged view of the Southern Junggar Fold-and-thrust Belt, with the black box indicating the area covered by InSAR coseismic modeling.

and underscores the need for a thorough investigation into the deep-seated mechanisms driving the Hutubi earthquake. Moreover, aseismic stress release affects the slip budget and is an essential consideration for seismic hazard assessment. The behaviour of décollements and splay ramps—not only in the Tian Shan but in other fold-and-thrust settings—remains obscure, and it is not known whether they rupture coseismically, creep inter- or post-seismically, or slip in a mix of these modes.

In this study, we use Sentinel-1A/1B data spanning the Hutubi earthquake to map line-of-sight (LOS) surface deformation, and invert downsampled data for the optimal fault geometry and coseismic slip distribution. We then process the first InSAR time-series data for this region, overcoming the challenges of small deformation signals and seasonal atmospheric effects. We reconstruct the spatiotemporal evolution of the surface displacement field from 2017 to 2022 and identify and quantify postseismic deformation. Furthermore, we compare the postseismic surface displacements to the local fold and fault geomorphology. We conduct the first high spatial-resolution investigation of the long-term deformation pattern in this region. Our InSAR velocities provide a fundamental dataset for studying regional tectonics and fault mechanics, with the potential to infer aspects of the rheology and slip behaviour of the shallow thrusts faults in the region, of critical importance for seismic hazard assessment along the northern Tian Shan foreland. Insights here could also shed light on the structural evolution of fault-related folds in other fold-and-thrust belts in the world, and how fault slip contributes to the growth of geological and topographic structures.

3.2 Background

3.2.1 Structural setting

The Cenozoic collision between the Indian and Eurasian plates has reactivated the Tian Shan mountains, causing uplift that extends from the range interior to the margins of the Junggar Basin in the north and the Tarim Basin in the south (Windley et al., 1990). GPS measurements indicate that the present-day shortening rate across the western Tian Shan is up to ~ 20 mm/yr (Abdrakhmatov et al., 1996; Zubovich et al., 2010). At the longitude of the southern Junggar Basin, the shortening rate is on the order of 6–9 mm/yr (Wu et al., 2023). The SJFB has developed up to 50 km north of the Northern Tian Shan Fault, and can be subdivided into three echelon zones of anticlines. Moving from south to north and from east to west, Zone

I includes the Changji, Qigu, and South Manas anticlines, zone II comprises the Tugulu, Manas, Huoerguosi, and South Anjihai anticlines, and zone III consists the Halaande, Anjihai, Dushanzi, and Tuositai anticlines (Avouac et al., 1993a; Burchfiel et al., 1999) (Figure 3.1). These anticlines are associated with south-dipping thrust faults either along the cores or the northern limbs that thrust Paleozoic bedrock strata over the Mesozoic and weakly cemented Cenozoic sediments. Rivers originating from the main Tian Shan cut the anticlines roughly perpendicular to their strike, forming fluvial terrace sequences. They also serve as structural traps for oil and gas, which motivated the collection of the seismic reflection data used in this study (Qiu et al., 2019).

Among these folds, the Tugulu Anticline in the eastern end of zone II, which measures 50 km in length and 10–15 km in width will be the main focus of this chapter. It is interpreted as a fault-propagation fold due to the lack of evidence for faulting or shortening north of the anticline (Burchfiel et al., 1999; Molnar et al., 1994). The surface of the anticline displays asymmetry, with the northern limb much steeper and narrower than the southern limb. Most of the shortening occurred after the deposition of a thick lower Quaternary conglomerate unit, with strata in the middle part of these conglomerates being deposited during the growth of the fold. The shortening rate of the Tugulu Anticline is estimated to be between 2.1 and 5.5 mm/yr, based on the initiation of deformation around 2.5 Ma (Burchfiel et al., 1999; Shackleton et al., 1984) and the rate of fold growth is estimated at 2 mm/yr (Molnar et al., 1994). The south-dipping Hutubi Fault beneath the Tugulu Anticline cuts through the anticline front, exposing the Eocene-Oligocene Anjihaihe Formation, Miocene Shawan Formation, and Taxihe Formation (Avouac et al., 1993b). Evidence from the late Quaternary shows the ongoing growth of the anticline as indicated by the warping of river terraces. Thrusting along the northern limb of the Tugulu Anticline has produced well-developed fault scarps in the alluvial terraces west of the Taxi River (Avouac et al., 1993b). Six terraces have been identified along the eastern flank of the Manas River. Dating the underlying fluvial sand and the overlying aeolian loess on these terraces, together with measurements across the fault scarps, suggests that the vertical slip rates of the Manas Fault is $\sim$0.74–1.6 mm/yr, while the Hutubi Fault has a lower vertical slip rate of $\sim$0.34–0.4 mm/yr (Gong et al., 2015).

3.2.2 Seismicity

Seismicity and active faulting in the past few hundred years imply rapid deformation within and around the Tian Shan. Several major active fault systems pose a threat to cities along the northern Tian Shan range front. The most significant historical event recorded in the area is the December 22, 1906, Manas earthquake, with an estimated magnitude between $M \sim$7–8 (Wang et al., 2004). The epicenter was located ∼30–40 km south of the surface trace of the SJFB (Avouac et al., 1993a; Burchfiel et al., 1999) (Figure 3.1a). Slip in the earthquake propagated along a steeply south-dipping fault into the basement but did not extend northward beneath the folds (Molnar and Ghose, 2000). This suggests that the fault responsible for the earthquake extends further south and ramps down below the northern Tian Shan range front, likely extending to the base of the seismogenic crust (Stockmeyer et al., 2014).

Field investigation have revealed three discontinuous surface ruptures associated with the Manas earthquake Deng et al. (1996). In the eastern section, the earthquake exhibited a maximum of 8 km of surface rupture along the Hutubi Fault, displacing the alluvial fan and the youngest terrace by 0.2–0.3 m vertically. The presence of small V-shaped gullies, incised into sedimentary layers that are 4000 to 5000 years old, suggests recent anticlinal uplift attributed to the Manas earthquake (Deng et al., 1996). Since the 1906 Manas earthquake, the region did not experience any magnitude 5 or greater earthquakes until the 2016 Hutubi earthquake. Paleoseismic trench studies along the Hutubi River terraces suggest that most of the deformation has been accommodated through gradual anticlinal uplift rather than surface fault rupture. This pattern of deformation implies that the II of the SJFB is still tectonic active, with a recurrence interval for major earthquakes estimated to be between 5000 and 6000 years (Deng et al., 1996).

3.3 Coseismic deformation and fault slip modelling

3.3.1 Coseismic data processing

We obtained raw data from the European Space Agency's C-band Sentinel-1A/B satellites. One ascending track (114A) and one descending track (092D) capture the Hutubi mainshock. We used GAMMA software to process two 24 day coseismic interferograms, from November 19–December 13, 2016 on the ascending track, and from November 24–December 18, 2016 on the descending track (Werner et al., 2000).

Interferograms were multi-looked to 20 looks in range and 4 in azimuth to achieve a ∼30 m × 30 m pixel resolution. The 30 m-resolution Shuttle Radar Topographic Mission Digital Elevation Model was used to simulate and remove the topographic phase contribution. Subsequent unwrapping of the two interferograms was achieved using the Minimum Cost Flow algorithm, which uses triangular irregular networks to improve the unwrapping performance in areas of low coherence (Werner et al., 2002). Finally, the unwrapped interferograms were geocoded from the SAR coordinates into WGS84 geographical coordinates.

3.3.2 Coseismic deformation field

Coseismic surface deformation manifests in both ascending and descending interferograms as a ∼15 km-long, ∼E–W, elliptical region containing motions towards the satellite (Figure 3.2 a, b). The general consistency in deformation pattern and magnitude between the two different satellite look directions suggests that the earthquake is primarily governed by dip-slip rather than lateral motion, and the symmetry of the signal along its long axis implies the involvement of either a south- or north-dipping buried thrust fault. Though the deformation signal is clear, it comprises at most only ∼half of a colour cycle, indicating that the ground has moved ∼2.5 cm towards the satellite. The center of the deformation ellipse is situated along the main Tian Shan mountain front, ∼25 km south of the Tugulu Anticline (the significance of this will become apparent later). The presence of incoherent noise is also notable, especially south of the deformation signal in Tian Shan, where it is likely the consequence of seasonal snow cover. There is no linear band of decorrelation as one would expect to observe along an earthquake surface rupture.

3.3.3 Coseismic modelling method and results

Next, we inverted the InSAR observations to solve for the mainshock geometry and slip distribution. Considering the complex fault structures in our study area, we tested both possible fault orientations, one dipping toward the south and the other toward the north. Quadtree downsampling was used to reduce the size of unwrapped datasets and to concentrate sampling in regions with high phase variance (Jónsson et al., 2002). We employed a two-step inversion strategy to estimate the causative fault parameters (e.g., Wright et al., 1999, 2004; Funning et al., 2005; Elliott et al., 2012). In the first step, we used Okada's formulae to invert the downsampled data for

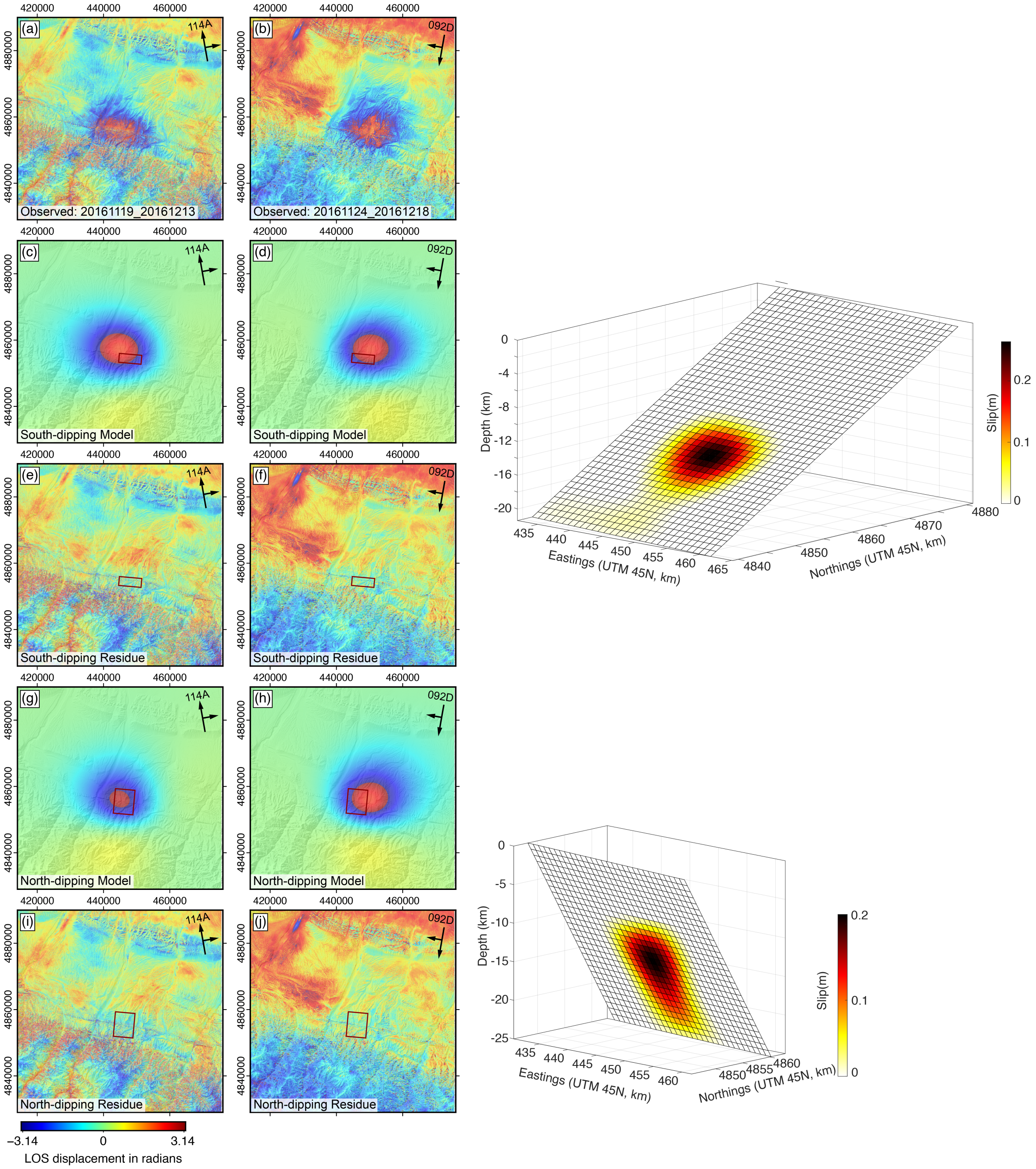

Figure 3.2: Maps on the left show ascending (left column) and descending (right column) observed interferograms for the 2020 Hutubi mainshock (1st row), model and residual interferograms for distributed slip on a S-dipping fault (2nd and 3rd rows), and model and residual interferograms for distributed slip on a N-dipping fault (4th and 5th rows). Modelling was performed using unwrapped LOS displacements, but here we plot the original, wrapped interferograms since these show more clearly the shape of the deformation field. The coordinates are in UTM zone 45N. Color cycles of blue through yellow to red indicate motion away from the satellite and one color cycle (2π radians) represents a half radar wavelength (2.77 cm) of LOS displacement. On the right of the figure, perspective views of the model slip distributions on the S-dipping (top) and N-dipping (bottom) faults.

the optimal strike, dip, rake, slip, length, and top and bottom depths of a rectangular, uniform slip dislocation plane (Okada, 1985). To minimize the misfit, we applied a non-linear optimization method using Powell's algorithm (Press et al., 1992), running 500 Monte Carlo restarts with randomly selected initial parameters to avoid local minima (Wright et al., 1999). Given the absence of firm constraints on how rheological properties vary with depth locally, we assumed a homogenous elastic half-space with standard Lamé parameters (λ and μ) of 3.2×10^{10} Pa.

In the second step, we estimated the slip distribution by extending the uniform slip model fault plane by a few kilometres along strike and up- and down-dip, dividing it into 1 km × 1 km sub-fault patches, and solving for slip on each patch (with rake fixed to the uniform slip solution). We used a Laplacian operator to vary smoothing (Wright et al., 2004; Funning et al., 2005) and a non-negative least squares algorithm to ensure positive slip (Bro and De Jong, 1997).

Both S- and N-dipping model faults can produce a good match to the observed interferograms, suggesting that the InSAR data considered alone are indiscriminate. The best fitting south-dipping fault plane strikes 95° strike and dips 28° at a centroid depth of 13.8 km and the best north-dipping plane strikes 275° and dips 60° at a depth of 14.5 km (Table 3.1). Both slip distributions remain buried, suggesting that coseismic slip is arrested well before reaching the surface. The predominant slip occurred at depths of 12–17 km with a peak magnitude of 36 cm for the south-dipping model and at depths of 13–16 km with a peak magnitude of 20 cm for the north-dipping model.

Table 3.1: Source parameters of the 2016 Hutubi mainshock derived from our model and other sources.

Source	Lat. (°)	Lon. (°)	South-dip			North-dip			Depth (km)	M_w
			Strike (°)	Dip (°)	Rake (°)	Strike (°)	Dip (°)	Rake (°)		
USGS	43.823	86.345	80	19	81	269	71	93	17.6	6.0
GCMT	43.98	86.32	87	22	85	272	68	92	17.6	6.0
CENC	43.83	86.35	103	21	96	277	69	88	19	6.2
GFZ	43.76	86.41	74	21	63	283	71	100	21	6.0
Wang et al. (2019)	-	-	87	29	85	268	57	93	15.5	5.8
Yang et al. (2019)	-	-	-	-	-	264.4	28.8	-	-	-
This study	44.07/43.77	86.38/86.32	95	28	98	275	60	105	13.8/14.5	5.8

3.4 Postseismic time series analysis

3.4.1 Time series data processing

We then extended our investigation to longer-term postseismic and interseismic measurements of the Hutubi earthquake through InSAR time series analysis, which takes multiple interferograms spanning several years to generate a time series of surface displacement changes, with an improved signal-to-noise ratio. This advanced processing technique has proven effective in detecting small amplitude, long-duration surface displacements associated with interseismic strain accumulation, postseismic deformation, and shallow creep (Fialko, 2006; Pousse Beltran et al., 2016; Daout et al., 2019).

For this study, we processed satellite images from Sentinel-1A/B spanning ∼5.5 years from one ascending track 114A_04598_131313 (13 December 2016 to 28 May 2022) and one descending track 092D_04679_141413 (18 December 2016 to 16 December 2021) using COMET's Looking Into Continents from Space with Synthetic Aperture Radar (LiCSAR) processing chain (Lazecký et al., 2020), which is based on the GAMMA software (Wegmuller, 1997; Werner et al., 2000) to process Sentinel-1 Single Look Complex (SLC) data. The 12/24-day revisit capability makes it possible to reduce noise contribution and temporal decorrelation in the time series analysis. We used Interferograms that were downsampled by a multilook factor of 20 in range and 5 in azimuth, resulting in ground pixels of ∼50×50 m. Interferogram networks were formed using the six closest acquisitions in time (three forward and three backward), supplemented by longer period interferograms to help deal with low-coherence due to vegetation in summer and snow cover in winter months(Weiss et al., 2020), and to minimize errors related to the short temporal baselines (Ansari et al., 2021). We generated a total of 979 and 1168 interferograms for the ascending and descending tracks, respectively. The networks of the interferograms are shown in Figure S1 of the Supporting Information.

Phase unwrapping was performed using the statistical-cost, network-flow algorithm SNAPHU (Chen and Zebker, 2002) to recognize the areas with inconsistency between local and global, which minimizes the cost associated with discontinuities in the phase data. To mitigate atmospheric contributions to the unwrapped interferograms, we applied an iterative troposphere decomposition model implemented in the Generic Atmospheric Correction Online Service (GACOS) (Yu et al., 2018), which

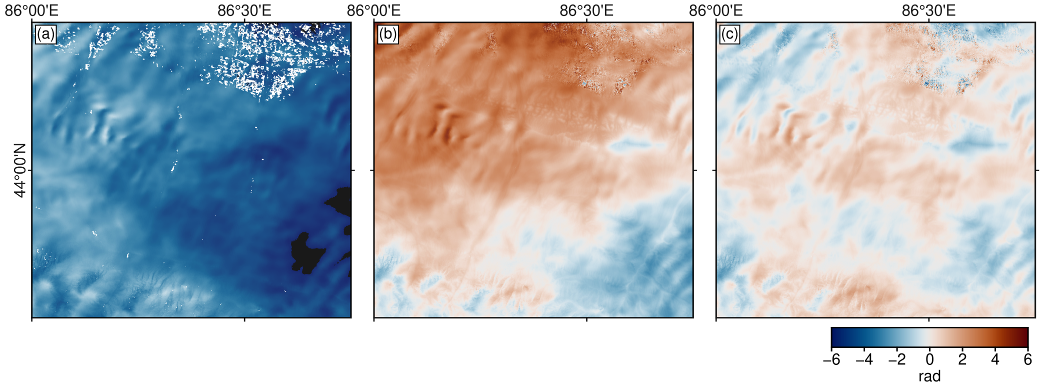

Figure 3.3: Examples of atmospheric correction (a) The original interferogram 20170908_20171026 before correction; (b) The interferogram corrected by the GACOS model; and (c) The interferogram after removing local tropospheric effects and a one-dimensional (1D) planar ramp. The colour scale indicates phase values in radians.

provides tropospheric delay maps derived from the European Center for Medium-Range Weather Forecasts (ECMWF). The GACOS products for each epoch were converted to radar coordinates, projected to the line-of-sight (LOS) direction, differenced in the same sequence as the interferometric pairs, and finally subtracted from the unwrapped interferograms. Despite these corrections, topography-related tropospheric phase delays existed in many interferograms, e.g., interferogram 20170906_20171026 (Figure 3.3b); therefore, we employed the method of Chaabane et al. (2007) to exploit the correlation between phase and topography when multiple interferograms and common acquisitions are available, aiming to correct local tropospheric effects. In this process, we also subtracted the best-fitting linear trend, a 1D planar ramp, using least squares inversion from the interferograms. This step separates the long wavelength component due to remaining orbital errors, ionosphere, and tropospheric delays, and the final results are shown in Figure 3.3c.

The remaining unwrapped data may still include unwrapping mistakes, visually as sharp phase jumps of multiples of 2π, which can cause significant errors in the derived time series and should be corrected or removed beforehand. Supposing that we have three different dates of images (ϕ_1, ϕ_2, and ϕ_3) and three unwrapped interferograms (ϕ_{12}, ϕ_{23}, and ϕ_{13}), a loop phase is calculated by

$$\phi_{123} = \phi_{12} + \phi_{23} - \phi_{13} \tag{3.1}$$

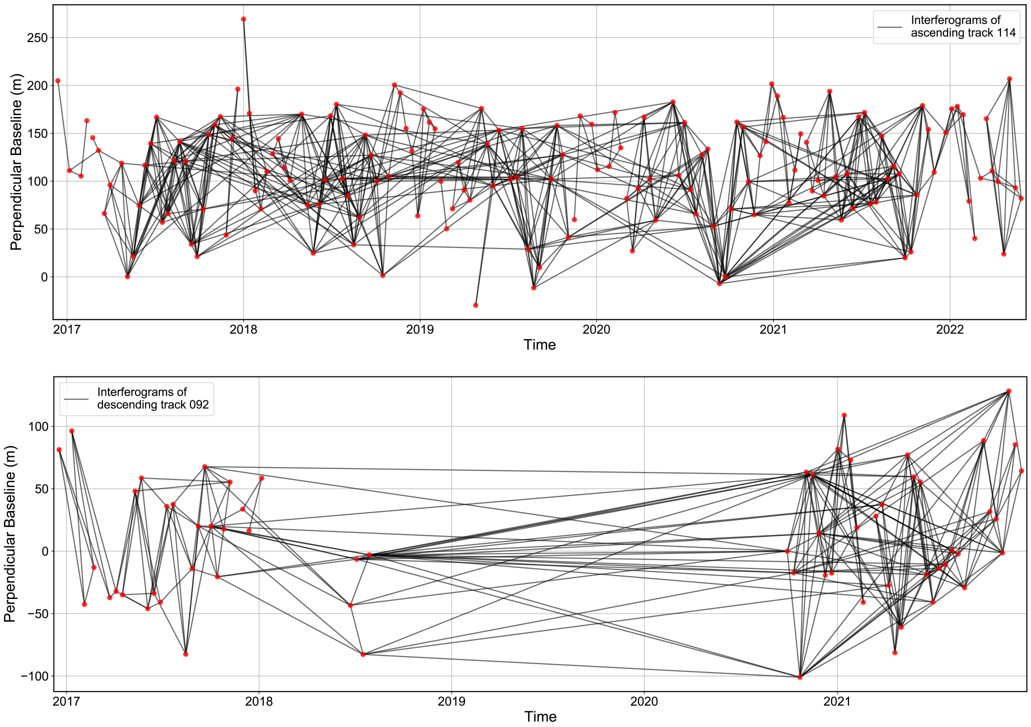

Figure 3.4: The refined spatio-temporal networks of ascending track 114 (top) and descending track 092 (bottom) are used to inverse the mean velocities. Red dots represent individual Sentinel-1A/B images, and black lines indicate the interferograms formed between pairs of images.

The loop phase should be close to zero if there are no unwrapping errors in the three loop interferograms as the tectonic, orbital, and atmospheric contributions to an interferogram should be conservative (Biggs et al., 2007). We manually corrected the loop errors and selected interferograms with good coherence. The final refined interferogram networks for both ascending and descending tracks are shown in Figure 3.4. Due to operational issues with Sentinel-1B's descending track 092 from July 2018 to September 2020, there is a gap in the network. To ensure network redundancy, we made longer temporal baselines to connect the entire network. These selected stacks of unwrapped interferograms are then inverted to derive the incremental displacements for each acquisition using the open-source Small Baseline InSAR time-series analysis package, LiCSBAS (Morishita et al., 2020). The mean displacement velocity is derived from the cumulative displacement by least-square fitting. Finally, a spatio-temporal filter of 1 km in space and 0.5 years in time is applied to the time series to mitigate the residual noise and derive the filtered time series and velocity.

3.4.2 Time series inversion results

The mean velocity map reveals detailed deformation patterns across the study area. The topographic relief ranges ∼2000 m from the mountain front to the foreland. In the mountainous area south of the map, most pixels are masked out because of the low coherence and steep topography relief. The velocity map from the ascending track (Figure 3.5b) is visually smoother compared with the velocity map from the descending track (Figure 3.5c). This disparity is mainly attributed to the 2.2-year observation lack of the descending data. In the LOS velocity map, negative values (blue) represent subsidence or movement away from the satellite, while positive values (red) represent uplift or movement towards the satellite. A noticeable deformation feature is observed north of the epicentre of the December 08, 2016, Hutubi earthquake, where there is an evident increase in surface displacements localized on the eastern side of the Hutubi Anticline with a velocity of 2.5–4.6 mm/yr (Point 1, 2, and 3) (Figure 3.5). Velocities on the eastern side of the fault are notably higher than those on the western side. Another rapid deformation is observed 10 km on the Qigu Anticline, south of the Tugulu Anticline, with a deformation rate of 2.2–2.7 mm/yr (Point 4 on Figure 3.5b, c, j, and k). The consistent observations from both ascending and descending tracks confirm the robustness of these deformation trends, offering a more comprehensive picture of the tectonic activity following the 2016 Hutubi earthquake.

The cumulative displacement maps from the ascending (Figure 3.6) and descending tracks (Figure 3.7) further provide a spatio-temporal view of the surface displacement from 2016 to 2022. Displacement is measured relative to a stable reference pixel selected by LiCSBAS, shown in Figure 3.5b and c. From 2017 to 2022, no earthquakes with M_w>4 occurred in this area, while surface displacements gradually increased to finally reach about 25 mm toward the satellite in both ascending and descending geometries. Farther south, on the Qigu Anticline, the cumulative displacement reached 14 mm. This pattern is indicative of ongoing accelerated tectonic activity after the 2016 earthquake in the region.

3.4.3 InSAR line-of-sight velocity decomposition

InSAR observations can only measure one-dimensional LOS displacement of ground points (Wright et al., 2004). However, by combining LOS observations from both ascending and descending tracks, it is possible to retrieve horizontal and vertical displacement components. For a single set of InSAR data, the LOS velocity (V_{los}) that was derived from LiCSBAS for each pixel can be expressed as follow:

$$V_{\text{los}} = V_v \cos\theta - (V_e \cos\alpha - V_n \sin\alpha)\sin\theta, \tag{3.2}$$

where α is the azimuth of the LOS vector, θ is the incidence angle, and V_e, V_n, V_v are the velocities in the east-west, north-south and vertical directions, respectively. Given the near-polar orbit of Sentinel-1, with its nearly north-south flight direction, the LOS displacements are not sensitive to the north-south direction (Motagh et al., 2017), especially in our study area where the shortening is of 2–3 mm/yr(Lu et al., 2019). By excluding this component, Eq. 3.2 is transformed into the following form:

$$V_{\text{los}} = V_v \cos\theta - V_e \cos\alpha \sin\theta. \tag{3.3}$$

Eq. 3.3 can be solved if for each pixel at least two independent measurements from descending and ascending orbits exist to form the following matrix of equations:

$$\begin{pmatrix} V_{\text{los}}^a \\ V_{\text{los}}^d \end{pmatrix} = \begin{pmatrix} \cos\theta^a & -\cos\alpha^a \sin\theta^a \\ \cos\theta^d & -\cos\alpha^d \sin\theta^d \end{pmatrix} \begin{pmatrix} V_v \\ V_e \end{pmatrix}, \tag{3.4}$$

where the superscripts a and d refer to ascending and descending geometries, respectively. Our decomposed vertical velocity and east-west horizontal velocity are shown in Figure 3.8. Most of the deformation are related to the verticle uplift with negligible horizontal component.

3.5 Discussion

3.5.1 Discriminating dip direction based on afterslip

Discriminating the correct dip direction of the fault responsible for the 2016 Hutubi earthquake is crucial for understanding fault mechanics and regional tectonics. Both a low-angle south-dipping plane and a high-angle north-dipping plane fit observed coseismic surface displacement patterns very well (e.g., Wang et al., 2019; Yang et al., 2019). However, a more detailed analysis of aftershocks and postseismic deformation offers crucial insights that help to distinguish between these two scenarios.

Benefiting from the acquisition of high-resolution seismic reflection data from oil and gas exploration, the geometry of seismogenic structures in the northern Tian Shan

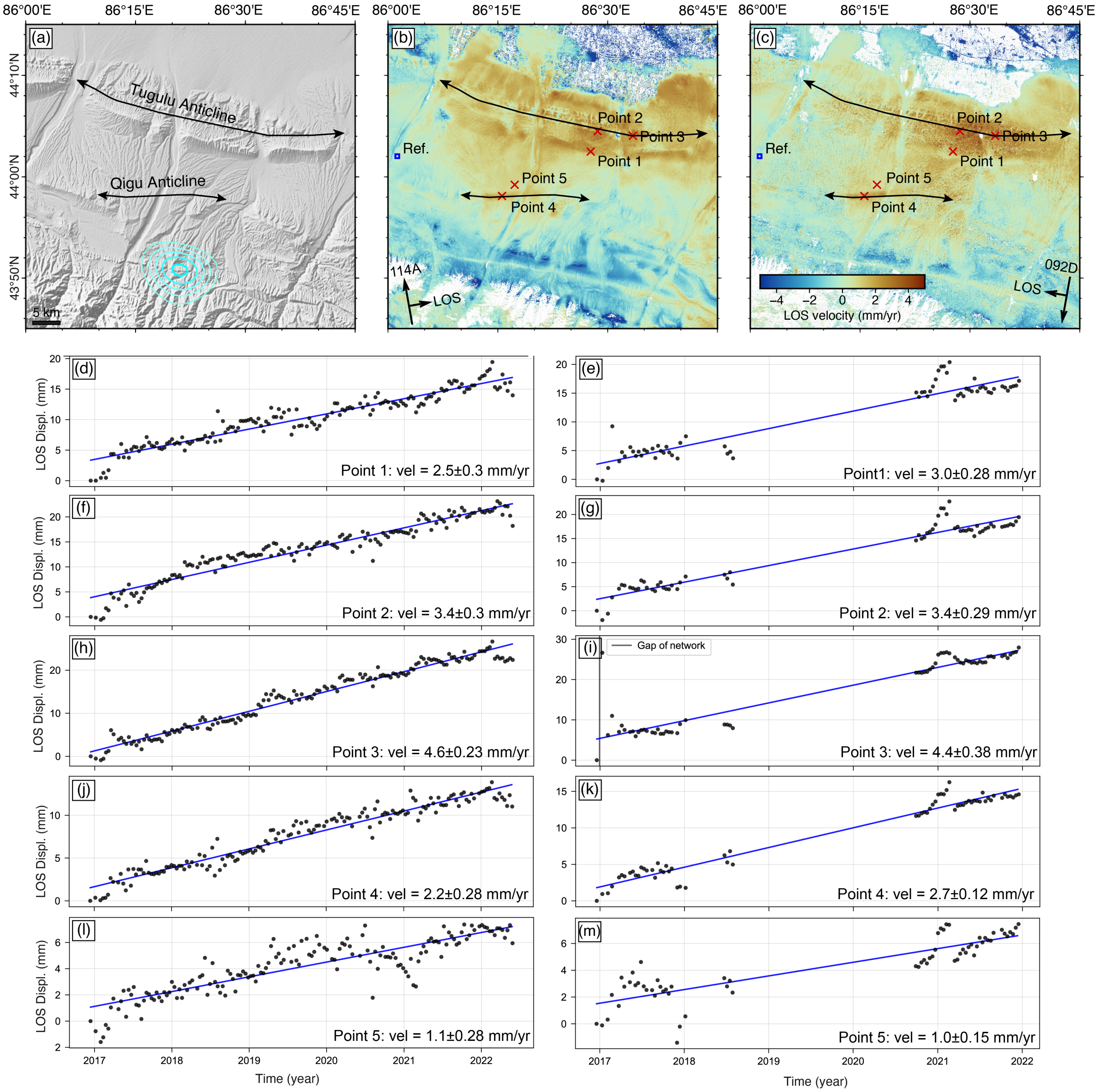

Figure 3.5: (a) Topographic map of the Tugulu Anticline with cyan contours representing coseismic slip, spaced at 5 cm intervals. The fold axis is indicated by a black arrow. Mean line-of-sight (LOS) velocities from the ascending track (b) and descending track (c), where positive values indicate motion towards the satellite and negative values indicate motion away from the satellite. (d)-(m) Time series of displacement for Points 1 to 5. The left column shows the time series from the ascending track 114, and the right column shows the time series from the descending track 092. Each time series plot includes a linear fit, with the estimated velocity and its uncertainty provided for each point. Note the gap in the descending track data between 2018 and 2020, which is marked as a thick gray line in (i).

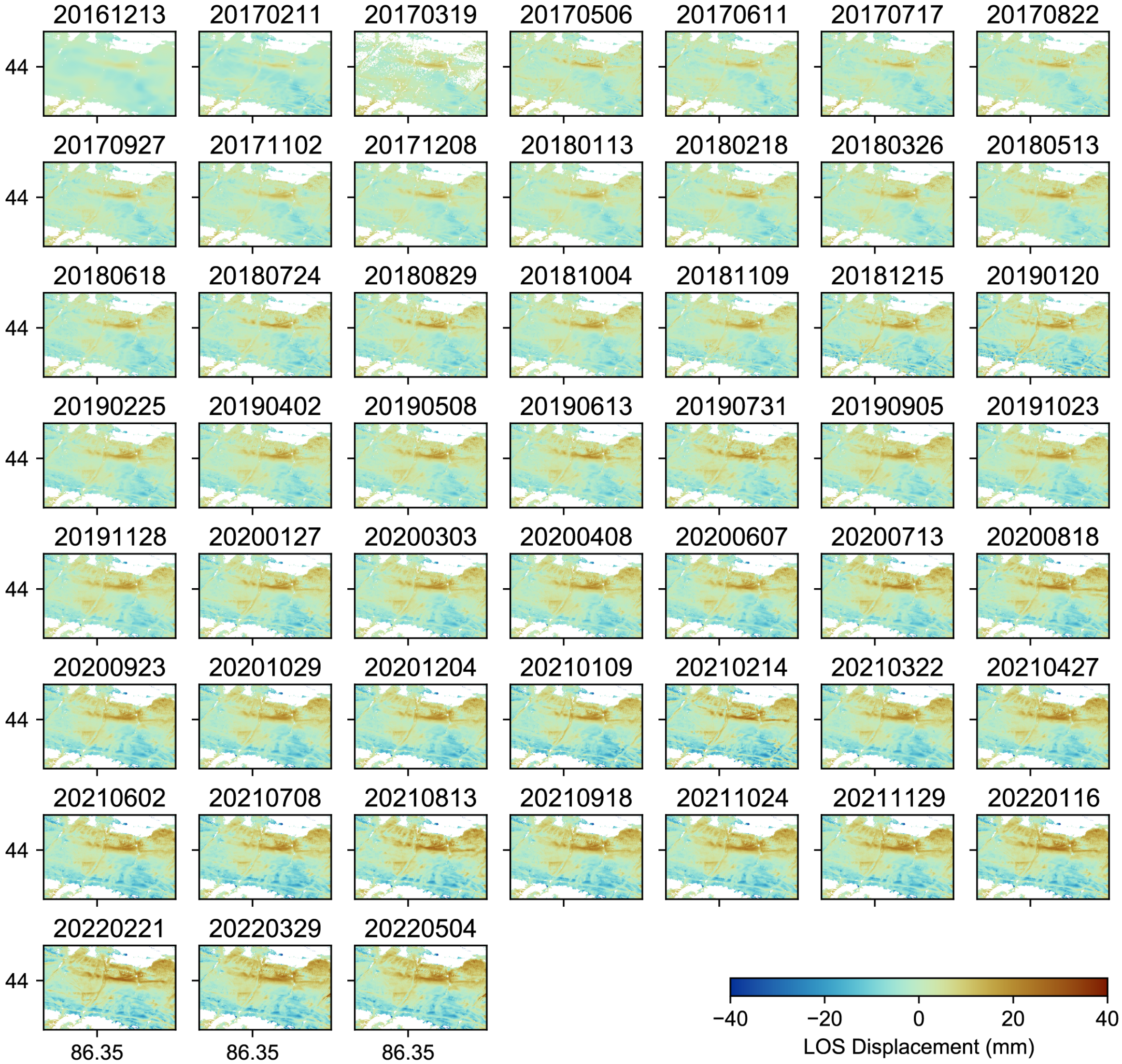

Figure 3.6: The cumulative displacement map derived from the ascending track. Red colours indicate areas of displacement towards the satellite, suggesting uplift or horizontal movement in the line-of-sight direction.

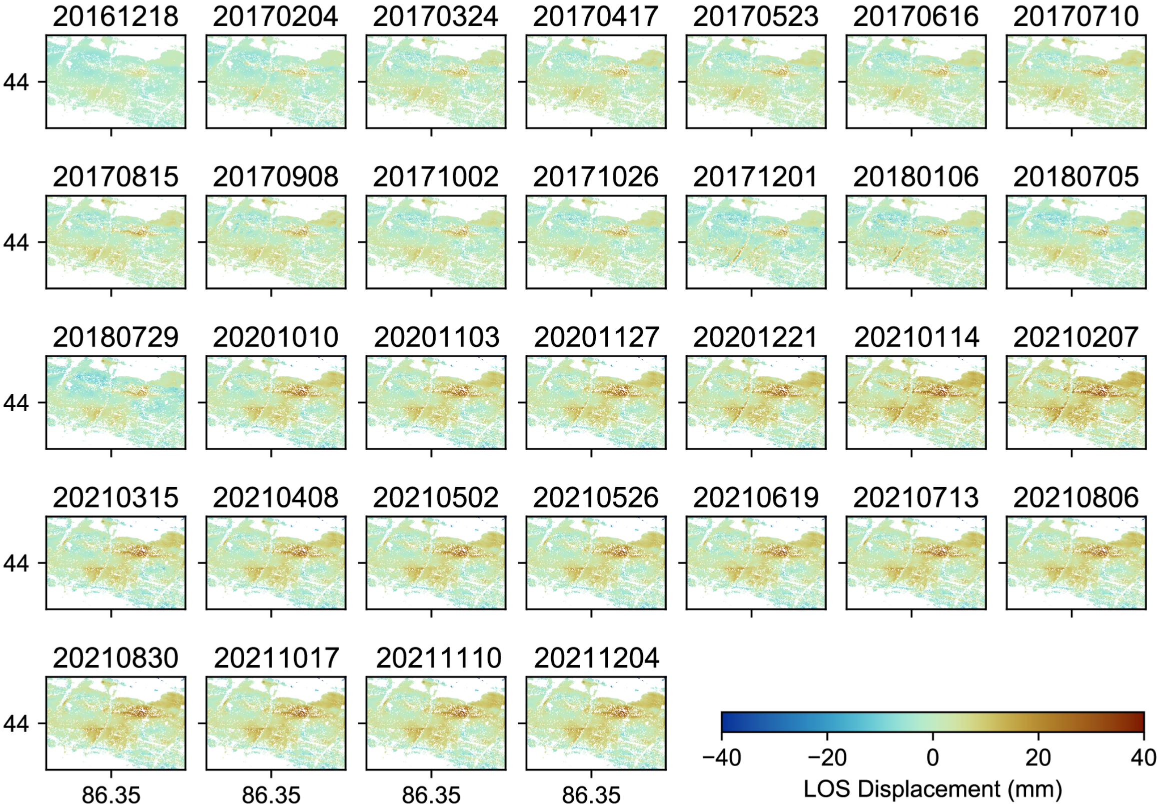

Figure 3.7: The cumulative displacement map derived from the descending track. Red colours indicate areas of displacement towards the satellite, suggesting uplift or horizontal movement in the line-of-sight direction.

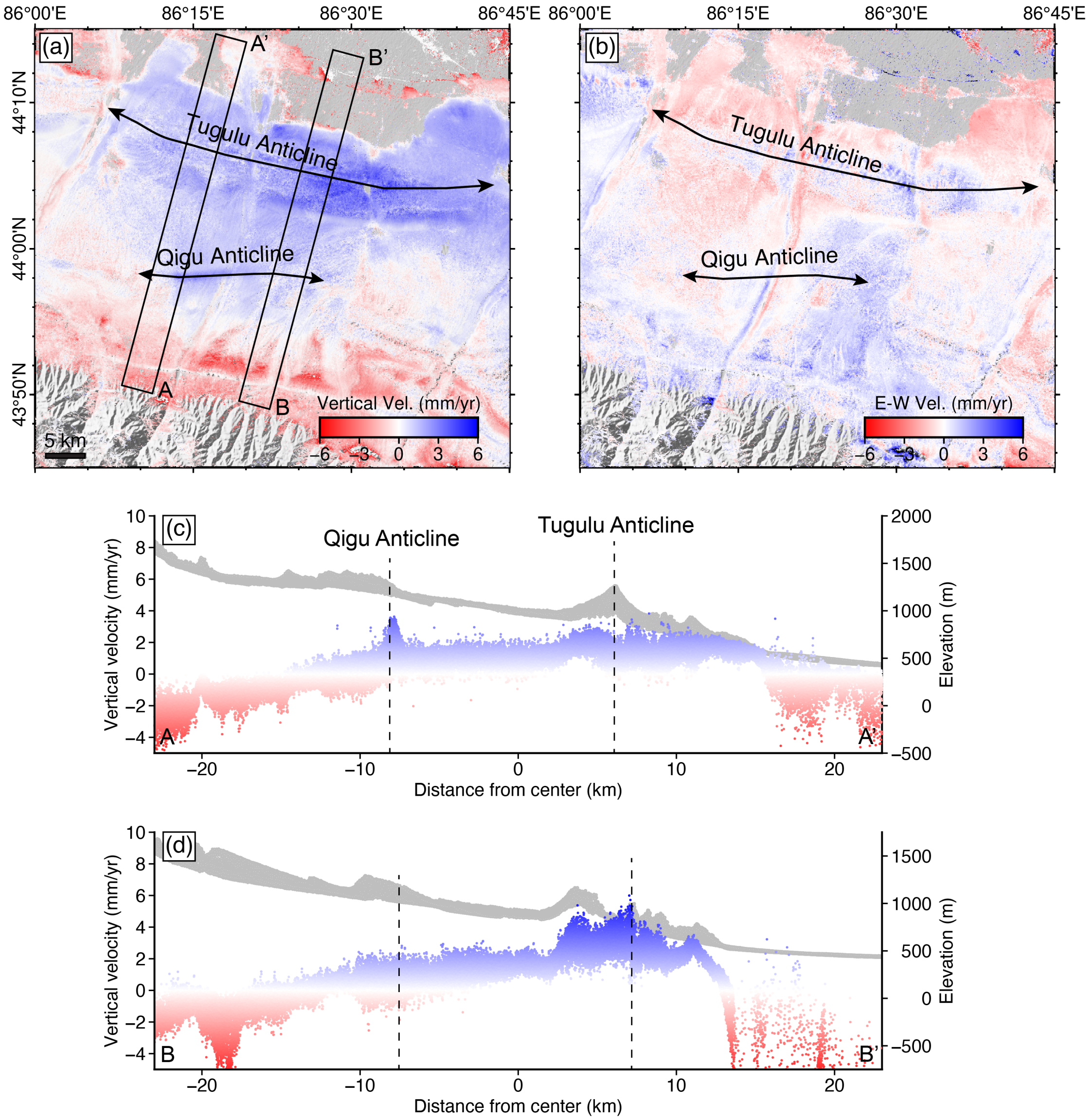

Figure 3.8: InSAR LOS velocities decomposed into (a) vertical components and (b) east-west components. The blue color indicates uplift in the vertical velocities and eastward motion in the E-W velocities. Each swath is 46 km long and 4 km wide. Topography data are sourced from SRTM3S using the Generic Mapping Tool (Wessel et al., 2019). Swath A–A', which crosses the Qigu anticline, shows a vertical velocity of ∼3.8 mm/yr while Swath B–B', crossing the Tugulu Anticline, indicates a vertical velocity of ∼5.8 mm/yr vertical velocity.

foreland has been well-imaged (Qiu et al., 2019). After the earthquake, two seismic reflection profiles closest to the epicentre were obtained and spliced together, forming the combined seismic reflection profile A-A' (Figure 3.9) (Lu et al., 2018). This profile crosses the Qigu and Tugulu anticlines and extends to a depth of 15 km, revealing a ramp-flat-ramp structure. By projecting the coseismic modelling results onto the profile, we found that the depth and location of the mainshock match well with the deeper segment of the ramp of the Hutubi Fault, confirming it as the seismogenic fault of the 2016 Hutubi earthquake.

Although aftershocks following the mainshock do not concentrate along a south-dipping plane, cluster along a steep north-dipping plane instead (Lu et al., 2018), the postseismic deformation time series reveals subsidence around the epicentre and continuous uplift farther north, particularly concentrated beneath the anticline with a maximum uplift rate of $\sim$5.8 mm/yr (Figure 3.8d), which is more indicative of a low-angle south-dipping fault. This distribution pattern of the mainshock and aftershock deformation may relate to a structural wedge, with coeval fore thrust and back thrust forming smaller imbricated structural wedges (Figure 3.9). Therefore, the concentration of aftershocks along the north-dipping fault is attributed to the back thrust fault. This confirms that the fault responsible for the 2016 Hutubi earthquake is indeed a low-angle south-dipping plane revealing that the fault responsible for the 2016 Hutubi earthquake is indeed a low-angle south-dipping plane (Lu et al., 2018) (Figure 3.9).

3.5.2 Shallow afterslip driven by deep coseismic slip

In this section, we discuss how InSAR provides new insights into earthquake-related processes along the northern margin of the Tian Shan. The faulting involved in the 2016 Hutubi earthquake and its postseismic afterslip play a crucial role in the growth of the foreland anticlines. Physical models of thrust and fold evolution show that long-term surface displacement results from the combination of slip along the fault at depth and distributed folding above the fault tip (Johnson, 2018). However, the contribution of anelastic deformation during the interseismic period is less clear. Using velocity data derived from InSAR, we identified anelastic contributions to fold growth (Figure 3.6 and 3.7). Unlike reversible coseismic elastic deformation, anelastic deformation is only partially reversible, with some deformation persisting after the load is removed.

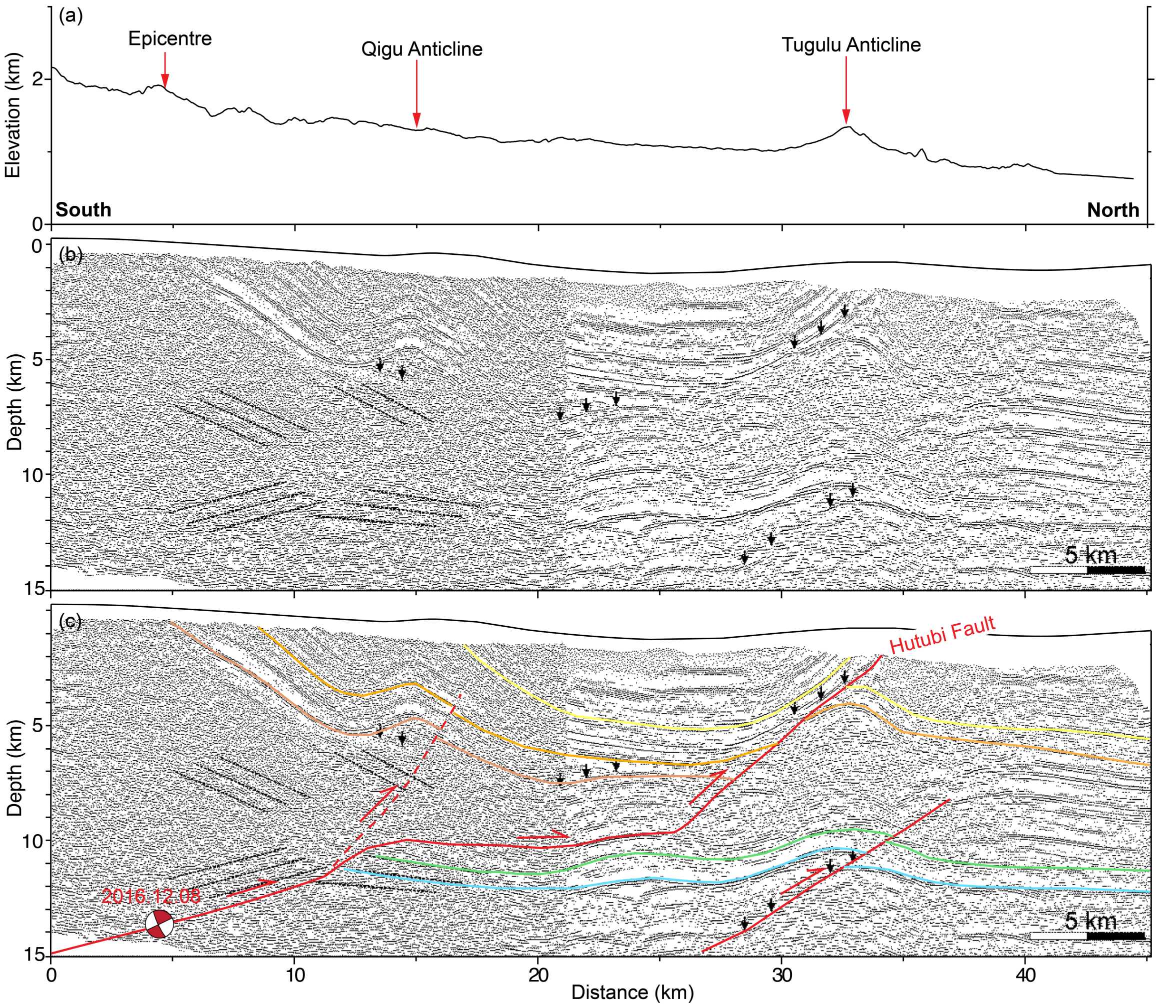

Figure 3.9: Interpreted seismic reflection profile (adapted from (Lu et al., 2018)). (a) The profile of topography along the line A-A' as indicated in Figure 3.1. (b) Uninterpreted and (c) interpreted Seismic reflection profiles highlighting the major boundaries between geological layers. The focal mechanism derived from InSAR coseismic south-dipping fault plane is located on the lower segment of the Hutubi Fault.

In the Hutubi earthquake, deep-seated rupture on the thrust fault may relieve stresses by slip on splay faults, connecting faults, or by creep. The sharp velocity change observed in the Tugulu Anticline indicates creeping along the shallow portion of the Hutubi Fault (Figure 3.8a, c, and d). Similar to the 1906 M 7-8 Manas earthquake, the Hutubi earthquake shared the same mechanism that the earthquake initiated at a relatively deep depth of 14 km and then propagated along a 10 km sub-horizontal detachment and then upwards causing the northward slip on the steeper Hutubi Fault (Figure 3.9). This is consistent with Yang et al. (2019)'s conclusion that moderate earthquakes with deep hypocentres have the potential to trigger the rupture of shallow overlying fault-related folds. The static Coulomb stress change indicates that dynamic stress may play a more critical role than static stress in triggering shallow movements, highlighting the potential seismic hazard in nearby regions.

Postseismic observations indicate that the fold associated with the earthquake continues to deform at a steady rate due to ongoing slow slip and propagation of the thrust fault (Figure 3.5). While individual earthquakes can cause local changes in the landscape and contribute to shaping the Earth's surface, the overall growth and formation of fold-and-thrust belts are due to the continuous and gradual processes of compression, folding, and faulting over geological scales. Jónsson et al. (2002) suggest that folds are generally built in a punctuated style by successive earthquakes over hundreds of thousands or millions of years, rather than by slow, steady deformation. The preservation of separate river terraces supports the idea that uplift was not gradual but sudden (Gong et al., 2014). However, the debate continues over whether fold growth is predominantly steady and aseismic or associated with abrupt faulting. Most faults exhibit stick-and-slip behaviour, leading to earthquakes. If fold growth were entirely due to earthquakes, these events should recur at regular intervals at the same sites, which has not been consistently observed. Therefore, it is evident that much of the fault slip and fold growth is steady, with stress being continuously relieved by creep, rather than accumulating until a sudden release.

It was reported that the southernmost part of anticlines in the SJFB was inactive during the late Quaternary (Deng et al., 1996). This is contradicted by our InSAR observations. Abandoned fluvial terraces have been extensively surveyed along the SJFB (Charreau et al., 2018; Yang et al., 2013; Gong et al., 2014). Since the long-term growth of fluvial terrace folds cannot be fully explained by repeated coseismic slip alone, the discrepancy between the long-term and present uplift rates has been partly attributed to other deformation mechanisms. Our InSAR time series analysis indicates ongoing deformation that could be attributed to postseismic slip or interseismic inelastic deformation. These mechanisms might play a significant role in the long-term evolution of the anticline.

3.6 Conclusion

By synthesizing observations from coseismic modelling, postseismic deformation, and high-resolution seismic reflection data, we conclude that the primary fault plane responsible for the 2016 Hutubi earthquake dips shallowly to the south. The coseismic deformation pattern was consistent with a shallowly south-dipping fault plane north front of Tian Shan with a dip angle of 28° at a depth of $\sim$14 km. The 5-year time series analysis suggests that deep coseismic slip potentially triggered movement along the shallower thrust fault, leading to accelerated deformation of the anticline, with the fault tip remaining locked.

The accelerated creeping rate indicates postseismic adjustments, where the fault is releasing residual stress that was not fully released during the main shock. This adjustment helps stabilize the region in the near term by gradually redistributing the remaining stress. However, while the creeping fault may reduce stress on itself, it can transfer stress to adjacent fault segments or nearby faults. This stress transfer can potentially increase the seismic hazard in neighbouring regions, possibly triggering aftershocks or new seismic activity on other faults. It may also lead to continued deformation that affects the shape and stability of the anticline. Continued monitoring of the fault creep rate is essential for hazard assessment and mitigation because creep contributes to the overall slip budget. In summary, Our InSAR-based study not only illuminates the coseismic mechanism but also provides valuable insights into the complex interplay of seismic and aseismic processes in the northern Tian Shan foreland. This comprehensive understanding is crucial for assessing seismic hazards in the region.

Chapter 4

Large-scale exhumation rate inversion and time-temperature history modelling of rocks around the Tarim Basin

Article information

Siyu Wang[1*], Ruohong Jiao[1], Huiping Zhang[2], Jiawei Zhang[2], and Jianzhang Pang[2]

[1]School of Earth and Ocean Sciences, University of Victoria, Victoria, BC, Canada
[2] State Key Laboratory of Earthquake Dynamics, Institute of Geology, China Earthquake Administration, Beijing, China

Status: In press
Manuscript ID: Lithosphere2024_114
Corresponding author: Siyu Wang (siyuwang@uvic.ca)

Abstract

The Tian Shan has been deformed during the Cenozoic as a far-field response to the India-Eurasia collision. We report new apatite fission track and apatite (U-Th)/He data from the northern Tian Shan, including areas along the southern margin of the Junggar Basin and adjacent to the western segment of the Bolokenu-Aqikekuduk Fault (BAF). Thermal history modelling of our data suggests that the Cenozoic exhumation along the basin margin started >20 Ma, and the oblique-slip BAF could have been active since at least ∼10 Ma with a total exhumation magnitude of ∼2 km during the late Cenozoic. Since then, the mean exhumation rate on southern wall of the BAF is comparable to the Quaternary uplift rate previously measured on the same segment of the fault. To examine the extent of the Miocene acceleration of the transpressional deformation pattern, we constrained an exhumation model by inverse modelling >1000 published and new apatite fission track and (U-Th)/He ages from the Tian Shan and the northeastern Tibetan Plateau. The model suggests that after the initial unroofing, a significant acceleration in exhumation occurred during 15–10 Ma, in regions including the interiors of northern and southwestern Tian Shan near major strike-slip structures. This change coincided with the northward propagation of the Pamir and the eastward expansion of the northeastern Tibetan Plateau along the west and south margins of the Tarim Basin, respectively.

4.1 Introduction

The evolution of the Tibetan Plateau and its surrounding regions is key for understanding the continental collision dynamics and the associated climate change in Central Asia. During the late Cenozoic, crustal stress from the converging Indian and Eurasian plates, or due to the growth of Tibetan topography, propagated northward into Central Asia (Aitken, 2011; Molnar and Tapponnier, 1975). This process led to the reactivation of weak structures in the Tian Shan that were inherited from the Paleozoic orogeny (Jun et al., 1998; Windley et al., 1990). The unroofing of the Tian Shan serves as a preeminent example of how the continental interior responded to the distant India-Eurasia collision, which occurred ∼1500 km to the south (Figure 4.1).

The Cenozoic uplift of the northeastern Tibetan Plateau was initially uplifted during the late Eocene–late Oligocene, as recorded by low-temperature thermochronology (Clark et al., 2010; Li et al., 2021a; Mock et al., 1999; Wang et al., 2016), while in

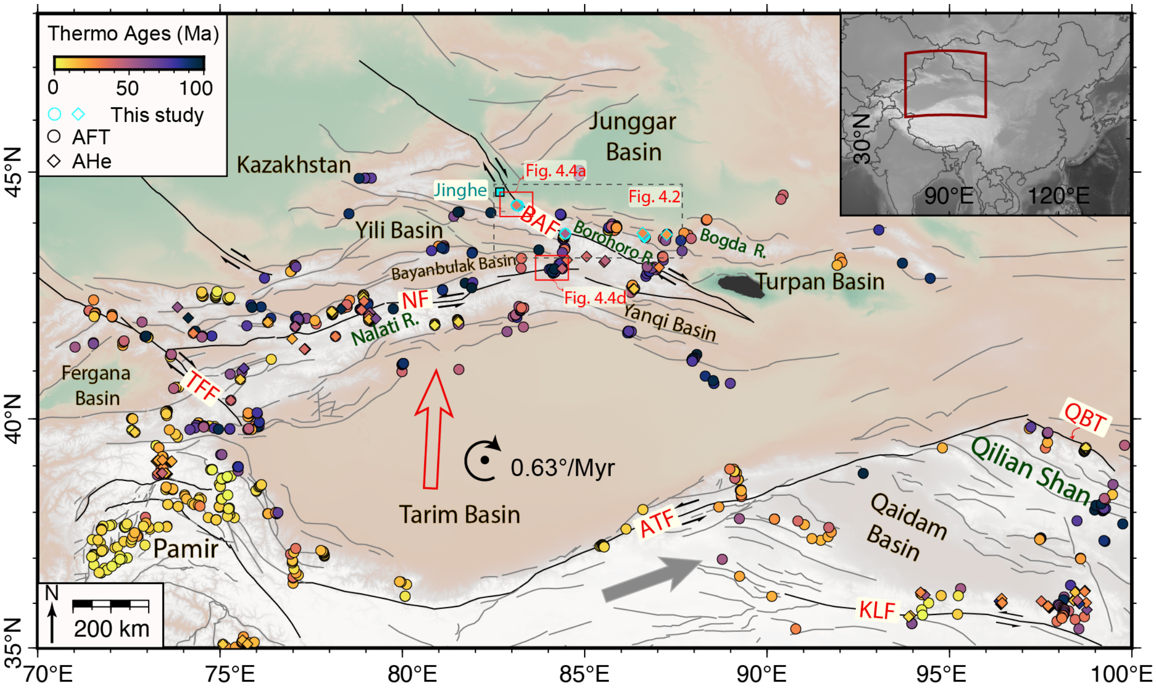

Figure 4.1: Map of the Tian Shan and adjacent regions, showing the topography, active faults, and thermochronological ages (<100 Ma) used in our exhumation rate model. Fault data are from Li et al. (2021b) (Tian Shan) and Mohadjer et al. (2016) (Pamir and NE Tibet). AFT ages (circle) and AHe ages (square) are from the literature (data and sources in the supplementary file) and this study (cyan outline; northern Tian Shan). The red arrow and semicircular arrow indicate the translation rate (13.8 ± 0.1 mm/yr) and rotation rate of the Tarim Block relative to the Eurasian Plate inferred from the GPS data (Wang et al., 2020a). BAF: Bolokenu-Aqikekuduk Fault; TFF: Talas-Fergana Fault; NF: Nalati Fault; ATF: Altyn Tagh Fault; QBT: Qilian Boundary Thrust; KLF: Kunlun Fault.

the far field Tian Shan, thermochronological studies suggest an extensive initial late Oligocene–early Miocene onset of the uplift and unroofing (Dumitru et al., 2001; De Grave et al., 2013; Hendrix et al., 1994; Sobel et al., 2006a) as a tectonic reactivation of the complex Paleozoic and Mesozoic lithospheric structures (Avouac et al., 1993a; De Grave et al., 2007), with a possible subsequent acceleration over the last ∼15–10 Ma (Bande et al., 2017b; Dumitru et al., 2001; De Grave et al., 2007, 2013; Jolivet et al., 2010; Macaulay et al., 2013, 2014; Sobel et al., 2006a,b). Therefore, the initial Cenozoic uplift of Tian Shan was either simultaneous or following that of northern Tibet, supporting it as a distant effect of the India-Eurasia collision, possibly due to the stress transferred from the elevated Tibetan Plateau through the rigid Tarim Basin (England and Houseman, 1986; Molnar and Tapponnier, 1975). However, after their initial uplift, the link in evolution between the Tian Shan and northeastern Tibet has not been investigated in detail. For example, the deformation style of northeastern Tibet changed at ∼15–10 Ma, from contraction along the plate convergence direction to the lateral, west-east motion, marked by the onset of transcurrent faulting in the region (Duvall et al., 2013; Lease et al., 2011). It remains unclear whether or how this change has influenced the deformation of the Tian Shan.

While most of the crustal shortening in the Tian Shan has been accommodated by the deformation of fold-and-thrust belts along the mountain boundaries (Avouac et al., 1993a; Burbank et al., 1999), deformation on regional-scale strike-slip faults within the mountain have also been clearly recognized (Burtman et al., 1996; Campbell et al., 2013). These structures include several northwest-southeast trending dextral faults, such as the Bolokenu-Aqikekuduk Fault (BAF, also named as Dzhungarian Fault), running parallel to the northern Tian Shan, and the Talas-Fergana Fault (TFF) on the boundary between southwestern Tian Shan and the Pamir, as well as the southwest-northeast trending sinistral Nalati Fault (NF) in the central Tian Shan (Figure 4.1). These major strike-slip faults are commonly oriented at 60°–75° in map view relative to the maximum compressive stress direction (σ_1), forming V-shaped conjugate fault sets. The transpressional deformation along these faults not only accommodates significant crustal shortening in the nearly north-south direction but also extension in the east-west direction (Burtman et al., 1996; Campbell et al., 2013; Selander et al., 2012; Tapponnier and Molnar, 1979; Wu et al., 2014; Zubovich et al., 2010). Some studies suggest that structural style changes are often observed during the later stages of convergent orogen development (Copley and Jackson, 2006; Duvall et al., 2013). Therefore, constraining the Cenozoic kinematic history of strike-slip faults within the Tian Shan, especially the timing and duration of their activity, is crucial for understanding the evolution of Tian Shan and its response to the collision dynamics and plateau uplift farther south.

To investigate the exhumation history of the Tian Shan and its relationship with large-scale strike-slip faults, we constrained thermal history and exhumation models of samples from sites near the western segment of the BAF, northern Tian Shan foreland, and the eastern end of the NF (Figure 4.1), using new and published apatite fission track (AFT) and apatite (U-Th)/He (AHe) data, respectively. By comparing the estimated million-year-scale exhumation rates with previously estimated kilo-year-scale late Quaternary fault slip and uplift rates, our results provide constraints on the transpressional deformation history of the Tian Shan. Because of the complex and asynchronous distribution of deformation across the Tian Shan, it is challenging to make generalizations about the entire range based on observations from only a small part of the mountains. To address this, we compiled over 1000 new and existing AFT and AHe ages from the Tian Shan, northeastern Pamir, and the northeastern Tibetan Plateau (Figure 4.1) to estimate the correlation between the deformation of the Tian Shan and other regions around the Tarim Basin. The compiled ages are used to constrain a large-scale exhumation model, reveal the main features of exhumation rate evolution, and identify the potential impact that the large strike-slip faults might have on the exhumation.

4.2 Tectonic setting and strike-slip deformation of the Tian Shan

The Tian Shan is a ∼2500 km long and 300–400 km wide orogenic belt, comprising a series of basement-cored ranges divided by strike-slip faults and intermontane basins. It is located between the Tarim Basin to the south and the Kazakh platform and Junggar Basin to the north (Figure 4.1). The ancestral Tian Shan orogen was formed during the Paleozoic plate convergence, through the accretion and amalgamation of micro-continents, accretionary wedges, and volcanic arcs of the paleo-Asian Ocean, which separated Eurasia and Gondwana (Carroll et al., 1995; Jun et al., 1998; Windley et al., 2007). The Mesozoic experienced localized deformation and small-magnitude rock exhumation within the Tian Shan (De Grave et al., 2007; Jolivet et al., 2010). The entire orogen was reactivated in the late Cenozoic in response to the collision of

India into Eurasia (Molnar and Tapponnier, 1975).

Ongoing indentation is the main driving force behind the present-day tectonic activity in the Tibetan Plateau and Tian Shan. GPS data reveal large velocity gradients exist across major strike-slip faults (Wang et al., 2020a). Strike-slip earthquakes mainly occur in the southwestern Tian Shan, near the boundary with the Pamir block, and within the interiors of the northern and central Tian Shan, e.g., along the BAF and NF, respectively. These faults were (re)activated episodically in response to distal plate collisions (Burtman et al., 1996). The BAF, stretching over 1000 km from the Kazakh Platform to the Turpan Basin and transecting the northern Tian Shan obliquely, is an inherited structure from the Paleozoic deformation. The late Quaternary mean dextral slip rate on the BAF is up to 5 mm/yr near the western Junggar Basin, and decreases to 1 mm/yr towards its eastern end (Shen et al., 2003). The NF, generally running along the strike of the southwestern Tian Shan, was also part of the Paleozoic suture zone between the Kazakh and Tarim blocks (Figure 4.1). This fault zone experienced significant transpressive deformation during the Paleozoic collision and accumulated a total of 60 km sinistral displacement (Bazhenov and Mikolaichuk, 2004). Further to the southwest, the TFF, another seismically active inherited Paleozoic structure, has accumulated a total of over 200 km right-lateral offset since its formation (Burbank et al., 1999).

4.3 Samples and methods

Low-temperature thermochronology is based on concentrations of parent isotopes and daughter products (e.g., fission tracks and alpha particles) of radioactive decay measured in minerals and is widely used in tectonic studies for estimating rock cooling and denudation histories. Apatite fission track and apatite (U-Th)/He thermochronometers are sensitive to the thermal evolution of rocks at temperatures below ∼120°C and ∼70°C, respectively (Farley, 2000; Ketcham et al., 2007), so are the most effective in resolving the rock exhumation history within the upper 4 km of the crust. Increases in exhumation rates are a common consequence of high topographic relief generated by dip-slip faulting but could also be related to deformation on strike-slip faults with a measurable vertical component (Duvall et al., 2013; Spotila et al., 2007).

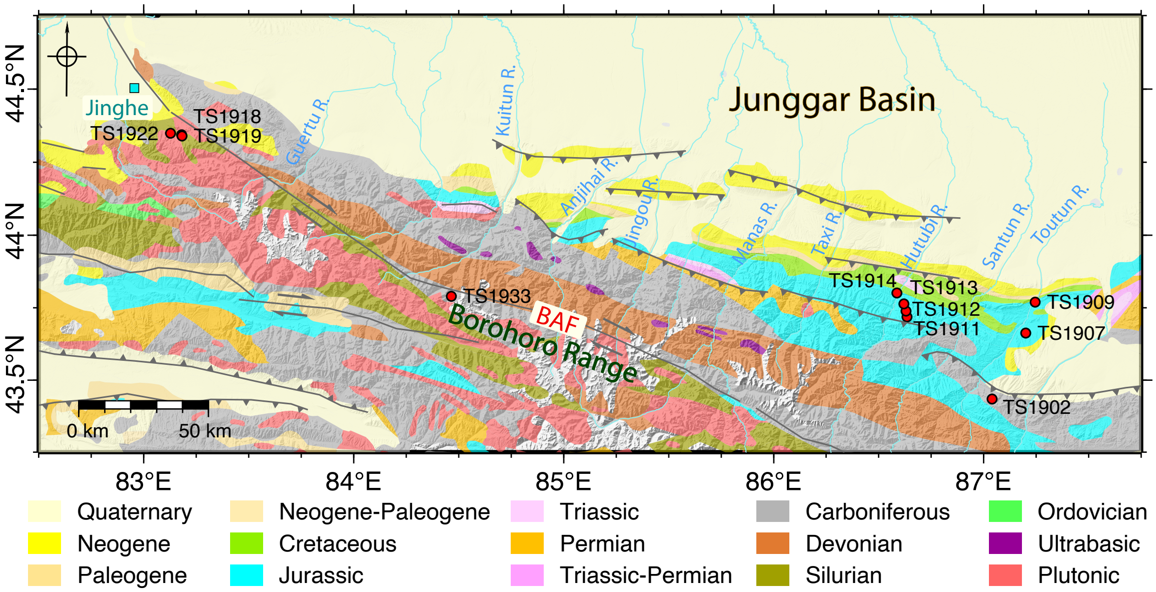

Figure 4.2: Geological map of northern Tian Shan, with red dots indicating the locations of new samples. The light blue lines represent the rivers. The extent of this map is shown in Figure 4.1.

4.3.1 New samples

We collected a total of 11 samples along the northern Tian Shan that were analyzed for apatite fission track and apatite (U-Th)/He dating (Figure 4.2, Table 4.1). Among these, three samples (TS1918, TS1919, TS1922) were from granitic intrusion rocks around Jinghe county, and one from the middle segment of BAF (TS1933). The remaining seven samples were collected from the Jurassic and Carboniferous sandstone along the Toutun River and Hutubi River on the southern margin of the Junggar Basin. Samples were crushed, sieved, and processed through traditional magnetic and density methods to separate apatite crystals.

4.3.2 Apatite fission track analysis

The apatite fission track analysis was performed at the State Key Laboratory of Earthquake Dynamics, Institute of Geology, China Earthquake Administration, using the laser ablation-inductively coupled plasma mass spectrometry (LA-ICP-MS) method (Hasebe et al., 2004; Pang et al., 2017). Apatite grains were mounted on glass slides with araldite epoxy. After grinding and polishing to expose internal surfaces, spontaneous tracks were etched with 5.5 M HNO_3 at 21°C for 20 seconds (Donelick et al., 1999). ^{238}U concentration was measured using LA-ICP-MS, and the National

Table 4.1: **Sample locations and lithology details.**

Sample	Latitude (°N)	Longitude (°E)	Elevation (m)	Intrusion/Depositional age	Lithology
TS1902	43.4232	86.8829	1713	Carboniferous	Sandstone
TS1907	43.6804	87.1661	1185	Jurassic	Sandstone
TS1909	43.7696	87.2452	1318	Jurassic	Sandstone
TS1911	43.7189	86.6352	2030	Jurassic	Sandstone
TS1912	43.7386	86.6303	1693	Jurassic	Sandstone
TS1913	43.7638	86.6195	1499	Jurassic	Sandstone
TS1914	43.8014	86.5862	1268	Jurassic	Sandstone
TS1918	44.3440	83.1802	1975	Silurian	Granite
TS1919	44.3401	83.1823	2080	Silurian	Granite
TS1922	44.3492	83.1275	1635	Silurian	Granite
TS1933	43.7900	84.4652	2635	Silurian	Granite

Bureau of Standards trace element glass NIST612 was used as the external standard. Fission track density and length were measured under a Zeiss Axioplan 2 microscope, with a dry objective and total magnification of 1000. Horizontal confined tracks for each sample were measured where possible. AFT ages were calculated using the formula described by Gleadow et al. (2015).

4.3.3 Apatite (U-Th)/He analysis

Apatite (U-Th)/He analysis was also conducted at the Institute of Geology, China Earthquake Administration following the standard procedures described in Farley and Stockli (2002). Euhedral crystals were hand-picked from separated apatite grains. For each sample, five apatite crystals were selected, photographed, and grain dimensions were measured under a high-power binocular microscope with a magnification of 100. Apatite grains were degassed by heating with an Nd-YAG laser (8A current) for 5 minutes, and He was measured with an Australian Scientific Instruments Alphachron noble gas mass spectrometer. After degassing, grains were dissolved in the 7 mol/L nitric acid with spikes of ^{235}U and ^{230}Th. The solutions of U and Th were analyzed by an Agilent 7900 ICP-MS. The raw apatite (U-Th)/He ages were corrected for α-ejection according to Farley et al. (1996).

4.3.4 Thermal history modelling

Near the BAF in the northern Tian Shan, we simulated the rock cooling histories using new AFT and AHe data from the plutonic rocks. On the southern margin of the Junggar Basin, five of the seven Mesozoic sedimentary rock samples were used for thermal history modelling. Despite the relatively older AFT ages, AHe data of these samples yield consistent Cenozoic ages, indicating that they had been fully reset after deposition. Two samples (TS1902 and TS1907) were not used for modelling, due to their scattered and mostly pre-Cenozoic single-grain AHe ages. In addition to the simulation of new data, we also simulated the cooling history on the southern margin of the Nalati range near the eastern NF (Figure 4.1), using AFT and AHe data from two samples (Bay D and Bay E) reported by Jolivet et al. (2010). This site was chosen due to its proximity to the NF and the availability of both AFT and AHe. The modelling procedure optimizes the thermal history using a Bayesian transdimensional Markov Chain Monte Carlo (MCMC) method implemented in the QTQt software (Gallagher, 2012). Each forward model of the thermal history is defined as a limited number of time-temperature points, and the model likelihood is quantified by the fit between the observed and predicted thermochronological data. To avoid overcomplex models, the method adds a penalty to the likelihood of increasing the number of time-temperature points to calculate the posterior probability. AFT and AHe data were predicted using the annealing model of Ketcham et al. (2007) and the He retention model of Flowers et al. (2009), respectively. During the inversion, a temperature offset between the uppermost and lowermost samples on a near-vertical profile is also sampled, allowing an estimate of the paleo-geothermal gradient. The random walk is performed in the 3D parameter space consisting of time (200–0 Ma), temperature (150–0°C), and temperature gradient (20–40°C), assuming a uniform prior distribution for all model parameters. The present-day temperature of the uppermost sample on a profile is prescribed at 5–25°C. For each inversion, we ran 200,000 MCMC iterations and discarded the initial 100,000 as the "burn-in" with the rest kept in the "post-burn-in" ensemble.

4.3.5 Inverse modelling of exhumation rates from thermochronometric ages

We compiled >1000 published and new AFT and AHe ages that are younger than 100 Ma from the Tian Shan and adjacent regions (Figure 4.1, Table C.1). The compiled ages were modelled using the method described in Fox et al. (2014) and modified by Herman and Brandon (2015) to infer the exhumation rate. This modelling approach considers the closure depth of a thermochronological age as a summation of exhumation rates of a limited number of time steps, over the period from the time indicated by the apparent cooling age to the present day. Dodson (1973)'s approximation is used to estimate the effective closure temperature of an age, which is dependent on the cooling rate when the rock passed through the closure temperature. The thermal model of the crust is solved in one dimension at each sample location. The a priori rate of 0.05 km/Ma was set according to the observation that in regions with slow exhumation in the Tian Shan, the total exhumation (<4 km) in the Cenozoic has not reset the AFT ages (e.g., (Dumitru et al., 2001)). Our thermal model has a thickness of 30 km with surface and base temperatures at 15°C and 615°C, respectively. This initial model setup mimics the current mean geothermal gradient (∼20 °C/km) in the Tarim Basin (LiuS et al., 2016), where we assume negligible exhumation has taken place. We used a spatial correlation distance (L_c) of 30 km and a time interval length (Δt) of 5 Ma for our reference model, but also tested different values for L_c (2–50 km) and Δt (3, 4, and 5 Ma). Each inversion contains 20 iterations. Detailed descriptions of the inversion method as well as discussions of its limitations were provided by Fox et al. (2014), Herman and Brandon (2015), Stalder et al. (2020), and Willett et al. (2020).

4.4 Results

4.4.1 Apatite fission track and apatite (U-Th)/He results

The 11 new apatite fission track ages reported vary between 37.6 Ma and 213 Ma (Table 4.2). Ten of them yield Mesozoic ages while only one has Cenozoic age. Figure 4.3 shows the radial plots of grain ages. Track length distributions are also shown for all samples except TS1909 and TS1933, in which only a very small number (≤ 5) of confined track lengths could be measured. The mean D_{par} values from these samples span between 1.58 and 3.19 µm, with the measured fission track lengths ranging from 11.3 to 13.65 µm (Figure 4.3). All ages passed the chi-squared (χ^2) test with low dispersion. The range and average values of length measurements remain relatively consistent despite differences in the AFT ages of the samples. Apatite (U-Th)/He ages derived from the same set of samples with the AFT samples. A total of 54 single-grain ages show significant variability, ranging from 8.11 to 237.73 Ma (Table 4.3). We excluded one sample (TS1902) from interpretation due to its large grain age dispersion. Additionally, we excluded single grain AHe ages prior to the Cenozoic from our thermal history modelling.

Table 4.2: Apatite fission track results from this study.

Sample	**Nc**^{a}	$\rho_s{}^b$ (10^5**cm**$^{-2}$)	**Ns**	**U (ppm)**	**P**(χ^2) (%)^e	**Central Age (Ma)**	**Error** (1σ)	**MTL** (μm)^f	**Error** (1σ)	**Nj**^{g}	**Standard Deviation**	**Dpar** (μm±SD)
TS1902	32	4.55	601	5.52	18	186.0	10	12.84	0.3	32	1.77	2.31
TS1907	35	6.34	1270	7.64	32	170.2	5.5	12.65	0.16	119	1.71	3.10
TS1909	33	1.89	139	1.74	100	213.0	18	12.02	0.9	5	2.12	3.19
TS1911	32	5.57	916	8.38	38	140.4	5	11.51	0.3	106	1.96	2.70
TS1912	34	6.3	637	11.84	59	105.8	4.9	12	0.3	44	2.01	2.27
TS1913	35	4.62	774	6.32	92	149.8	5.5	11.3	0.2	52	1.48	2.60
TS1914	35	5.69	563	8.12	37	150.7	7.5	11.63	0.2	58	1.65	3.18
TS1918	34	6.24	1042	12.88	33	97.1	3.5	12.13	0.15	96	1.45	2.15
TS1919	33	4.47	559	9.42	98	101.9	4.4	12.18	0.16	103	1.59	2.44
TS1922	33	4.12	456	10.24	65	82.2	4.5	11.92	0.3	36	1.66	2.15
TS1933	34	8.55	96	4.39	99	37.6	3.9	13.65	0.45	2	0.64	1.58

[a] N_c is the number of individual crystals (grains) dated.

[b] ρ_s is the spontaneous track density ($\times 10^6$ tracks per square centimeter).

[c] N_s is the number of spontaneous tracks counted.

[d] U concentration is the calculated uranium density (in ppm).

[e] P(χ^2) is the probability in % of χ^2 for ν degrees of freedom. Degrees of freedom ν = number of crystals − 1 (Galbraith et al., 1999; Green et al., 1989).

[f] Mean track length (MTL) is the measured mean fission track length in μm. Track length measurements were performed on horizontal confined fission tracks in crystal sections parallel to the c axis. Error is $\pm 1\sigma$.

[g] N_j are total numbers of tracks measured for length.

[h] Measured Dpar is the measured mean diameter (μm) of the etched trace of the intersection of a fission track with the surface of the analyzed apatite crystal, measured parallel to the c axis.

Table 4.3: **Apatite (U-Th)/He age data from this study.**

Sample	^{238}U (ppm)[a]	Error[b]	^{232}Th (ppm)	Error	^{4}He (ppm)	Error	eU (ppm)[c]	Raw Age	Error	R (μm)[d]	L (μm)[e]	Mass (μg)[f]	Rs (μm)[g]	F_T[h]	Corrected Age	Error
TS1902																
01	2.87	0.10	1.98	0.14	1.39E-02	1.43E-04	3.34	190.66	6.32	55.1	156.9	3.96	54.9	0.802	237.73	7.88
02	1.09	0.09	3.80	0.27	2.05E-03	2.96E-05	2.00	47.65	2.81	42.9	133.8	2.05	43.6	0.735	64.83	3.82
03	11.01	0.28	29.06	0.43	2.26E-02	2.37E-04	17.93	58.26	1.13	42.9	126.9	1.94	43.1	0.738	78.94	1.53
04	1.75	0.10	6.24	0.22	1.35E-03	2.10E-05	3.23	19.37	0.76	42.2	139.7	2.07	43.5	0.732	26.46	1.04
05	8.40	0.31	19.85	0.62	4.79E-02	5.21E-04	13.13	167.54	4.74	38.9	109.4	1.38	38.6	0.714	234.65	6.64
TS1907																
01	6.81	0.18	16.22	0.28	2.20E-02	2.25E-04	10.67	95.03	1.96	74.0	174.8	3.96	54.9	0.802	112.20	2.31
02	55.64	1.29	65.16	1.12	5.37E-02	5.52E-04	71.15	34.98	0.74	76.7	213.1	2.05	43.6	0.735	43.24	0.91
03	8.12	0.21	22.74	0.52	2.36E-02	2.42E-04	13.53	80.67	1.68	53.6	157.1	1.94	43.1	0.738	105.87	2.20
04	8.95	0.26	24.63	0.54	2.88E-02	3.00E-04	14.81	89.71	1.97	51.9	197.2	2.07	43.5	0.732	117.88	2.59
05	6.11	0.19	17.08	0.34	2.57E-02	2.61E-04	10.17	116.37	2.67	58.9	176.9	1.38	38.6	0.714	144.38	3.31
TS1909																
01	1.35	0.09	7.91	0.28	1.53E-03	2.76E-05	3.23	21.95	0.84	39.0	163.2	1.78	41.9	0.681	32.23	1.23
02	1.34	0.11	12.78	0.61	1.60E-03	4.57E-05	4.38	16.99	0.86	33.2	113.4	0.86	34.0	0.616	27.58	1.40
03	1.10	0.11	3.87	0.41	5.76E-04	2.47E-05	2.02	13.22	1.14	31.0	142.7	1.14	33.9	0.64	20.66	1.78
04	-	-	-	-	-	-	-	0.00	0.00	30.5	127.3	-	-	-	-	-
05	2.33	0.18	9.46	0.28	1.20E-03	2.57E-05	4.59	12.14	0.57	51.3	137.1	1.7	46.7	0.688	17.65	0.83

Table 4.3: (continued)

Sample	^{238}U (ppm)[a]	Error[b]	^{232}Th (ppm)	Error	^{4}He (ppm)	Error	eU (ppm)[c]	Raw Age	Error	R (μm)[d]	L (μm)[e]	Mass (μg)[f]	Rs (μm)[g]	F_T[h]	Corrected Age	Error
TS1911																
01	0.05	0.00	0.20	0.04	2.54E-05	2.43E-06	0.10	12.30	1.72	77.9	277.0	13.98	81.4	0.851	14.45	2.02
02	25.54	0.64	86.52	1.90	2.34E-02	2.41E-04	46.13	23.53	0.47	50.1	148.0	3.09	50.3	0.717	32.82	0.66
03	24.92	0.67	43.75	0.91	1.16E-02	1.28E-04	35.33	15.17	0.34	51.7	158.1	2.19	50.1	0.716	21.19	0.47
04	3.10	0.11	14.34	0.38	1.70E-03	2.26E-05	6.52	12.10	0.30	56.4	188.4	4.12	57.5	0.772	15.67	0.39
05	92.74	2.25	39.78	0.64	5.98E-02	6.09E-04	102.20	27.09	0.66	61.8	180.5	4.6	60.7	0.802	33.78	0.82
TS1912																
01	177.59	4.22	17.04	0.38	2.37E-01	2.42E-03	181.64	60.28	1.52	39.7	124.1	1.63	40.4	0.734	82.13	2.07
02	44.47	1.37	55.19	1.39	2.95E-02	3.20E-04	57.61	23.71	0.63	33.7	118.4	0.93	34.8	0.648	36.59	0.97
03	526.48	12.35	213.63	3.51	7.99E-01	8.18E-03	577.33	63.93	1.51	36.1	148.2	1.61	38.7	0.658	97.16	2.29
04	12.94	0.34	5.98	0.34	3.54E-03	4.48E-05	14.36	11.44	0.32	43.2	134.7	2.09	43.9	0.751	15.23	0.43
05	21.98	0.84	60.21	1.07	1.99E-02	2.07E-04	36.31	25.36	0.67	35.5	152.6	1.38	38.3	0.661	38.37	1.01
TS1913																
01	3.92	0.12	14.04	0.28	1.20E-03	1.72E-05	7.26	7.67	0.18	63.4	149.9	5.01	60.3	0.818	9.38	0.22
02	4.57	0.11	26.86	0.58	1.79E-03	2.42E-05	10.96	7.61	0.16	50.6	165.8	3.53	52.0	0.719	10.58	0.22
03	15.46	0.46	84.49	1.28	1.10E-02	1.17E-04	35.57	14.34	0.27	62.2	160.7	5.17	60.5	0.758	18.92	0.36
04	1.17	0.06	5.94	0.11	4.87E-03	5.04E-05	2.58	87.13	2.37	68.0	245.1	9.42	71.2	0.792	110.01	2.99
05	3.99	0.12	20.36	0.40	1.46E-02	1.49E-04	8.83	76.35	1.55	80.0	214.3	11.4	78.5	0.853	89.51	1.82

Table 4.3: (continued)

Sample	^{238}U (ppm)[a]	Error[b]	^{232}Th (ppm)	Error	^{4}He (ppm)	Error	eU (ppm)[c]	Raw Age	Error	R (μm)[d]	L (μm)[e]	Mass (μg)[f]	Rs (μm)[g]	F_T[h]	Corrected Age	Error
TS1914																
01	21.48	0.62	40.55	0.84	4.09E-03	4.81E-05	31.13	6.10	0.15	44.8	131.8	2.2	45.0	0.752	8.11	0.20
02	7.10	0.32	11.32	0.36	1.25E-03	2.99E-05	9.80	5.91	0.25	47.2	134.8	1.49	44.4	0.683	8.65	0.37
03	2.38	0.15	15.15	0.41	3.98E-03	5.25E-05	5.99	30.85	1	34.7	120.0	1.2	36.0	0.668	46.18	1.50
04	3.56	0.20	16.91	0.64	5.59E-03	7.17E-05	7.58	34.2	1.22	35.4	126.9	1.32	37.0	0.621	55.07	1.96
05	0.74	0.12	9.41	0.51	1.20E-03	2.34E-05	2.98	18.67	1.12	47.8	162.9	2.57	49.0	0.724	25.79	1.55
TS1918																
01	14.26	0.46	18.73	0.57	1.62E-02	1.71E-04	18.72	40.13	1.10	192.5	56.2	4.2	57.7	0.782	51.32	1.41
02	20.34	0.53	38.04	0.73	2.93E-02	3.08E-04	29.39	46.18	1.01	169.7	49.5	3.46	51.3	0.775	59.59	1.30
03	29.98	0.50	40.22	0.47	2.39E-02	2.46E-04	39.55	28.01	0.46	185.8	49.4	3.77	52.2	0.775	36.14	0.59
04	9.93	0.30	12.68	0.29	5.13E-03	5.53E-05	12.95	18.39	0.48	169.9	49.9	2.32	50.3	0.72	25.54	0.67
05	18.28	0.34	22.13	0.42	2.39E-02	2.43E-04	23.55	47.01	0.85	196.6	54.8	4.12	56.9	0.778	60.42	1.09
TS1919																
01	17.66	0.42	21.21	0.30	1.32E-02	1.41E-04	22.71	26.86	0.58	160.3	40.3	1.9	42.8	0.707	37.99	0.82
02	11.77	0.18	25.60	0.44	1.42E-02	1.46E-04	17.86	36.83	0.57	191.5	46.1	3.38	49.5	0.758	48.59	0.75
03	24.52	0.44	30.04	0.53	3.39E-02	3.66E-04	31.67	49.47	0.89	133.1	36.9	1.27	38.4	0.678	72.96	1.31
04	7.83	0.15	13.80	0.24	9.55E-03	1.05E-04	11.12	39.76	0.73	153.8	46.2	2.73	47.6	0.759	52.38	0.96
05	51.93	0.90	54.85	1.01	8.49E-02	8.66E-04	64.98	60.40	1.06	167.1	46.5	2.04	47.7	0.707	85.43	1.50

Table 4.3: (continued)

Sample	^{238}U (ppm)^{a}	Error^{b}	^{232}Th (ppm)	Error	^{4}He (ppm)	Error	eU (ppm)^{c}	Raw Age	Error	R (μm)^{d}	L (μm)^{e}	Mass (μg)^{f}	Rs (μm)^{g}	F$_{T}$^{h}	Corrected Age	Error
TS1922																
01	27.15	0.40	54.61	0.83	2.53E-02	2.59E-04	40.15	29.25	0.44	200.4	57.3	4.57	59.1	0.783	37.36	0.56
02	29.41	0.44	62.04	0.76	4.24E-02	4.29E-04	44.18	44.42	0.66	204.5	58.4	4.84	60.3	0.787	56.44	0.84
03	15.39	0.29	34.21	0.51	1.04E-02	1.10E-04	23.54	20.51	0.35	154.6	43.9	2.07	45.4	0.72	28.49	0.49
04	5.08	0.19	9.01	0.28	3.40E-03	4.29E-05	7.22	21.86	0.66	162.2	41.3	1.96	43.8	0.709	30.83	0.93
05	8.65	0.17	11.36	0.23	4.61E-03	5.10E-05	11.35	18.84	0.37	177.7	56.0	2.95	55.1	0.744	25.32	0.50
TS1933																
01	3.86	0.13	17.27	0.32	7.05E-03	7.49E-05	7.97	40.97	0.88	44.7	149.5	2.48	46.1	0.743	55.14	1.18
02	3.19	0.09	22.08	0.33	2.57E-03	3.97E-05	8.45	14.12	0.30	43.6	115.1	1.82	42.6	0.664	21.27	0.45
03	2.62	0.16	9.32	0.31	1.79E-03	3.71E-05	4.83	17.19	0.72	41.2	115.7	1.63	40.9	0.691	24.88	1.04
04	6.28	0.15	29.35	0.71	2.00E-02	2.15E-04	13.27	69.64	1.41	44.0	116.8	1.1	39.9	0.636	109.50	2.22
05	8.75	0.19	34.07	0.63	1.22E-02	1.34E-04	16.86	33.55	0.61	46.7	138.0	1.5	44.6	0.675	49.70	0.90

Table 4.3: (continued)

Sample	^{238}U (ppm)[a]	Error[b]	^{232}Th (ppm)	Error	^{4}He (ppm)	Error	eU (ppm)[c]	Raw Age	Error	R (μm)[d]	L (μm)[e]	Mass (μg)[f]	Rs (μm)[g]	F_T[h]	Corrected Age	Error

[a] U, Th, and He concentration in parts per million (ppm).

[b] Concentration of each element computed from the absolute amount of the measured isotopes. Uncertainties on U, Th, and He concentration are reported at 1σ and include the propagated total analytical uncertainties.

[c] Effective uranium (eU) calculated by U + (0.235 * Th). Values stated as parts per million (ppm).

[d] R describes the width of the apatite.

[e] L describes the total length of the apatite.

[f] Mass is the mass of the crystal.

[g] Rs is the radius of a sphere with an equivalent alpha-ejection correction as the grain.

[h] FT is the α-ejection correction calculated using mass-weighted average radii.

4.4.2 Modelled thermal history of the BAF, east NF, and southern Junggar

At the western BAF site (Figure 4.4a), thermal history modelling results suggest that the rock had been exhumed to shallow levels of the crust, in the temperature range of ∼55–65°C, by ∼50 Ma (Figure 4.4c). Then the samples had experienced a long-term thermal quiescence until their final exhumation to the surface during the late Cenozoic. As the modelled temperature prior to the final cooling was near the upper boundary of the partial annealing/retention zones of the AFT and AHe methods, the predicted onset age of the final rapid cooling should be treated with caution (see Discussion 4.5.1). Throughout the Cenozoic, the modelling results suggest a paleogeothermal gradient at ∼20 °C/km (Figure 4.4b). This final cooling event (<70°C; Figure 4.4) is of moderate magnitude and therefore has not fully "reset" the AFT and AHe ages.

At the east NF site (Figure 4.4d), the thermal history models suggest very similar rock cooling paths as that from the western BAF: the rocks were cooled to <60°C before ∼50–40 Ma, and had most likely remained at the same temperature until the final cooling during the late Cenozoic (Figure 4.4f). At this site, the models are based on data from only two samples on a profile with < 100 m offset in elevation, and thus the post-burn-in ensemble contains a larger uncertainty (Figure 4.4f). As a result, the time for final exhumation of the rocks during the late Cenozoic tectonics cannot be tightly constrained. Based on a paleogeothermal gradient of 20–30°C/km, the predicted total magnitude of the final exhumation is less than 2 km.

Among the five modelled samples on the southern margin of the Junggar Basin, four thermal history models (TS1909, TS1912, TS1913, and TS1914) show an apparent late Cenozoic increase in the cooling rate (Figure 4.5). The models of TS1909 and TS1913 indicate the onset of cooling rate acceleration around ∼20 Ma. This is consistent with the rock cooling histories inferred from AFT and AHe data on the margin along the Manas and Guertu Rivers (Hendrix et al., 1994; Yu et al., 2022). Compared to the regions further west, the total magnitude of exhumation and cooling appears to lower near the eastern end of northern Tian Shan (Figure 4.2), where all AFT and some AHe data have not been reset. As a consequence, some of the modelled thermal histories either show no late Cenozoic acceleration in cooling rates (TS1911; Figure 4.5b) or the timing of this acceleration is not well constrained (TS1912 and TS1914; Figure 4.5c and 4.5e).

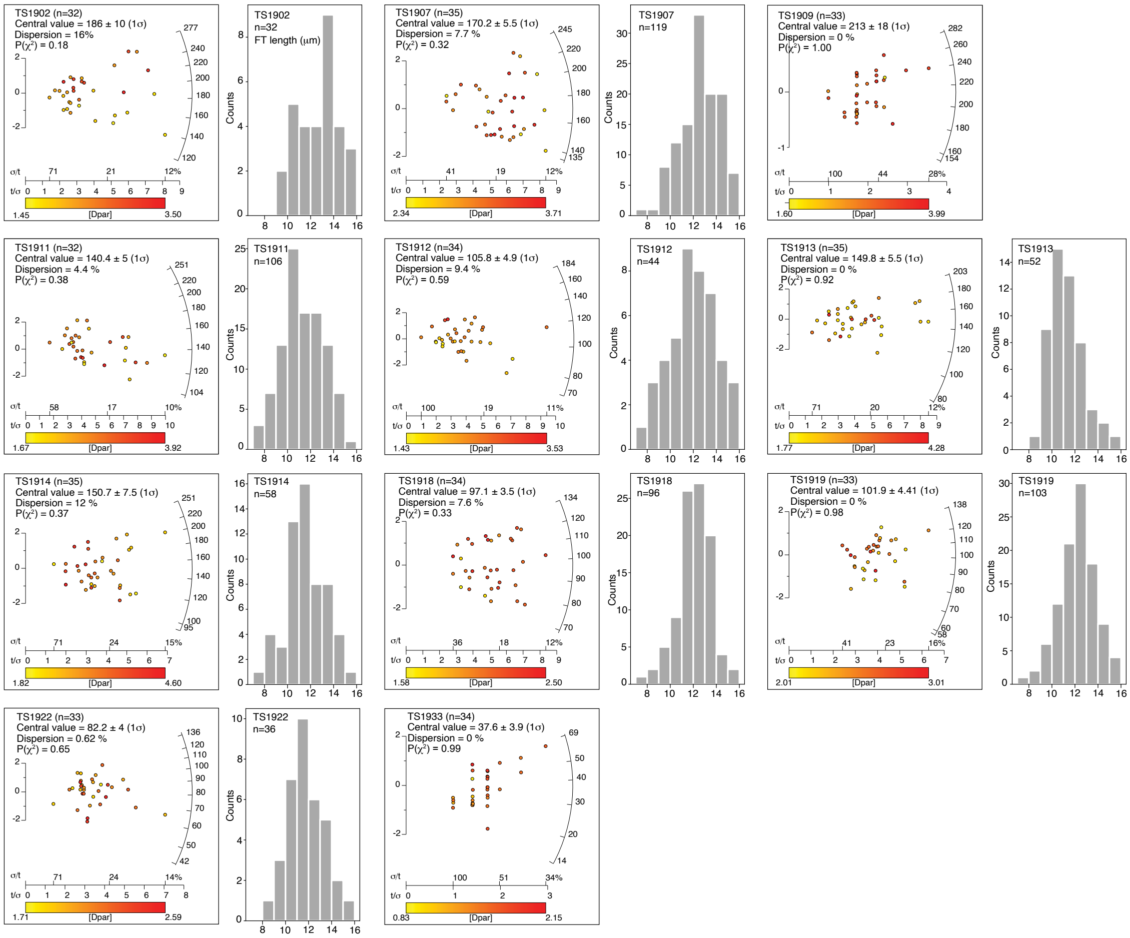

Figure 4.3: Radial plots of single-grain AFT ages for new samples collected from the northern Tian Shan and the fission track length distribution histograms for these samples. Track length is in unit of μm. Samples TS1909 and TS1933 have only 5 and 2 track lengths measured, so histograms are not shown.

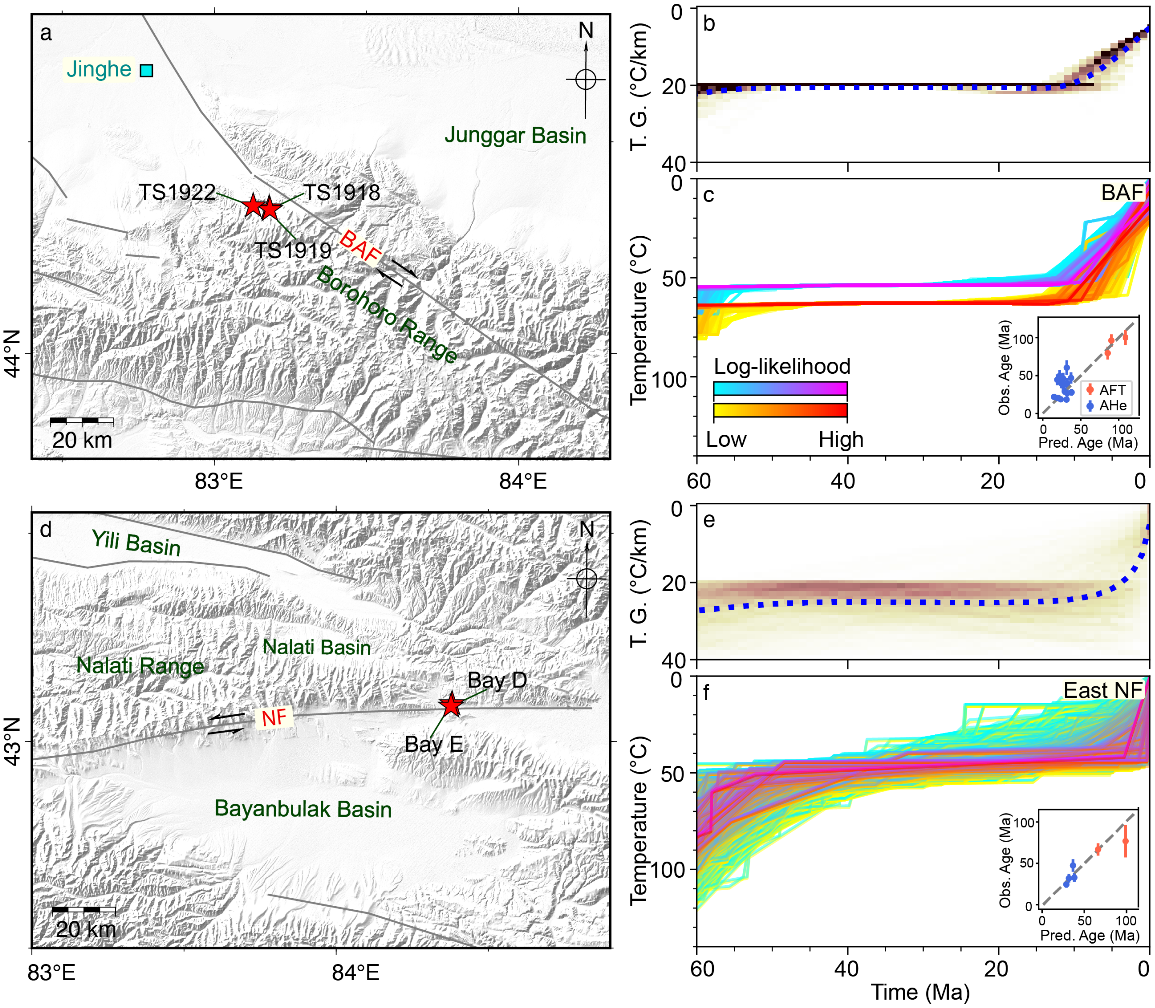

Figure 4.4: Sample locations and time-temperature history modelling results from the western BAF (a, b, and c) and eastern NF (d, e, and f) using the method of Gallagher (2012). (a) The shaded relief map showing the three samples from the Jinghe, western BAF. The AFT and AHe dating results can be found in Tables 4.2 and 4.3. (b) Predicted temperature gradient (T. G.) based on modelled thermal histories between the uppermost and lowermost samples. (c) Modelled time-temperature paths. Results are shown as a randomly thinned (5%) assemblage of the “post-burn-in” models for the uppermost (cold) and lowermost (hot) samples, color coded by their likelihood. Inset figure indicates observed ages versus that predicted by the weighted mean model from the ”post-burn-in” assemblage. (d), (e), and (f) are the same as (a), (b), and (c), but for data from eastern NF Jolivet et al. (2010).

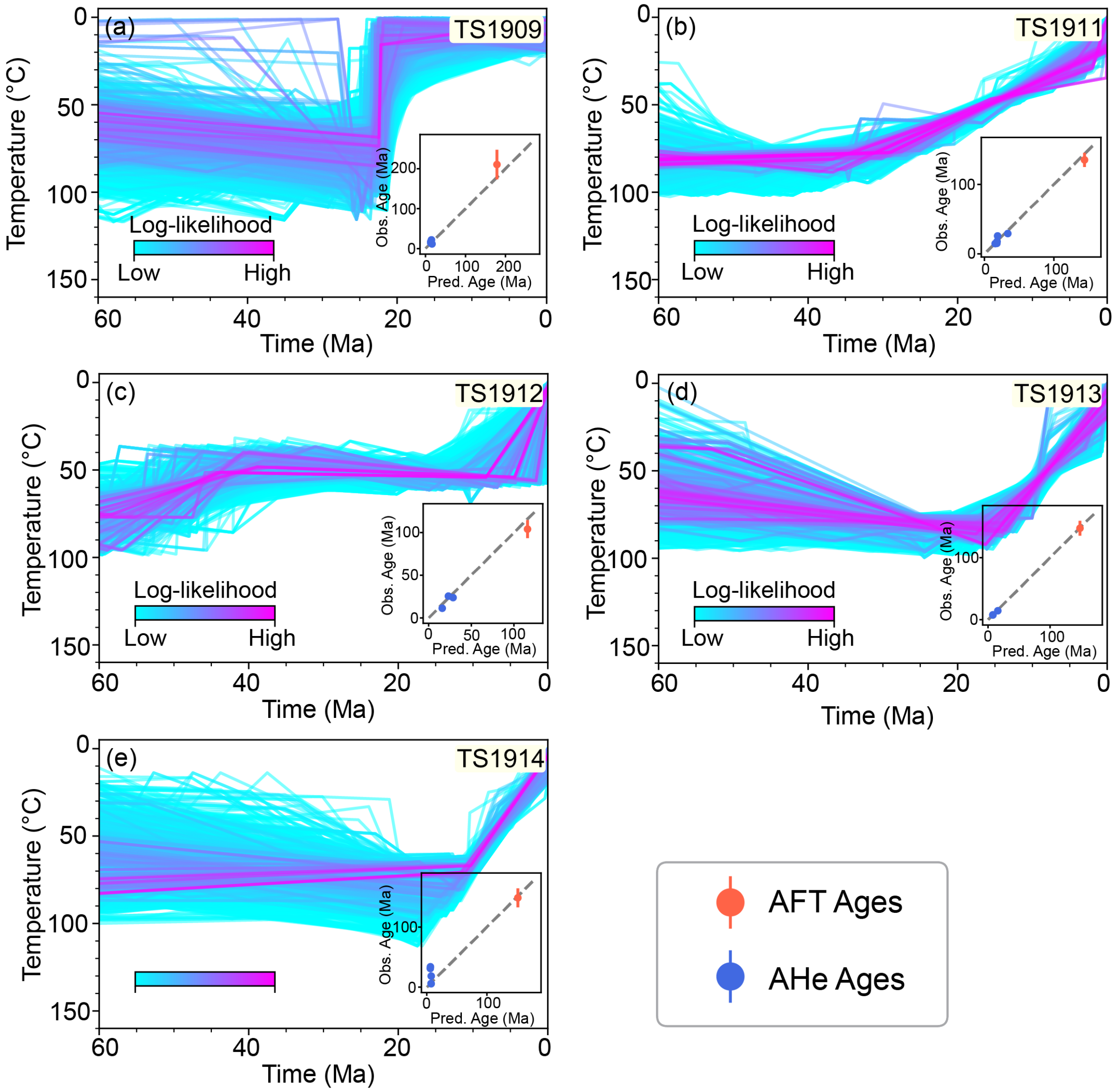

Figure 4.5: Time-temperature history modelling results of sandstone samples from northern Tian Shan using the method of Gallagher (2012). The AFT and AHe dating results can be found in Tables 4.2 and 4.3. Five panels show the modelled time-temperature paths for samples TS1909, TS1911, TS1912, TS1913, and TS1914, respectively. Results are shown as a randomly thinned (5%) assemblage of the "post-burn-in" models for each sample, color coded by their likelihood. Inset panel indicates observed ages versus that predicted by the weighted mean model from the "post-burn-in" assemblage.

4.4.3 Inversed exhumation rate histories in the Tian Shan and regions surrounding the Tarim Basin

The performances of inverse exhumation models, which were set up with various L_c and Δt values, are shown in Figures 4.6 and 4.7, respectively. All optimized models with different L_c and Δt predict normal distributions of age misfit centred at 0 Ma (see Figures 4.6b and 4.7b). For models with the same Δt, those set up with a higher L_c show faster decreases in the residual; models with L_c >20 km achieved minimized residuals after 10 iterations (Figure 4.6a). Similarly, among models with the same L_c, those with longer Δt show quicker reductions in residuals (Figure 4.7a). The pre-Cenozoic part of the exhumation history was poorly solved in our inversion. Finally, the model with 30 km correlation distance and 5 Ma time interval yields good convergence performance and reasonable fit to the data, and thus is presented here; the resolved exhumation rates and their corresponding resolution for this model are shown in Figures 4.8 and 4.9.

In addition, our tests of models with varying time interval lengths suggest that the choices of L_c and Δt have a more significant influence on the estimated exhumation rates than the timing of rate changes (Figures 4.10 and 4.11). We selected six representative locations (labelled a to f) along major strike-slip faults and NE Tibet frontal thrusts (Figure 4.8) to show the predicted exhumation rates from models with different correlation distances (Figure 4.10) and time intervals (Figure 4.11). Our results suggest that while the Cenozoic unroofing of the Tian Shan may have occurred since 25–20 Ma, substantial increases in exhumation rates at many locations also occurred between approximately 15 and 10 Ma.

4.5 Discussion

4.5.1 Magnitude and rate estimates of the late Cenozoic exhumation on the BAF and NF

Our thermochronological data offer constraints on the Cenozoic deformation of the BAF in northern Tian Shan. Throughout the early Cenozoic, the modelled thermal history suggests no significant cooling that could be related to exhumation along the fault planes. During this period, based on the modelled temperature offset between the uppermost and lowermost samples on the elevation profile, the simulated geother-

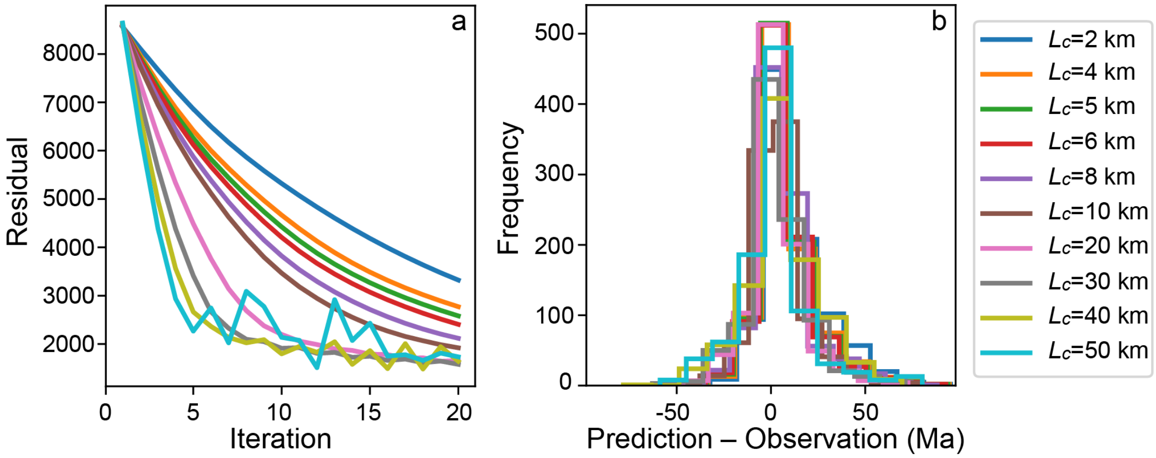

Figure 4.6: Performance of the inverse exhumation model with varied spatial correlation distance L_c. (a) Reduction in residuals during inversion using different spatial correlation distances ranging from 2 km to 50 km. The residual is a combined value of the misfits from the exhumation model and cooling ages. (b) Distribution of misfits between model prediction and observed ages with different spatial correlation distances.

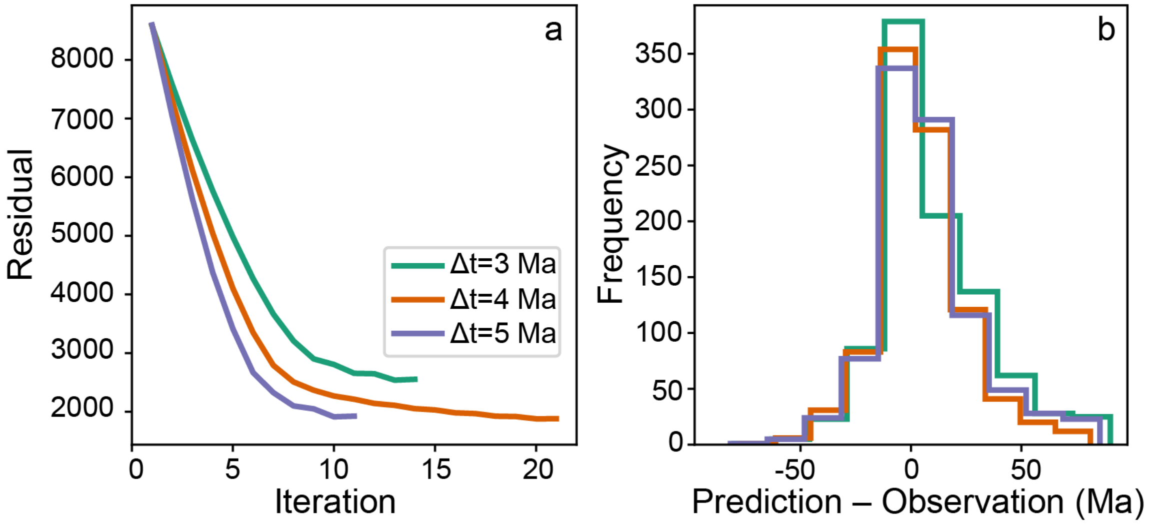

Figure 4.7: Performance of the inverse exhumation model with varied time interval lengths Δt. (a) Reduction in residuals during inversion using different time interval lengths of 3 Ma, 4 Ma, and 5 Ma, respectively. The residual is a combined value of the misfits from the exhumation model and cooling ages. (b) Distribution of misfits between model prediction and observed ages with different time intervals.

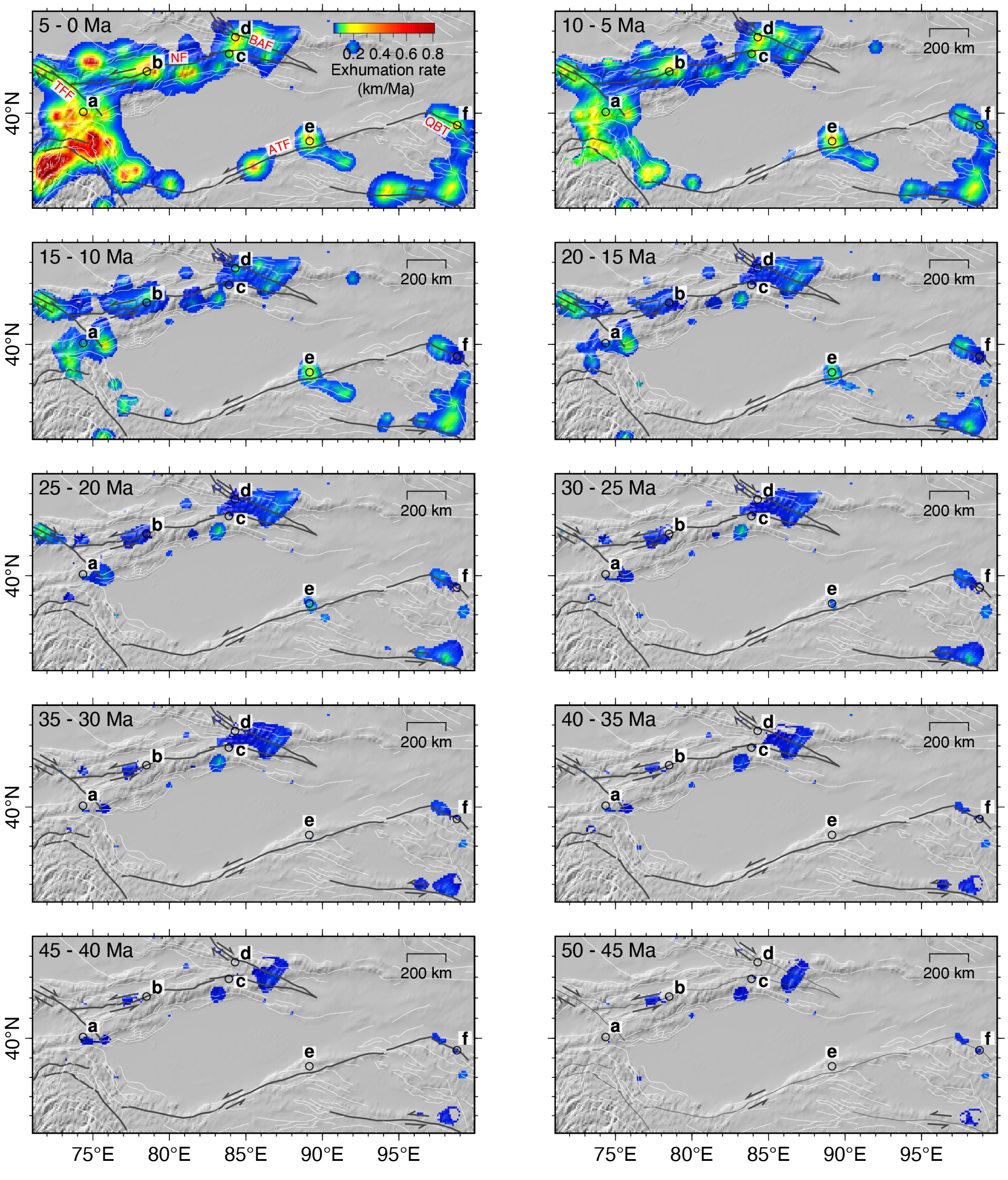

Figure 4.8: Exhumation model of regions around the Tarim Basin since 50 Ma at 5 Ma time intervals, based on a correlation distance of 30 km. The model prior to 50 Ma is poorly resolved and thus not presented. Areas with temporal resolution <0.05 are masked gray and white lines depict active faults. The resolution of the model is shown in Figure 4.9. Open circles with labels from a-f indicate locations of exhumation rates shown in Figures 4.10and 4.11.

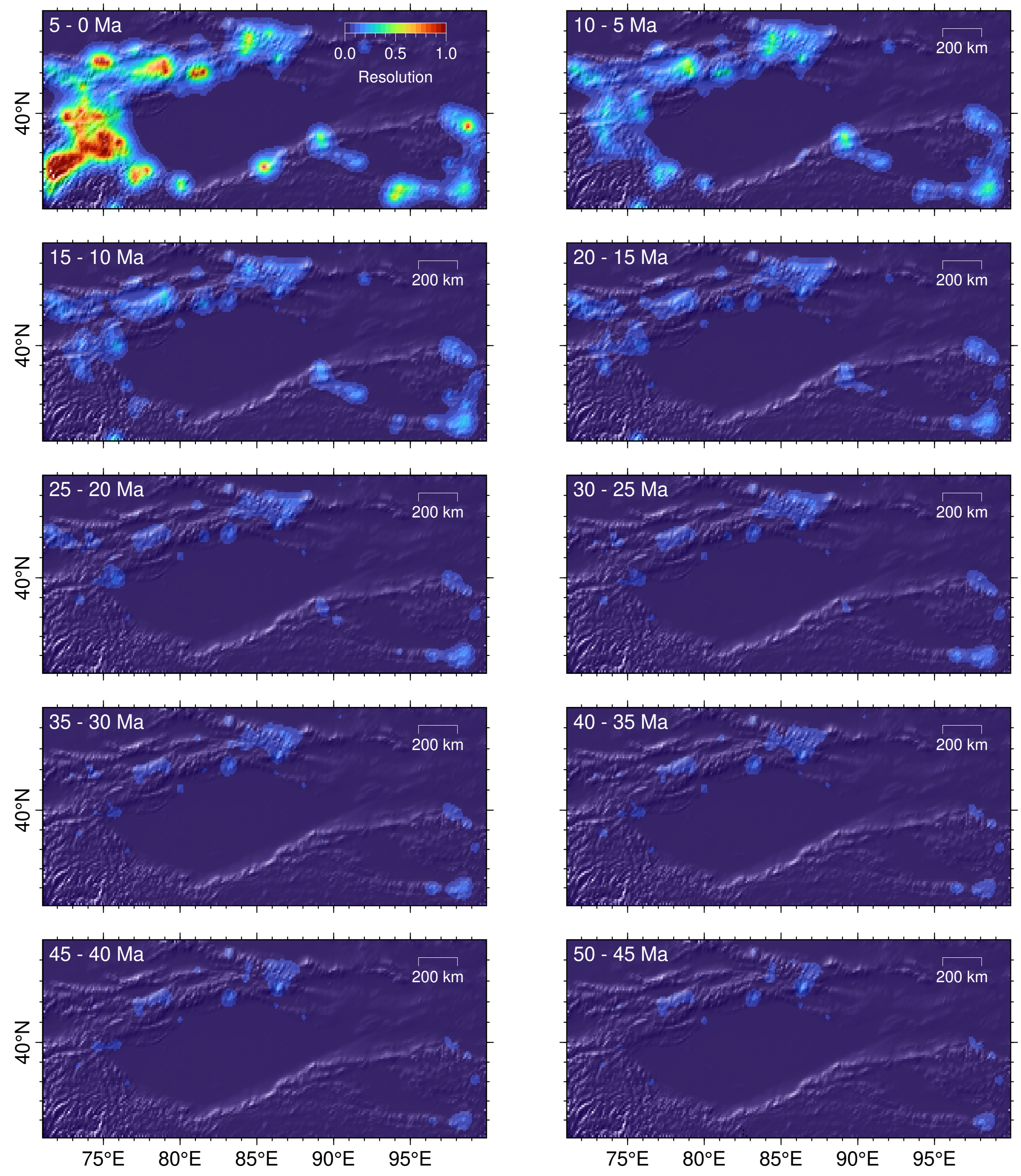

Figure 4.9: Resolution of the exhumation model shown in Figure 4.8.

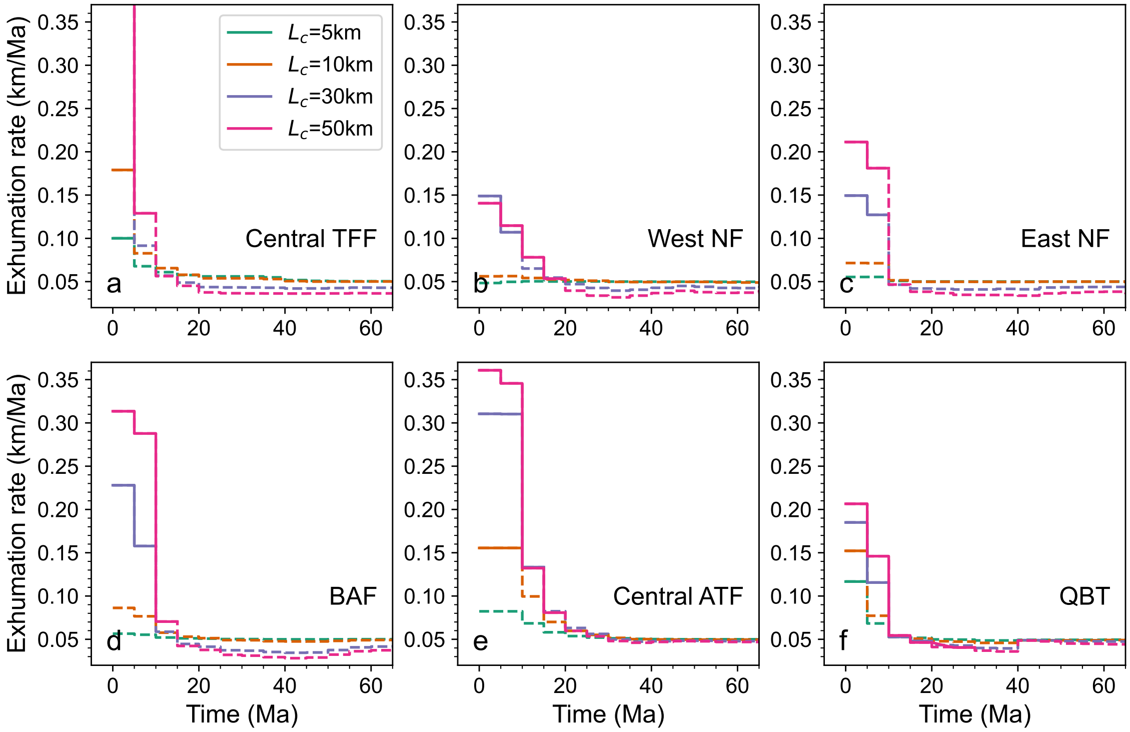

Figure 4.10: Predicted exhumation rates at selected sites (a, b, c, d, e, and f in Figure 4.8) near major strike-slip structures and on the NE margin of the Tibetan Plateau. Models shown here used different correlation distances (5 km, 10 km, 30 km, and 50 km) and a time interval length of 5 Ma. Solid and dashed lines depict rates with higher (>0.05) and lower (<0.05) resolution, respectively. TFF: Talas-Fergana Fault; NF: Nalati Fault; BAF: Bolokenu-Aqikekuduk Fault; ATF: Altyn Tagh Fault; QBT: Qilian Boundary Thrust.

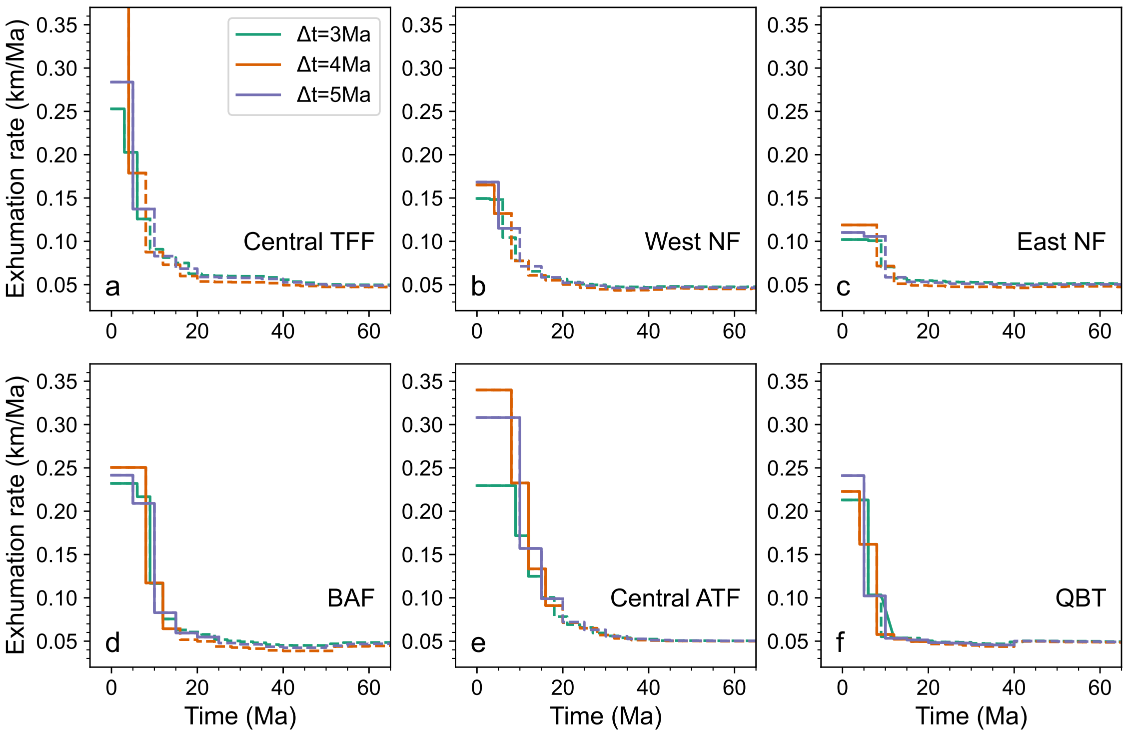

Figure 4.11: Predicted exhumation rates at selected sites (a, b, c, d, e, and f in Figure 4.8) near major strike-slip structures and on the NE margin of the Tibetan Plateau. Models shown here used a correlation distance of 30 km and different time interval lengths. Solid and dashed lines depict rates with higher (>0.05) and lower (<0.05) resolution, respectively. TFF: Talas-Fergana Fault; NF: Nalati Fault; BAF: Bolokenu-Aqikekuduk Fault; ATF: Altyn Tagh Fault; QBT: Qilian Boundary Thrust.

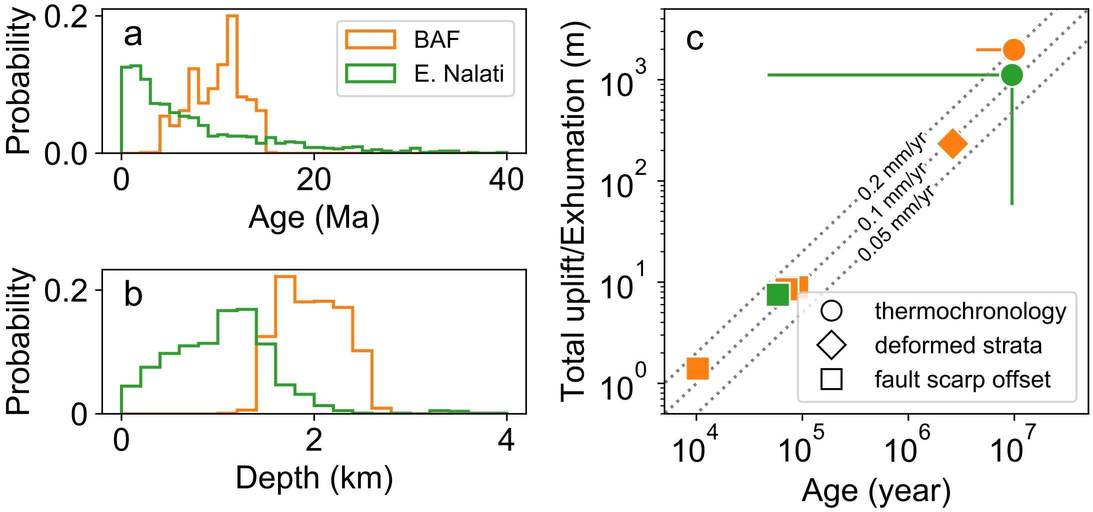

Figure 4.12: (a) Distribution of ages for onsets of the final exhumation, according to the thermal history models (Figure 4.4). (b) Distribution of samples' depths prior to the final exhumation. (c) Uplift and exhumation estimate from the western BAF (orange) and eastern NF (green). Data are from geomorphic features (Wu et al., 2014; Hu et al., 2021), geological structures (England and Molnar, 1997), and rock cooling and exhumation models (this study).

mal gradient is 20°C/km. This value aligns with the current value measured from the Tarim Basin (LiuS et al., 2016), which may reflect the thermal structure of the crust in this region with no strong tectonic activity. On the BAF, although the predominant motion during the Cenozoic is strike-slip, a significant dip-slip component exists (Green et al., 1989). Therefore, we infer that this Paleozoic structure was not likely active over the early Cenozoic.

During the late Cenozoic, based on the modelled geothermal gradient at ∼20 °C/km, the final exhumation since the Miocene had a magnitude of <2.3 km. The best-fit models from the post-burn-in ensemble suggest that rapid cooling started at ∼10 Ma, and thus indicates an exhumation rate of ∼0.2 km/Ma. It is worth noting that prior to the final cooling, the samples resided at a relatively low temperature (<70°C) for a long period (>30 Ma), and thus the thermochronological data may not be sensitive enough to provide a tight constraint on the onset age of the final exhumation and therefore the rate of this exhumation. However, we argue that the predicted temperature ranges for the samples during the early Cenozoic quiescence are reliable. Therefore, a trade-off should exist between the exhumation rate and the onset time of the final exhumation, such that a shorter duration of the final exhumation requires a higher exhumation rate. For example, if the final exhumation took twice as long as our best-fit model prediction, i.e., it started at ∼20 Ma, the exhumation rate would be half of the model prediction, i.e., at ∼0.1 km/Ma. During the Cenozoic, thermal history models from previous work (Dumitru et al., 2001; Hendrix et al., 1994; Yu et al., 2022) and this study (Figure 4.5) suggest that the northern Tian Shan started to unroof during the Oligocene to early Miocene. Sedimentary records along the southern margin of the Junggar Basin indicate possible acceleration in the middle Miocene (Charreau et al., 2005). We propose that the BAF was most likely reactivated during these periods, and near the Jinghe region, displacement on the fault resulted in an average exhumation rate at ∼0.1–0.2 km/Ma. At the site near the east NF, due to the limited elevation difference between samples on the vertical profile (Figure 4.4d), the uncertainties in estimating the magnitude and rate of the final cooling and exhumation (Figure 4.4f) are even larger compared to those from the BAF. This uncertainty is clearly presented by thermal history models in the post-burn-in ensemble, as well as in the probability distributions of the onset age of the final exhumation and the sample depths during the early Cenozoic (Figure 4.12b). Similarly, our exhumation rate models, simulated with different time interval lengths, also reveal a discernible negative linear correlation between the rate and duration for the last phase of rapid exhumation at some sites (Figure 4.11). This implies that low-temperature thermochronological data provide a better estimate of the total magnitude than either the age or rate of the late Cenozoic exhumation independently.

4.5.2 Comparing the late Cenozoic exhumation and late Quaternary slip rates on BAF and NF

Over the late Quaternary, a substantial portion (23%) of crustal shortening in the northern Tian Shan has been accommodated by strike-slip faulting (Hu et al., 2021). On the Jinghe segment of the BAF based on the displaced geomorphic markers and age constraints, Hu et al. (2021) calculated a late Quaternary dextral slip rate at 3.2+1.4/-1.1 mm/yr and a secondary but significant uplift of 8 m over 74 ka; the strike-slip rate is consistent with the post-Pliocene average of 3 ± 1 mm/yr (England and Molnar, 1997). Lu et al. (2019) compared the published late Pleistocene–Holocene deformation rates and the modern GPS measurements in the northern Tian Shan and suggested that the deformation pattern and rates of both the mountain range and its foreland have remained constant throughout the late Quaternary. Assuming that this steady deformation pattern also applies to the segment of BAF in the northern Tian Shan, the observed ratio between the strike-slip and uplift rates on the fault is expected to have remained constant over the Quaternary, leading to a total uplift of >200 m. Therefore, both the post-Pleistocene and the Quaternary average uplift rate estimates are on the same order of magnitude as the prediction of our thermal history model (Figure 4.12c), which suggests a total exhumation of $\sim$2 km over the past 10±5 Ma for the lowermost sample on the profile at the Jinghe site (Figure 4.12a). Even if the late Cenozoic activity on the BAF started in the early Miocene 25–20 Ma and the mean exhumation is slower (see Discussion 4.5.1), this uncertainty does not affect the consistency between the inferred exhumation rate and the Quaternary uplift rates. Given the arid climate, the average denudation rate of Tian Shan may be outpaced by the tectonic uplift (Charreau et al., 2017). However, near the boundary between the mountain and the foreland, especially close to the fault scarps, the localized exhumation rate could be much higher and comparable to the uplift rate (Haeussler et al., 2015). This consistency in uplift or exhumation rates over different time scales implies that the uplift and deformation rates on the BAF have been relatively constant since its Miocene reactivation in the (Figure 4.12c). Near the Bayanbulak Basin on the eastern NF, Wu et al. (2014) measured a vertical offset of >7 m on an alluvial fan that was abandoned at ∼59 ka, which is similar to the observed displacement on the BAF during the same period (Figure 4.12c). This uplift rate estimate is also consistent with the mean exhumation rate (∼0.1 km/Ma) on the basin margin predicted by our thermal history model, despite its large uncertainties (Figure 4.12c).

4.5.3 Correlation of the Tian Shan strike-slip deformation to the Pamir and NE Tibet

The spatial variation in precipitation rate has been invoked as a key factor for the different erosion rates in Central Asia (Jepson et al., 2021), climate change is unlikely to be the driver for the late Cenozoic increase in exhumation rate in the Tian Shan. Since the early Eocene, the uplift of the Tibetan Plateau gradually blocked the northward transport of monsoonal moisture from South Asia, and as a result, the climate in interior Asia has been dominantly controlled by the mid-latitude westerlies (Caves et al., 2015). During the Neogene, the uplift of Tian Shan and other mountain ranges in the region decreased the moisture transport by the westerlies, leading to a progressive aridity of the interior of Central Asia (Caves et al., 2016). Therefore, we attribute the Miocene increase in exhumation rate around the Tarim Basin to the evolution of the tectonic deformation rather than climate change.

In both northern and southwestern Tian Shan, the Miocene increases in exhumation rates occurred not only along the mountain-basin boundaries but also in the interior of the ranges (Figure 4.8, 4.10b, 4.10c, 4.11b, and 4.11c). This pattern cannot be explained solely by a sequential thrust model, where deformation propagates from the high mountains toward the basin margins. Instead, it suggests that hinterland deformation is necessary to maintain topography within a thrust wedge and that out-of-sequence faulting is more common than previously thought (ARMSTRONG and ORIEL, 1965; Yu et al., 2014; Dahlen, 1984). In addition, the general spatial correlation between rapid exhumation (i.e., sites b, c and d in Figures 4.8, 4.10, and 4.11) and large strike-slip faults (i.e., the BAF and NF) suggests a tectonic control on the renewed or intensified episode of crustal deformation (Charreau et al., 2009; Jia et al., 2020; Haijian et al., 2015), implying a possible transition in deformation style from predominant thrust faulting to more active strike-slip faulting. It is worth noting that after 15 Ma around the Tarim Basin, the NE margin of the Tibetan Plateau (Figures 4.10f and 4.11f) and the NE Pamir (Figures 4.10a and 4.11a) also experienced important changes in the deformation style, suggesting a potential correlation in the deformation mechanism of these regions surrounding the Tarim Basin.

To the southeast of the Tarim Basin, deformation of the NE Tibetan Plateau is mainly accommodated by sinistral slip on the Altyn Tagh Fault (ATF) and shortening on the NW-SE trending fold-and-thrust belts (Zheng et al., 2017). Currently, the strike-slip deformation on the northwestern and southeastern margins of the Tarim Basin complies with a model in which the internally stable Tarim block rotates clockwise relative to the Eurasian plate (Wang et al., 2020a) (Figure 4.1). Similar to the Tian Shan, the present-day deformation rates in the NE Tibetan Plateau are also consistent with millennial-scale rates estimated from ages and offsets of geomorphic features (Cowgill, 2007; Mériaux et al., 2005). Extrapolation of the late Quaternary slip rates on two faults conjugate to the ATF suggests a total displacement accumulated over 8–12 Ma (Yuan et al., 2011), and thus the faulting activity probably started when the deformation of northeastern Tibet changed from nearly north-south shortening to eastward expansion at ∼15–8 Ma (Lease et al., 2011). This transition is coincident with or younger than our inferred age of the accelerated strike-slip deformation in Tian Shan, suggesting that by then a clockwise rotation of the Tarim block relative to Eurasia has been established. Moreover, if the rotation rate (0.63°/Ma) modelled from geodetic data (Wang et al., 2020a) is representative of the mean rate over the geological time scale, the total late Cenozoic rotation of the Tarim block (7° ± 2.5°) (Avouac et al., 1993a) would also suggest a mid-Miocene (∼11 Ma) onset of the deformation around the basin margins.

Between the Tian Shan and northeastern Tibetan Plateau, the apparent synchronization in their transitions of deformation styles supports the significant role of the Tarim block in the strain distribution within the interior of the Eurasian Plate during the continental collision. It has been demonstrated that the presence of the strong Tarim block not only transformed the deformation of the Tibetan Plateau from contraction in the plate convergence direction to W-E motions towards weaker zones but also, due to its weak internal deformation (Laborde et al., 2019), effectively transferred strains to the far-field domains from the collision boundary (Huangfu et al., 2021; Neil and Houseman, 1997). Our work further indicates that the transferred strains were not only restricted to crustal shortening on the direction of India-Asia convergence and consequent thickening, but also the lateral deformation on the south margins of the Tarim block. The relative rotation of the Tarim is a result of differential shortening across as well as strike-slip deformation along the basin margins

(Laborde et al., 2019), which may be related to the asymmetrical lateral extrusion occurring between the northwestern (i.e., the NE Pamir) and northeastern parts of the Tibetan Plateau. Due to the complexity of the preexisting Paleozoic structures, this lateral deformation in Tian Shan is accommodated by motions on a series of dextral, NW-SE trending faults (e.g., the BAF, TFF) and their conjugate, the sinistral NF.

4.6 Conclusion

We presented new AFT and AHe data from the northern Tian Shan near the western BAF and the southern margin of the Junggar Basin, which are used to invert thermal history models to investigate the relationship between rock exhumation and the major strike-slip structures. The modelling results suggest that following the initial unroofing of northern Tian Shan during the late Cenozoic, there was a significant increase in the exhumation rate near the western BAF during the Miocene, with a total exhumation magnitude of $\sim$2 km. This increase is consistent with the uplift magnitude estimated by extrapolating the late Quaternary uplift rate on the BAF to the modelled onset of final exhumation, supporting that the Paleozoic fault was reactivated during the Miocene. This inferred timing of the strike-slip deformation acceleration in the northern Tian Shan coincides with other major changes in the deformation pattern along the margins of the Tarim Basin, such as the eastward expansion of the NE Tibetan Plateau and the northward advance of the Pamir. These observations imply that the current lateral deformation around the Tarim Basin was established by the Miocene.

Chapter 5

Conclusions

This dissertation examines the deformation of the Tian Shan, ranging from coseismic events that occurred over several seconds to long-term, million-year scale deformation. In this chapter, I summarise the key findings of this dissertation and provide suggestions for future research.

5.1 Summary of research outcomes

Fold-and-thrust belts pose seismic hazards in the foreland areas of the Tian Shan during the process of intercontinental deformation. In Chapter 2, I analyzed the fault geometry associated with the 2020 M_w 6.0 Jiashi earthquake in the Kepingtag fold-and-thrust belt located in the southern Tian Shan foreland using InSAR coseismic modelling. This analysis reveals a shallow, north-dipping fault plane beneath the Kepingtag Anticline, specifically, the intersection between the Kepingtag Thrust and the décollement. By integrating constraints from seismology body-waveforms modelling, I confirmed that the slip distribution modelled with InSAR was coseismic. Published aftershocks that are vertically separated from the mainshock, along with relocated background seismicity from this study, indicate that the earthquake depths are influenced by rheological controls extending to the basement. This study is not only relevant for seismic hazard assessment in the southern Tian Shan foreland, but also applicable to other fold-and-thrust belts worldwide.

Moving to the northern Tian Shan foreland, in Chapter 3, I used both InSAR coseismic modelling and time series analysis with InSAR data of five years to examine the fault that ruptured during the mainshock and the subsequent postseismic deformation patterns. The coseismic deformation pattern could be explained by either a shallow, south-dipping fault plane or a steep, north-dipping plane at a depth of ∼14 km. However, the afterslip pattern observed on the thrust sheet beneath the Tugulu Anticline suggests that the coseismic rupture occurred on the shallow, north-dipping fault plane with a dip angle of 28°. This deep coseismic slip likely triggered movement on the shallower thrust fault, resulting in an accelerated deformation rate of the anticline. These findings provide important insights into the mechanisms of seismic activity and long-term topography deformation in the northern Tian Shan foreland.

The fold-and-thrust belts were not the only structures to accommodate the deformation of Tian Shan. Large-scale, weak, Paleozoic inherited strike-slip faults within the range also contributed to accommodating the interior deformation. In Chapter 4, I presented new thermochronological data and thermal history modelling from northern Tian Shan. Thermal history modelling results suggest that Cenozoic exhumation along the basin margin began from >20 Ma, and the oblique-slip Borohoro-Aqikekuduk Fault (BAF) likely experienced accelerated exhumation at least ∼10 Ma with an estimated total exhumation magnitude of ∼2 km during the late Cenozoic. To examine the overall exhumation pattern of the Tian Shan and its adjacent regions, I compiled over 1000 published thermochronological data from the Tian Shan, Pamir, and northeastern Tibetan Plateau. The reconstructed exhumation history model suggests that after the initial unroofing in the Cenozoic, a significant acceleration in exhumation occurred during 15–10 Ma in the interiors of northern and southwestern Tian Shan near major strike-slip structures. This change coincided with the northward propagation of the Pamir and the eastward expansion of the northeastern Tibetan Plateau along the west and south margins of the Tarim Basin. These findings provide a comprehensive understanding of the exhumation and tectonic evolution of the Tian Shan and its surrounding regions during the late Cenozoic.

5.2 Future work

The InSAR time series results from the northern Tian Shan represent the first application of this method in a challenging area with slow deformation rates. Beyond the implications for seismic hazard assessment, the growing volume of satellite data, large spatial coverage, and high-resolution InSAR velocity maps and time series data from the northern Tian Shan, which covers the right-lateral strike-slip Borohoro-

Aqikekuduk Fault (BAF) and the foreland area, contain valuable information that can be further analyzed to gain insights into strain accumulation and regional tectonics.

Furthermore, my results indicate very rapid subsidence in the rural areas of the northern Tian Shan foreland due to water extraction for agriculture. The detected ground subsidence rate of ∼100 mm/yr should be given great attention and intervention by the relevant departments. Investigating the causes of this rapid subsidence and exploring potential mitigation strategies are crucial steps for ensuring the sustainability of agricultural practices and preventing further ground instability.

It is also crucial to study the relationship between the foreland subsidence and the uplift of the mountain range, such as the bending of the upper crust. Subsidence in the foreland can lead to isostatic adjustments where the crust compensates for the changes in mass distribution. The removal of water from the subsurface reduces the overall mass in the foreland area, potentially causing the lithosphere to flex. This flexural response can lead to changes in the vertical movement of adjacent regions, influencing the overall tectonic behaviour and stability. Future research could focus on monitoring and modelling of groundwater levels, subsidence rates, and stress changes to fully understand these processes and their implications.

Currently, most of the thermochronology data from Tian Shan are derived from apatite fission track analysis. To better understand the most recent and upper crust exhumation, it would be beneficial to obtain more (U-Th)/He data. On the other hand, the compilation of a large amount of thermochronological data from the Tian Shan and its adjacent regions has provided a general exhumation rate map. However, the application of this method is limited by the insufficient data on the geothermal structures of the mountain ranges. This could be circumvented by more sampling along steep slopes, in order to retrieve information from the age-elevation relationships from the data. Additionally, the current model could not provide constraints for the foreland basins or basin margins with Cenozoic strata, where apparent thermochronological ages do not reflect cooling associated with the Cenozoic orogeny. More detailed work in both data analysis and numerical modelling will further improve our understanding of the deformation history and its implications for the region's tectonic evolution.

Appendix A

Additional Information for Chapter 2

Table A.1: Slip sensitivity tests of the InSAR uniform slip fault model for the 2020 Jiashi mainshock with fixed slip of 0.5 m, 1.0 m, 1.5 m, and 2.0 m, respectively. All the other parameters were kept free.

Strike (°)	Dip (°)	Rake (°)	Slip (m)	Longitude (km)	Latitude (km)	Length (m)	Top depth (km)	Bottom depth (km)
278.77	7.0005	115.15	0.5	686.5726	4365.3267	22.0201	6.4528	6.9059
279.11	7.4599	115.93	1.0	686.2966	4365.6583	21.8359	6.9538	7.2009
278.98	7.2551	115.87	1.5	686.1856	4364.3720	21.7741	6.9674	7.1264
279.12	7.5453	116.10	2.0	686.3413	4366.040	21.8007	7.0438	7.1684

Table A.2: The 1-D velocity structure determined from and used in our calibrated earthquake relocation. Below 120 km, we used velocities from the ak135 model of Kennett et al. (1995)

Depth (km)	V_p (km/s)	V_s (km/s)
0–10	5.300	3.100
10–20	5.800	3.300
20–50	6.300	3.650

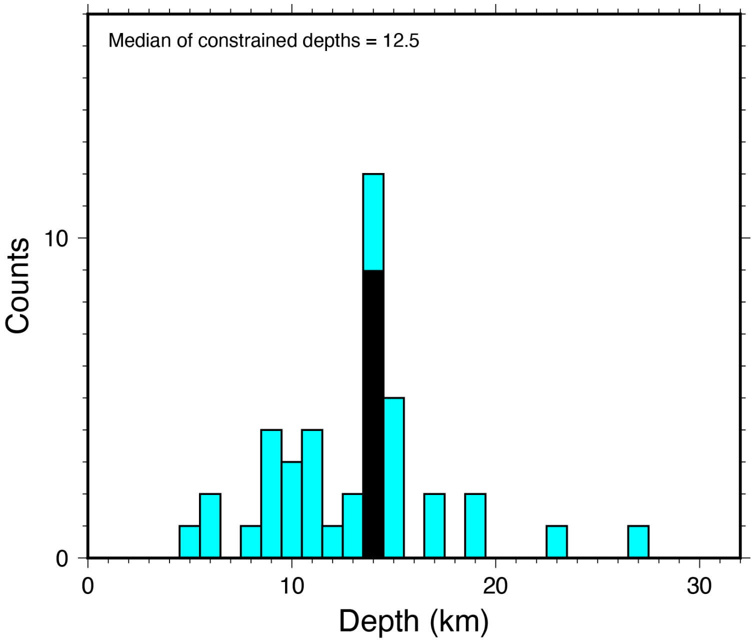

Figure A.1: Histogram of focal depths from our calibrated relocation. The black bar represents the cluster default depth of 14 km, used for events lacking in robust depth constraints. For events with good depth constraints, the median focal depth is 12.5 km.

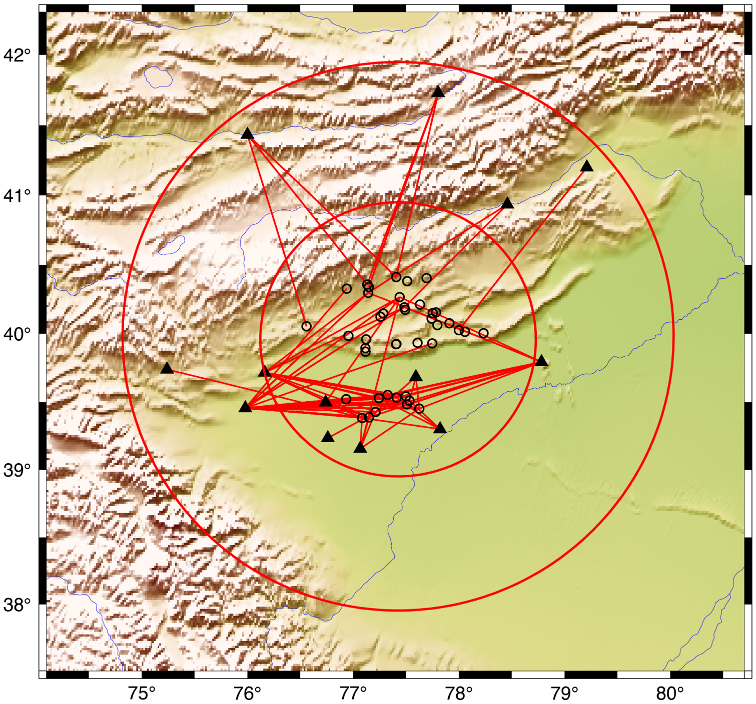

Figure A.2: Stations (black triangles), earthquakes (black open circles), and ray paths (red straight lines) used to determine the hypocentroid of the 2003–2020 Jiashi cluster. The large circles show radii of 1° and 2° about the hypocentroid.

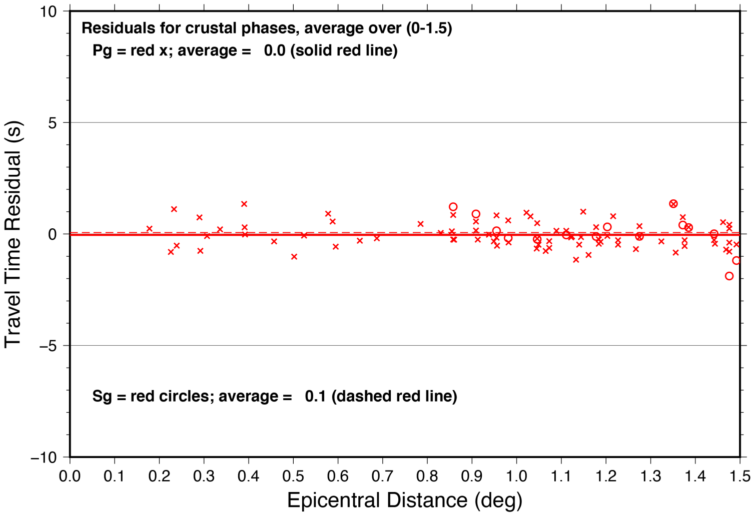

Figure A.3: The residual of each arrival in the distance range used for estimating the hypocentroid. Pg phases are indicated by crosses and Sg phases by red circles. Solid and dashed horizontal red lines indicate average residuals of 0.0 sec for Pg and 0.1 sec for Sg.

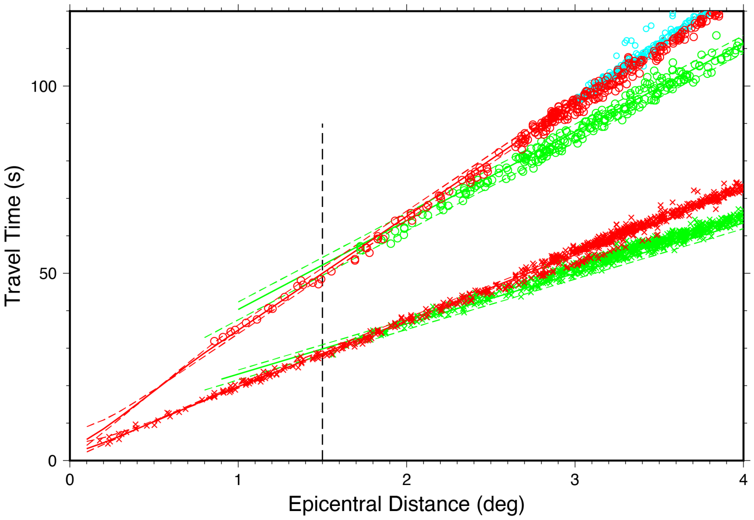

Figure A.4: Observed phase arrivals (symbols) and theoretical travel times (lines) calculated from the velocity model in Table A.2 for epicentral distances of up to 4°. P phases are indicated by crosses (Pg in red and Pn in green) and S phases are indicated by circles (Sg in red, Sn in green and Lg in cyan). The vertical dashed line at 1.5° represents the distance limit used to estimate the hypocentroid.

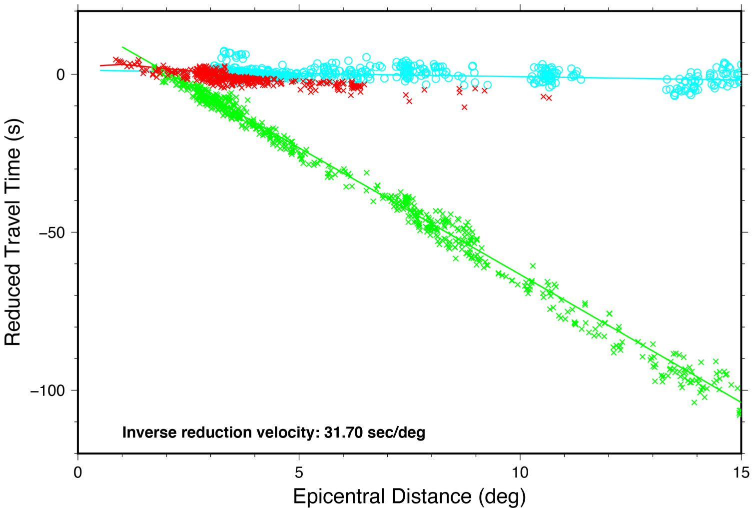

Figure A.5: Observed shear phase arrivals (symbols) and theoretical travel times (lines) calculated from the velocity model in Table A.2 for epicentral distances of up to 15°, plotted using a reduction velocity of 31.7 sec/° for legibility. Sg phases are red crosses, Sn are green crosses, and Lg are cyan circles.

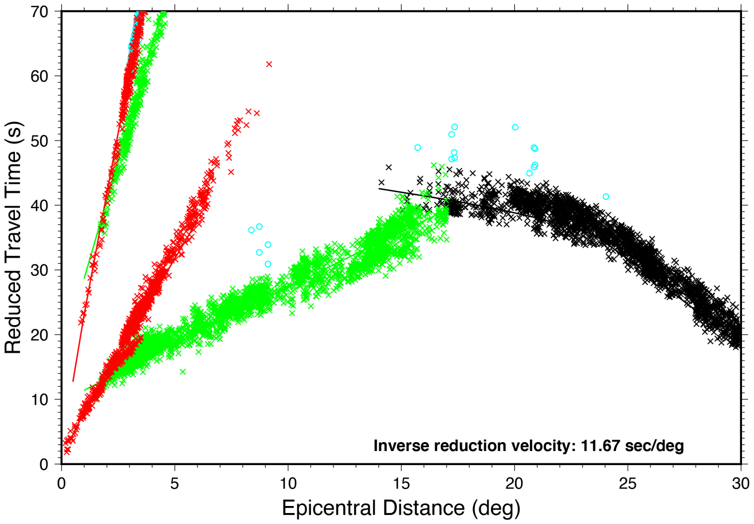

Figure A.6: Observed phase arrivals (symbols) and theoretical travel times (lines) calculated from the velocity model in Table A.2 for epicentral distances of up to 30°, plotted using a reduction velocity of 11.67 sec/° for legibility. Pg and Sg phases are red crosses, Pn and Sn phases are green crosses, P phases are black crosses, and Lg phases are cyan circles.

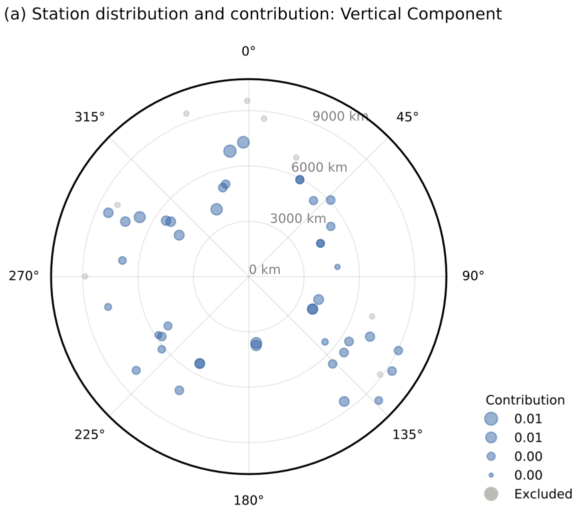

Figure A.7: Station distributions for waveforms used in teleseismic body waveform inversion for (a) vertical and (b) transverse components. Symbol size indicates the contribution of each station to the misfit for the best-fitting solution (Figure 2.6d in the main text).

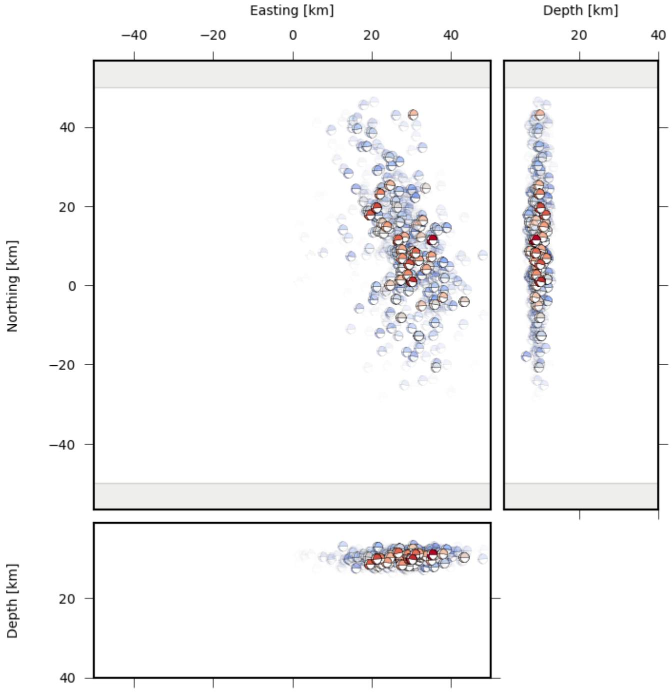

Figure A.8: Scatter plots of centroid locations and depths of the January 19 2020 Jiashi mainshock inferred from teleseismic waveform modelling. Best double-couple mechanisms are coloured by relative misfit, with red indicating lower misfit and blue indicating higher misfit. These are useful for evaluating the resolution of source parameters and for identifying parameters trade-offs.

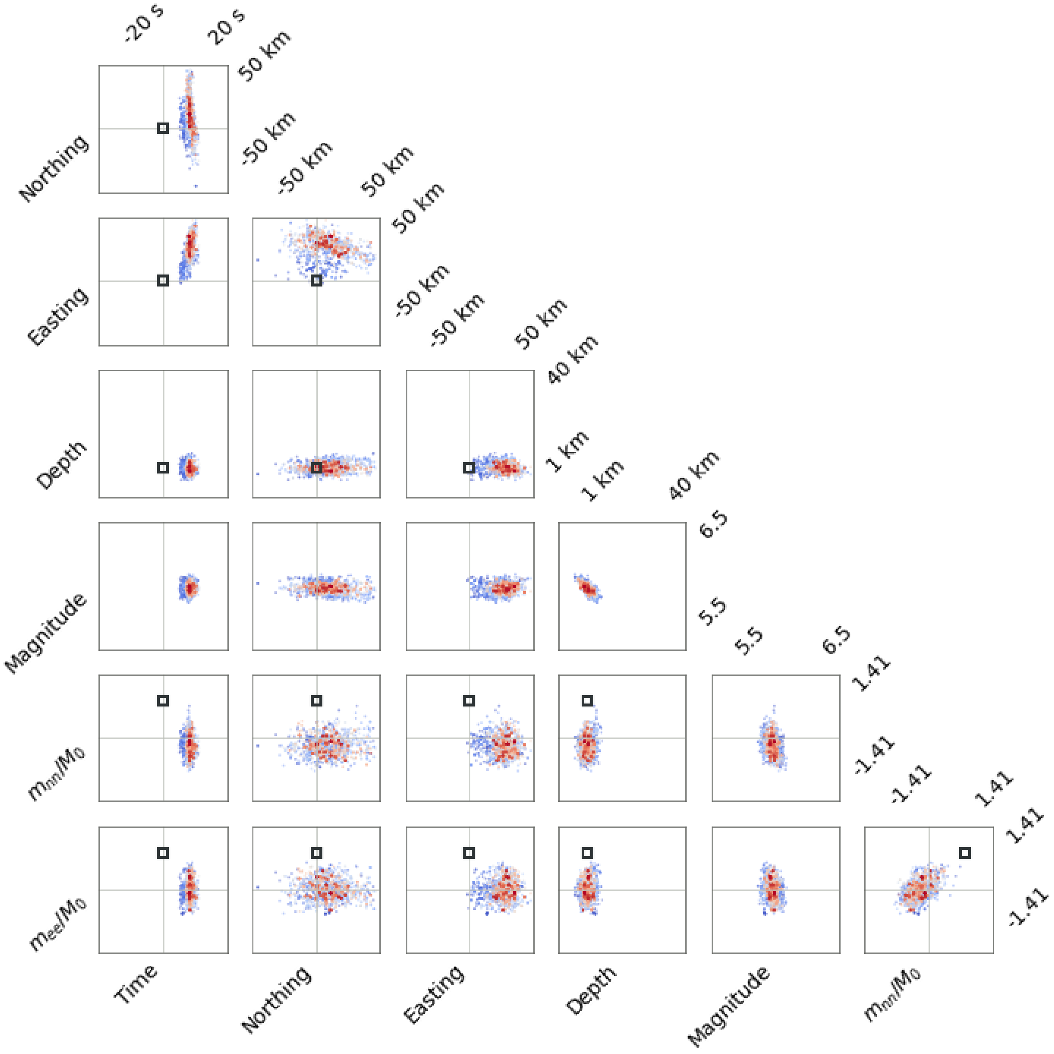

Figure A.9: Scatter plots of other source parameters of the January 19 2020 Jiashi mainshock inferred from teleseismic waveform modelling. Parameter pairs are coloured by relative misfit, with red indicating lower misfit and blue indicating higher misfit. These are useful for evaluating the resolution of source parameters and for identifying parameters trade-offs.

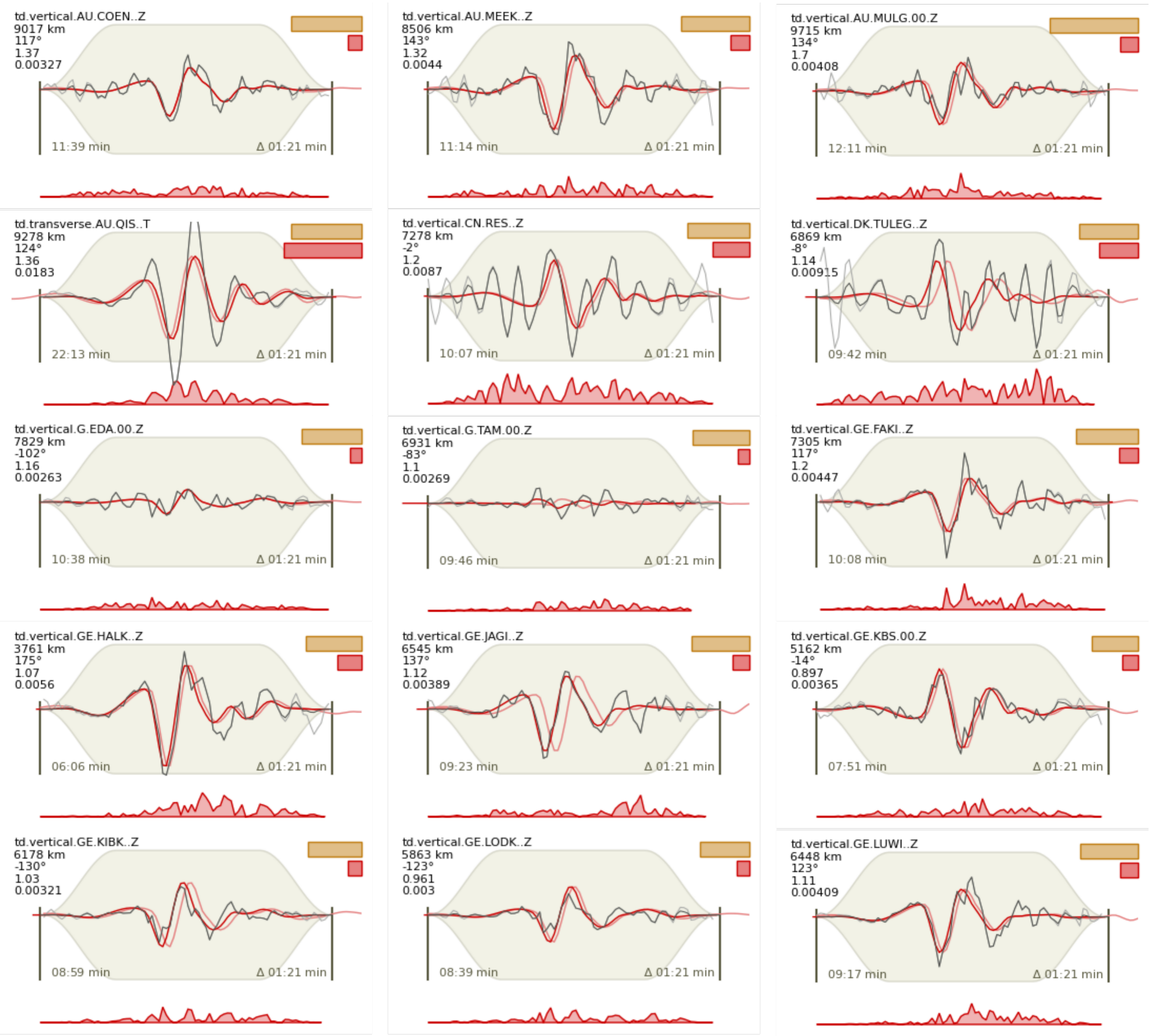

Figure A.10: Vertical component of waveform misfits for optimum global solution for the Jiashi mainshock. Traces are filtered observed data with (black) and without (grey) tapering, synthetic waveforms for the unshifted optimum solution (pink), and synthetic waveforms for the optimum solution after filtering, tapering, and realignment with observed waveform by cross correlation (red). Inset text gives the station name and component, distance, azimuth of the station relative to the initial event location, the weight assigned to the waveform during inversion, and the subsequent misfit. Inset boxes (top right of each panel) are scaled such that their length shows the relative weight of each trace within the full dataset and the relative contribution to the overall misfit of the optimum solution.

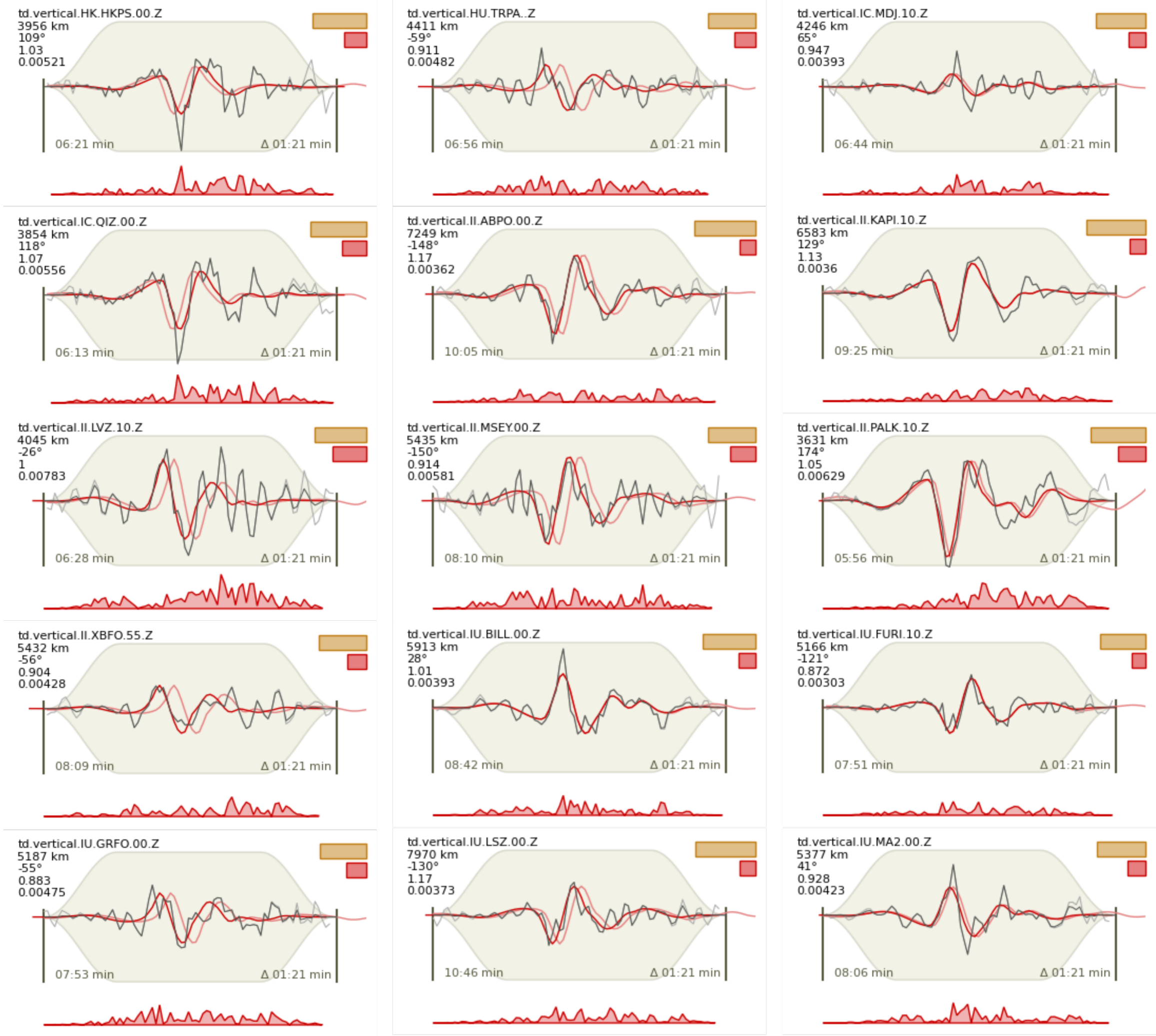

Figure A.10: Continued.

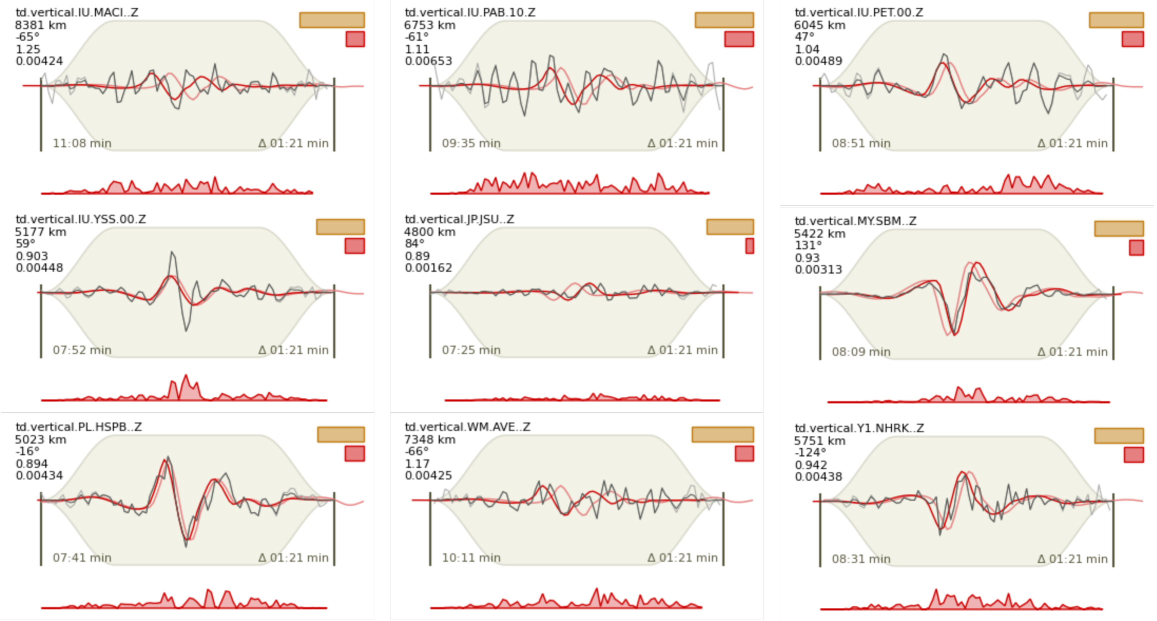

Figure A.10: Continued.

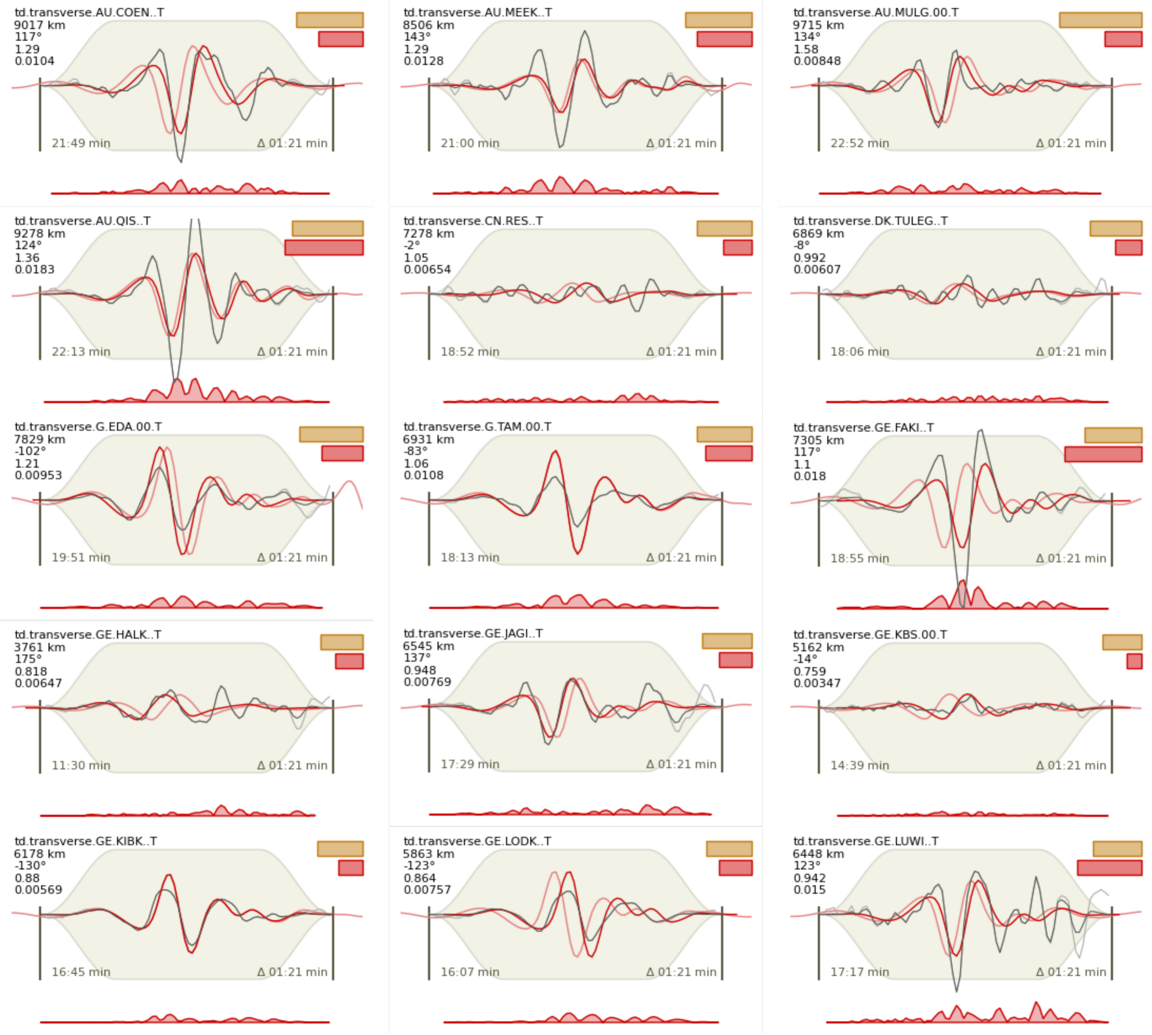

Figure A.11: Transverse component of waveform misfits for optimum global solution for the Jiashi mainshock. Traces are filtered observed data with (black) and without (grey) tapering, synthetic waveforms for the unshifted optimum solution (pink), and synthetic waveforms for the optimum solution after filtering, tapering, and realignment with observed waveform by cross correlation (red). Inset text gives the station name and component, distance, azimuth of the station relative to the initial event location, the weight assigned to the waveform during inversion, and the subsequent misfit. Inset boxes (top right of each panel) are scaled such that their length shows the relative weight of each trace within the full dataset and the relative contribution to the overall misfit of the optimum solution.

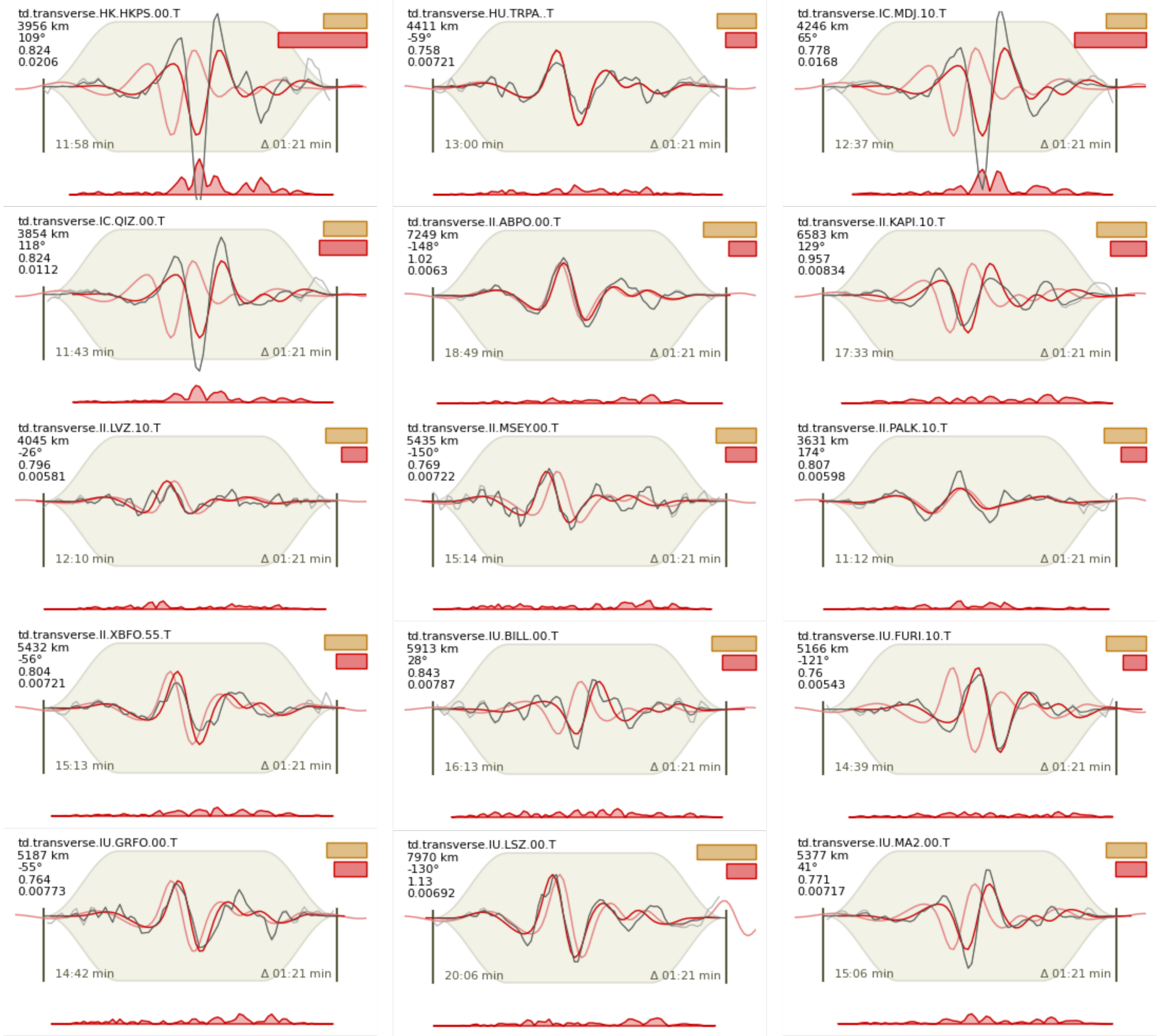

Figure A.11: Continued.

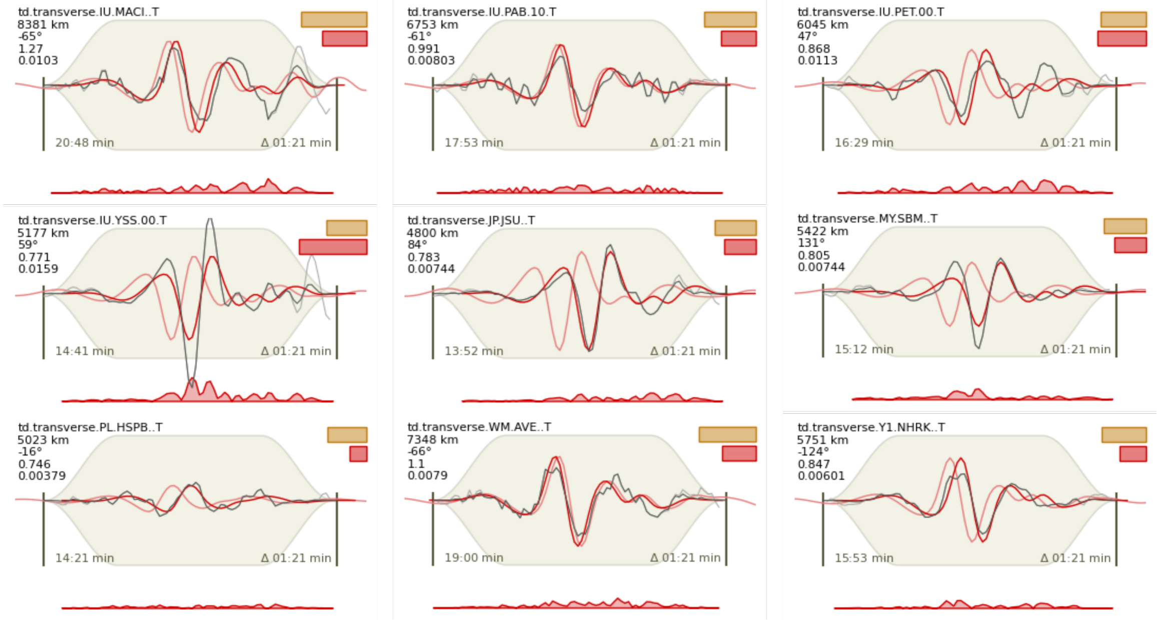

Figure A.11: Continued.

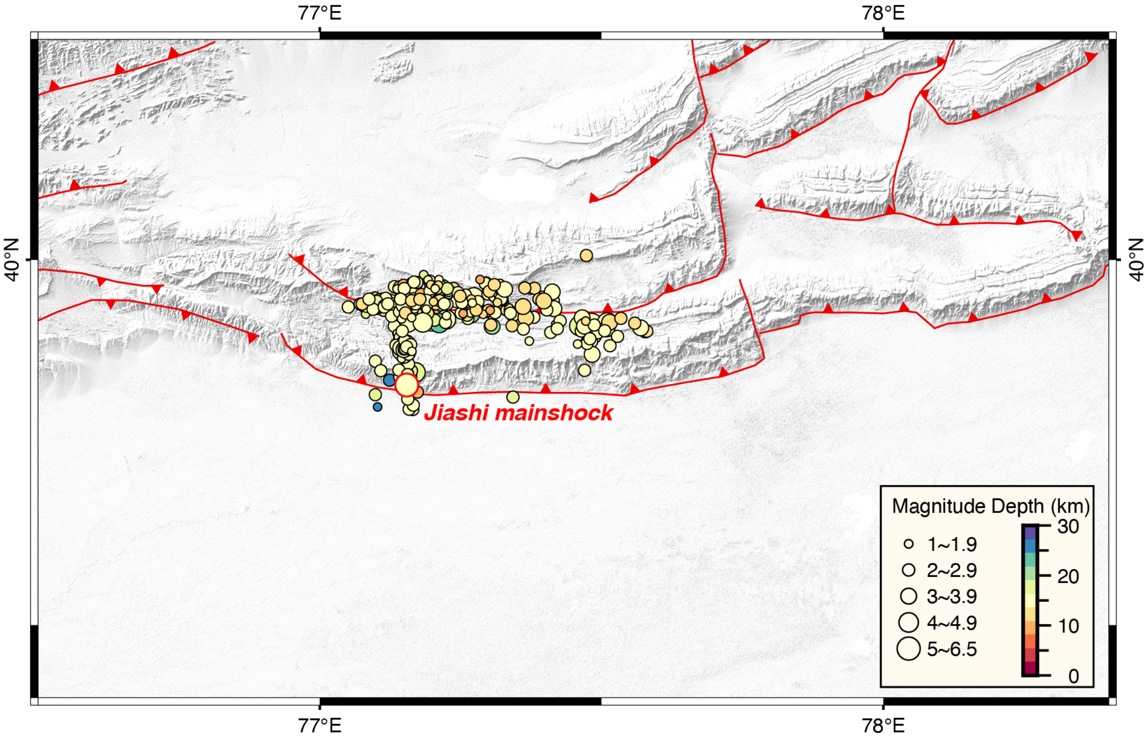

Figure A.12: Relocated aftershocks of the 2020 Jiashi sequence from Ran et al. (2020). The 2020 Jiashi mainshock is marked as a circle with a red border.

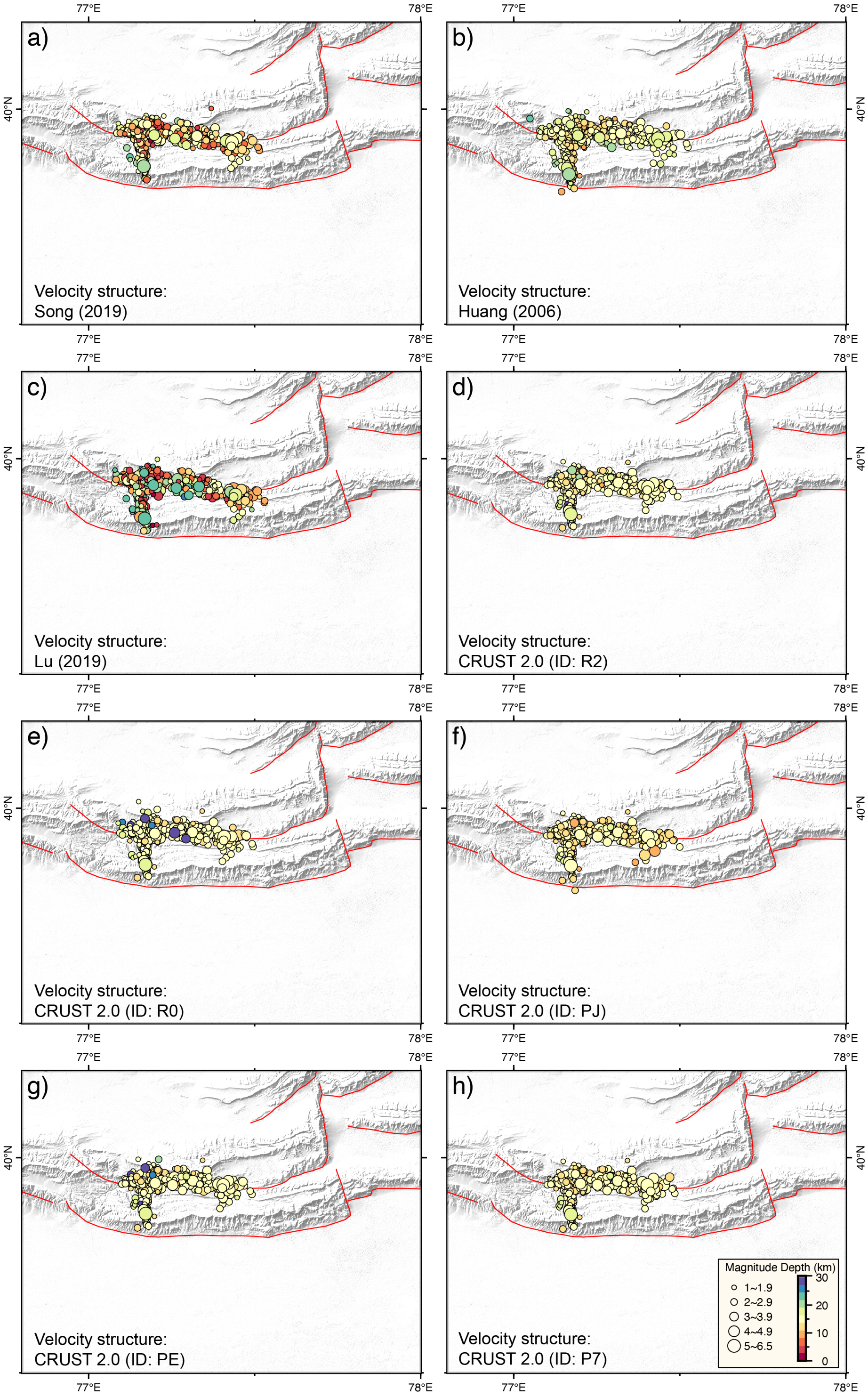

Figure A.13: Relocated hypocenters of the 2020 Jiashi sequence from Yao et al. (2021a). Depth distributions are determined using eight different velocity models.

Appendix B

Additional Information for Chapter 3

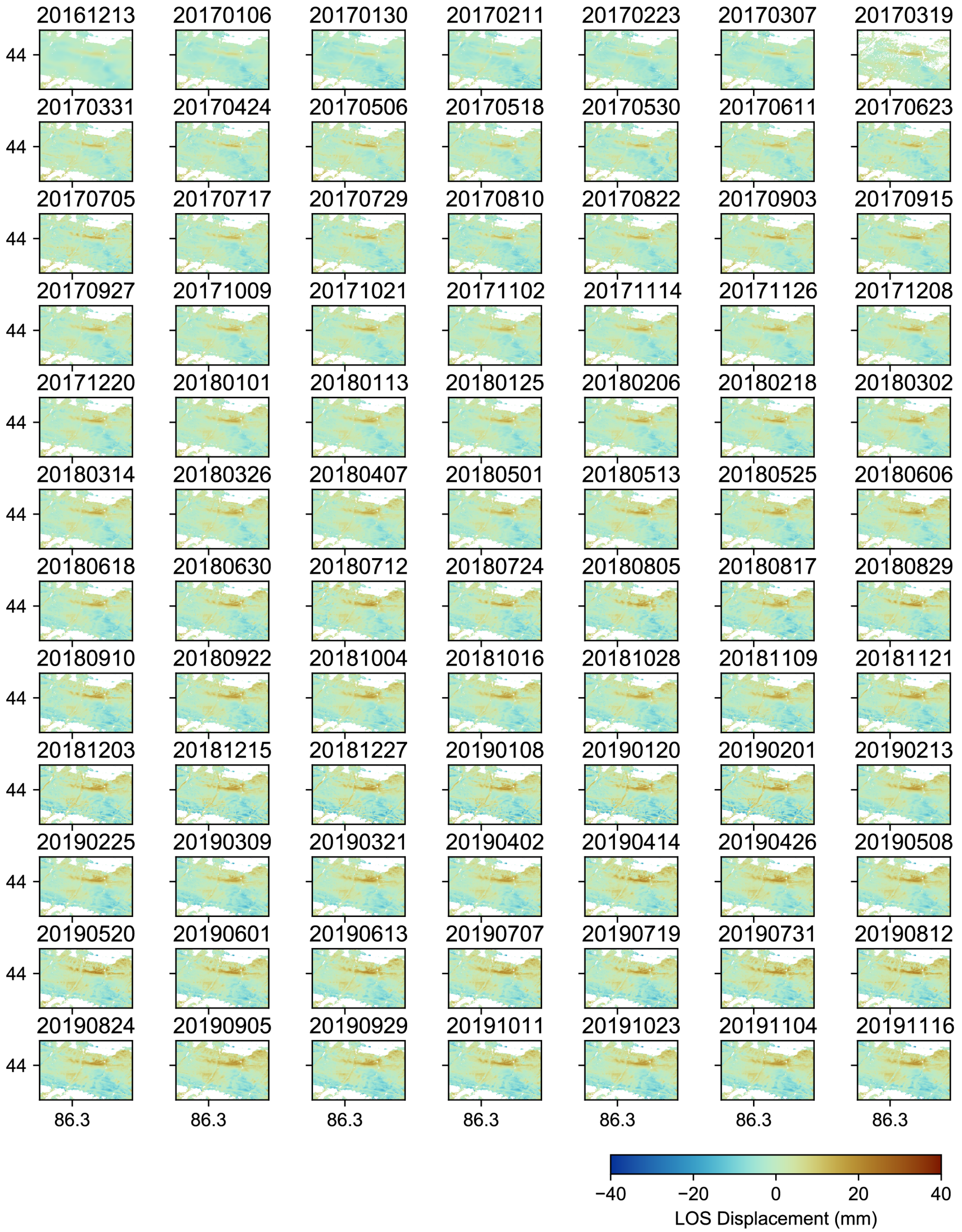

Figure B.1: The full cumulative displacement map of the ascending track

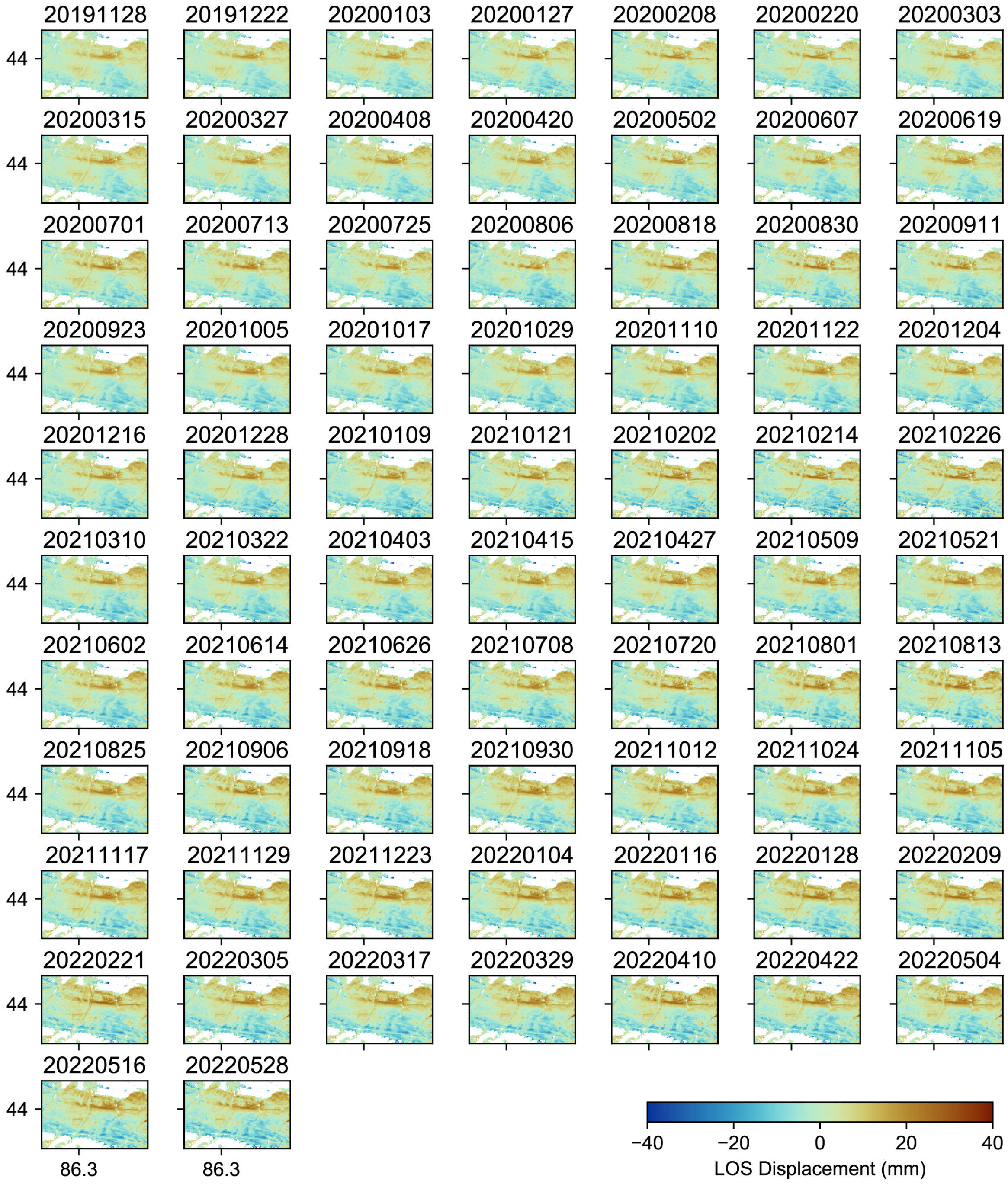

Figure B.1: Continued.

Figure B.2: The full cumulative displacement map of the descending track

Appendix C

Additional Information for Chapter 4

Table C.1: Complied apatite fission track and apatite (U-Th)/He age data (<100 Ma) from this study and previous studies used from exhumation rate history modelling.

Sample	Longitude	Latitude	Elevation	Age (Ma)	Error (Ma)	Method	Reference
TS1918	83.1802	44.344	1975	97.1	1.45	AFT	This study
TS1922	83.1275	44.3492	1635	82.2	1.66	AFT	This study
TS1933	84.4652	43.79	2635	37.6	0.64	AFT	This study
TS1909	87.2451	43.7696	1318	24.5	1.31	AHe	This study
TS1911	86.6352	43.7189	2030	23.6	0.87	AHe	This study
TS1912	86.6303	43.7386	1693	53.9	1.35	AHe	This study
TS1913	86.6195	43.7638	1499	47.7	1.12	AHe	This study
TS1914	86.5862	43.8014	1268	28.8	1.12	AHe	This study
TS1918	83.1802	44.344	1975	46.6	1.01	AHe	This study
TS1919	83.1823	44.3401	2080	59.5	1.07	AHe	This study
TS1922	83.1275	44.3492	1635	35.7	0.66	AHe	This study
TS1933	84.4652	43.79	2635	52.1	1.16	AHe	This study
P917-1	73.557	38.825	5465	39.8	2.79	AHe	Amidon and Hynek (2010)
P917-2	73.532	38.83	4900	31.5	2.21	AHe	Amidon and Hynek (2010)
P917-3	73.524	38.837	4497	17.1	1.2	AHe	Amidon and Hynek (2010)
P916-4	73.435	38.838	4098	37.2	2.6	AHe	Amidon and Hynek (2010)
P918-1	73.324	38.84	3947	69.9	20.97	AHe	Amidon and Hynek (2010)

Table C.1: continued

Sample	Longitude	Latitude	Elevation	Age (Ma)	Error (Ma)	Method	Reference
P918-2	73.291	38.843	3950	32.9	2.3	AHe	Amidon and Hynek (2010)
P916-3	73.42	38.843	4560	44.3	3.1	AHe	Amidon and Hynek (2010)
P916-2	73.394	38.845	5069	64.6	4.52	AHe	Amidon and Hynek (2010)
P917-4	73.515	38.845	4112	15.4	1.08	AHe	Amidon and Hynek (2010)
P916-1	73.418	38.846	4654	43	3.01	AHe	Amidon and Hynek (2010)
taj-102	73.628	39.078	4212	15.3	1.07	AHe	Amidon and Hynek (2010)
taj-99	73.653	39.085	4663	17.7	1.24	AHe	Amidon and Hynek (2010)
taj-96	73.664	39.093	5094	19.1	1.34	AHe	Amidon and Hynek (2010)
taj-93	73.673	39.101	5579	17.2	1.2	AHe	Amidon and Hynek (2010)
P919-2	73.25	39.102	4915	18.8	1.32	AHe	Amidon and Hynek (2010)
P919-3	73.281	39.11	4423	18.4	1.29	AHe	Amidon and Hynek (2010)
P919-1	73.302	39.119	3929	17.8	1.25	AHe	Amidon and Hynek (2010)
P919-1a	73.42	39.126	3937	22	1.54	AHe	Amidon and Hynek (2010)
K90G34	75.072	38.744	3162	0.9	0.9	AFT	Arnaud et al. (1993)
K90G14	75.182	38.746	2770	1.4	1.4	AFT	Arnaud et al. (1993)
K90G15	75.198	38.756	2991	0.8	0.9	AFT	Arnaud et al. (1993)
HS1-01	98.1345	39.875	1890	99	10	AFT	An et al. (2020)
HS1-02	98.1347	39.8751	1848	110	13	AFT	An et al. (2020)
HS1-03	98.1355	39.8754	1836	136	13	AFT	An et al. (2020)
HS1-04	98.1364	39.8756	1833	86.2	9.8	AFT	An et al. (2020)
HS2-01	98.1274	39.8479	1746	175	18	AFT	An et al. (2020)
HS-2-03	98.1281	39.8446	1747	135	18	AFT	An et al. (2020)
HS2-04	98.1285	39.8425	1742	118	20	AFT	An et al. (2020)
HS2-06	98.1276	39.8398	1728	146	19	AFT	An et al. (2020)
HS3-01	98.0403	39.8458	1848	72	12	AFT	An et al. (2020)
HS3-02	98.0391	39.8455	1849	60.5	9.9	AFT	An et al. (2020)
HS3-03	98.9386	39.8444	1842	96.8	8	AFT	An et al. (2020)
HS4-01	97.9139	39.9918	1665	33.9	8.3	AFT	An et al. (2020)
HS4-02	97.9133	39.9916	1656	36	4.2	AFT	An et al. (2020)
HS4-04	97.9124	39.9912	1646	22.3	2.6	AFT	An et al. (2020)
KTS1-01	97.3983	40.0712	1628	29.4	2.8	AFT	An et al. (2020)
KTS1-03	97.396	40.0712	1619	39.1	2.6	AFT	An et al. (2020)
KTS2-01	97.3659	40.1956	1485	50	7.1	AFT	An et al. (2020)

Table C.1: continued

Sample	Longitude	Latitude	Elevation	Age (Ma)	Error (Ma)	Method	Reference
KTS2-02	97.3656	40.1956	1488	80	9.5	AFT	An et al. (2020)
KTS3-01	97.3561	40.1779	1521	81.4	4.9	AFT	An et al. (2020)
KTS3-03	97.3558	40.1765	1518	55	5.7	AFT	An et al. (2020)
KTS4-02	97.3534	40.1445	1572	82.9	5.3	AFT	An et al. (2020)
KTS4-04	97.3536	40.135	1594	60.5	6.8	AFT	An et al. (2020)
10TR02	72.0405	42.1632	2571	22	3.1	AFT	Bande et al. (2017a)
10TR03	72.0405	42.1382	2678	23	2.3	AFT	Bande et al. (2017a)
10TR04	72.0426	42.1085	3120	25.4	2.9	AFT	Bande et al. (2017a)
10TR05	72.0371	42.122	2921	25.1	3.1	AFT	Bande et al. (2017a)
10TR17	71.5338	42.4589	1269	25.2	2.8	AFT	Bande et al. (2017a)
10UM12	71.4067	42.2331	3456	51.5	2.8	AFT	Bande et al. (2017a)
10UM14	71.4098	42.2401	2082	27.5	3.2	AFT	Bande et al. (2017a)
10UM15	71.4133	42.2415	2945	37.6	3.8	AFT	Bande et al. (2017a)
10TR19	71.5856	42.1992	2978	29.8	2.4	AFT	Bande et al. (2017a)
10TR20	71.5742	42.1855	2815	27.4	3.5	AFT	Bande et al. (2017a)
10TR21	71.5697	42.1837	2778	24.5	2.6	AFT	Bande et al. (2017a)
10TR22	71.5576	42.1287	2458	26.4	2.9	AFT	Bande et al. (2017a)
10TR23	71.5466	42.1195	2713	11	1.6	AFT	Bande et al. (2017a)
10CK37	71.0236	41.4967	1762	53.6	3.8	AFT	Bande et al. (2017a)
10CK41	71.227	41.438	1369	120	6.7	AFT	Bande et al. (2017a)
10CK43	71.527	41.5842	1874	51	5.5	AFT	Bande et al. (2017a)
10CK44	71.5292	41.5658	1695	64.7	5	AFT	Bande et al. (2017a)
10SU67	72.3318	41.5306	922	19.2	5.6	AFT	Bande et al. (2017a)
10SU65	72.3641	41.613	2578	20.8	1.9	AFT	Bande et al. (2017a)
10SU61	72.3286	41.59	1985	16.4	2	AFT	Bande et al. (2017a)
10SU62	72.3561	41.6092	2386	23.9	2.1	AFT	Bande et al. (2017a)
10SU64	72.3676	41.6229	2767	43	2.7	AFT	Bande et al. (2017a)
10FR69	72.9562	41.7191	1844	25.5	2.4	AFT	Bande et al. (2017b)
10FR71	72.9985	41.7104	2131	46.5	3.2	AFT	Bande et al. (2017b)
10FR72	73.0284	41.6998	1939	22	3	AFT	Bande et al. (2017b)
10FR73	73.0148	41.6888	1789	10.4	1	AFT	Bande et al. (2017b)
11TS532	73.655	41.3058	2758	6.3	0.9	AFT	Bande et al. (2017b)
11TS533	73.6358	41.2944	2911	8.2	1.2	AFT	Bande et al. (2017b)

Table C.1: continued

Sample	Longitude	Latitude	Elevation	Age (Ma)	Error (Ma)	Method	Reference
11TS534	73.6474	41.3383	2036	41.6	3.5	AFT	Bande et al. (2017b)
11TS535	73.6642	41.346	2122	51	3.9	AFT	Bande et al. (2017b)
12FE27	73.8711	40.6615	1947	10.7	2.1	AFT	Bande et al. (2017b)
12FE28	73.7926	40.6596	1424	38	2.9	AFT	Bande et al. (2017b)
12FE29	73.7877	40.6586	3605	11.4	3.3	AFT	Bande et al. (2017b)
12FE30	73.731	40.6375	3605	48.7	5.3	AFT	Bande et al. (2017b)
11T23	74.8436	39.8382	3117	6.7	0.9	AFT	Bande et al. (2017b)
11T75	74.4984	39.8504	2800	6.9	0.9	AFT	Bande et al. (2017b)
12KA21	72.5818	40.0033	3475	13.6	1.3	AFT	Bande et al. (2017b)
12KA22	72.572	40.0047	3860	21.5	1.8	AFT	Bande et al. (2017b)
12KA23	72.5765	40.0056	3660	20.4	1.7	AFT	Bande et al. (2017b)
12KA24	72.6057	39.9983	3122	11.4	1.1	AFT	Bande et al. (2017b)
12KA25	72.6081	39.9989	3297	13	1.2	AFT	Bande et al. (2017b)
12NU12	73.5256	40.1286	1838	9.8	1.3	AFT	Bande et al. (2017b)
12NU13	73.5573	40.1659	2890	36.9	2.7	AFT	Bande et al. (2017b)
12NU14	73.5531	40.1658	2670	9.5	1.1	AFT	Bande et al. (2017b)
12NU15	73.5489	40.1615	2500	9	0.7	AFT	Bande et al. (2017b)
12NU16	73.5429	40.1519	2210	6.9	1.1	AFT	Bande et al. (2017b)
12NU17	73.5395	40.1452	2056	7.9	0.9	AFT	Bande et al. (2017b)
12NU02	73.8372	39.6163	2930	10.7	1.3	AFT	Bande et al. (2017b)
12NU11	73.7777	39.6747	2939	11.8	1.3	AFT	Bande et al. (2017b)
212-8	74.526	42.53	3400	15.9	2.2	AFT	Bullen et al. (2003)
212-9	74.52	42.536	3200	14.7	1.7	AFT	Bullen et al. (2003)
212-12	74.541	42.538	3970	20.3	5.5	AFT	Bullen et al. (2003)
98-30	74.509	42.546	2800	10.5	2.1	AFT	Bullen et al. (2003)
212-14	74.507	42.548	2690	11.5	1.3	AFT	Bullen et al. (2003)
212-16	74.492	42.595	2240	15.6	2.3	AFT	Bullen et al. (2003)
98-33	74.498	42.617	1800	10.8	2.7	AFT	Bullen et al. (2003)
WK16	75.999	38.453	2336	9.2	0.55	AFT	Cao et al. (2013)
WK17	75.987	38.474	2270	6	0.3	AFT	Cao et al. (2013)
WK20	76.063	38.552	2074	7	0.45	AFT	Cao et al. (2013)
WK22	76.093	38.566	2009	10.3	0.6	AFT	Cao et al. (2013)
WK23	76.115	38.573	1956	8.9	0.8	AFT	Cao et al. (2013)

Table C.1: continued

Sample	Longitude	Latitude	Elevation	Age (Ma)	Error (Ma)	Method	Reference
WK24	76.136	38.596	1897	10	0.6	AFT	Cao et al. (2013)
WK77	75.239	38.774	2603	3.3	0.55	AFT	Cao et al. (2013)
WK78	75.304	38.784	2394	2.7	0.25	AFT	Cao et al. (2013)
WK82	75.494	38.892	1973	62	5	AFT	Cao et al. (2013)
WK108	75.054	38.73	3567	2.1	0.4	AFT	Cao et al. (2013)
WK100	75.394	37.883	3011	7.2	0.5	AFT	Cao et al. (2013)
WK102	75.271	37.957	3520	5.5	0.25	AFT	Cao et al. (2013)
WK103	75.245	38.015	3061	8	0.55	AFT	Cao et al. (2013)
WK105	75.201	37.914	3278	7.5	0.5	AFT	Cao et al. (2013)
WK68	74.985	38.108	3544	10.6	0.6	AFT	Cao et al. (2013)
WK69	74.979	38.127	3595	10.8	0.6	AFT	Cao et al. (2013)
WK73	74.983	38.609	3308	8.8	0.4	AFT	Cao et al. (2013)
P-01	80.8893	41.9733	2300	21.8	3.6	AFT	Chang et al. (2021)
P-06	80.8913	41.9484	2277	11.3	1.2	AFT	Chang et al. (2021)
P-06	80.8913	41.9484	2277	4.95	0.55	AHe	Chang et al. (2021)
P-07	80.8873	41.9419	2163	10.5	1.3	AFT	Chang et al. (2021)
P-07	80.8873	41.9419	2163	5.38	0.88	AHe	Chang et al. (2021)
T-03	81.5209	42.0473	1741	18.1	2.1	AFT	Chang et al. (2021)
T-03	81.5209	42.0473	1741	6.9	1.2	AHe	Chang et al. (2021)
T-05	81.5276	42.0364	1722	8.8	0.4	AHe	Chang et al. (2021)
T-08	81.5329	42.0132	1691	27.6	4.4	AFT	Chang et al. (2021)
T-10	81.5368	42.0099	1686	35.6	3.5	AFT	Chang et al. (2021)
T-10	81.5368	42.0099	1686	7.7	0.3	AHe	Chang et al. (2021)
99711-1	89.295	38.3409	4196	36.4	3.2	AFT	Chen et al. (2001)
99713-1	89.3014	38.3406	3993	31.6	3	AFT	Chen et al. (2001)
99722-2	89.2915	38.3765	3691	27.1	2.6	AFT	Chen et al. (2001)
99725-2	89.265	38.4788	3652	33.9	3.2	AFT	Chen et al. (2001)
99728	89.2821	38.4881	3481	26.7	2.3	AFT	Chen et al. (2001)
997321	89.2099	38.7115	3298	22.4	2.1	AFT	Chen et al. (2001)
99731-2	89.2086	38.7062	3085	13.8	2.2	AFT	Chen et al. (2001)
99738	89.1581	38.8486	2914	19.7	2.8	AFT	Chen et al. (2001)
997310	89.111	38.8683	2627	18.8	2.3	AFT	Chen et al. (2001)
997314	89.0882	38.93	2271	28.4	2.7	AFT	Chen et al. (2001)

Table C.1: continued

Sample	Longitude	Latitude	Elevation	Age (Ma)	Error (Ma)	Method	Reference
99725-3	89.2672	38.4772	3600	66.1	6.9	AFT	Chen et al. (2006a)
99724	89.2919	38.4678	3500	17.3	1.9	AFT	Chen et al. (2006a)
99734-1	89.1201	38.732	3194	16.7	0.8	AFT	Chen et al. (2006a)
99734-2	89.1182	38.7339	3115	42	4.1	AFT	Chen et al. (2006a)
997311-1	89.1098	38.8757	2636	11.1	1.2	AFT	Chen et al. (2006a)
997312	89.1015	38.8824	2438	10.1	1.2	AFT	Chen et al. (2006a)
03806	85.4125	37.2592	3100	5.5	0.9	AFT	Chen et al. (2006a)
03812	85.4539	37.2831	3100	4.6	0.9	AFT	Chen et al. (2006a)
03831	85.4475	37.2722	3220	10.2	1.8	AFT	Chen et al. (2006a)
03853	85.4803	37.2964	2956	1.8	0.4	AFT	Chen et al. (2006a)
03856	85.4869	37.2903	3048	2.1	0.6	AFT	Chen et al. (2006a)
03864	85.5003	37.2794	3145	7.3	1.1	AFT	Chen et al. (2006a)
03882	85.5108	37.2614	3364	2.1	0.4	AFT	Chen et al. (2006a)
03891	85.5278	37.2533	3564	4.5	0.7	AFT	Chen et al. (2006a)
03893	85.5311	37.2661	3613	2	0.6	AFT	Chen et al. (2006a)
03901	85.5336	37.2469	3674	8.1	10	AFT	Chen et al. (2006a)
Y04-1	80.99	43.55	1880	106.7	10.6	AFT	Chen et al. (2006b)
Y04-2	81	43.55	1800	116.8	11.3	AFT	Chen et al. (2006b)
Y09-1	81.14	43.55	1702	45.3	5.3	AFT	Chen et al. (2006b)
Y04-3	80.99	43.54	1750	24.1	3.1	AFT	Chen et al. (2006b)
Y09-2	81.14	43.52	2072	47	8.5	AFT	Chen et al. (2006b)
Y09-5	81.14	43.49	2450	86.5	9.5	AFT	Chen et al. (2006b)
Y12-2	81.92	43.42	1304	85.3	9.3	AFT	Chen et al. (2006b)
Y12-3	81.91	43.4	1342	89.3	10.2	AFT	Chen et al. (2006b)
Y12-6	81.88	43.39	1515	111.6	12.9	AFT	Chen et al. (2006b)
Y10-1	81.14	43.26	2166	122.8	8.8	AFT	Chen et al. (2006b)
Y10-3	81.14	43.22	2100	156.7	10.2	AFT	Chen et al. (2006b)
Y10-4	81.14	43.21	1999	158.3	12.3	AFT	Chen et al. (2006b)
S-3201	81.56	44.22	1800	89.7	9.3	AFT	Zhengle et al. (2008)
S-303	81.41	44.13	1600	62.7	6.7	AFT	Zhengle et al. (2008)
S-3171	81.08	43.51	1705	91	9.6	AFT	Zhengle et al. (2008)
S-3112	80.8	43.45	1700	77.7	8.1	AFT	Zhengle et al. (2008)
04KL01	97.745	35.897	4491	71	6.16	AHe	Clark et al. (2010)

Table C.1: continued

Sample	Longitude	Latitude	Elevation	Age (Ma)	Error (Ma)	Method	Reference
04KL02	97.733	35.904	4223	62	4.7	AHe	Clark et al. (2010)
04KL03	97.731	35.922	4002	64	4.9	AHe	Clark et al. (2010)
04KL04	97.724	35.925	3770	44	3.33	AHe	Clark et al. (2010)
04KL05	97.713	35.928	3610	32	2.42	AHe	Clark et al. (2010)
04KL06	97.707	35.931	3410	26	1.97	AHe	Clark et al. (2010)
04KL07	97.704	35.937	3281	27	1.82	AHe	Clark et al. (2010)
04KL11	96.383	36.039	3965	28	2.17	AHe	Clark et al. (2010)
04KL10	96.383	36.042	4143	33	2.53	AHe	Clark et al. (2010)
04KL12	96.425	36.045	3496	24	2.12	AHe	Clark et al. (2010)
04KL09	96.38	36.047	4406	39	2.98	AHe	Clark et al. (2010)
04KL08A	97.522	36.049	2926	33	2.47	AHe	Clark et al. (2010)
04KL08B	96.375	36.052	4674	83	5.61	AHe	Clark et al. (2010)
04KL13	96.432	36.105	3317	24	2.07	AHe	Clark et al. (2010)
04KL15	94.329	36.187	4318	56	4.85	AHe	Clark et al. (2010)
04KL19	94.211	36.244	3102	27	2.37	AHe	Clark et al. (2010)
11-07	79.0167	44.8833	1718	58	16	AFT	De Pelsmaeker et al. (2015)
11-09	79.15	44.8833	1763	73	3	AFT	De Pelsmaeker et al. (2015)
11-11	78.9667	44.8833	2029	72	4	AFT	De Pelsmaeker et al. (2015)
SK-21	78.5333	44.1833	1542	91	6	AFT	De Pelsmaeker et al. (2015)
11-27	76.9667	43.05	2510	9	1	AFT	De Pelsmaeker et al. (2015)
11-28	76.9333	43.0333	3379	16	1	AFT	De Pelsmaeker et al. (2015)
SK-31	76.2167	42.9	3076	78	4	AFT	De Pelsmaeker et al. (2015)
TS22	77.165	42.05	3500	69.3	7.2	AFT	De Grave (2003)
TS23	77.159	42.053	3310	72	5	AFT	De Grave (2003)
TS20	77.368	42.084	2150	61.9	3.9	AFT	De Grave (2003)
AI-37	73.5237	40.12967	1810	18.8	1.6	AFT	De Grave et al. (2012)
AI-38	73.5354	40.1393	1990	14	1.4	AFT	De Grave et al. (2012)
AI-40	72.5814	39.7639	4510	8.4	0.3	AFT	De Grave et al. (2012)
AI-40	72.5814	39.7639	4510	5	0.3	AHe	De Grave et al. (2012)
AI-42	72.6654	39.7139	3100	22.3	1.1	AFT	De Grave et al. (2012)
AI-42	72.6654	39.7139	3100	9.7	0.6	AHe	De Grave et al. (2012)
Kyr-10	73.5411	40.0664	2000	15.9	1.5	AFT	De Grave et al. (2012)
Kyr-06A	73.2486	39.4333	3710	206.6	12.2	AFT	De Grave et al. (2012)

Table C.1: continued

Sample	Longitude	Latitude	Elevation	Age (Ma)	Error (Ma)	Method	Reference
Kyr-06B	73.2486	39.4333	3710	71.8	6.8	AFT	De Grave et al. (2012)
Kyr-06C	73.2486	39.4333	3710	18.4	1.7	AFT	De Grave et al. (2012)
Kyr-06D	73.2486	39.4333	3710	3.3	0.7	AFT	De Grave et al. (2012)
Kyr-07A	73.325	39.3867	4380	208	16.6	AFT	De Grave et al. (2012)
Kyr-07B	73.325	39.3867	4380	80.7	7	AFT	De Grave et al. (2012)
Kyr-07C	73.325	39.3867	4380	18.9	3.1	AFT	De Grave et al. (2012)
ALMA03-01	77.0458	43.1633	1640	22.9	4	AFT	De Grave et al. (2013)
ALMA03-02	77.0592	43.1486	1960	29.4	1.4	AFT	De Grave et al. (2013)
ALMA03-03	77.0842	43.125	2400	70.9	4	AFT	De Grave et al. (2013)
TS-02	75.8892	42.6842	1370	128	13	AFT	De Grave et al. (2013)
TS-04	76.5775	42.8553	2360	132	7	AFT	De Grave et al. (2013)
TS-06	76.8308	42.7264	3950	137	7	AFT	De Grave et al. (2013)
TS-07	76.8436	42.7231	3700	147	8	AFT	De Grave et al. (2013)
TS-08	76.8439	42.7181	3515	147	6	AFT	De Grave et al. (2013)
TS-09	76.8497	42.7169	3300	116	4	AFT	De Grave et al. (2013)
TS-10	76.8586	42.7206	3085	134	5	AFT	De Grave et al. (2013)
TS-11	76.8642	42.7047	2860	138	7	AFT	De Grave et al. (2013)
TS-12	76.8508	42.6778	2420	130	8	AFT	De Grave et al. (2013)
TS-13	77.5236	42.7692	1850	163	9	AFT	De Grave et al. (2013)
TS-14	77.5306	42.8019	2080	153	8	AFT	De Grave et al. (2013)
TS-18	76.0144	42.4642	1630	126	8	AFT	De Grave et al. (2013)
TS-15	75.8608	42.4492	2150	149	8	AFT	De Grave et al. (2013)
TS-16	75.8564	42.4517	1960	111	6	AFT	De Grave et al. (2013)
TS-17	75.8569	42.4536	1830	120	6	AFT	De Grave et al. (2013)
IK-01	75.8469	42.3578	2100	81.3	3.4	AFT	De Grave et al. (2013)
AI-88	76.1274	42.3178	1740	91	3.1	AFT	De Grave et al. (2013)
TS-19	77.1417	42.1197	2020	108	17	AFT	De Grave et al. (2013)
TS-20	77.3678	42.0842	2150	61.9	3.9	AFT	De Grave et al. (2013)
TS-22	77.1653	42.05	3500	69.3	7.2	AFT	De Grave et al. (2013)
TS-23	77.1586	42.0533	3310	72	5	AFT	De Grave et al. (2013)

Table C.1: continued

Sample	Longitude	Latitude	Elevation	Age (Ma)	Error (Ma)	Method	Reference
TS-24	77.1519	42.0544	3080	103	9	AFT	De Grave et al. (2013)
TS-26	77.1386	42.0706	2700	78.4	6.6	AFT	De Grave et al. (2013)
TS-27	77.0681	42.0947	2060	99.4	5.7	AFT	De Grave et al. (2013)
TS-28	77.1167	42.125	1700	85.7	10.7	AFT	De Grave et al. (2013)
AI-01	77.1593	42.047	3435	64.1	3.2	AFT	De Grave et al. (2013)
AI-04	77.1581	42.0411	3350	68.2	3.6	AFT	De Grave et al. (2013)
AI-05	77.1524	42.0425	3145	5	0.5	AFT	De Grave et al. (2013)
AI-09	77.1444	42.0682	2940	68.9	7.9	AFT	De Grave et al. (2013)
KYR-33	77.0683	42.0967	2030	116	21	AFT	De Grave et al. (2013)
KYR-35	77.6361	41.9697	2450	38.1	2	AFT	De Grave et al. (2013)
KYR-38	77.7361	41.8708	3815	108	6	AFT	De Grave et al. (2013)
KYR-39	77.6575	41.9019	3430	110	7	AFT	De Grave et al. (2013)
KYR-42	77.5978	42.0394	2255	17.6	0.8	AFT	De Grave et al. (2013)
IK-11	79.0208	42.4228	3200	130	9	AFT	De Grave et al. (2013)
IK-12	78.9511	42.4308	2900	38.6	14.4	AFT	De Grave et al. (2013)
IK-13	78.5517	42.4519	1970	26.3	1.3	AFT	De Grave et al. (2013)
AI-27	79.0533	42.3811	3765	123	7	AFT	De Grave et al. (2013)
AI-33	76.7909	42.1458	2220	198	41	AFT	De Grave et al. (2013)
MN1	85.8133	43.8569		26	2	AFT	Du et al. (2007)
MN2	85.8394	43.8833		45	6	AFT	Du et al. (2007)
MN3	85.8494	43.8997		38	4	AFT	Du et al. (2007)
MN4	85.8833	43.9092		17	2	AFT	Du et al. (2007)
MN6	85.7722	43.9547		98	8	AFT	Du et al. (2007)
MN7	85.7725	43.9567		75	7	AFT	Du et al. (2007)
MN10	85.7514	43.9814		64	5	AFT	Du et al. (2007)
TTH3	87.2178	43.6697		99	10	AFT	Du et al. (2007)
TTH5	87.1569	43.6953		46	3	AFT	Du et al. (2007)
TTH6	87.2603	43.7789		85	6	AFT	Du et al. (2007)
KC1	82.8714	41.8144		58	4	AFT	Du et al. (2007)
KC2	83.3172	41.9075		50	2.6	AFT	Du et al. (2007)
KC3	83.0381	42.1186		55	4	AFT	Du et al. (2007)
KC5	83.14	42.1025		81	7	AFT	Du et al. (2007)
KC7	83.1053	42.1478		39	4	AFT	Du et al. (2007)

Table C.1: continued

Sample	Longitude	Latitude	Elevation	Age (Ma)	Error (Ma)	Method	Reference
KC8	83.1106	42.1583		28	3	AFT	Du et al. (2007)
KC9	83.2564	43.1011		41	4	AFT	Du et al. (2007)
KC10	83.2564	42.2678		42	4	AFT	Du et al. (2007)
HXG1	86.7789	43.035		82	4	AFT	Du et al. (2007)
HXG2	86.7689	43.0328		84	5	AFT	Du et al. (2007)
HXG3	86.7092	42.9936		75	4	AFT	Du et al. (2007)
HXG4	86.6811	42.9383		76	4	AFT	Du et al. (2007)
BLT5	86.3072	42.7503		49	3	AFT	Du et al. (2007)
BLT6	86.3072	42.7558		22	3	AFT	Du et al. (2007)
BLT7	86.3058	42.7339		49	3	AFT	Du et al. (2007)
BLT8	86.2947	42.7164		60	4	AFT	Du et al. (2007)
BLT9	86.2731	42.6958		57	8	AFT	Du et al. (2007)
BLT10	86.2797	42.6656		59	4	AFT	Du et al. (2007)
BLT11	86.2733	42.6492		59	3	AFT	Du et al. (2007)
BLT12	86.3117	42.6603		74	4	AFT	Du et al. (2007)
BLT13	86.3278	42.6658		63	4	AFT	Du et al. (2007)
BLT14	86.3675	42.6931		67	4	AFT	Du et al. (2007)
KCH15	83.2703	42.2947		61	4	AFT	Du et al. (2007)
KCH16	83.2697	42.2953		54	3	AFT	Du et al. (2007)
KCH17	83.2617	43.2997		36	2	AFT	Du et al. (2007)
KCH18	83.2686	42.2897		35	2	AFT	Du et al. (2007)
KCH19	83.2728	42.2828		37	3	AFT	Du et al. (2007)
KCH20	83.2761	42.2894		49	3	AFT	Du et al. (2007)
KCH22	83.325	42.2975		43	4	AFT	Du et al. (2007)
BY25	84.1222	43.0292		94	5	AFT	Du et al. (2007)
BY27	84.175	43.0211		70	4	AFT	Du et al. (2007)
BY28	84.1761	43.0206		72	4	AFT	Du et al. (2007)
BY29	84.1775	43.0203		89	5	AFT	Du et al. (2007)
BY31	84.1683	43.0844		98	7	AFT	Du et al. (2007)
QM44	84.4033	43.6881		77	5	AFT	Du et al. (2007)
QM55	84.4206	43.6911		72	5	AFT	Du et al. (2007)
QM47	84.4411	43.7175		62	8	AFT	Du et al. (2007)
QM48	84.4289	43.7267		25	2	AFT	Du et al. (2007)

Table C.1: continued

Sample	Longitude	Latitude	Elevation	Age (Ma)	Error (Ma)	Method	Reference
QM49	84.4194	43.7431		11	1	AFT	Du et al. (2007)
QM50	84.4425	43.7575		16	1	AFT	Du et al. (2007)
K-3	83.108	42.158	1682	50	4.4	AFT	Dumitru et al. (2001)
K-4	83.233	42.239	1863	96.7	12	AFT	Dumitru et al. (2001)
K-5	83.242	42.242	1812	96.7	9.3	AFT	Dumitru et al. (2001)
K-6	83.256	42.258	1837	67.1	5.5	AFT	Dumitru et al. (2001)
K-7	83.275	42.289	1959	86.3	5.4	AFT	Dumitru et al. (2001)
DK68	83.195	42.328	2000	52.2	6.1	AFT	Dumitru et al. (2001)
DK53	84.293	43.182	2640	70.8	10	AFT	Dumitru et al. (2001)
DK41	84.45	43.477	3360	35.8	3	AFT	Dumitru et al. (2001)
DK37	84.452	43.492	3280	9.1	6.5	AFT	Dumitru et al. (2001)
DK36	84.457	43.51	3010	22.7	6.8	AFT	Dumitru et al. (2001)
DK30	84.422	43.728	3480	22.4	1.5	AFT	Dumitru et al. (2001)
DK29	84.43	43.73	3760	23.4	1.1	AFT	Dumitru et al. (2001)
DK27	84.425	43.74	3440	12	0.5	AFT	Dumitru et al. (2001)
DK28	84.425	43.74	3440	10.7	1.4	AFT	Dumitru et al. (2001)
DK26	84.437	43.743	3200	28.6	2.2	AFT	Dumitru et al. (2001)
DK25	84.45	43.762	3360	32	3.5	AFT	Dumitru et al. (2001)
DK23	84.468	43.767	2800	38.7	3.5	AFT	Dumitru et al. (2001)
DK24	84.468	43.767	2800	15.3	2.1	AFT	Dumitru et al. (2001)
M5	85.817	43.856	1299	29.7	5.7	AFT	Dumitru et al. (2001)
M4	85.828	43.864	1318	38.1	4	AFT	Dumitru et al. (2001)
M3	85.878	43.919	1126	32.5	5.3	AFT	Dumitru et al. (2001)
M2	85.864	43.944	1257	97.6	9.9	AFT	Dumitru et al. (2001)
KFW1	93.933	35.724	4755	17.45	1.97	AHe	Duvall et al. (2013)
KFW2	93.884	35.699	4935	7.52	0.74	AHe	Duvall et al. (2013)
DCH12	98.405	36.073	4302	45.49	19.1	AHe	Duvall et al. (2013)
DCH13	98.407	36.071	4198	37.15	11.72	AHe	Duvall et al. (2013)
DCH14	98.406	36.069	4093	15.2	2.96	AHe	Duvall et al. (2013)
DCH15	98.406	36.066	3986	16.18	0.78	AHe	Duvall et al. (2013)
DCH16	98.409	36.064	3867	12.7	1.09	AHe	Duvall et al. (2013)
DCH17	98.472	36.256	4598	35.26	2.41	AHe	Duvall et al. (2013)
DCH18	98.467	36.258	4473	26.81	5.95	AHe	Duvall et al. (2013)

Table C.1: continued

Sample	Longitude	Latitude	Elevation	Age (Ma)	Error (Ma)	Method	Reference
DCH19	98.46	36.254	4276	21.02	2.19	AHe	Duvall et al. (2013)
DCH20	98.454	36.25	4100	13.88	2.17	AHe	Duvall et al. (2013)
DCH21	98.45	36.248	3924	12.55	1.99	AHe	Duvall et al. (2013)
DCH22	98.719	36.28	4808	45.22	8.95	AHe	Duvall et al. (2013)
DCH23	98.712	36.277	4548	18.7	5.85	AHe	Duvall et al. (2013)
DCH24	98.708	36.27	4407	62.97	13.17	AHe	Duvall et al. (2013)
DCH25	98.711	36.267	4328	14.16	4.11	AHe	Duvall et al. (2013)
DCH26	98.705	36.263	4160	28.09	7.86	AHe	Duvall et al. (2013)
DCH27	98.769	35.856	4143	64.2	3.6	AHe	Duvall et al. (2013)
DCH28	98.751	36.015	4083	27.66	7.98	AHe	Duvall et al. (2013)
DCH29	98.566	35.992	4123	86.08	7.83	AHe	Duvall et al. (2013)
DCH30	98.513	36.067	4106	45.39	6.7	AHe	Duvall et al. (2013)
GC740-4	97.189	39.794	3000	19.8	2.3	AFT	George et al. (2001)
GC740-15	97.231	39.825	2500	72.9	5.1	AFT	George et al. (2001)
BH17	93.7103	43.2007	1851	92.6	6.6	AFT	Gillespie et al. (2017)
BH25	93.0644	43.8632	1794	81.5	6	AFT	Gillespie et al. (2017)
BH36	94.4724	42.8965	2270	90.1	5	AFT	Gillespie et al. (2017)
KYR-03	73.8372	42.31	2770	57.6	3.5	AHe	Glorie et al. (2011)
IK-02	75.8769	42.3097	1745	96.6	3.4	AFT	Glorie et al. (2011)
TF-21	74.1256	42.0933	2010	98.6	6.5	AHe	Glorie et al. (2011)
IK-07	75.7372	41.9317	2450	75	11	AFT	Glorie et al. (2011)
TF-17	74.2669	41.78	1775	33.8	2.1	AFT	Glorie et al. (2011)
TF-17	74.2669	41.78	1775	29.4	1.8	AHe	Glorie et al. (2011)
TF-19	74.3239	41.8228	2030	97.1	4.6	AFT	Glorie et al. (2011)
AI-74	75.294	40.388	3591	47.4	2.5	AFT	Glorie et al. (2011)
AI-74	75.294	40.388	3591	41.4	2.5	AHe	Glorie et al. (2011)
AI-77	75.557	40.827	3990	19.5	1.1	AFT	Glorie et al. (2011)
AI-77	75.557	40.827	3990	10.7	0.6	AHe	Glorie et al. (2011)
AI-75	75.556	40.828	4005	21	1.9	AFT	Glorie et al. (2011)
Kyr-31	75.278	40.935	2830	60.7	7.5	AFT	Glorie et al. (2011)
AI-62	75.599	40.983	2667	62.1	4.4	AFT	Glorie et al. (2011)
AI-69	75.656	41.05	2628	85.1	5.4	AHe	Glorie et al. (2011)
AI-73	75.651	41.057	2345	73.2	4.4	AHe	Glorie et al. (2011)

Table C.1: continued

Sample	Longitude	Latitude	Elevation	Age (Ma)	Error (Ma)	Method	Reference
Kyr-21	76.407	41.244	2620	8.4	0.9	AFT	Glorie et al. (2011)
AI-29	78.164	41.715	3773	56.5	3.9	AFT	Glorie et al. (2011)
AI-29	78.164	41.715	3773	30.8	1.8	AHe	Glorie et al. (2011)
AI-16	79.14	42.02	3497	58.9	2.7	AFT	Glorie et al. (2011)
AI-11	79.103	42.042	2470	9.8	1.1	AFT	Glorie et al. (2011)
AI-14	79.084	42.062	2590	12.8	0.8	AFT	Glorie et al. (2011)
AI-14	79.084	42.062	2590	14.9	0.9	AHe	Glorie et al. (2011)
AI-13	79.087	42.064	2790	7.9	0.5	AFT	Glorie et al. (2011)
AI-13	79.087	42.064	2790	6.6	0.4	AHe	Glorie et al. (2011)
AI-15	79.069	42.111	2614	23	1.3	AFT	Glorie et al. (2011)
AI-20	79.116	42.2	2727	57	3.4	AHe	Glorie et al. (2011)
DZ-06	78.8124	44.8773	1114	93	8.4	AFT	Glorie et al. (2019)
BY0312	84.0283	43.0769	2638	72.5	4.1	AFT	Guo et al. (2006)
DK43-1	84.4369	43.4942	3145	37.3	40.2	AFT	Guo et al. (2006)
DK39-1	84.4464	43.5142	2903	73.4	11.6	AFT	Guo et al. (2006)
DK35-1	84.4217	43.7433	3236	14.3	1.4	AFT	Guo et al. (2006)
DK33-1	84.455	43.7778	2766	50.2	6.8	AFT	Guo et al. (2006)
WS01-6	84.3514	44.1592	1560	87.2	6.5	AFT	Guo et al. (2006)
WS02-17	84.3342	44.1739	1420	78.4	7.6	AFT	Guo et al. (2006)
HX06-7	87.1524	43.2586	2170	68.4	4.6	AFT	Guo et al. (2006)
HX10-4	87.1311	43.3326	2193	74.1	4.5	AFT	Guo et al. (2006)
HX11-4	87.1313	43.3326	2211	37.8	2.7	AFT	Guo et al. (2006)
HX13-6	87.1429	43.3261	2127	36.9	3	AFT	Guo et al. (2006)
HJ02-1	87.215	43.6544	1213	60.6	6.1	AFT	Guo et al. (2006)
M2	85.8639	43.9444		97.6	9.9	AFT	Hendrix et al. (1994)
M3	85.8778	43.9194		32.5	5.3	AFT	Hendrix et al. (1994)
M4	85.8278	43.8639		38.1	4	AFT	Hendrix et al. (1994)
M5	85.8167	43.8556		29.7	5.7	AFT	Hendrix et al. (1994)
TK-09	75.7854	40.0992	2508	81.3	4.7	AFT	Jia et al. (2015)
TK-12	75.7935	40.0577	2406	28.8	2.5	AFT	Jia et al. (2015)
TK-13	75.785	40.044	2374	25.7	3	AFT	Jia et al. (2015)
KKTM-8	75.9467	39.8435	1785	30.1	3.1	AFT	Jia et al. (2015)
WY-2	76.0705	39.8374	1598	68.1	8.5	AFT	Jia et al. (2015)

Table C.1: continued

Sample	Longitude	Latitude	Elevation	Age (Ma)	Error (Ma)	Method	Reference
KKTM-4	76.0280	39.8321	1578	96.2	10.8	AFT	Jia et al. (2015)
AT118	90.129	36.155	5500	17.3	1.8	AFT	Jolivet et al. (2001)
AT113	89.244	36.6	5000	19.3	1.8	AFT	Jolivet et al. (2001)
AT103	88.772	36.973	4377	52.8	7.2	AFT	Jolivet et al. (2001)
AT140	86.133	37.637	2691	10.1	0.9	AFT	Jolivet et al. (2001)
AT131	91.022	37.733	3400	17.6	1.5	AFT	Jolivet et al. (2001)
AT120	89.242	37.864	4100	55.1	3.9	AFT	Jolivet et al. (2001)
AT142	86.594	38.061	1800	9.8	1.3	AFT	Jolivet et al. (2001)
WQ122	88.676	38.117	4000	20.7	2.3	AFT	Jolivet et al. (2001)
AT49	92.635	38.84	3300	97.3	6.3	AFT	Jolivet et al. (2001)
AT68	88.977	38.931	2300	30.3	3.5	AFT	Jolivet et al. (2001)
AT8	94.808	39.382	4000	16.9	1.6	AFT	Jolivet et al. (2001)
BJ30	99.802	39.438	3780	48.4	3.7	AFT	Jolivet et al. (2001)
Bay D	84.3805	43.091	2583	65.1	4.8	AFT	Jolivet et al. (2010)
Bay E	84.3803	43.0896	2550	72.7	10.1	AFT	Jolivet et al. (2010)
Bay F	84.0768	43.0824	2766	91.6	12.1	AFT	Jolivet et al. (2010)
TS-03-12	83.7397	43.4648	1038	98.3	13.4	AFT	Jolivet et al. (2010)
TS-03-14	84.4443	43.4716	3361	34.4	4.4	AFT	Jolivet et al. (2010)
TS-03-15	84.3848	43.4149	2506	69.2	6.5	AFT	Jolivet et al. (2010)
TS-03-17	84.3382	43.1938	2238	76.3	13.9	AFT	Jolivet et al. (2010)
Bay D	84.3805	43.091	2583	43.9		AHe	Jolivet et al. (2010)
TS12b	73.6121	39.7680	3920	17.1	2.2	AFT	Käßner et al. (2016)
96TS1	73.5282	40.1053	1888	20.6	1	AFT	Käßner et al. (2016)
96TS2	73.5053	40.1395	1808	16.1	0.8	AFT	Käßner et al. (2016)
Z28-1	84.86	45.03	680	74.8	12.2	AFT	Li et al. (2008)
Z28-2	84.84	44.93	670	73	10	AFT	Li et al. (2008)
03_46	90.44	44.55	1229	41.6	4.7	AFT	Li et al. (2008)
03_45	90.38	44.47	1224	43.2	4.5	AFT	Li et al. (2008)
03_31	92	43.31	1785	23.5	2.9	AFT	Li et al. (2008)
03_35	92.05	43.22	886	23.5	3.7	AFT	Li et al. (2008)
03_30	91.92	43.16	1880	16.3	3.9	AFT	Li et al. (2008)
WK17-35-1	77.004	36.446	3781	15.9	1	AFT	Li et al. (2019)

Table C.1: continued

Sample	Longitude	Latitude	Elevation	Age (Ma)	Error (Ma)	Method	Reference
WK17-37	77	36.561	4789	28.4	3.2	AFT	Li et al. (2019)
WK17-38	77.003	36.579	4969	35.5	3.3	AFT	Li et al. (2019)
WK17-40	77.147	36.627	4001	11.3	1.5	AFT	Li et al. (2019)
WK17-41	77.083	36.674	3606	20.5	2.1	AFT	Li et al. (2019)
WK17-42	77.026	36.763	3170	6.7	0.6	AFT	Li et al. (2019)
WK17-43	76.982	36.895	2952	11.5	2.2	AFT	Li et al. (2019)
WK17-44	76.993	36.928	2802	16.3	1.4	AFT	Li et al. (2019)
WK17-45	76.985	36.949	2674	12.5	1.2	AFT	Li et al. (2019)
WK17-48	76.935	37.09	3150	38.5	2.5	AFT	Li et al. (2019)
WK17-49	77.024	37.128	2549	13.1	1.3	AFT	Li et al. (2019)
WK17-50	77.074	37.213	2342	35.2	5.8	AFT	Li et al. (2019)
WK17-2	80.113	36.419	2555	11.3	1.6	AFT	Li et al. (2019)
WK17-9	79.959	36.473	2159	14.9	1.1	AFT	Li et al. (2019)
WK17-10	79.923	36.48	2082	14.6	1.3	AFT	Li et al. (2019)
WK17-17-2	77.861	37.042	2612	9.6	0.5	AFT	Li et al. (2019)
NMH01	96.4116	35.9799	4491	32.46	2.52	AHe	Li et al. (2021a)
NMH02	96.4144	35.9815	4344	46.12	5.7	AHe	Li et al. (2021a)
NMH03	96.4162	35.9833	4244	41.25	4.4	AHe	Li et al. (2021a)
NMH04	96.4197	35.9886	4049	38.8	3.37	AHe	Li et al. (2021a)
NMH05	96.4253	35.9928	3918	31.01	4.53	AHe	Li et al. (2021a)
NMH06	96.4392	35.9982	3760	30.01	3.49	AHe	Li et al. (2021a)
NMH07	96.4442	36.0115	3641	26.31	1.06	AHe	Li et al. (2021a)
QMG17	90.8453	37.8117	3626	38.72		AFT	Liu et al. (2017)
QMG11	90.2047	37.8545	4319	29.21		AFT	Liu et al. (2017)
QMG8	90.2035	37.8532	4424	50.43		AFT	Liu et al. (2017)
QMG6	90.2028	37.851	4500	25.5		AFT	Liu et al. (2017)
W2	98.5919	36.9993	3360	18.6	2.1	AFT	Lu et al. (2012)
W3	98.5921	36.9941	3590	19.9	1.6	AFT	Lu et al. (2012)
W4	98.5947	36.9875	3760	17.9	1.7	AFT	Lu et al. (2012)
W5	98.6008	36.9846	3950	22.2	2.2	AFT	Lu et al. (2012)
BLT1	86.3319	42.6854	2480	63.1	6.4	AFT	Lü et al. (2013)
BLT2	86.3337	42.6849	2386	92.2	8.2	AFT	Lü et al. (2013)

Table C.1: continued

Sample	Longitude	Latitude	Elevation	Age (Ma)	Error (Ma)	Method	Reference
BLT3	86.3354	42.6847	2251	65.3	9.8	AFT	Lü et al. (2013)
BLT4	86.3375	42.6849	2147	59.9	4.3	AFT	Lü et al. (2013)
BLT6	86.3452	42.683	1956	43.2	3.7	AFT	Lü et al. (2013)
BLT8	86.3534	42.6797	1796	63.9	5.6	AFT	Lü et al. (2013)
BLT2	86.3337	42.6849	2386	38.7	0.7	AHe	Lü et al. (2013)
BLT4	86.3375	42.6849	2147	31.1	0.6	AHe	Lü et al. (2013)
BLT7	86.3333	42.6667	1862	44	0.8	AHe	Lü et al. (2013)
BLT8	86.3534	42.6797	1796	10.9	0.3	AHe	Lü et al. (2013)
TRN1.1	76.3906	42.0882	3223	87.2	11.8	AFT	Macaulay et al. (2014)
TRN2.2	77.0598	41.9141	3918	87.6	4.7	AFT	Macaulay et al. (2014)
TRN3.1	78.0818	42.1613	3594	59.1	8.2	AFT	Macaulay et al. (2014)
TRN3.2	78.08	42.1649	3438	64.2	8.4	AFT	Macaulay et al. (2014)
TRN3.3	78.091	42.1739	3095	51.7	8.7	AFT	Macaulay et al. (2014)
TRN3.4	78.0931	42.1827	2939	29.1	2.8	AFT	Macaulay et al. (2014)
TRN3.5	78.0757	42.2114	2534	21.5	2.7	AFT	Macaulay et al. (2014)
TRN3.6	78.0655	42.224	2407	30.2	3.6	AFT	Macaulay et al. (2014)
TRN4.1	78.3605	42.2864	3445	23.9	2.1	AFT	Macaulay et al. (2014)
TRN5.1	78.4892	42.3238	2866	13.4	1.5	AFT	Macaulay et al. (2014)
TRN5.2	78.482	42.3219	2752	14.4	2.5	AFT	Macaulay et al. (2014)
TRN5.3	78.4749	42.3213	2569	20.4	1.9	AFT	Macaulay et al. (2014)
TRN5.4	78.4771	42.3139	2551	31.9	7.1	AFT	Macaulay et al. (2014)
TRN5.5	78.4697	42.3601	2402	39.4	11.8	AFT	Macaulay et al. (2014)
TRN6.1	78.9368	42.5433	3410	21.9	2.2	AFT	Macaulay et al. (2014)
TRN6.2	78.9362	42.5476	3262	19.1	1.4	AFT	Macaulay et al. (2014)
TRN6.3	78.938	42.5517	3106	15.7	1.7	AFT	Macaulay et al. (2014)
TRN6.4	78.9268	42.5609	2704	17.9	1.8	AFT	Macaulay et al. (2014)
TRN6.5	78.9172	42.5322	2540	10.7	1.3	AFT	Macaulay et al. (2014)
TRN6.6	78.9362	42.5012	2719	17.2	1.9	AFT	Macaulay et al. (2014)
TRN7.1	78.9584	42.4436	3264	50.2	7.4	AFT	Macaulay et al. (2014)
TRN7.2	78.9501	42.4345	2893	46.7	14.9	AFT	Macaulay et al. (2014)
TRN7.3	78.9476	42.4498	2875	38.4	5.5	AFT	Macaulay et al. (2014)
TRN7.4	78.9504	42.4173	2816	37.9	6.9	AFT	Macaulay et al. (2014)
TRS1.1	76.3093	42.0054	3835	64.7	3.7	AFT	Macaulay et al. (2014)

Table C.1: continued

Sample	Longitude	Latitude	Elevation	Age (Ma)	Error (Ma)	Method	Reference
TRS1.2	76.3199	42.001	3558	21	2.3	AFT	Macaulay et al. (2014)
TRS2.1	78.8378	42.2718	4060	72.9	6.5	AFT	Macaulay et al. (2014)
TRS2.2	78.8452	42.2717	3792	67.4	12.1	AFT	Macaulay et al. (2014)
TRS2.3	78.8495	42.2681	3616	73.3	10.4	AFT	Macaulay et al. (2014)
TRS2.4	78.858	42.2662	3453	70	6.8	AFT	Macaulay et al. (2014)
TRS2.5	78.8828	42.2566	3374	79.4	4.4	AFT	Macaulay et al. (2014)
TRS3.1	79.0607	42.3888	3788	81	3.3	AFT	Macaulay et al. (2014)
TRS3.2	79.0455	42.3621	3393	88	3.4	AFT	Macaulay et al. (2014)
NA3.1	79.0924	42.1212	3292	88.3	9.5	AFT	Macaulay et al. (2014)
NA3.3	79.08	42.1291	2679	44.7	7.7	AFT	Macaulay et al. (2014)
NA3.4	79.0937	42.1743	2657	75.2	7.7	AFT	Macaulay et al. (2014)
Sar1.1	79.1014	42.0541	3430	16.6	2.2	AFT	Macaulay et al. (2014)
Sar1.2	79.0981	42.0535	3204	21.5	4.8	AFT	Macaulay et al. (2014)
Sar1.3	79.0944	42.0545	2992	18.7	4.4	AFT	Macaulay et al. (2014)
Sar1.4	79.0944	42.0548	2992	15.3	2.8	AFT	Macaulay et al. (2014)
Sar1.5	79.0913	42.0545	2857	14.6	3.8	AFT	Macaulay et al. (2014)
Sar1.6	79.0912	42.0545	2857	12.4	2.1	AFT	Macaulay et al. (2014)
Sar1.7	79.0847	42.0542	2698	13.7	3.3	AFT	Macaulay et al. (2014)
Sar1.8	79.0807	42.0569	2568	23	3.7	AFT	Macaulay et al. (2014)
Sar1.9	79.0758	42.0426	2611	6.9	0.7	AFT	Macaulay et al. (2014)
Sar1.10	79.0833	42.0695	2612	11.3	1.7	AFT	Macaulay et al. (2014)
Sar2.1	79.7506	42.2772	3812	96.1	7.7	AFT	Macaulay et al. (2014)
TRN2.1	77.068	41.9154	4054	87.8	26	AHe	Macaulay et al. (2014)
TRN2.2	77.0598	41.9141	3918	49.7	14.4	AHe	Macaulay et al. (2014)
TRN3.1	78.0818	42.1613	3594	62.8	35.9	AHe	Macaulay et al. (2014)
TRN3.2	78.08	42.1649	3438	35.5	14.1	AHe	Macaulay et al. (2014)
TRN3.3	78.091	42.1739	3095	42.9	13.3	AHe	Macaulay et al. (2014)
TRN3.4	78.0931	42.1827	2939	11	2.8	AHe	Macaulay et al. (2014)
TRN3.5	78.0757	42.2114	2534	7.7	2	AHe	Macaulay et al. (2014)
TRN3.6	78.0655	42.224	2407	8.7	1.8	AHe	Macaulay et al. (2014)
TRN4.2	78.3215	42.2745	2508	95.4	15.3	AHe	Macaulay et al. (2014)
TRN6.1	78.9368	42.5433	3410	11.8	3	AHe	Macaulay et al. (2014)
TRN6.2	78.9362	42.5476	3262	13.3	4.7	AHe	Macaulay et al. (2014)

Table C.1: continued

Sample	Longitude	Latitude	Elevation	Age (Ma)	Error (Ma)	Method	Reference
TRN6.3	78.938	42.5517	3106	9.4	0.6	AHe	Macaulay et al. (2014)
TRN6.4	78.9268	42.5609	2704	11.1	1.4	AHe	Macaulay et al. (2014)
TRN6.5	78.9172	42.5322	2540	7	2.0	AHe	Macaulay et al. (2014)
TRN6.6	78.9362	42.5012	2719	8	0.5	AHe	Macaulay et al. (2014)
TRN7.2	78.9501	42.4345	2893	33.1	9.6	AHe	Macaulay et al. (2014)
TRS1.1	76.3093	42.0054	3835	16.5	6.9	AHe	Macaulay et al. (2014)
TRS2.5	78.8828	42.2566	3374	37.1	10.8	AHe	Macaulay et al. (2014)
Kar1.6	76.9755	41.6648	2988	18.3	12.2	AHe	Macaulay et al. (2014)
NA1.1	77.3417	41.4505	4061	68.8	11.9	AHe	Macaulay et al. (2014)
NA1.2	77.3357	41.4493	3855	59.8	16.7	AHe	Macaulay et al. (2014)
NA1.3	77.3285	41.4548	3581	86.1	40.4	AHe	Macaulay et al. (2014)
NA1.4	77.3254	41.4609	3232	62.4	4.8	AHe	Macaulay et al. (2014)
NA1.5	77.3159	41.4502	3089	38	11	AHe	Macaulay et al. (2014)
NA3.2	79.0931	42.1261	3039	22.6	6.55	AHe	Macaulay et al. (2014)
NA3.3	79.08	42.1291	2679	40.6	12.8	AHe	Macaulay et al. (2014)
Sar1.2	79.0981	42.0535	3204	43.25	12.55	AHe	Macaulay et al. (2014)
Sar1.9	79.0758	42.0426	2611	6.55	1.9	AHe	Macaulay et al. (2014)
Sar1.10	79.0833	42.0695	2612	16	8.2	AHe	Macaulay et al. (2014)
Bor1.2	79.2755	42.0796	3367	65.4	18.95	AHe	Macaulay et al. (2014)
S-21	95.306	36.327	2950	52.9	3.4	AFT	McRivette et al. (2019)
S-25	94.215	36.218	3245	16.3	1.7	AFT	McRivette et al. (2019)
S-24	94.252	36.194	3327	14.1	1.4	AFT	McRivette et al. (2019)
S-22	94.774	36.173	3091	11.9	2.5	AFT	McRivette et al. (2019)
S-75	95.244	36.17	3477	5.1	1.4	AFT	McRivette et al. (2019)
S-76	94.431	36.006	4117	3.7	0.8	AFT	McRivette et al. (2019)
S-74	94.238	35.857	3796	2.4	0.6	AFT	McRivette et al. (2019)
S-73	95.224	35.757	4088	10	1.8	AFT	McRivette et al. (2019)
S-26	94.26	35.739	4236	0.9	0.3	AFT	McRivette et al. (2019)
TF06	72.8606	42.0092	1355	53.2	2.8	AFT	Nachtergaele et al. (2018)
KYR04	72.9433	41.7117	1625	73.5	7.4	AFT	Nachtergaele et al. (2018)
KYR05	72.9681	41.7222	2110	97.5	6.7	AFT	Nachtergaele et al. (2018)
KB121	74.7759	41.7257	2756	80.2	5.6	AFT	Nachtergaele et al. (2018)
KB133	74.5166	41.7205	3387	98.6	4.8	AFT	Nachtergaele et al. (2018)

Table C.1: continued

Sample	Longitude	Latitude	Elevation	Age (Ma)	Error (Ma)	Method	Reference
KB134	74.5091	41.7085	2980	64.1	3.1	AFT	Nachtergaele et al. (2018)
KB135	74.5056	41.7034	2822	53.5	3	AFT	Nachtergaele et al. (2018)
DLH1	97.507	37.431	4054	80.6	3.9	AFT	Pang et al. (2019)
DLH2	97.504	37.439	3930	76.8	4	AFT	Pang et al. (2019)
DLH3	97.504	37.442	3927	84.9	4.2	AFT	Pang et al. (2019)
DLH4	97.498	37.443	3780	87.8	4.1	AFT	Pang et al. (2019)
DLH6	97.474	37.427	3464	17.4	1.1	AFT	Pang et al. (2019)
DLH7	97.474	37.408	3310	19.3	1.1	AFT	Pang et al. (2019)
B315-1	99.75	37.75	4025	93	10	AFT	Qi et al. (2016)
B354-2	99.05	38.1333	4351	93	7	AFT	Qi et al. (2016)
B405-1	99.2667	37.3667	3498	89	9	AFT	Qi et al. (2016)
B412-1	99.2333	37.3833	3495	88	11	AFT	Qi et al. (2016)
B447-1	98.5	37.8167	3918	74	10	AFT	Qi et al. (2016)
B614-1	98.9833	38.05	4242	98	8	AFT	Qi et al. (2016)
B671-2	99.2	38.0333	4164	70	8	AFT	Qi et al. (2016)
B673-2	99.2	38.0333	4168	77	9	AFT	Qi et al. (2016)
B1095-2	99.0167	38.15	4274	98	8	AFT	Qi et al. (2016)
B030-1	99.2167	38.05	4049	50	3	AFT	Qi et al. (2016)
B030-2	99.2167	38.05	4049	69	4	AFT	Qi et al. (2016)
B1217-3	99.2	38.0833	4042	68	4	AFT	Qi et al. (2016)
B385-1	99.1833	38.1	4155	59	4	AFT	Qi et al. (2016)
B386-4	99.1833	38.1	4084	52	3	AFT	Qi et al. (2016)
B387-1	99.1833	38.1	4084	78	5	AFT	Qi et al. (2016)
B039-3	99.2333	38.0667	4019	78	5	AFT	Qi et al. (2016)
B077-1	99.2667	38.0667	4013	66	5	AFT	Qi et al. (2016)
B043-2	99.2333	38.0667	3985	93	6	AFT	Qi et al. (2016)
B044-1	99.25	38.0833	3985	94	7	AFT	Qi et al. (2016)
B048-1	99.2833	38.0833	3954	79	6	AFT	Qi et al. (2016)
B074-1	99.2333	38.0833	4079	72	7	AFT	Qi et al. (2016)
B645-4	99.1667	38.1833	4427	96	9	AFT	Qi et al. (2016)
B362-1	99.2833	38.2833	3939	32	4	AFT	Qi et al. (2016)
B363-1	99.4667	38.3833	3939	13	0	AFT	Qi et al. (2016)
B384-1	99.25	38.3	4155	49	5	AFT	Qi et al. (2016)

Table C.1: continued

Sample	Longitude	Latitude	Elevation	Age (Ma)	Error (Ma)	Method	Reference
B054-1	99.4833	38.6	4018	60	5	AFT	Qi et al. (2016)
P2sf	73.8522	38.1278	3600	11	3	AFT	Schmalholz (2004)
P5sf	73.5633	38.17	3560	10	3	AFT	Schmalholz (2004)
P17sf	73.5313	38.5454	4803	16	3	AFT	Schmalholz (2004)
P15sf	73.6728	38.5116	4177	15	3	AFT	Schmalholz (2004)
Pa4460	73.5362	38.5028	4460	10	1	AFT	Rutte et al. (2017)
96Ak2c	73.5313	38.4970	4594	9	2	AFT	Rutte et al. (2017)
Pa5360	73.513	38.4903	5360	8	1	AFT	Rutte et al. (2017)
0827A1	73.6981	38.4886	4698	11	1	AFT	Rutte et al. (2017)
0826A1	74.0293	38.3762	3828	7.7	0.6	AFT	Rutte et al. (2017)
96M9a	74.038	38.3473	3760	16	2	AFT	Rutte et al. (2017)
9919G4	74.4387	38.3154	4536	11	0.8	AFT	Rutte et al. (2017)
A96M18g	74.0790	38.2895	4371	15	1	AFT	Rutte et al. (2017)
9920B1	74.4865	38.2826	4268	13	1	AFT	Rutte et al. (2017)
0907D1	74.4153	38.2683	4564	8.1	0.4	AFT	Rutte et al. (2017)
A96K1a	73.565	38.52	4803	14	2	AFT	Rutte et al. (2017)
A96S1a	73.6804	38.5122	4550	21	2	AFT	Rutte et al. (2017)
A96S1b	73.6804	38.5122	4550	13	2	AFT	Rutte et al. (2017)
L96A9	74.2471	38.1946	4000	5.7	0.6	AFT	Rutte et al. (2017)
4725C	74.2942	38.1679	3699	14	8	AFT	Rutte et al. (2017)
M96A7	74.4051	38.1573	4141	16.9	0.8	AFT	Rutte et al. (2017)
96A10b	74.4495	38.135	4285	29	3	AFT	Rutte et al. (2017)
4725B1	74.6760	37.8875	3864	10	1	AFT	Rutte et al. (2017)
4724D1	74.8961	37.8428	5158	15	3	AFT	Rutte et al. (2017)
4.724E1	74.8936	37.8405	4906	7.7	0.8	AFT	Rutte et al. (2017)
4724B1	74.8868	37.8362	4580	15	8	AFT	Rutte et al. (2017)
4724K1a	74.8949	37.8344	4778	10	1	AFT	Rutte et al. (2017)
P2-43	73.852	38.128	3600	10.7	1.5	AFT	Schmalholz (2004)
P5-40	73.568	38.17	3550	10.1	1.7	AFT	Schmalholz (2004)
P15-43	73.706	38.507	4365	15.4	1.7	AFT	Schmalholz (2004)
P17-40	73.521	38.546	4560	15.7	1.4	AFT	Schmalholz (2004)
P20-40	73.284	38.802	3950	55.7	4.1	AFT	Schmalholz (2004)
P22-40	73.381	38.932	3950	39.8	2.2	AFT	Schmalholz (2004)

Table C.1: continued

Sample	Longitude	Latitude	Elevation	Age (Ma)	Error (Ma)	Method	Reference
P24-43	73.443	38.935	3950	25.2	2.3	AFT	Schmalholz (2004)
P25-40	73.443	39.19	4230	18.8	1.9	AFT	Schmalholz (2004)
P26-40	73.417	39.2	4100	18	2.1	AFT	Schmalholz (2004)
TS1-59	73.525	40.105	2248	10.9	1.3	AFT	Schmalholz (2004)
BG-1	87.8309	43.7684	1223	31.4	5.7	AFT	Shen et al. (2006)
BG-2	87.7198	43.8013	938	24.2	4.4	AFT	Shen et al. (2006)
BG-3	87.9189	43.6941	1666	43.9	8.2	AFT	Shen et al. (2006)
BG-4	88.3303	44.0549	1087	42.6	5.6	AFT	Shen et al. (2006)
BG-5	88.3496	44.0699	998	28.8	2.8	AFT	Shen et al. (2006)
1	85.6404	43.855	2175	37.1	6.5	AFT	Shen et al. (2008)
2	85.6447	43.8611	2014	9.8	1.3	AFT	Shen et al. (2008)
3	85.6632	43.9007	1548	65.5	4.8	AFT	Shen et al. (2008)
4	86.6644	43.7089	1977	36.2	3.7	AFT	Shen et al. (2008)
5	87.6707	43.4476	1425	68.2	10.6	AFT	Shen et al. (2008)
A3	76.551	37.965	1803	54.8	6.1	AFT	Sobel and Dumitru (1997)
F1	76.306	37.969	1789	18.2	0.9	AFT	Sobel and Dumitru (1997)
F2	76.322	37.969	1732	17.5	1.4	AFT	Sobel and Dumitru (1997)
A2	76.554	37.98	1744	52.3	3.9	AFT	Sobel and Dumitru (1997)
A4	76.548	37.984	1693	42.5	6.1	AFT	Sobel and Dumitru (1997)
A5	76.542	37.991	1747	71.1	8.8	AFT	Sobel and Dumitru (1997)
A6	76.535	37.994	1742	48.6	5.8	AFT	Sobel and Dumitru (1997)
A7	76.529	37.994	1847	59.1	6.4	AFT	Sobel and Dumitru (1997)
A8	76.527	37.994	1832	33	2.8	AFT	Sobel and Dumitru (1997)
A9	76.525	37.994	1812	25	3.7	AFT	Sobel and Dumitru (1997)
A1	76.585	37.994	1869	71.8	12	AFT	Sobel and Dumitru (1997)
U8	75.486	38.981	2003	57	8.1	AFT	Sobel and Dumitru (1997)
U7	75.488	38.981	1995	66	7.5	AFT	Sobel and Dumitru (1997)
U6	75.49	38.982	1970	74.9	9.5	AFT	Sobel and Dumitru (1997)
U5	75.492	38.982	1940	75.4	11	AFT	Sobel and Dumitru (1997)
U4	75.494	38.982	1912	65.7	7.7	AFT	Sobel and Dumitru (1997)
U3	75.496	38.982	1895	93.3	11	AFT	Sobel and Dumitru (1997)
U2	75.498	38.982	1888	71.8	5	AFT	Sobel and Dumitru (1997)
U1	75.5	38.983	1887	82.5	11	AFT	Sobel and Dumitru (1997)

Table C.1: continued

Sample	Longitude	Latitude	Elevation	Age (Ma)	Error (Ma)	Method	Reference
K10	75.863	39.772	1733	18.3	2.3	AFT	Sobel and Dumitru (1997)
W4	75.788	39.793	1836	46	6.2	AFT	Sobel and Dumitru (1997)
K9	75.763	39.775	1863	55.8	11	AFT	Sobel and Dumitru (1997)
K7	75.265	39.78	2344	97.3	11	AFT	Sobel and Dumitru (1997)
K6	75.267	39.784	2385	84.4	16	AFT	Sobel and Dumitru (1997)
K5	75.269	39.787	2457	77.2	8.5	AFT	Sobel and Dumitru (1997)
W1	75.79	39.79	1832	18.4	3.1	AFT	Sobel and Dumitru (1997)
W2	75.79	39.791	1833	24.1	3.2	AFT	Sobel and Dumitru (1997)
W3	75.789	39.792	1880	46.3	5.6	AFT	Sobel and Dumitru (1997)
04TW-01	76.076	39.925	1740	18.9	3.3	AFT	Sobel et al. (2006a)
04TW-02	76.076	39.933	1740	83.5	6.9	AFT	Sobel et al. (2006a)
03-FT1	75.767	40.048	2392	18.1	4.9	AFT	Sobel et al. (2006a)
99WT-4	76.023	40.109	2255	25.7	6.1	AFT	Sobel et al. (2006a)
03-FT3	75.779	40.11	2552	19.8	1.5	AFT	Sobel et al. (2006a)
99WT-11	75.77	40.119	2637	25.8	2.4	AFT	Sobel et al. (2006a)
03-FT4	75.769	40.122	2579	22.7	2	AFT	Sobel et al. (2006a)
99WT-3	76.014	40.128	2325	79	6.6	AFT	Sobel et al. (2006a)
TS170	75.234	42.456	3770	91.1	5.6	AFT	Sobel et al. (2006b)
TS167	75.219	42.471	3160	66.6	3.4	AFT	Sobel et al. (2006b)
TS166	75.216	42.488	2870	17	2	AFT	Sobel et al. (2006b)
TS165	75.217	42.497	2610	6.7	1.8	AFT	Sobel et al. (2006b)
TS161	74.882	42.502	3290	7.6	1.9	AFT	Sobel et al. (2006b)
TS164	75.269	42.512	2250	6.3	0.8	AFT	Sobel et al. (2006b)
TS159	74.874	42.518	2850	6.9	0.6	AFT	Sobel et al. (2006b)
TS158	74.87	42.539	2560	4.7	0.7	AFT	Sobel et al. (2006b)
TS162	74.889	42.557	2350	4.4	0.6	AFT	Sobel et al. (2006b)
TS163	74.903	42.581	2090	5.4	2.8	AFT	Sobel et al. (2006b)
Mav38	74.918	42.632	1840	3.9	0.7	AFT	Sobel et al. (2006b)
99WT-39	75.0161	39.2375	2712	74	15	AFT	Sobel et al. (2013)
99WT-43	75.0514	39.2425	2450	61	12	AFT	Sobel et al. (2013)
_99WT-60	74.7017	39.8497	3080	9.9	1	AFT	Sobel et al. (2013)
P05T-33	74.9805	38.1229	3625	11.5	1.4	AFT	Sobel et al. (2013)
4726A1	73.0796	37.6343	3876	7.3	0.5	AFT	Stübner et al. (2013)

Table C.1: continued

Sample	Longitude	Latitude	Elevation	Age (Ma)	Error (Ma)	Method	Reference
4726C1	72.7499	37.4871	4206	27	1.1	AFT	Stübner et al. (2013)
4726D1	72.7278	37.4764	3955	21.2	2.1	AFT	Stübner et al. (2013)
4726G1	72.3744	37.6983	3174	9	0.4	AFT	Stübner et al. (2013)
4726K1	72.02665	37.7293	2806	5.7	0.7	AFT	Stübner et al. (2013)
4727A1	71.9694	37.7108	2728	4.7	0.3	AFT	Stübner et al. (2013)
4727C1	71.758	37.6163	2483	8.6	0.7	AFT	Stübner et al. (2013)
6821A1	71.8360	36.7768	4260	5.1	0.4	AFT	Stübner et al. (2013)
6822C1	72.1625	36.9017	2869	2	0.2	AFT	Stübner et al. (2013)
6822D1	72.45447	37.005	2809	3	0.2	AFT	Stübner et al. (2013)
682EE4	72.3107	36.97777	2764	2.1	0.2	AFT	Stübner et al. (2013)
6822T1	71.7404	36.6738	2582	4.1	0.4	AFT	Stübner et al. (2013)
6822W1	71.7324	36.6742	2558	2.2	0.2	AFT	Stübner et al. (2013)
6823A3	71.9072	36.7407	2696	3.6	0.3	AFT	Stübner et al. (2013)
6823C1	71.5396	36.8535	2464	3.2	0.3	AFT	Stübner et al. (2013)
6824B4	71.5354	37.0839	4603	6.9	0.4	AFT	Stübner et al. (2013)
6824D1	71.5357	37.0782	4299	4.5	0.3	AFT	Stübner et al. (2013)
6.82E+04	71.5378	37.0766	4096	7.8	1.1	AFT	Stübner et al. (2013)
6824F1	71.5392	37.073	3847	6.3	0.9	AFT	Stübner et al. (2013)
6824H1	71.5407	37.0532	3118	4	0.2	AFT	Stübner et al. (2013)
6825B1	71.4837	37.029	2507	4.8	1	AFT	Stübner et al. (2013)
6826B1	71.4964	37.405	2137	6.1	1.1	AFT	Stübner et al. (2013)
6826D1	71.7174	37.333	2585	6.3	0.4	AFT	Stübner et al. (2013)
6827A1	71.6498	37.3978	2383	9.4	1.2	AFT	Stübner et al. (2013)
6828A1	71.7986	37.1816	3373	9.7	1.2	AFT	Stübner et al. (2013)
6829B1	71.7475	37.1439	4372	8.4	1.1	AFT	Stübner et al. (2013)
6829C1	71.7598	37.1607	4014	8	0.5	AFT	Stübner et al. (2013)
6831A1	72.1201	37.2244	3045	9.2	0.4	AFT	Stübner et al. (2013)
6831C3	72.1894	37.2417	3104	6.4	0.3	AFT	Stübner et al. (2013)
6901A2	72.3672	37.3673	3376	10.1	1.2	AFT	Stübner et al. (2013)
6901B1	72.5625	37.3429	3702	10	0.8	AFT	Stübner et al. (2013)
6901C1	72.5822	37.4089	4060	6	0.4	AFT	Stübner et al. (2013)
6901D1	72.6063	37.4728	4288	15.9	0.8	AFT	Stübner et al. (2013)
6.90E+04	72.6584	37.5572	3716	15.5	0.7	AFT	Stübner et al. (2013)

Table C.1: continued

Sample	Longitude	Latitude	Elevation	Age (Ma)	Error (Ma)	Method	Reference
6902B1	72.392	37.6715	3901	6.6	0.9	AFT	Stübner et al. (2013)
6902G1	72.4041	37.688	3307	4	0.2	AFT	Stübner et al. (2013)
6903B1	72.4524	37.7501	3283	6.6	0.8	AFT	Stübner et al. (2013)
6904G1	71.7893	37.7003	3690	6.3	0.2	AFT	Stübner et al. (2013)
6904M1	71.7451	37.6303	3077	9.3	0.6	AFT	Stübner et al. (2013)
6904P1	71.7448	37.64	3544	9.4	0.5	AFT	Stübner et al. (2013)
6904Q3	71.7497	37.6221	2850	10.4	1.2	AFT	Stübner et al. (2013)
6905A1	71.7536	37.6138	2592	8.6	0.6	AFT	Stübner et al. (2013)
6905B1	71.7536	37.6138	2592	9.8	1.2	AFT	Stübner et al. (2013)
9911A3	72.9419	37.2851	3622	4.6	0.2	AFT	Stübner et al. (2013)
9912B1	73.5483	37.6969	4063	5.1	0.2	AFT	Stübner et al. (2013)
9912C1	73.5405	37.6842	4119	11.1	1.2	AFT	Stübner et al. (2013)
9914D2	73.3159	37.679	4082	6.9	0.4	AFT	Stübner et al. (2013)
9915A2	73.0478	37.6722	3878	10.4	1.4	AFT	Stübner et al. (2013)
9916H1	72.9569	37.8944	4314	38.6	4.3	AFT	Stübner et al. (2013)
9917B1	72.967	37.7672	3743	17.7	2.2	AFT	Stübner et al. (2013)
9918B1	72.9008	37.6971	4417	7.4	0.4	AFT	Stübner et al. (2013)
996A1	71.6864	36.6825	2606	6.6	0.8	AFT	Stübner et al. (2013)
997B1	72.0377	36.8219	2745	2.7	0.3	AFT	Stübner et al. (2013)
998C1	72.252	37.045	4560	4.8	0.6	AFT	Stübner et al. (2013)
999B5	72.2594	36.9744	3183	2.8	0.4	AFT	Stübner et al. (2013)
X16	87.6364	43.655	1076	85.6	10.1	AFT	Tang et al. (2015)
P05-T13	74.7464	38.9212	3720	5.3	0.6	AFT	Thiede et al. (2013)
P05-T14	74.7455	38.9164	3630	4.4	0.4	AFT	Thiede et al. (2013)
P05-T17	74.7868	38.9259	3980	3.4	0.5	AFT	Thiede et al. (2013)
P05-T21	74.7808	38.9208	4230	2.9	0.7	AFT	Thiede et al. (2013)
P05-T23	74.7849	38.9153	3810	2.5	0.5	AFT	Thiede et al. (2013)
P05-T31	75.0342	38.2933	4640	1.7	0.3	AFT	Thiede et al. (2013)
P05-T32	75.0506	38.2885	5380	3.9	0.7	AFT	Thiede et al. (2013)
P05-T37	75.257	38.094	3765	6.1	1	AFT	Thiede et al. (2013)
P05-T39	75.2365	38.0816	3580	5.4	0.8	AFT	Thiede et al. (2013)
P05-T41	75.2305	38.0763	3510	5	0.6	AFT	Thiede et al. (2013)
P05-T63	75.2123	38.3746	3987	1.7	0.2	AFT	Thiede et al. (2013)

Table C.1: continued

Sample	Longitude	Latitude	Elevation	Age (Ma)	Error (Ma)	Method	Reference
P05-T65	75.0081	38.5604	3660	5.9	0.9	AFT	Thiede et al. (2013)
P05-T65	75.0081	38.5604	3380	5.8	0.6	AFT	Thiede et al. (2013)
P05-T72	75.061	38.7159	4862	1.6	0.5	AFT	Thiede et al. (2013)
P05-T75	75.0466	38.7226	3600	2.3	0.6	AFT	Thiede et al. (2013)
P05-T77	75.1972	38.7712	2790	1.1	0.2	AFT	Thiede et al. (2013)
Pk05-16	75.0784	35.0826	3432	14.6	1.1	AFT	van Der Beek et al. (2009)
Pk05-17	75.1555	35.0241	3689	21.6	1.6	AFT	van Der Beek et al. (2009)
Pk05-20	75.4216	35.0165	3961	20.7	1.2	AFT	van Der Beek et al. (2009)
Pk05-28	75.5913	35.1205	3501	27	3.5	AFT	van Der Beek et al. (2009)
Pk05-29	75.6051	35.1411	3291	23.6	2.4	AFT	van Der Beek et al. (2009)
Pk05-30	75.6111	35.1538	3128	21.2	2.4	AFT	van Der Beek et al. (2009)
Pk05-31	75.6413	35.2521	2594	22.6	2.8	AFT	van Der Beek et al. (2009)
Pk06-51	75.7931	35.1181	3481	19	2.3	AFT	van Der Beek et al. (2009)
Pk06-54	75.9409	35.1292	2534	15.4	1.5	AFT	van Der Beek et al. (2009)
Pk05-16	75.0784	35.0826	3432	10.9	1	AHe	van Der Beek et al. (2009)
PK06-36	75.6194	35.1742	2960	15.1	0.7	AHe	van Der Beek et al. (2009)
Pk06-50	75.7533	35.0914	3991	14.9	0.6	AHe	van Der Beek et al. (2009)
K1L-23/24	80.2083	34.5023	5158	17.2	0.6	AHe	van Der Beek et al. (2009)
KP01	90.785	35.429	5200	28.6	2.8	AFT	Wang et al. (2008)
KL-2	93.97	35.55	4694	72.7	9.8	AFT	Wang et al. (2008)
KL-4	93.97	35.55	4711	70.3	7.3	AFT	Wang et al. (2008)
KL-1	93.97	35.55	4690	61.5	12.4	AFT	Wang et al. (2008)
KCH19	83.273	42.283	1922	37	3	AFT	Wang et al. (2009)
KCH18	83.269	42.289	1912	35	2	AFT	Wang et al. (2009)
KCH20	83.276	42.289	1979	49	3	AFT	Wang et al. (2009)
KCH15	83.27	42.295	1949	61	4	AFT	Wang et al. (2009)
KCH16	83.27	42.295	1952	54	3	AFT	Wang et al. (2009)
KCH22	83.325	42.297	2226	43	4	AFT	Wang et al. (2009)
KCH17	83.262	42.3	1958	36	2	AFT	Wang et al. (2009)
BLT11	86.273	42.649	1588	59	3	AFT	Wang et al. (2009)
BLT12	86.312	42.66	1717	74	4	AFT	Wang et al. (2009)
BLT10	86.28	42.666	1649	59	4	AFT	Wang et al. (2009)

Table C.1: continued

Sample	Longitude	Latitude	Elevation	Age (Ma)	Error (Ma)	Method	Reference
BLT13	86.328	42.666	1855	63	4	AFT	Wang et al. (2009)
BLT14	86.368	42.693	1877	67	4	AFT	Wang et al. (2009)
BLT9	86.273	42.696	1715	57	8	AFT	Wang et al. (2009)
BLT8	86.295	42.716	1710	60	4	AFT	Wang et al. (2009)
BLT7	86.307	42.734	1824	49	3	AFT	Wang et al. (2009)
BLT5	86.307	42.75	1803	49	3	AFT	Wang et al. (2009)
BLT6	86.307	42.756	1858	22	3	AFT	Wang et al. (2009)
HXG4	86.681	42.938	2675	76	4	AFT	Wang et al. (2009)
HXG3	86.709	42.994	2926	75	4	AFT	Wang et al. (2009)
QM49	84.131	42.999	2479	11	1	AFT	Wang et al. (2009)
	84.127	43.003	2454	10	4	AFT	Wang et al. (2009)
	84.145	43.014	2461	10	2	AFT	Wang et al. (2009)
	84.178	43.02	2519	13	0	AFT	Wang et al. (2009)
BY29	84.178	43.02	2517	89	5	AFT	Wang et al. (2009)
BY28	84.176	43.021	2514	72	4	AFT	Wang et al. (2009)
BY27	84.175	43.021	2512	70	4	AFT	Wang et al. (2009)
BY25	84.122	43.029	2493	94	5	AFT	Wang et al. (2009)
HXG2	86.769	43.033	3580	84	5	AFT	Wang et al. (2009)
HXG1	86.779	43.035	3443	82	4	AFT	Wang et al. (2009)
BY31	84.168	43.085	2724	98	7	AFT	Wang et al. (2009)
QM44	84.403	43.688	2867	77	5	AFT	Wang et al. (2009)
QM45	84.421	43.691	2953	72	5	AFT	Wang et al. (2009)
QM47	84.441	43.718	3246	62	8	AFT	Wang et al. (2009)
QM48	84.429	43.727	3474	25	2	AFT	Wang et al. (2009)
QM49	84.419	43.743	3341	11	1	AFT	Wang et al. (2009)
QM50	84.443	43.758	3205	16	1	AFT	Wang et al. (2009)
	77.8589	37.0635	2640	6.8	0.6	AFT	Wang (2015)
	77.8585	37.0651	2631	8.6	0.7	AFT	Wang (2015)
	77.857	37.0759	2798	11.3	1	AFT	Wang (2015)
	77.8398	37.1068	2576	11.5	0.8	AFT	Wang (2015)
	77.8399	37.1178	2530	16.4	1.2	AFT	Wang (2015)
	77.8389	37.1206	2514	12.6	0.8	AFT	Wang (2015)
	77.8331	37.1359	2504	14.3	1.1	AFT	Wang (2015)

Table C.1: continued

Sample	Longitude	Latitude	Elevation	Age (Ma)	Error (Ma)	Method	Reference
	77.8084	37.152	2430	12.4	1	AFT	Wang (2015)
	77.7656	37.1685	2400	15	1.2	AFT	Wang (2015)
	80.0763	36.1567	3864	9.3	1.4	AFT	Wang (2015)
	80.0742	36.1578	4187	4.8	1.6	AFT	Wang (2015)
C14JH33	82.4267	44.2033	1125	96.4	3.9	AFT	Wang et al. (2018)
C13YN92	81.5219	44.2181	1603	98.5	4.4	AFT	Wang et al. (2018)
C14KK10	81.7211	42.7983	2573	98.5	3.3	AFT	Wang et al. (2018)
C14KK21	81.9303	42.8106	2494	76.8	5.5	AFT	Wang et al. (2018)
C14KK42	81.8994	42.7056	1439	99.8	13.2	AFT	Wang et al. (2018)
C13ZS42	81.1017	42.6675	1965	90.9	4.4	AFT	Wang et al. (2018)
C13ZS46	81.1039	42.6589	1971	87.6	3	AFT	Wang et al. (2018)
WC100110-1A	98.11	35.8	3391	44	3	AFT	Wu et al. (2019)
WC100110-1B	98.27	35.83	3654	42	4	AFT	Wu et al. (2019)
WC100110-5A	98.1	35.9	3268	57	4	AFT	Wu et al. (2019)
WC100210-2C	98.45	35.64	3900	37	4	AFT	Wu et al. (2019)
WC100110-4B	98.55	35.43	3179	58	3	AFT	Wu et al. (2019)
WC100210-2B	97.95	35.6	3755	34	2	AFT	Wu et al. (2019)
WC051511-1B	91.47	37.39	3630	16	1	AFT	Wu et al. (2019)
WC051411-4A	91.67	37.47	3492	17	1	AFT	Wu et al. (2019)
WC051411-4B	91.23	37.43	3972	17	1	AFT	Wu et al. (2019)
WC051511-2B	91.76	37.57	3071	22	1	AFT	Wu et al. (2019)
WC051511-2A	91.69	37.67	3270	42	4	AFT	Wu et al. (2019)

Table C.1: continued

Sample	Longitude	Latitude	Elevation	Age (Ma)	Error (Ma)	Method	Reference
	87.9367	41.2244		92	6	AFT	Xiao et al. (2011)
	88.3067	40.8953		88	6	AFT	Xiao et al. (2011)
	88.3067	40.8953		100	16	AFT	Xiao et al. (2011)
	88.5403	40.7439		79	5	AFT	Xiao et al. (2011)
	88.5403	40.7439		84	5	AFT	Xiao et al. (2011)
	88.9919	40.7447		73	6	AFT	Xiao et al. (2011)
	89.4181	40.7922		100	6	AFT	Xiao et al. (2011)
XT73	98.322	36.401	3266	77	14	AFT	Yuan et al. (2006)
XT72	98.113	36.185	3244	114	14	AFT	Yuan et al. (2006)
XT70	98.142	36.142	3369	57	3	AFT	Yuan et al. (2006)
XT69	98.128	36.08	3473	93	6	AFT	Yuan et al. (2006)
XT68	98.065	36.039	3314	103	8	AFT	Yuan et al. (2006)
XT66	97.991	36.023	3175	130	10	AFT	Yuan et al. (2006)
XT63	97.96	36.003	3267	107	8	AFT	Yuan et al. (2006)
XT64	97.982	35.97	3140	78	5	AFT	Yuan et al. (2006)
XT4	98.01	35.944	3224	43	6	AFT	Yuan et al. (2006)
XT4-1	98.01	35.944	3224	57	5	AFT	Yuan et al. (2006)
XT5	98.051	35.913	3180	66	6	AFT	Yuan et al. (2006)
XT7	98.101	35.898	3236	47	5	AFT	Yuan et al. (2006)
XT59	98.13	35.884	3335	53	3	AFT	Yuan et al. (2006)
XT60	98.152	35.865	3330	45	8	AFT	Yuan et al. (2006)
XT10-2	98.159	35.845	3346	51	4	AFT	Yuan et al. (2006)
XT11	98.147	35.812	3369	56	4	AFT	Yuan et al. (2006)
XT58-2	98.144	35.781	3391	66	4	AFT	Yuan et al. (2006)
XT12	98.132	35.743	3385	56	5	AFT	Yuan et al. (2006)
XT13	98.109	35.726	3429	31	3	AFT	Yuan et al. (2006)
XT14	98.702	35.702	3448	34	3	AFT	Yuan et al. (2006)
XT15	98.07	35.69	3467	28	3	AFT	Yuan et al. (2006)
XT20	98.085	35.6666	3450	30	2	AFT	Yuan et al. (2006)
UC01	74.4128	39.9156	2578	18.5	5.2	AFT	Yang et al. (2014)
UC02	74.4067	39.9125	2572	16.6	2.8	AFT	Yang et al. (2014)
UC04	74.3589	39.8664	2486	87.4	42.3	AFT	Yang et al. (2014)
UC05	74.3439	39.8597	2508	69.3	3.5	AFT	Yang et al. (2014)

Table C.1: continued

Sample	Longitude	Latitude	Elevation	Age (Ma)	Error (Ma)	Method	Reference
UC07	74.3167	39.8089	2525	72.1	4.3	AFT	Yang et al. (2014)
UC08	74.1728	39.7725	2603	72.4	4.2	AFT	Yang et al. (2014)
KA02	74.8447	39.8039	2820	76.5	3.7	AFT	Yang et al. (2014)
ZKS01	74.9567	39.7797	2538	95	4.1	AFT	Yang et al. (2014)
Mi-1	74.5469	39.8506	2825	48.3	2.9	AFT	Yang et al. (2014)
Ni-2	74.5403	39.8461	2846	40.6	5.3	AFT	Yang et al. (2014)
Mi-3	74.5628	39.8456	2806	39.9	2.6	AFT	Yang et al. (2014)
Mi-4	74.5578	39.8431	2804	47.1	7.8	AFT	Yang et al. (2014)
Mi-5	74.5456	39.8397	2803	42.6	3.2	AFT	Yang et al. (2014)
Mi-6	74.5472	39.8356	2772	37.2	2.4	AFT	Yang et al. (2014)
Mi-7	74.555	39.8328	2765	45.6	3	AFT	Yang et al. (2014)
Mi-8	74.5522	39.8269	2735	53.5	5.3	AFT	Yang et al. (2014)
NJ11-001	81.5102	42.0594	1824	30.1	5.3	AFT	Yang et al. (2017)
NJ11-007	81.5208	42.0425	1775	13.7	1.7	AFT	Yang et al. (2017)
NJ11-008	81.5298	42.0316	1756	14.2	1.8	AFT	Yang et al. (2017)
NJ11-009	81.5313	42.0226	1744	11.9	2	AFT	Yang et al. (2017)
NJ11-010	81.5372	42.0126	1741	24.9	2.3	AFT	Yang et al. (2017)
NJ11-011	81.538	41.9999	1715	74.2	10.1	AFT	Yang et al. (2017)
NJ11-012	81.5393	41.9924	1711	76.7	7.9	AFT	Yang et al. (2017)
NJ11-013	81.5353	41.9723	1667	98.4	23.1	AFT	Yang et al. (2017)
NJ11-015	81.5469	41.9701	1679	67.7	4.9	AFT	Yang et al. (2017)
NJ11-016	81.5463	41.9607	1670	59.6	9.7	AFT	Yang et al. (2017)
NJ11-018	81.5494	41.0318	1636	46.2	4.6	AFT	Yang et al. (2017)
14DK02	84.4167	43.7333	3248	11.5	5.2	AHe	Yin et al. (2018)
14DK03	84.45	43.7667	2784	8.2	1.5	AHe	Yin et al. (2018)
C14NL23	84.5172	43.2669	1883	34.4	0.8	AHe	Yin et al. (2018)
TS1303/04	87.04	43.1161	2563	26.1	4.7	AHe	Yin et al. (2018)
SC03-04	85.6658	43.9031	1503	85.4	5.7	AFT	Zhang et al. (2007a)
SC03-10	85.6608	43.9044	1428	87.8	5.9	AFT	Zhang et al. (2007a)
SC04-07	85.6589	43.9156	1428	81.3	4.7	AFT	Zhang et al. (2007a)
SC06-03	85.7336	43.9303	1350	44	5.4	AFT	Zhang et al. (2007a)
MN09-04	85.8597	43.9089	1120	11.8	1.1	AFT	Zhang et al. (2007a)
MN10-03	85.8725	43.9092	1115	22.5	3.2	AFT	Zhang et al. (2007a)

Table C.1: continued

Sample	Longitude	Latitude	Elevation	Age (Ma)	Error (Ma)	Method	Reference
WS01-06	84.3514	44.1592	1560	87.2	6.5	AFT	Zhang et al. (2007a)
WS02-17	84.3342	44.1739	1420	78.4	7.6	AFT	Zhang et al. (2007a)
A-1	79.9893	41.1326	1147	62.5	5.6	AFT	Zhang et al. (2009)
A-3	80.0038	41.1411	1148	81.4	7.4	AFT	Zhang et al. (2009)
A-4	80.0171	41.1495	1157	74.8	7.8	AFT	Zhang et al. (2009)
A-5	80.0171	41.1495	1157	69	6	AFT	Zhang et al. (2009)
A-6	80.0303	41.1564	1144	90	8.2	AFT	Zhang et al. (2009)
F20	88.4997	40.8642	908	148.8	9.2	AFT	Zhang et al. (2011)
F22	88.5833	41.0153	1062	139.2	8.9	AFT	Zhang et al. (2011)
F23	88.4844	41.2181	1307	166	10.3	AFT	Zhang et al. (2011)
F25	88.2908	41.2917	1503	123.9	7.9	AFT	Zhang et al. (2011)
F26	88.0719	41.3436	1678	99.6	6.6	AFT	Zhang et al. (2011)
F28	88.1653	41.3736	1800	110.9	7.2	AFT	Zhang et al. (2011)
F29	88.0847	41.3553	1700	117.2	7.6	AFT	Zhang et al. (2011)
K4	86.2242	41.7867	1131	107.6	8.2	AFT	Zhang et al. (2011)
K5	86.2297	41.7964	1167	85.6	6	AFT	Zhang et al. (2011)
K6	86.2356	41.8036	1198	93	6.4	AFT	Zhang et al. (2011)
K7	86.2419	41.8075	1229	90.1	6.5	AFT	Zhang et al. (2011)
K8	86.2419	41.8075	1229	91.4	6.8	AFT	Zhang et al. (2011)
T2	86.1861	41.79	965	83.2	5.9	AFT	Zhang et al. (2011)
T4	86.1892	41.8167	990	82.1	5.4	AFT	Zhang et al. (2011)
F14	88.5189	40.8	968	95	12	AFT	Zhang et al. (2016)
K3	86.2242	41.7867	1131	85	5	AFT	Zhang et al. (2016)
K9	86.2419	41.8075	1229	72	4	AFT	Zhang et al. (2016)
K11	86.2781	41.8156	1209	72	3	AFT	Zhang et al. (2016)
T1	86.1758	41.7886	1005	84	11	AFT	Zhang et al. (2016)
T3	86.1922	41.8092	992	100	16	AFT	Zhang et al. (2016)
T6	86.1967	41.8222	1017	96	5	AFT	Zhang et al. (2016)
T7	86.1994	41.8211	1028	77	3	AFT	Zhang et al. (2016)
T8	86.2031	41.8206	1039	85	6	AFT	Zhang et al. (2016)
T9	86.2031	41.8206	1039	75	4	AFT	Zhang et al. (2016)
A33	79.9919	40.9894	1294	53	6	AFT	Zhang et al. (2016)
A34	79.9917	40.9872	1272	42	5	AFT	Zhang et al. (2016)

Table C.1: continued

Sample	Longitude	Latitude	Elevation	Age (Ma)	Error (Ma)	Method	Reference
A1	79.9893	41.1326	1147	62.5	5.6	AFT	Zhang et al. (2016)
A3	80.0038	41.1411	1148	81.4	7.4	AFT	Zhang et al. (2016)
A4	80.0171	41.1495	1157	74.8	7.8	AFT	Zhang et al. (2016)
A5	80.0171	41.1495	1157	69	6	AFT	Zhang et al. (2016)
A6	80.0302	41.1564	1144	90	8.2	AFT	Zhang et al. (2016)
TS1307	86.9688	43.0708	3419	59.1	2.5	AFT	Zhang et al. (2020)
TS1308	86.9016	43.1216	3291	53.4	5.5	AFT	Zhang et al. (2020)
TS1309	86.8392	43.1014	3715	65.8	3	AFT	Zhang et al. (2020)
TS1314	86.7142	43.13	3828	56.2	2.9	AFT	Zhang et al. (2020)
TS1316	86.2647	42.6108	1556	46.6	5	AFT	Zhang et al. (2020)
TS1329	85.5309	43.2214	3775	41.3	1	AHe	Zhang et al. (2020)
TS1332	85.5617	43.2492	3611	46.4	2	AHe	Zhang et al. (2020)
TS1384	85.0478	43.3319	3580	40.2	0.9	AHe	Zhang et al. (2020)
05FT-04	98.694	39.307	2840	40	6	AHe	Zheng et al. (2010)
05FT-06	98.698	39.318	2750	21	3.5	AHe	Zheng et al. (2010)
05FT-07	98.702	39.324	2636	9.5	0.25	AHe	Zheng et al. (2010)
05FT-09	98.723	39.341	2403	9	0.85	AHe	Zheng et al. (2010)
05FT-10	98.715	39.36	2260	7.9	1.25	AHe	Zheng et al. (2010)
05FT-11	98.726	39.373	2080	7.8	1.2	AHe	Zheng et al. (2010)
05FT-12	98.741	39.388	1970	7.2	0.3	AHe	Zheng et al. (2010)
04-Y-33	97.63	39.38	3930	33.1	3.7	AFT	Zheng et al. (2017)
04-Y-34-1	97.69	39.5	3228	17.6	4.5	AFT	Zheng et al. (2017)
04-Y-37	97.69	39.7	2564	98.2	12	AFT	Zheng et al. (2017)
04-Y-39	97.68	39.69	2590	71.1	9.6	AFT	Zheng et al. (2017)
04-Y-40	97.69	39.7	2491	75.2	8.6	AFT	Zheng et al. (2017)
04-Y-41	97.691	39.7	2478	51.3	6.1	AFT	Zheng et al. (2017)
04-Y-44	97.7	39.71	2451	58	7.1	AFT	Zheng et al. (2017)
F5(1428)	87.9519	41.2481	1428	98.5	9.2	AFT	Zhu et al. (2007)
F7(1386)	87.9489	41.205	1386	76.2	7.4	AFT	Zhu et al. (2007)
F9(1478)	87.9731	41.2622	1478	70.7	7.4	AFT	Zhu et al. (2007)
F10(1505)	88.0139	41.2644	1505	67.6	6.7	AFT	Zhu et al. (2007)
F11	88.3944	41.2825	1466	146	13.4	AFT	Zhu et al. (2009)
F10	88.0139	41.2644	1505	67.6	6.7	AFT	Zhu et al. (2009)

Table C.1: continued

Sample	Longitude	Latitude	Elevation	Age (Ma)	Error (Ma)	Method	Reference
F9	87.9731	41.2622	1478	70.7	7.4	AFT	Zhu et al. (2009)
F3	87.6906	41.2608	1575	109.4	10.6	AFT	Zhu et al. (2009)
F2	87.6883	41.2569	1558	109.5	11.2	AFT	Zhu et al. (2009)
F4	87.9606	41.2525	1444	106.3	10.2	AFT	Zhu et al. (2009)
F5	87.9519	41.2481	1428	98.5	9.2	AFT	Zhu et al. (2009)
F8	87.9411	41.2333	1430	110.7	10.4	AFT	Zhu et al. (2009)
F7	87.9489	41.205	1386	76.2	7.4	AFT	Zhu et al. (2009)

Bibliography

Abdrakhmatov, K. Y., Aldazhanov, S. A., Hager, B. H., Hamburger, M. W., Herring, T. A., Kalabaev, K. B., Makarov, V. I., Molnar, P., Panasyuk, S. V., Prilepin, M. T., Reilinger, R. E., Sadybakasov, I. S., Souter, B. J., Trapeznikov, Y. A., Tsurkov, V. Y., and Zubovich, A. V. (1996). Relatively recent construction of the Tien Shan inferred from GPS measurements of present-day crustal deformation rates. *Nature*, 384(6608):450–453.

Abels, H. A., Dupont-Nivet, G., Xiao, G., Bosboom, R., and Krijgsman, W. (2011). Stepwise change of asian interior climate preceding the eocene–oligocene transition (eot). *Palaeogeography, Palaeoclimatology, Palaeoecology*, 299(3-4):399–412.

Ainscoe, E. A., Elliott, J. R., Copley, A., Craig, T. J., Li, T., Parsons, B. E., and Walker, R. T. (2017). Blind Thrusting, Surface Folding, and the Development of Geological Structure in the Mw 6.3 2015 Pishan (China) Earthquake. *Journal of Geophysical Research: Solid Earth*, 122(11):9359–9382.

Aitken, A. R. (2011). Did the growth of tibetan topography control the locus and evolution of tien shan mountain building? *Geology*, 39(5):459–462.

Allen, M., Windley, B., and Zhang, C. (1993). Palaeozoic collisional tectonics and magmatism of the chinese tien shan, central asia. *Tectonophysics*, 220(1-4):89–115.

Allen, M. B., Vincent, S. J., and Wheeler, P. J. (1999). Late Cenozoic tectonics of the Kepingtage thrust zone: Interactions of the Tien Shan and Tarim Basin, northwest China. *Tectonics*, 18(4):639–654.

Allen, M. B., Windley, B. F., Zhang, C., Zhao, Z., and Wang, G. (1991). Basin evolution within and adjacent to the Tien Shan range, NW China. *Journal of the Geological Society*, 148(2):369–378.

Amelung, F., Galloway, D. L., Bell, J. W., Zebker, H. A., and Laczniak, R. J. (1999). Sensing the ups and downs of Las Vegas: InSAR reveals structural control of land subsidence and aquifer-system deformation. *Geology*, 27(6):483–486.

Amidon, W. H. and Hynek, S. A. (2010). Exhumational history of the north central pamir. *Tectonics*, 29(5).

An, K., Lin, X., Wu, L., Yang, R., Chen, H., Cheng, X., Xia, Q., Zhang, F., Ding, W., Gao, S., et al. (2020). An immediate response to the indian-eurasian collision along the northeastern tibetan plateau: Evidence from apatite fission track analysis in the kuantan shan-hei shan. *Tectonophysics*, 774:228278.

Ansari, H., De Zan, F., and Parizzi, A. (2021). Study of Systematic Bias in Measuring Surface Deformation with SAR Interferometry. *IEEE Transactions on Geoscience and Remote Sensing*, 59(2):1285–1301.

Argand, E. (1922). La tectonique de l'asie. conférence faite á bruxelles, le 10 août 1922. In *Congrès géologique international (XIIIe session)-Belgique 1922*, pages 171–372.

ARMSTRONG, F. C. and ORIEL, S. S. (1965). TECTONIC DEVELOPMENT OF IDAHO-WYOMING THRUST BELT1. *AAPG Bulletin*, 49(11):1847–1866.

Arnaud, N., Brunel, M., Cantagrel, J., and Tapponnier, P. (1993). High cooling and denudation rates at kongur shan, eastern pamir (xinjiang, china) revealed by 40ar/39ar alkali feldspar thermochronology. *Tectonics*, 12(6):1335–1346.

Avouac, J. P., Tapponnier, P., Bai, M., You, H., and Wang, G. (1993a). Active Thrusting and Folding Along the Northern Tien Shan and Late Cenozoic Rotation of the Tarim Relative to Dzungaria and Kazakhstan. *Journal of Geophysical Research*, 98(B4):6755–6804.

Avouac, J.-P., Tapponnier, P., Bai, M., You, H., and Wang, G. (1993b). Active thrusting and folding along the northern tien shan and late cenozoic rotation of the tarim relative to dzungaria and kazakhstan. *Journal of Geophysical Research: Solid Earth*, 98(B4):6755–6804.

Bande, A., Sobel, E. R., Mikolaichuk, A., and Acosta, V. T. (2017a). Talas–fergana fault cenozoic timing of deformation and its relation to pamir indentation.

Bande, A., Sobel, E. R., Mikolaichuk, A., Schmidt, A., and Stockli, D. F. (2017b). Exhumation history of the western kyrgyz tien shan: Implications for intramontane basin formation. *Tectonics*, 36(1):163–180.

Bayasgalan, A., Jackson, J., and McKenzie, D. (2005). Lithosphere rheology and active tectonics in mongolia: relations between earthquake source parameters, gravity and gps measurements. *Geophysical Journal International*, 163(3):1151–1179.

Bazhenov, M. and Mikolaichuk, A. (2004). Structural evolution of central asia to the north of tibet: A synthesis of paleomagnetic and geological data. *Geotectonics*, 38(5):379–393.

Beckers, J. and Lay, T. (1995). Very broadband seismic analysis of the 1992 Flores, Indonesia, earthquake (M_w = 7.9). *Journal of Geophysical Research: Solid Earth*, 100(B9):18,179–18,193.

Béjar-Pizarro, M., Socquet, A., Armijo, R., Carrizo, D., Genrich, J., and Simons, M. (2013). Andean structural control on interseismic coupling in the north chile subduction zone. *Nature Geoscience*, 6(6):462–467.

Berardino, P., Fornaro, G., Lanari, R., and Sansosti, E. (2002). A new algorithm for surface deformation monitoring based on small baseline differential SAR interferograms. *IEEE Transactions on Geoscience and Remote Sensing*, 40(11):2375–2383.

Bergman, E. A., Benz, H. M., Yeck, W. L., Karasözen, E., Engdahl, E. R., Ghods, A., Hayes, G. P., and Earle, P. S. (2022). A Global Catalog of Calibrated Earthquake Locations. *Seismological Research Letters*, 94(1):485–495.

Bie, L., Ryder, I., Nippress, S. E. J., and Bürgmann, R. (2014). Coseismic and post-seismic activity associated with the 2008 M_w 6.3 Damxung earthquake, Tibet, constrained by InSAR. *Geophysical Journal International*, 196(2):788–803.

Biggs, J., Burgmann, R., Freymueller, J. T., Lu, Z., Parsons, B., Ryder, I., Schmalzle, G., and Wright, T. (2009). The postseismic response to the 2002 m 7.9 denali fault earthquake: Constraints from insar 2003–2005. *Geophysical Journal International*, 176(2):353–367.

Biggs, J., Wright, T., Lu, Z., and Parsons, B. (2007). Multi-interferogram method for measuring interseismic deformation: Denali fault, alaska. *Geophysical Journal International*, 170(3):1165–1179.

Bosboom, R. E., Abels, H. A., Hoorn, C., van den Berg, B. C., Guo, Z., and Dupont-Nivet, G. (2014). Aridification in continental asia after the middle eocene climatic optimum (meco). *Earth and Planetary Science Letters*, 389:34–42.

Braun, J., Beek, P. v. d., and Batt, G. (2006). *Introduction*, page 1–18. Cambridge University Press.

Bro, R. and De Jong, S. (1997). A fast non-negativity-constrained least squares algorithm. *Journal of Chemometrics*, 11(5):393–401.

Bullen, M., Burbank, D., and Garver, J. (2003). Building the northern tien shan: Integrated thermal, structural, and topographic constraints. *The Journal of Geology*, 111(2):149–165.

Burbank, McLean, Bullen, and Abdrakhmatov (1999). Partitioning of intermontane basins by thrust-related folding, tien shan, kyrgyzstan. *Basin Research*, 11(1):75–92.

Burchfiel, B. C., Brown, E. T., Qidong, D., Xianyue, F., Jun, L., Molnar, P., Jianbang, S., Zhangming, W., and Huichuan, Y. (1999). Crustal shortening on the margins of the tien shan, Xinjiang, China. *International Geology Review*, 41(8):665–700.

Bürgmann, R., Ergintav, S., Segall, P., Hearn, E. H., McClusky, S., Reilinger, R. E., Woith, H., and Zschau, J. (2002). Time-dependent distributed afterslip on and deep below the izmit earthquake rupture. *Bulletin of the Seismological Society of America*, 92(1):126–137.

Bürgmann, R., Fielding, E., and Sukhatme, J. (1998). Slip along the hayward fault, california, estimated from space-based synthetic aperture radar interferometry. *Geology*, 26(6):559–562.

Bürgmann, R., Rosen, P. A., and Fielding, E. J. (2000). Synthetic aperture radar interferometry to measure earth's surface topography and its deformation. *Annual review of earth and planetary sciences*, 28(1):169–209.

Bürgmann, R., Schmidt, D., Nadeau, R. M., d'Alessio, M., Fielding, E., Manaker, D., McEvilly, T. V., and Murray, M. H. (2000). Earthquake Potential Along the Northern Hayward Fault, California. *Science*, 289(5482):1178–1182.

Burtman, V. (1975). Structural geology of variscan tien shan, ussr. *Am. J. Sci*, 275:157–186.

Burtman, V. S., Skobelev, S. F., and Molnar, P. (1996). Late cenozoic slip on the talas-ferghana fault, the tien shan, central asia. *Geological Society of America Bulletin*, 108(8):1004–1021.

Buslov, M., Klerkx, J., Abdrakhmatov, K., Delvaux, D., Batalev, V. Y., Kuchai, O., Dehandschutter, B., and Muraliev, A. (2003). Recent strike-slip deformation of the northern tien shan. *Geological Society, London, Special Publications*, 210(1):53–64.

Campbell, G., Walker, R., Abdrakhmatov, K., Schwenninger, J., Jackson, J., Elliott, J., and Copley, A. (2013). The dzhungarian fault: Late quaternary tectonics and slip rate of a major right-lateral strike-slip fault in the northern tien shan region. *Journal of Geophysical Research: Solid Earth*, 118(10):5681–5698.

Cao, K., Wang, G.-C., van der Beek, P., Bernet, M., and Zhang, K.-X. (2013). Cenozoic thermo-tectonic evolution of the northeastern pamir revealed by zircon and apatite fission-track thermochronology. *Tectonophysics*, 589:17–32.

Carroll, A., Graham, S., Hendrix, M., Ying, D., and Zhou, D. (1995). Late paleozoic tectonic amalgamation of northwestern china: sedimentary record of the northern tarim, northwestern turpan, and southern junggar basins. *Geological Society of America Bulletin*, 107(5):571–594.

Casu, F., Manzo, M., and Lanari, R. (2006). A quantitative assessment of the sbas algorithm performance for surface deformation retrieval from dinsar data. *Remote Sensing of Environment*, 102(3-4):195–210.

Caves, J. K., Moragne, D. Y., Ibarra, D. E., Bayshashov, B. U., Gao, Y., Jones, M. M., Zhamangara, A., Arzhannikova, A. V., Arzhannikov, S. G., and Chamberlain, C. P. (2016). The neogene de-greening of central asia. *Geology*, 44(11):887–890.

Caves, J. K., Winnick, M. J., Graham, S. A., Sjostrom, D. J., Mulch, A., and Chamberlain, C. P. (2015). Role of the westerlies in central asia climate over the cenozoic. *Earth and Planetary Science Letters*, 428:33–43.

Chaabane, F., Avallone, A., Tupin, F., Briole, P., and Maître, H. (2007). A multitemporal method for correction of tropospheric effects in differential SAR interferometry: Application to the gulf of corinth earthquake. *IEEE Transactions on Geoscience and Remote Sensing*, 45(6):1605–1615.

Chang, J., Glorie, S., Qiu, N., Min, K., Xiao, Y., and Xu, W. (2021). Late miocene (10.0 6.0 ma) rapid exhumation of the chinese south tianshan: Implications for the timing of aridification in the tarim basin. *Geophysical Research Letters*, 48(3):e2020GL090623.

Charreau, J., Chen, Y., Gilder, S., Barrier, L., Dominguez, S., Augier, R., Sen, S., Avouac, J. P., Gallaud, A., Graveleau, F., and Wang, Q. (2009). Neogene uplift of the Tian Shan Mountains observed in the magnetic record of the Jingou River section (northwest China). *Tectonics*, 28(2).

Charreau, J., Chen, Y., Gilder, S., Dominguez, S., Avouac, J.-P., Sen, S., Sun, D., Li, Y., and Wang, W.-M. (2005). Magnetostratigraphy and rock magnetism of the neogene kuitun he section (northwest china): implications for late cenozoic uplift of the tianshan mountains. *Earth and Planetary Science Letters*, 230(1-2):177–192.

Charreau, J., Saint-Carlier, D., Dominguez, S., Lavé, J., Blard, P.-H., Avouac, J.-P., Jolivet, M., Chen, Y., Wang, S., Brown, N. D., et al. (2017). Denudation outpaced by crustal thickening in the eastern tianshan. *Earth and Planetary Science Letters*, 479:179–191.

Charreau, J., Saint-Carlier, D., Lavé, J., Dominguez, S., Blard, P.-H., Avouac, J.-P., Brown, N. D., Malatesta, L. C., Wang, S., and Rhodes, E. J. (2018). Late pleistocene acceleration of deformation across the northern tianshan piedmont (china) evidenced from the morpho-tectonic evolution of the dushanzi anticline. *Tectonophysics*, 730:132–140.

Chen, C. W. and Zebker, H. A. (2002). Phase unwrapping for large SAR interferograms: Statistical segmentation and generalized network models. *IEEE Transactions on Geoscience and Remote Sensing*, 40(8):1709–1719.

Chen, J., Ran, Y., Yang, X., and Xu, X. (2006a). Character of Late Quaternary activity of the east segment of the front-edge faults of Kalpintag. *Seismology and Geology*, 28(2):258–268 (in Chinese with English abstract).

Chen, Z.-l., Wan, J.-l., Liu, J., Li, S.-x., and Zhen, E.-j. (2006b). Multi-stage uplift and exhumation of the west tianshan mountain: Evidence from the apatite fission-track dating. *Acta Geoscientia Sinica*, 27(2):97.

Chen, Z.-l., Zhang, Y.-q., Wang, X.-f., Chen, X.-h., and Washburn, Z. (2001). Fission track dating of apatite constrains on the cenozoic uplift of the altyn tagh mountain. *Acta Geoscientia Sinica*, 22(5; ISSU 65):413–417.

Chounet, A., Vallée, M., Causse, M., and Courboulex, F. (2018). Global catalog of earthquake rupture velocities shows anticorrelation between stress drop and rupture velocity. *Tectonophysics*, 733:148–158.

Clark, M. K., Farley, K. A., Zheng, D., Wang, Z., and Duvall, A. R. (2010). Early cenozoic faulting of the northern tibetan plateau margin from apatite (u–th)/he ages. *Earth and Planetary Science Letters*, 296(1-2):78–88.

Colesanti, C. and Wasowski, J. (2006). Investigating landslides with space-borne synthetic aperture radar (sar) interferometry. *Engineering Geology*, 88(3):173–199.

Copley, A. (2014). Postseismic afterslip 30 years after the 1978 Tabas-e-Golshan (Iran) earthquake: observations and implications for the geological evolution of thrust belts. *Geophysical Journal International*, 197(2):665–679.

Copley, A. and Jackson, J. (2006). Active tectonics of the turkish-iranian plateau. *Tectonics*, 25(6).

Copley, A., Karasozen, E., Oveisi, B., Elliott, J. R., Samsonov, S., and Nissen, E. (2015). Seismogenic faulting of the sedimentary sequence and laterally variable material properties in the Zagros Mountains (Iran) revealed by the August 2014 Murmuri (E. Dehloran) earthquake sequence. *Geophysical Journal International*, 203(2):1436–1459.

Costantini, M., Falco, S., Malvarosa, F., and Minati, F. (2008). A new method for identification and analysis of persistent scatterers in series of sar images. In *IGARSS 2008-2008 IEEE International Geoscience and Remote Sensing Symposium*, volume 2, pages II–449. IEEE.

Cowgill, E. (2007). Impact of riser reconstructions on estimation of secular variation in rates of strike–slip faulting: Revisiting the cherchen river site along the altyn tagh fault, nw china. *Earth and Planetary Science Letters*, 254(3-4):239–255.

Dahlen, F. A. (1984). Noncohesive critical coulomb wedges: An exact solution. *Journal of Geophysical Research: Solid Earth*, 89(B12):10125–10133.

Daout, S., Sudhaus, H., Kausch, T., Steinberg, A., and Dini, B. (2019). Interseismic and postseismic shallow creep of the north qaidam thrust faults detected with a multitemporal insar analysis. *Journal of Geophysical Research: Solid Earth*, 124(7):7259–7279.

Davis, T. L., Namson, J., and Yerkes, R. F. (1989). A cross section of the Los Angeles area: seismically active fold and thrust belt, the 1987 Whittier Narrows earthquake, and earthquake hazard. *Journal of Geophysical Research*, 94(B7):9644–9664.

De Grave, J. (2003). *Apatite fission-track thermochronology of the Altai Mountains (South Siberia, Russia) and the Tien Shan Mountains (Kyrgyzstan): relevance to Meso-Cenozoic tectonics and denudation in Central Asia*. PhD thesis, Ghent University.

De Grave, J., Buslov, M. M., et al. (2007). Distant effects of india–eurasia convergence and mesozoic intracontinental deformation in central asia: Constraints from apatite fission-track thermochronology. *Journal of Asian Earth Sciences*, 29(2-3):188–204.

De Grave, J., Buslov, M. M., and Van den haute, P. (2007). Distant effects of India-Eurasia convergence and Mesozoic intracontinental deformation in Central Asia: Constraints from apatite fission-track thermochronology. *Journal of Asian Earth Sciences*, 29(2-3):188–204.

De Grave, J., Glorie, S., Buslov, M. M., Stockli, D. F., McWilliams, M. O., Batalev, V. Y., et al. (2013). Thermo-tectonic history of the issyk-kul basement (kyrgyz northern tien shan, central asia). *Gondwana Research*, 23(3):998–1020.

De Grave, J., Glorie, S., Ryabinin, A., Zhimulev, F., Buslov, M., Izmer, A., Elburg, M., Vanhaecke, F., et al. (2012). Late palaeozoic and meso-cenozoic tectonic evolution of the southern kyrgyz tien shan: Constraints from multi-method thermochronology in the trans-alai, turkestan-alai segment and the southeastern ferghana basin. *Journal of Asian Earth Sciences*, 44:149–168.

De Pelsmaeker, E., Glorie, S., Buslov, M. M., Zhimulev, F. I., Poujol, M., Korobkin, V. V., Vanhaecke, F., Vetrov, E. V., and De Grave, J. (2015). Late-paleozoic emplacement and meso-cenozoic reactivation of the southern kazakhstan granitoid basement. *Tectonophysics*, 662:416–433.

Deng, Q., Zhang, P., Xu, X., Yang, X., Peng, S., and Feng, X. (1996). Paleoseismology of the northern piedmont of Tianshan Mountains, northwestern China. *Journal of Geophysical Research: Solid Earth*, 101(3):5895–5920.

Dodson, M. H. (1973). Closure temperature in cooling geochronological and petrological systems. *Contributions to Mineralogy and Petrology*, 40(3):259–274.

Donelick, R. A., Ketcham, R. A., and Carlson, W. D. (1999). Variability of apatite fission-track annealing kinetics: Ii. crystallographic orientation effects. *American Mineralogist*, 84(9):1224–1234.

Donelick, R. A., O'Sullivan, P. B., and Ketcham, R. A. (2005). Apatite fission-track analysis. *Reviews in Mineralogy and Geochemistry*, 58(1):49–94.

Du, Z., Wang, Q., and Zhou, X. (2007). Mesozoic and cenozoic uplifting history of the kuqa-south tianshan basin-mountain system from the evidence of apatite fission track analysis. *Acta Petrologica et Mineralogica*, 26(5):399–408.

Dumitru, T. A., Zhou, D., Chang, E. Z., Graham, S. A., Hendrix, M. S., Sobel, E. R., and Carroll, A. R. (2001). Uplift, exhumation, and deformation in the chinese tian shan. *Memoirs-Geological Society of America*, pages 71–100.

Dupont-Nivet, G., Krijgsman, W., Langereis, C. G., Abels, H. A., Dai, S., and Fang, X. (2007). Tibetan plateau aridification linked to global cooling at the eocene–oligocene transition. *Nature*, 445(7128):635–638.

Duvall, A. R., Clark, M. K., Kirby, E., Farley, K. A., Craddock, W. H., Li, C., and Yuan, D.-Y. (2013). Low-temperature thermochronometry along the kunlun and haiyuan faults, ne tibetan plateau: Evidence for kinematic change during late-stage orogenesis. *Tectonics*, 32(5):1190–1211.

Elliott, J., Jolivet, R., González, P. J., Avouac, J.-P., Hollingsworth, J., Searle, M., and Stevens, V. (2016). Himalayan megathrust geometry and relation to topography revealed by the gorkha earthquake. *Nature Geoscience*, 9(2):174–180.

Elliott, J. R., Bergman, E. A., Copley, A. C., Ghods, A. R., Nissen, E. K., Oveisi, B., Tatar, M., Walters, R. J., and Yamini-Fard, F. (2015). The 2013 Mw 6.2 Khaki-Shonbe (Iran) Earthquake: Insights into seismic and aseismic shortening of the Zagros sedimentary cover. *Earth and Space Science*, 2(11):435–471.

Elliott, J. R., Copley, A. C., Holley, R., Scharer, K., and Parsons, B. (2013). The 2011 Mw 7.1 Van (Eastern Turkey) earthquake. *Journal of Geophysical Research (Solid Earth)*, 118(4):1619–1637.

Elliott, J. R., Nissen, E. K., England, P. C., Jackson, J. A., Lamb, S., Li, Z., Oehlers, M., and Parsons, B. (2012). Slip in the 2010-2011 Canterbury earthquakes, New Zealand. *Journal of Geophysical Research: Solid Earth*, 117(3).

Elliott, J. R., Parsons, B., Jackson, J. A., Shan, X., Sloan, R. A., and Walker, R. T. (2011). Depth segmentation of the seismogenic continental crust: The 2008 and 2009 Qaidam earthquakes. *Geophysical Research Letters*, 38(6):1–6.

Engdahl, R. E., Jackson, J. A., Myers, S. C., Bergman, E. A., and Priestley, K. (2006). Relocation and assessment of seismicity in the Iran region. *Geophysical Journal International*, 167(2):761–778.

England, P. and Houseman, G. (1986). Finite strain calculations of continental deformation: 2. comparison with the india-asia collision zone. *Journal of Geophysical Research: Solid Earth*, 91(B3):3664–3676.

England, P. and Molnar, P. (1990). Surface uplift, uplift of rocks, and exhumation of rocks. *Geology*, 18(12):1173–1177.

England, P. and Molnar, P. (1997). The field of crustal velocity in asia calculated from quaternary rates of slip on faults. *Geophysical Journal International*, 130(3):551–582.

Fan, G., Ni, J. F., and Wallace, T. C. (1994). Active tectonics of the Pamirs and Karakorum. *Journal of Geophysical Research*, 99(B4):7131.

Fang, X., Zan, J., Appel, E., Lu, Y., Song, C., Dai, S., and Tuo, S. (2015). An eocene–miocene continuous rock magnetic record from the sediments in the xining basin, nw china: indication for cenozoic persistent drying driven by global cooling and tibetan plateau uplift. *Geophysical Journal International*, 201(1):78–89.

Farley, K. (2000). Helium diffusion from apatite: General behavior as illustrated by durango fluorapatite. *Journal of Geophysical Research: Solid Earth*, 105(B2):2903–2914.

Farley, K., Wolf, R., and Silver, L. (1996). The effects of long alpha-stopping distances on (u-th)/he ages. *Geochimica et cosmochimica acta*, 60(21):4223–4229.

Farley, K. A. and Stockli, D. F. (2002). (u-th)/he dating of phosphates: Apatite, monazite, and xenotime. *Reviews in mineralogy and geochemistry*, 48(1):559–577.

Ferretti, A., Fumagalli, A., Novali, F., Prati, C., Rocca, F., and Rucci, A. (2011). A new algorithm for processing interferometric data-stacks: SqueeSAR. *IEEE Transactions on Geoscience and Remote Sensing*, 49(9):3460–3470.

Ferretti, A., Prati, C., and Rocca, F. (2001). Permanent scatterers in sar interferometry. *IEEE Transactions on Geoscience and Remote Sensing*, 39(1):8–20.

Fialko, Y. (2006). Interseismic strain accumulation and the earthquake potential on the southern san andreas fault system. *Nature*, 441(7096):968–971.

Fielding, E. J., Wright, T. J., Muller, J., Parsons, B. E., and Walker, R. (2004). Aseismic deformation of a fold-and-thrust belt imaged by synthetic aperture radar interferometry near Shahdad, southeast Iran. *Geology*, 32(7):577–580.

Flower, B. P. and Kennett, J. P. (1994). The middle miocene climatic transition: East antarctic ice sheet development, deep ocean circulation and global carbon cycling. *Palaeogeography, palaeoclimatology, palaeoecology*, 108(3-4):537–555.

Flowers, R. M., Ketcham, R. A., Shuster, D. L., and Farley, K. A. (2009). Apatite (u–th)/he thermochronometry using a radiation damage accumulation and annealing model. *Geochimica et Cosmochimica acta*, 73(8):2347–2365.

Fox, M., Herman, F., Willett, S. D., and May, D. A. (2014). A linear inversion method to infer exhumation rates in space and time from thermochronometric data. *Earth Surface Dynamics*, 2(1):47–65.

Freed, A. M. (2007). Afterslip (and only afterslip) following the 2004 parkfield, california, earthquake. *Geophysical Research Letters*, 34(6).

Freed, A. M. and Lin, J. (2001). Delayed triggering of the 1999 hector mine earthquake by viscoelastic stress transfer. *Nature*, 411(6834):180–183.

Funning, G. J., Parsons, B., Wright, T. J., Jackson, J. A., and Fielding, E. J. (2005). Surface displacements and source parameters of the 2003 Bam (Iran) earthquake from Envisat advanced synthetic aperture radar imagery. *Journal of Geophysical Research: Solid Earth*, 110(B9):B09406.

Gabriel, A. K., Goldstein, R. M., and Zebker, H. A. (1989). Mapping small elevation changes over large areas: Differential radar interferometry. *Journal of Geophysical Research: Solid Earth*, 94(B7):9183–9191.

Gaherty, J. B., Zheng, W., Shillington, D. J., Pritchard, M. E., Henderson, S. T., Chindandali, P. R., Mdala, H., Shuler, A., Lindsey, N., Oliva, S. J., Nooner, S., Scholz, C. A., Schaff, D., Ekström, G., and Nettles, M. (2019). Faulting processes during early-stage rifting: Seismic and geodetic analysis of the 2009-2010 Northern Malawi earthquake sequence. *Geophysical Journal International*, 217(3):1767–1782.

Galbraith, R. F., Roberts, R. G., Laslett, G. M., Yoshida, H., and Olley, J. M. (1999). Optical dating of single and multiple grains of quartz from jinmium rock shelter, northern australia: Part i, experimental design and statistical models. *Archaeometry*, 41(2):339–364.

Gallagher, K. (2012). Transdimensional inverse thermal history modeling for quantitative thermochronology. *Journal of Geophysical Research: Solid Earth*, 117(B2).

Gao, J., Long, L., Klemd, R., Qian, Q., Liu, D., Xiong, X., Su, W., Liu, W., Wang, Y., and Yang, F. (2009). Tectonic evolution of the south tianshan orogen and adjacent regions, nw china: geochemical and age constraints of granitoid rocks. *International Journal of Earth Sciences*, 98:1221–1238.

Gao, R., Hou, H., Cai, X., Knapp, J. H., He, R., Liu, J., Xiong, X., Guan, Y., Li, W., Zeng, L., and Roecker, S. W. (2013). Fine crustal structure beneath the junction of the southwest Tian Shan and Tarim Basin, NW China. *Lithoshere*, 5(4):382–392.

Gaudreau, É., Nissen, E., Bergman, E. A., Benz, H. M., Tan, F., and Karasözen, E. (2019). The August 2018 Kaktovik earthquakes: Active tectonics in northeastern Alaska revealed with InSAR and seismology. *Geophysical Research Letters*, 46(24):14412–14420.

George, A. D., Marshallsea, S. J., Wyrwoll, K.-H., Jie, C., and Yanchou, L. (2001). Miocene cooling in the northern qilian shan, northeastern margin of the tibetan plateau, revealed by apatite fission-track and vitrinite-reflectance analysis. *Geology*, 29(10):939–942.

Ghose, S., Hamburger, M. W., and Ammon, C. J. (1998). Source parameters of moderate-sized earthquakes in the Tien Shan, central Asia from regional moment tensor inversion. *Geophysical Research Letters*, 25(16):3181–3184.

Gillespie, J., Glorie, S., Jepson, G., Zhang, Z., Xiao, W., Danišík, M., and Collins, A. (2017). Differential exhumation and crustal tilting in the easternmost tianshan (xinjiang, china), revealed by low-temperature thermochronology. *Tectonics*, 36(10):2142–2158.

Gleadow, A., Harrison, M., Kohn, B., Lugo-Zazueta, R., and Phillips, D. (2015). The fish canyon tuff: A new look at an old low-temperature thermochronology standard. *Earth and Planetary Science Letters*, 424:95–108.

Glorie, S., De Grave, J., Buslov, M., Zhimulev, F., Stockli, D., Batalev, V. Y., Izmer, A., Van den Haute, P., Vanhaecke, F., and Elburg, M. (2011). Tectonic history of the kyrgyz south tien shan (atbashi-inylchek) suture zone: The role of inherited structures during deformation-propagation. *Tectonics*, 30(6).

Glorie, S., Otasevic, A., Gillespie, J., Jepson, G., Danišík, M., Zhimulev, F., Gurevich, D., Zhang, Z., Song, D., and Xiao, W. (2019). Thermo-tectonic history of the junggar alatau within the central asian orogenic belt (se kazakhstan, nw china): Insights from integrated apatite u/pb, fission track and (u–th)/he thermochronology. *Geoscience Frontiers*, 10(6):2153–2166.

Goldstein, R. M., Zebker, H. A., and Werner, C. L. (1988). Satellite radar interferometry: Two-dimensional phase unwrapping. *Radio Science*, 23(4):713–720.

Gomberg, J. S., Shedlock, K. M., and Roecker, S. W. (1990). The effect of S-wave arrival times on the accuracy of hypocenter estimation. *Bulletin of the Seismological Society of America*, 80(6A):1605–1628.

Gong, Z., Li, S. H., and Li, B. (2014). The evolution of a terrace sequence along the Manas River in the northern foreland basin of Tian Shan, China, as inferred from optical dating. *Geomorphology*, 213:201–212.

Gong, Z., Li, S. H., and Li, B. (2015). Late Quaternary faulting on the Manas and Hutubi reverse faults in the northern foreland basin of Tian Shan, China. *Earth and Planetary Science Letters*, 424:212–225.

Graham, S. A., Chamberlain, C. P., Yue, Y., Ritts, B. D., Hanson, A. D., Horton, T. W., Waldbauer, J. R., Poage, M. A., and Feng, X. (2005). Stable isotope records of cenozoic climate and topography, tibetan plateau and tarim basin. *American Journal of Science*, 305(2):101–118.

Green, P., Duddy, I., Laslett, G., Hegarty, K., Gleadow, A. W., and Lovering, J. (1989). Thermal annealing of fission tracks in apatite 4. quantitative modelling techniques and extension to geological timescales. *Chemical Geology: Isotope Geoscience Section*, 79(2):155–182.

Guan, S., Stockmeyer, J. M., Shaw, J. H., Plesch, A., and Zhang, J. (2016). Structural inversion, imbricate wedging, and out-of-sequence thrusting in the southern Junggar fold-and-thrust belt, northern Tian Shan, China. *AAPG Bulletin*, 100(9):1443–1468.

Guo, Z., Zhang, Z., Wu, C., Fang, S., Zhang, R., et al. (2006). The mesozoic and cenozoic exhumation history of tianshan and comparative studies to the junggar and altai mountains. *Acta Geologica Sinica*, 80(1):1–15.

Haeussler, P. J., Armstrong, P. A., Liberty, L. M., Ferguson, K. M., Finn, S. P., Arkle, J. C., and Pratt, T. L. (2015). Focused exhumation along megathrust splay faults in prince william sound, alaska. *Quaternary Science Reviews*, 113:8–22.

Haijian, L., Haibing, L., and Dongliang, L. (2015). The major two-stage shortening deformation of the northern tibet and tian shan area since the latest oligocene. *Acta Geologica Sinica-English Edition*, 89(5):1546–1560.

Hanssen, R. F. (2001). *Radar interferometry: data interpretation and error analysis*, volume 2. Springer Science & Business Media.

Harris, N. (2006). The elevation history of the Tibetan Plateau and its implications for the Asian monsoon. *Palaeogeography, Palaeoclimatology, Palaeoecology*, 241(1):4–15.

Hasebe, N., Barbarand, J., Jarvis, K., Carter, A., and Hurford, A. J. (2004). Apatite fission-track chronometry using laser ablation icp-ms. *Chemical Geology*, 207(3-4):135–145.

He, Y., Wang, T., Fang, L., and Zhao, L. (2021). The 2020 Mw 6.0 Jiashi Earthquake: Coinvolvement of Thin-Skinned Thrusting and Basement Shortening in Shaping the Keping-Tage Fold-and-Thrust Belt in Southwestern Tian Shan. *Seismological Research Letters.*

Heimann, S., Isken, M., Kühn, D., Sudhaus, H., Steinberg, A., Daout, S., Cesca, S., Bathke, H., and Dahm, T. (2018). Grond: A probabilistic earthquake source inversion framework.

Helmstetter, A. and Sornette, D. (2003). Foreshocks explained by cascades of triggered seismicity. *Journal of Geophysical Research: Solid Earth*, 108(B10).

Hendrix, M. S., Dumitru, T. A., and Graham, S. A. (1994). Late oligocene-early miocene unroofing in the chinese tian shan: An early effect of the india-asia collision. *Geology*, 22(6):487–490.

Hendrix, M. S., Graham, S. A., Carroll, A. R., Sobel, E. R., McKNIGHT, C. L., Schulein, B. J., and Wang, Z. (1992). Sedimentary record and climatic implications of recurrent deformation in the tian shan: Evidence from mesozoic strata of the north tarim, south junggar, and turpan basins, northwest china. *Geological Society of America Bulletin*, 104(1):53–79.

Herman, F. and Brandon, M. (2015). Mid-latitude glacial erosion hotspot related to equatorial shifts in southern westerlies. *Geology*, 43(11):987–990.

Hooper, A., Bekaert, D., Spaans, K., and Arikan, M. (2012). Recent advances in SAR interferometry time series analysis for measuring crustal deformation. *Tectonophysics*, 514-517:1–13.

Hooper, A., Segall, P., and Zebker, H. (2007). Persistent scatterer interferometric synthetic aperture radar for crustal deformation analysis, with application to Volcán Alcedo, Galápagos. *Journal of Geophysical Research: Solid Earth*, 112(7):1–21.

Hooper, A., Zebker, H., Segall, P., and Kampes, B. (2004). A new method for measuring deformation on volcanoes and other natural terrains using InSAR persistent scatterers. *Geophysical Research Letters*, 31(23):1–5.

Hu, Z., Yang, X., Yang, H., Huang, W., Wu, G., Miao, S., and Zhang, L. (2021). Slip rate and paleoseismology of the bolokenu-aqikekuduk (dzhungarian) right-lateral strike-slip fault in the northern tian shan, nw china. *Tectonics*, 40(8):e2020TC006604.

Huang, Y., Yang, J. S., and Zhang, T. Z. (2006). Relocation of the Bachu-Jiashi, Xinjiang earthquake sequence in 2003 using the double-difference location algorithm. *Acta Geophysica Sinica*, 49(1):162–169.

Huangfu, P., Li, Z.-H., Zhang, K.-J., Fan, W., Zhao, J., and Shi, Y. (2021). India-tarim lithospheric mantle collision beneath western tibet controls the cenozoic building of tian shan. *Geophysical Research Letters*, 48(14):e2021GL094561.

Jackson, J., Bouchon, M., Fielding, E., Funning, G., Ghorashi, M., Hatzfeld, D., Nazari, H., Parsons, B., Priestley, K., Talebian, M., Tatar, M., Walker, R., and Wright, T. (2006). Seismotectonic, rupture process, and earthquake-hazard aspects of the 2003 December 26 Bam, Iran, earthquake. *Geophysical Journal International*, 166(3):1270–1292.

Jamalreyhani, M., Pousse-Beltran, L., Büyükakpınar, P., Cesca, S., Nissen, E., Ghods, A., López-Comino, J. Á., Rezapour, M., and Najafi, M. (2021). The 2019-2020 Khalili (Iran) Earthquake Sequence—Anthropogenic Seismicity in the Zagros Simply Folded Belt? *Journal of Geophysical Research (Solid Earth)*, 126(12):e22797.

Jepson, G., Carrapa, B., Gillespie, J., Feng, R., DeCelles, P. G., Kapp, P., Tabor, C. R., and Zhu, J. (2021). Climate as the great equalizer of continental-scale erosion. *Geophysical Research Letters*, 48(20):e2021GL095008.

Jia, Y., Fu, B., Jolivet, M., and Zheng, S. (2015). Cenozoic tectono-geomorphological growth of the sw chinese tian shan: Insight from aft and detrital zircon u–pb data. *Journal of Asian Earth Sciences*, 111:395–413.

Jia, Y., Sun, J., Lü, L., Pang, J., and Wang, Y. (2020). Late oligocene-miocene intracontinental mountain building of the harke mountains, southern chinese tian shan: Evidence from detrital aft and ahe analysis. *Journal of Asian Earth Sciences*, 191:104198.

Johnson, K. M. (2018). Growth of Fault-Cored Anticlines by Flexural Slip Folding: Analysis by Boundary Element Modeling. *Journal of Geophysical Research: Solid Earth*, 123(3):2426–2447.

Jolivet, M., Brunel, M., Seward, D., Xu, Z., Yang, J., Roger, F., Tapponnier, P., Malavieille, J., Arnaud, N., and Wu, C. (2001). Mesozoic and cenozoic tectonics of the northern edge of the tibetan plateau: fission-track constraints. *Tectonophysics*, 343(1-2):111–134.

Jolivet, M., Dominguez, S., Charreau, J., Chen, Y., Li, Y., and Wang, Q. (2010). Mesozoic and cenozoic tectonic history of the central chinese tian shan: Reactivated tectonic structures and active deformation. *Tectonics*, 29(6).

Jones, L., Aki, K., Boore, D., Celebi, M., Donnellan, A., Hall, J., Harris, R., Hauksson, E., Heaton, T., Hough, S., Hudnut, K., Hutton, K., Johnston, M., Joyner, W., Kanamori, H., Marshall, G., Michael, A., Mori, J., Murray, M., Ponti, D., Reasenberg, P., Schwartz, D., Seeber, L., Shakal, A., Simpson, R., Thio, H., Tinsley, J., Todorovska, M., Trifunac, M., Wald, D., and Zoback, M. L. (1994). The magnitude 6.7 Northridge, California, earthquake of 17 January 1994. *Science*, 266(5184):389–397.

Jónsson, S., Zebker, H., Segall, P., and Amelung, F. (2002). Fault slip distribution of the 1999 Mw 7.1 Hector Mine, California, earthquake, estimated from satellite radar and GPS measurements. *Bulletin of the Seismological Society of America*, 92(4):1377–1389.

Jordan, T. H. and Sverdrup, K. A. (1981). Teleseismic location techniques and their application to earthquake clusters in the South-Central Pacific. *Bulletin of the Seismological Society of America*, 71:1105–1130.

Jun, G., Maosong, L., Xuchang, X., Yaoqing, T., and Guoqi, H. (1998). Paleozoic tectonic evolution of the tianshan orogen, northwestern china. *Tectonophysics*, 287(1-4):213–231.

Karasözen, E., Nissen, E., Bergman, E. A., and Ghods, A. (2019). Seismotectonics of the Zagros (Iran) From Orogen-Wide, Calibrated Earthquake Relocations. *Journal of Geophysical Research: Solid Earth*, 124(8):9109–9129.

Karasözen, E., Nissen, E., Bergman, E. A., Johnson, K. L., and Walters, R. J. (2016). Normal faulting in the Simav graben of western Turkey reassessed with calibrated earthquake relocations. *Journal of Geophysical Research: Solid Earth*, 121(6):4553–4574.

Karasözen, E., Nissen, E., Büyükakpınar, P., Cambaz, M. D., Kahraman, M., KalkanÂ Ertan, E., Abgarmi, B., Bergman, E., Ghods, A., and Özacar, A. A. (2018). The 2017 July 20 M_w 6.6 Bodrum-Kos earthquake illuminates active faulting in the Gulf of Gökova, SW Turkey. *Geophysical Journal International*, 214(1):185–199.

Käßner, A., Ratschbacher, L., Jonckheere, R., Enkelmann, E., Khan, J., Sonntag, B.-L., Gloaguen, R., Gadoev, M., and Oimahmadov, I. (2016). Cenozoic intracontinental deformation and exhumation at the northwestern tip of the india-asia collision—southwestern tian shan, tajikistan, and kyrgyzstan. *Tectonics*, 35(9):2171–2194.

Kennett, B. L. N., Engdahl, E. R., and Buland, R. (1995). Constraints on seismic velocities in the Earth from traveltimes. *Geophysical Journal International*, 122(1):108–124.

Ketcham, R. A., Carter, A., Donelick, R. A., Barbarand, J., and Hurford, A. J. (2007). Improved modeling of fission-track annealing in apatite. *American Mineralogist*, 92(5-6):799–810.

Ketcham, R. A., Donelick, R. A., and Carlson, W. D. (1999). Variability of apatite fission-track annealing kinetics: II. Crystallographic orientation effects. *American Mineralogist*, 84(9):1224–1234.

Koppes, M., Gillespie, A. R., Burke, R. M., Thompson, S. C., and Stone, J. (2008). Late quaternary glaciation in the kyrgyz tien shan. *Quaternary Science Reviews*, 27(7-8):846–866.

Korjenkov, A., Bobrovskii, A., and Mamyrov, E. (2010). Evidence for strong paleoearthquakes along the talas-fergana fault near the kök-bel pass, kyrgyzstan. *Geotectonics*, 44(3):262–270.

Kulikova, G. and Krüger, F. (2017). Historical seismogram reproductions for the source parameters determination of the 1902, Atushi (Kashgar) earthquake. *Journal of Seismology*, 21(6):1577–1597.

Laborde, A., Barrier, L., Simoes, M., Li, H., Coudroy, T., van Der Woerd, J., and Tapponnier, P. (2019). Cenozoic deformation of the tarim basin and surrounding ranges (xinjiang, china): A regional overview. *Earth-Science Reviews*, 197:102891.

Laurent-Charvet, S., Charvet, J., Monié, P., and Shu, L. (2003). Late paleozoic strike-slip shear zones in eastern central asia (nw china): New structural and geochronological data. *Tectonics*, 22(2).

Lazeckỳ, M., Spaans, K., González, P. J., Maghsoudi, Y., Morishita, Y., Albino, F., Elliott, J., Greenall, N., Hatton, E., Hooper, A., Juncu, D., McDougall, A., Walters, R. J., Watson, C. S., Weiss, J. R., and Wright, T. J. (2020). LiCSAR: An automatic InSAR tool for measuring and monitoring tectonic and volcanic activity. *Remote Sensing*, 12(15).

Lease, R. O., Burbank, D. W., Clark, M. K., Farley, K. A., Zheng, D., and Zhang, H. (2011). Middle miocene reorganization of deformation along the northeastern tibetan plateau. *Geology*, 39(4):359–362.

Li, C., Zheng, D., Zhou, R., Yu, J., Wang, Y., Pang, J., Wang, Y., Hao, Y., and Li, Y. (2021a). Late oligocene tectonic uplift of the east kunlun shan: expansion of the northeastern tibetan plateau. *Geophysical Research Letters*, 48(3):e2020GL091281.

Li, G., Sandiford, M., Fang, A., Kohn, B., Sandiford, D., Fu, B., Zhang, T., Cao, Y., and Chen, F. (2019). Multi-stage exhumation history of the west kunlun orogen and the amalgamation of the tibetan plateau. *Earth and Planetary Science Letters*, 528:115833.

Li, L., Zhengle, C., Wanxiu, Q., ShiXin, W., XuanHua, C., YiPing, W., HongLiang, G., XinChang, W., Yi, Y., and XueZhi, L. (2008). Apatite fission track evidence for uplifting-exhumation processes of mountains surrounding the junggar basin. *Acta Petrologica Sinica*, 24(5):1011–1020.

Li, S. and Barnhart, W. D. (2020). Impacts of Topographic Relief and Crustal Heterogeneity on Coseismic Deformation and Inversions for Fault Geometry and Slip: A Case Study of the 2015 Gorkha Earthquake in the Central Himalayan Arc. *Geochemistry, Geophysics, Geosystems*, 21(12):e09413.

Li, X., Zhang, R., Zhang, Z., and Yan, Q. (2018). What enhanced the aridity in eocene asian inland: Global cooling or early tibetan plateau uplift? *Palaeogeography, Palaeoclimatology, Palaeoecology*, 510:6–14.

Li, Y., Liu, M., Hao, M., Zhu, L., Cui, D., and Wang, Q. (2021b). Active crustal deformation in the tian shan region, central asia. *Tectonophysics*, 811:228868.

Lin, J. and Stein, R. S. (2004). Stress triggering in thrust and subduction earthquakes and stress interaction between the southern San Andreas and nearby thrust and strike-slip faults. *Journal of Geophysical Research (Solid Earth)*, 109(B2):B02303.

Liu, D., Li, H., Sun, Z., Pan, J., Wang, M., Wang, H., et al. (2017). Aft dating constrains the cenozoic uplift of the qimen tagh mountains, northeast tibetan plateau, comparison with la-icpms zircon u–pb ages. *Gondwana Research*, 41:438–450.

LiuS, L. et al. (2016). Estimationofsubsurfaceformationtemperatureinthetarim basin, northwestchina: implicationsforhydrocarbongenerationandpreservation. *InternationalJournalofEarthSciences*, 105(5):1329–1351.

Lü, H., Chang, Y., Wang, W., and Zhou, Z. (2013). Rapid exhumation of the tianshan mountains since the early miocene: Evidence from combined apatite fission track and (u-th)/he thermochronology. *Science China Earth Sciences*, 56:2116–2125.

Lu, H., Li, B., Wu, D., Zhao, J., Zheng, X., Xiong, J., and Li, Y. (2019). Spatiotemporal patterns of the Late Quaternary deformation across the northern Chinese Tian Shan foreland. *Earth-Science Reviews*, 194(April):19–37.

Lu, H., Wang, E., Shi, X., and Meng, K. (2012). Cenozoic tectonic evolution of the elashan range and its surroundings, northern tibetan plateau as constrained by paleomagnetism and apatite fission track analyses. *Tectonophysics*, 580:150–161.

Lu, R., He, D., Xu, X., Wang, X., Tan, X., and Wu, X. (2018). Seismotectonics of the 2016 M 6.2 hutubi earthquake: Implications for the 1906 M 7.7 manas earthquake in the northern tian shan belt, China. *Seismological Research Letters*, 89(1):13–21.

Macaulay, E. A., Sobel, E. R., Mikolaichuk, A., Kohn, B., and Stuart, F. M. (2014). Cenozoic deformation and exhumation history of the central kyrgyz tien shan. *Tectonics*, 33(2):135–165.

Macaulay, E. A., Sobel, E. R., Mikolaichuk, A., Landgraf, A., Kohn, B., and Stuart, F. (2013). Thermochronologic insight into late cenozoic deformation in the basement-cored terskey range, kyrgyz tien shan. *Tectonics*, 32(3):487–500.

Mallick, R., Bürgmann, R., Johnson, K., and Hubbard, J. (2021). A unified framework for earthquake sequences and the growth of geological structure in fold-thrust belts. *Journal of Geophysical Research: Solid Earth*.

Marone, C. J., Scholtz, C., and Bilham, R. (1991). On the mechanics of earthquake afterslip. *Journal of Geophysical Research: Solid Earth*, 96(B5):8441–8452.

Massonnet, D. and Feigl, K. L. (1998). Radar interferometry and its application to changes in the earth's surface. *Reviews of geophysics*, 36(4):441–500.

Massonnet, D., Rossi, M., Carmona, C., Adragna, F., Peltzer, G., Feigl, K., and Rabaute, T. (1993). The displacement field of the landers earthquake mapped by radar interferometry. *nature*, 364(6433):138–142.

Massonnet, D. and Sigmundsson, F. (2000). Remote sensing of volcano deformation by radar interferometry from various satellites. *Geophysical Monograph Series*, 116:207–221.

McInerney, F. A. and Wing, S. L. (2011). The paleocene-eocene thermal maximum: A perturbation of carbon cycle, climate, and biosphere with implications for the future. *Annual Review of Earth and Planetary Sciences*, 39:489–516.

McRivette, M. W., Yin, A., Chen, X., and Gehrels, G. E. (2019). Cenozoic basin evolution of the central Tibetan plateau as constrained by U-Pb detrital zircon geochronology, sandstone petrology, and fission-track thermochronology. *Tectonophysics*, 751:150–179.

Mériaux, A.-S., Tapponnier, P., Ryerson, F., Xiwei, X., King, G., Van der Woerd, J., Finkel, R., Haibing, L., Caffee, M., Zhiqin, X., et al. (2005). The aksay segment of the northern altyn tagh fault: Tectonic geomorphology, landscape evolution, and holocene slip rate. *Journal of Geophysical Research: Solid Earth*, 110(B4).

Mock, C., Arnaud, N. O., and Cantagrel, J.-M. (1999). An early unroofing in northeastern tibet? constraints from 40ar/39ar thermochronology on granitoids from the eastern kunlun range (qianghai, nw china). *Earth and Planetary Science Letters*, 171(1):107–122.

Mohadjer, S., Ehlers, T. A., Bendick, R., Stübner, K., and Strube, T. (2016). A quaternary fault database for central asia. *Natural Hazards and Earth System Sciences*, 16(2):529–542.

Molnar, P., Brown, E. T., Burchfiel, B. C., Deng, Q., Feng, X., Li, J., Raisbeck, G. M., Shi, J., Zhangming, W., Yiou, F., and You, H. (1994). Quaternary Climate Change and the Formation of River Terraces across Growing Anticlines on the North Flank of the Tien Shan, China. *The Journal of Geology*, 102(5):583–602.

Molnar, P. and Ghose, S. (2000). Seismic moments of major earthquakes and the rate of shortening across the Tien Shan. *Geophysical Research Letters*, 27(16):2377–2380.

Molnar, P. and Tapponnier, P. (1975). Cenozoic tectonics of asia: Effects of a continental collision: Features of recent continental tectonics in asia can be interpreted as results of the india-eurasia collision. *Science*, 189(4201):419–426.

Morishita, Y., Lazecky, M., Wright, T. J., Weiss, J. R., Elliott, J. R., and Hooper, A. (2020). LiCSBAS: An Open-Source InSAR Time Series Analysis Package Integrated with the LiCSAR Automated Sentinel-1 InSAR Processor. *Remote Sensing*, 12(3):424.

Motagh, M., Shamshiri, R., Haghighi, M. H., Wetzel, H.-U., Akbari, B., Nahavandchi, H., Roessner, S., and Arabi, S. (2017). Quantifying groundwater exploitation induced subsidence in the rafsanjan plain, southeastern iran, using insar time-series and in situ measurements. *Engineering geology*, 218:134–151.

Nachtergaele, S., De Pelsmaeker, E., Glorie, S., Zhimulev, F., Jolivet, M., Danišík, M., Buslov, M. M., and De Grave, J. (2018). Meso-Cenozoic tectonic evolution of the Talas-Fergana region of the Kyrgyz Tien Shan revealed by low-temperature basement and detrital thermochronology. *Geoscience Frontiers*, 9(5):1495–1514.

Neil, E. A. and Houseman, G. A. (1997). Geodynamics of the tarim basin and the tian shan in central asia. *Tectonics*, 16(4):571–584.

Nishidai, T. and Berry, J. L. (1990). Structure and Hydrocarbon Potential of the Tarim Basin (Nw China) From Satellite Imagery. *Journal of Petroleum Geology*, 13(1):35–58.

Nissen, E., Ghorashi, M., Jackson, J., Parsons, B., and Talebian, M. (2007). The 2005 Qeshm Island earthquake (Iran) - A link between buried reverse faulting and surface folding in the Zagros Simply Folded Belt? *Geophysical Journal International*, 171(1):326–338.

Nissen, E., Jackson, J., Jahani, S., and Tatar, M. (2014). Zagros "phantom earthquakes" reassessed - The interplay of seismicity and deep salt flow in the Simply Folded Belt? *Journal of Geophysical Research: Solid Earth*, 119(4):3561–3583.

Nissen, E., Tatar, M., Jackson, J. A., and Allen, M. B. (2011). New views on earthquake faulting in the Zagros fold-and-thrust belt of Iran. *Geophysical Journal International*, 186(3):928–944.

Nissen, E., Yamini-Fard, F., Tatar, M., Gholamzadeh, A., Bergman, E., Elliott, J. R., Jackson, J. A., and Parsons, B. (2010). The vertical separation of mainshock rupture and microseismicity at Qeshm island in the Zagros fold-and-thrust belt, Iran. *Earth and Planetary Science Letters*, 296(3-4):181–194.

Okada, Y. (1985). Surface deformation due to shear and tensile faults in a half-space. *Bulletin of the seismological society of America*, 75(4):1135–1154.

Osmanoğlu, B., Sunar, F., Wdowinski, S., and Cabral-Cano, E. (2016). Time series analysis of insar data: Methods and trends. *ISPRS Journal of Photogrammetry and Remote Sensing*, 115:90–102. Theme issue 'State-of-the-art in photogrammetry, remote sensing and spatial information science'.

Pang, J., Yu, J., Zheng, D., Wang, W., Ma, Y., Wang, Y., Li, C., Li, Y., and Wang, Y. (2019). Neogene Expansion of the Qilian Shan, North Tibet: Implications for the Dynamic Evolution of the Tibetan Plateau. *Tectonics*, 38(3):1018–1032.

Pang, J., Zheng, D., Ma, Y., Wang, Y., Wu, Y., Wan, J., Yu, J., Li, Y., and Wang, Y. (2017). Combined apatite fission-track dating, chlorine and ree content analysis by la-icpms. *Science Bulletin*, 62(22):1497–1500.

Peltzer, G., Rosen, P., Rogez, F., and Hudnut, K. (1996). Postseismic rebound in fault step-overs caused by pore fluid flow. *Science*, 273(5279):1202–1204.

Pousse-Beltran, L., Nissen, E., Bergman, E. A., Cambaz, M. D., Gaudreau, É., Karasözen, E., and Tan, F. (2020). The 2020 M_w 6.8 Elazığ (Turkey) Earthquake Reveals Rupture Behavior of the East Anatolian Fault. , 47(13):e88136.

Pousse Beltran, L., Pathier, E., Jouanne, F., Vassallo, R., Reinoza, C., Audemard, F., Doin, M. P., and Volat, M. (2016). Spatial and temporal variations in creep rate along the El Pilar fault at the Caribbean-South American plate boundary (Venezuela), from InSAR. *Journal of Geophysical Research: Solid Earth*, 121(11):8276–8296.

Press, W. H., Flannery, B. P., Teukolsky, S. A., and Vetterling, W. T. (1992). Numeric recipes in C: the art of scientific computing. *Camb. Univ. Press Camb.*

Qi, B., Hu, D., Yang, X., Zhang, Y., Tan, C., Zhang, P., and Feng, C. (2016). Apatite fission track evidence for the cretaceous–cenozoic cooling history of the qilian shan (nw china) and for stepwise northeastward growth of the northeastern tibetan plateau since early eocene. *Journal of Asian Earth Sciences*, 124:28–41.

Qiu, J., Rao, G., Wang, X., Yang, D., and Xiao, L. (2019). Effects of fault slip distribution on the geometry and kinematics of the southern Junggar fold-and-thrust belt, northern Tian Shan. *Tectonophysics*, 772(38):228209.

Ramstein, G., Fluteau, F., Besse, J., and Joussaume, S. (1997). Effect of orogeny, plate motion and land–sea distribution on eurasian climate change over the past 30 million years. *Nature*, 386(6627):788–795.

Ran, H., Shangguan, W., and Liu, D. (2020). Location study of Xinjiang Jiashi Ms6.4 earthquake and aftershocks sequence on January 19th, 2020. *Inland Earthquake*, 34(1):56–61.

Ran, Y., Yang, X., Xu, X., Cheng, J., and Chen, L. (2006). Deformation pattern and shortening rates in the east part of Kalpin Thrust system in southwest Tianshan during late Quaternary. *Seismology and Geology (in Chinese with English abstract)*, 28(2):179–193.

Raymo, M. E. and Ruddiman, W. F. (1992). Tectonic forcing of late cenozoic climate. *nature*, 359(6391):117–122.

Reid, H. F. (1910). The california earthquake of april 18, 1906. *Report of the state earthquake investigation commission*, 2:16–18.

Reigber, C., Michel, G. W., Galas, R., Angermann, D., Klotz, J., Chen, J. Y., Papschev, A., Arslanov, R., Tzurkov, V. E., and Ishanov, M. C. (2001). New space geodetic constraints on the distribution of deformation in Central Asia. *Earth and Planetary Science Letters*, 191(1-2):157–165.

Reiners, P. W. and Brandon, M. T. (2006). Using thermochronology to understand orogenic erosion. *Annu. Rev. Earth Planet. Sci.*, 34(1):419–466.

Rignot, E. and Kanagaratnam, P. (2006). Changes in the Velocity Structure of the Greenland Ice Sheet. *Science*, 311(5763):986–990.

Ring, U., Brandon, M. T., Willett, S. D., and Lister, G. S. (1999). Exhumation processes. *Geological Society, London, Special Publications*, 154(1):1–27.

Rosen, P. A., Hensley, S., Joughin, I. R., Li, F. K., Madsen, S. N., Rodriguez, E., and Goldstein, R. M. (2000). Synthetic aperture radar interferometry. *Proceedings of the IEEE*, 88(3):333–382.

Roustaei, M., Nissen, E., Abbassi, M., Gholamzadeh, A., Ghorashi, M., Tatar, M., Yamini-Fard, F., Bergman, E., Jackson, J., and Parsons, B. (2010). The 2006 March 25 Fin earthquakes (Iran)-insights into the vertical extents of faulting in the Zagros Simply Folded Belt. *Geophysical Journal International*, 181(3):1275–1291.

Ruddiman, W. F. and Kutzbach, J. E. (1991). Plateau uplift and climatic change. *Scientific American*, 264(3):66–75.

Rutte, D., Ratschbacher, L., Khan, J., Stübner, K., Hacker, B. R., Stearns, M. A., Enkelmann, E., Jonckheere, R., Pfänder, J. A., Sperner, B., and Tichomirowa, M. (2017). Building the pamir-tibetan plateau-crustal stacking, extensional collapse, and lateral extrusion in the central pamir: 2. timing and rates: Building the pamir-tibetan plateau. *Tectonics*, 36(3):385–419.

Ryder, I., Parsons, B., Wright, T. J., and Funning, G. J. (2007). Post-seismic motion following the 1997 manyi (tibet) earthquake: Insar observations and modelling. *Geophysical Journal International*, 169(3):1009–1027.

Savage, J. C. (1983). Strain accumulation in western united states. *Annual review of earth and planetary sciences*, 11(1):11–41.

Savin, S. M., Douglas, R. G., and Stehli, F. G. (1975). Tertiary marine paleotemperatures. *Geological Society of America Bulletin*, 86(11):1499–1510.

Schmalholz, M. (2004). *The Amalgamation of the Pamirs and Their Subsequent Evolution in the Far Field of the India-Asia Collision*. Tübinger Geowissenschaftliche Arbeiten: Reihe A, Geologie, Paläontologie, Stratigraphie. IFG.

Schmidt, D. A. and Bürgmann, R. (2003). Time-dependent land uplift and subsidence in the Santa Clara valley, California, from a large interferometric synthetic aperture radar data set. *Journal of Geophysical Research: Solid Earth*, 108(B9):1–13.

Selander, J., Oskin, M., Ormukov, C., and Abdrakhmatov, K. (2012). Inherited strike-slip faults as an origin for basement-cored uplifts: Example of the kungey and zailiskey ranges, northern tian shan. *Tectonics*, 31(4).

Semmane, F., Cotton, F., and Campillo, M. (2005). The 2000 Tottori earthquake: A shallow earthquake with no surface rupture and slip properties controlled by depth. *Journal of Geophysical Research: Solid Earth*, 110(3):1–13.

Şengör, A., Natal'In, B., and Burtman, V. (1993). Evolution of the altaid tectonic collage and palaeozoic crustal growth in eurasia. *Nature*, 364(6435):299–307.

Shackleton, N. J. (1975). Paleotemperature history of the cenozoic and the initiation of antarctic glaciation: oxygen and carbon isotope analyses in dsdp sites 277, 279, and 281. *Initial Reports Deep Sea Drilling Project*, 29:743–755.

Shackleton, N. J., Backman, J., Zimmerman, H. t., Kent, D. V., Hall, M., Roberts, D. G., Schnitker, D., Baldauf, J., Desprairies, A., Homrighausen, R., et al. (1984). Oxygen isotope calibration of the onset of ice-rafting and history of glaciation in the north atlantic region. *Nature*, 307(5952):620–623.

Shen, C., Mei, L., Peng, L., Zhang, S., Liu, L., and Tang, J. (2006). Fission track evidence for the mesozoic-cenozoic tectonic uplift of mt. bogda, xinjiang, northwest china. *Chinese Journal of Geochemistry*, 25(2):143–151.

Shen, C. B., Mei, L. F., Zhang, S. W., Liu, L., Tang, J. G., Zhou, F., Yan, S. L., and Luo, J. C. (2008). Fission-track dating evidence on space-time difference of Mesozoic-Cenozoic uplift of the Yilianhabierga Mountain and Bogeda Mountain. *Journal of Mineralogy and Petrology*, 28(2):63–70.

Shen, J., Wang, Y., and Li, Y. (2011). Characteristics of the late quaternary right-lateral strike-slip movement of bolokenu-aqikekuduk fault in northern tianshan mountains, nw china. *Geoscience Frontiers*, 2(4):519–527.

Shen, J., Wang, Y., Li, Y., Jiang, H., and Xiang, Z. (2003). Late quaternary right-lateral strike-slip faulting along the bolokenu-aqikekuduke fault in chinese tian shan. *Seismology and Geology*, 25(2):183–194.

Shu, L., Charvet, J., Guo, L., Lu, H., and Laurent-Charvet, S. (1999). A Large-Scale Palaeozoic Dextral Ductile Strike-Slip Zone: the Aqqikkudug-Weiya Zone along the Northern Margin of the Central Tianshan Belt, Xinjiang, NW China. *Acta Geologica Sinica*, 73(2):148–162.

Sloan, R. A., Jackson, J. A., Mckenzie, D., and Priestley, K. (2011). Earthquake depth distributions in central Asia, and their relations with lithosphere thickness, shortening and extension. *Geophysical Journal International*, 185(1):1–29.

Sobel, E. R. (1999). Basin analysis of the Jurassic-Lower Cretaceous southwest Tarim basin, northwest China. *Bulletin of the Geological Society of America*, 111(5):709–724.

Sobel, E. R., Chen, J., and Heermance, R. V. (2006a). Late oligocene–early miocene initiation of shortening in the southwestern chinese tian shan: implications for neogene shortening rate variations. *Earth and Planetary Science Letters*, 247(1-2):70–81.

Sobel, E. R., Chen, J., Schoenbohm, L. M., Thiede, R., Stockli, D. F., Sudo, M., and Strecker, M. R. (2013). Oceanic-style subduction controls late Cenozoic deformation of the Northern Pamir orogen. *Earth and Planetary Science Letters*, 363:204–218.

Sobel, E. R. and Dumitru, T. A. (1997). Thrusting and exhumation around the margins of the western tarim basin during the india-asia collision. *Journal of Geophysical Research: Solid Earth*, 102(B3):5043–5063.

Sobel, E. R., Oskin, M., Burbank, D., and Mikolaichuk, A. (2006b). Exhumation of basement-cored uplifts: Example of the kyrgyz range quantified with apatite fission track thermochronology. *Tectonics*, 25(2).

Spotila, J. A., Niemi, N., Brady, R., House, M., Buscher, J., and Oskin, M. (2007). Long-term continental deformation associated with transpressive plate motion: The san andreas fault. *Geology*, 35(11):967–970.

Stalder, N. F., Herman, F., Fellin, M. G., Coutand, I., Aguilar, G., Reiners, P. W., and Fox, M. (2020). The relationships between tectonics, climate and exhumation in the central andes (18–36 s): Evidence from low-temperature thermochronology. *Earth-Science Reviews*, 210:103276.

Stein, R. S. and King, G. C. (1984). Seismic potential revealed by surface folding: 1983 Coalinga, California, earthquake. *Science*, 224(4648):869–872.

Stockmeyer, J. M., Shaw, J. H., Brown, N. D., Rhodes, E. J., Richardson, P. W., Wang, M., Lavin, L. C., and Guan, S. (2017). Active thrust sheet deformation over multiple rupture cycles: A quantitative basis for relating terrace folds to fault slip rates. *Bulletin of the Geological Society of America*, 129(9-10):1337–1356.

Stockmeyer, J. M., Shaw, J. H., and Guan, S. (2014). Seismic hazards of multisegment thrust-fault ruptures: Insights from the 1906 Mw 7.4-8.2 Manas China, Earthquake. *Seismological Research Letters*, 85(4):801–808.

Styron, R. and Pagani, M. (2020). The gem global active faults database. *Earthquake Spectra*, 36(1_suppl):160–180.

Stübner, K., Ratschbacher, L., Weise, C., Chow, J., Hofmann, J., Khan, J., Rutte, D., Sperner, B., Pfänder, J. A., Hacker, B. R., Dunkl, I., Tichomirowa, M., and Stearns, M. A. (2013). The giant shakhdara migmatitic gneiss dome, pamir, india-asia collision zone: 2. timing of dome formation. *Tectonics*, 32(5):1404–1431.

Sun, X. and Wang, P. (2005). How old is the Asian monsoon system? - Palaeobotanical records from China. *Palaeogeography, Palaeoclimatology, Palaeoecology*, 222(3-4):181 – 222.

Tang, W., Zhang, Z., Li, J., Li, K., Luo, Z., and Chen, Y. (2015). Mesozoic and cenozoic uplift and exhumation of the bogda mountain, nw china: Evidence from apatite fission track analysis. *Geoscience Frontiers*, 6(4):617–625.

Tapponnier, P. and Molnar, P. (1979). Active faulting and cenozoic tectonics of the tien shan, mongolia, and baykal regions. *Journal of Geophysical Research: Solid Earth*, 84(B7):3425–3459.

Thatcher, W. (1975). Strain accumulation and release mechanism of the 1906 san francisco earthquake. *Journal of Geophysical Research*, 80(35):4862–4872.

Thiede, R. C., Sobel, E. R., Chen, J., Schoenbohm, L. M., Stockli, D. F., Sudo, M., and Strecker, M. R. (2013). Late cenozoic extension and crustal doming in the india-eurasia collision zone: New thermochronologic constraints from the ne chinese pamir. *Tectonics*, 32(3):763–779.

Thompson, S. C., Weldon, R. J., Rubin, C. M., Abdrakhmatov, K., Molnar, P., and Berger, G. W. (2002). Late quaternary slip rates across the central tien shan, kyrgyzstan, central asia. *Journal of Geophysical Research: Solid Earth*, 107(B9):ETG–7.

Tong, X., Sandwell, D. T., and Fialko, Y. (2010). Coseismic slip model of the 2008 Wenchuan earthquake derived from joint inversion of interferometric synthetic aperture radar, GPS, and field data. *Journal of Geophysical Research*, 115(B4):1–19.

Torres, R., Navas-Traver, I., Bibby, D., Lokas, S., Snoeij, P., Rommen, B., Osborne, S., Ceba-Vega, F., Potin, P., and Geudtner, D. (2017). Sentinel-1 sar system and mission. In *2017 IEEE Radar Conference (RadarConf)*, pages 1582–1585.

Torres, R., Snoeij, P., Geudtner, D., Bibby, D., Davidson, M., Attema, E., Potin, P., Rommen, B., Floury, N., Brown, M., Traver, I. N., Deghaye, P., Duesmann, B., Rosich, B., Miranda, N., Bruno, C., L'Abbate, M., Croci, R., Pietropaolo, A., Huchler, M., and Rostan, F. (2012). GMES Sentinel-1 mission. *Remote Sensing of Environment*, 120:9–24.

van Der Beek, P., Van Melle, J., Guillot, S., Pêcher, A., Reiners, P. W., Nicolescu, S., and Latif, M. (2009). Eocene tibetan plateau remnants preserved in the northwest himalaya. *Nature Geoscience*, 2(5):364–368.

Walker, R., Jackson, J., and Baker, C. (2003). Surface expression of thrust faulting in eastern Iran: source parameters and surface deformation of the 1978 Tabas and 1968 Ferdows earthquake sequences. *Geophysical Journal International*, 152(3):749–765.

Walker, R. T., Bergman, E. A., Szeliga, W., and Fielding, E. J. (2011). Insights into the 1968-1997 Dasht-e-Bayaz and Zirkuh earthquake sequences, eastern Iran, from calibrated relocations, InSAR and high-resolution satellite imagery. *Geophysical Journal International*, 187(3):1577–1603.

Wang, C. (2015). Cenozoic tectonic uplift and sedimentary evolution of the Tiklik area, Western Kunlun orogen. Master's thesis, Zhejiang University.

Wang, C., Zhao, X., Liu, Z., Lippert, P. C., Graham, S. A., Coe, R. S., Yi, H., Zhu, L., Liu, S., and Li, Y. (2008). Constraints on the early uplift history of the tibetan plateau. *Proceedings of the National Academy of Sciences*, 105(13):4987–4992.

Wang, C. Y., Yang, Z. E., Luo, H., and Mooney, W. D. (2004). Crustal structure of the northern margin of the eastern Tien Shan, China, and its tectonic implications for the 1906 M7.7 Manas earthquake. *Earth and Planetary Science Letters*, 223(1-2):187–202.

Wang, D., Zhao, B., Yu, J., and Tan, K. (2020a). Active tectonic deformation around the Tarim Basin inferred from dense GPS measurements. *Geodesy and Geodynamics*, 11(6):418–425.

Wang, F., Feng, H., Shi, W., Zhang, W., Wu, L., Yang, L., Wang, Y., Zhang, Z., and Zhu, R. (2016). Relief history and denudation evolution of the northern tibet margin: Constraints from 40ar/39ar and (u–th)/he dating and implications for far-field effect of rising plateau. *Tectonophysics*, 675:196–208.

Wang, P. (1990). Neogene stratigraphy and paleoenvironments of china. *Palaeogeography, Palaeoclimatology, Palaeoecology*, 77(3-4):315–334.

Wang, Q., Li, S., and Du, Z. (2009). Differential uplift of the chinese tianshan since the cretaceous: constraints from sedimentary petrography and apatite fission-track dating. *International Journal of Earth Sciences*, 98(6):1341–1363.

Wang, S., Jiao, R., Ren, Z., Wu, C., Ren, G., Zhang, H., and Lei, Q. (2020b). Active thrusting in an intermontane basin: The kumysh fault, eastern tian shan. *Tectonics*, 39(8):e2019TC006029.

Wang, X., Xu, C., Wen, Y., Wang, S., Xu, G., Xiao, Z., and Fang, L. (2019). The 2016 Mw 6.0 Hutubi earthquake: A blind thrust event along the northern Tian Shan front. *Journal of Asian Earth Sciences*, 173(July 2018):79–87.

Wang, Y., Cai, K., Sun, M., Xiao, W., De Grave, J., Wan, B., and Bao, Z. (2018). Tracking the multi-stage exhumation history of the western chinese tianshan by apatite fission track (aft) dating: Implication for the preservation of epithermal deposits in the ancient orogenic belt. *Ore Geology Reviews*, 100:111–132.

Wegmuller, U. (1997). Gamma sar processor and interferometry software. In *3rd ERS Symposium, Florence, Italy, March 1997*.

Wei, S., Barbot, S., Graves, R., Lienkaemper, J. J., Wang, T., Hudnut, K., Fu, Y., and Helmberger, D. (2015). The 2014 Mw 6.1 South Napa Earthquake: A unilateral rupture with shallow asperity and rapid afterslip. *Seismological Research Letters*, 86(2A):344–354.

Weiss, J. R., Walters, R. J., Morishita, Y., Wright, T. J., Lazecky, M., Wang, H., Hussain, E., Hooper, A. J., Elliott, J. R., Rollins, C., Yu, C., González, P. J., Spaans, K., Li, Z., and Parsons, B. (2020). High-Resolution Surface Velocities and Strain for Anatolia From Sentinel-1 InSAR and GNSS Data. *Geophysical Research Letters*, 47(17).

Werner, C., Wegmüller, U., Strozzi, T., and Wiesmann, A. (2000). Gamma SAR and interferometric processing software. In *Proceedings of the ERS-ENVISAT symposium, Gothenburg, Sweden*.

Werner, C., Wegmüller, U., Strozzi, T., and Wiesmann, A. (2002). Processing strategies for phase unwrapping for insar applications. In *proceedings of the European conference on synthetic aperture radar (EUSAR 2002)*, volume 1, pages 353–356.

Werner, C., Wegmüller, U., Strozzi, T., and Wiesmann, A. (2003). Interferometric Point Target Analysis for Deformation Mapping. *International Geoscience and Remote Sensing Symposium (IGARSS)*, 7(1):4362–4364.

Wessel, P., Luis, J. F., Uieda, L., Scharroo, R., Wobbe, F., Smith, W. H. F., and Tian, D. (2019). The generic mapping tools version 6. *Geochemistry, Geophysics, Geosystems*, 20(11):5556–5564.

Weston, J., Ferreira, A. M. G., and Funning, G. J. (2011). Global compilation of interferometric synthetic aperture radar earthquake source models: 1. Comparisons with seismic catalogs. *Journal of Geophysical Research: Solid Earth*, 116(B8):B08408.

Willett, S. D., Herman, F., Fox, M., Stalder, N., Ehlers, T. A., Jiao, R., and Yang, R. (2020). Bias and error in modelling thermochronometric data: Resolving a potential increase in plio-pleistocene erosion rate. *Earth surface dynamics discussions*, 2020:1–78.

Wimpenny, S. and Scott Watson, C. (2020). gWFM: A global catalog of moderate-magnitude earthquakes studied using teleseismic body waves. *Seismological Research Letters*, 92(1):212–226.

Windley, B. F., Alexeiev, D., Xiao, W., Kroner, A., and Badarch, G. (2007). Tectonic models for accretion of the central asian orogenic belt. *Journal of the Geological Society*, 164(1):31–47.

Windley, B. F., Allen, M. B., Zhang, C., Zhao, Z. Y., and Wang, G. R. (1990). Paleozoic accretion and Cenozoic redeformation of the Chinese Tien Shan Range, central Asia.

Wolf, R. A., Farley, K. A., and Kass, D. M. (1998). Modeling of the temperature sensitivity of the apatite (U-Th)/He thermochronometer. *Chemical Geology*, 148(1-2):105–114.

Wright, T. J. (2002). Remote monitoring of the earthquake cycle using satellite radar interferometry. *Philosophical Transactions of the Royal Society of London. Series A: Mathematical, Physical and Engineering Sciences*, 360(1801):2873–2888.

Wright, T. J., Lu, Z., and Wicks, C. (2004). Constraining the slip distribution and fault geometry of the Mw 7.9, 3 November 2002, Denali fault earthquake with Interferometric Synthetic Aperture Radar and Global Positioning System data. *Bulletin of the Seismological Society of America*, 94(6 SUPPL. B):175–189.

Wright, T. J., Parsons, B. E., Jackson, J. A., Haynes, M., Fielding, E. J., England, P. C., and Clarke, P. J. (1999). Source parameters of the 1 October 1995 Dinar (Turkey) earthquake from SAR interferometry and seismic bodywave modelling. *Earth and Planetary Science Letters*, 172(1-2):23–37.

Wu, C., Wu, G., Shen, J., Chen, J., Alimujiang, and Xiangde, C. (2014). The late-Quaternary activity of the Nalati Fault and its implications for the crustal deformation in the interior of the Tianshan Mountains. *Quaternary Sciences*, 34(2):269–280.

Wu, C., Zhang, P., Zhang, Z., Zheng, W., Xu, B., Wang, W., Yu, Z., Dai, X., Zhang, B., and Zang, K. (2023). Slip partitioning and crustal deformation patterns in the Tianshan orogenic belt derived from GPS measurements and their tectonic implications. *Earth-Science Reviews*, 238(August 2022):104362.

Wu, C., Zuza, A. V., Zhou, Z., Yin, A., McRivette, M. W., Chen, X., Ding, L., and Geng, J. (2019). Mesozoic-cenozoic evolution of the eastern kunlun range, central tibet, and implications for basin evolution during the indo-asian collision. *Lithosphere*, 11(4):524–550.

Xiao, H., Lin, Z., Diao, J., Wang, Q., Shi, B., and Song, L. (2011). The tectonic-thermal evolution history in the Kuruketage uplift, Xinjiang, China. *Earth Science Frontiers*, 18(3):33.

Xinjiang Bureau of Geology and Mineral Resources (1993). *Regional Geology of Xinjiang Uygur Autonomous Region.* Geological Publishing House, Beijing.

Xu, Y., Roecker, S. W., Wei, R., Zhang, W., and Wei, B. (2006). Analysis of seismic activity in the crust from earthquake relocation in the central Tien Shan. *Bulletin of the Seismological Society of America*, 96(2):737–744.

Yang, H., Li, Y., Shi, J., Xiao, A., Huang, S., Wu, G., Wang, H., Wang, X., Zhao, Y., and Liu, Y. (2010). Tectonic characteristics of the Late Cenozoic south Tianshan fold-and-thrust belt. *Quaternary Sciences*, 30(5):1030–1043 (in Chinese with English abstract).

Yang, W., Jolivet, M., Dupont-Nivet, G., and Guo, Z. (2014). Mesozoic – cenozoic tectonic evolution of southwestern tian shan: Evidence from detrital zircon u/pb and apatite fission track ages of the ulugqat area, northwest china. *Gondwana Research*, 26(3–4):986–1008.

Yang, W., LI, J., GUO, Z., JOLIVET, M., and HEILBRONN, G. (2017). New apatite fission-track ages of the western kuqa depression: Implications for the mesozoic–cenozoic tectonic evolution of south tianshan, xinjiang. *Acta Geologica Sinica - English Edition*, 91(2):396–413.

Yang, X., Li, A., and Hunag, W. (2013). Uplift differential of active fold zones during the late quaternary, northern piedmonts of the tianshan mountains, china. *Science China Earth Sciences*, 56:794–805.

Yang, X., Ran, Y., Song, F., Xu, X., Cheng, J., Min, W., Han, Z., and Chen, L. (2006). The analysis for crust shortening of Kalpin Thrust tectonic zone, south-western Tianshan, Xinjiang, China. *Seismology and Geology (in Chinese with English abstract)*, 28(2):194–204.

Yang, Y. H., Hu, J. C., Chen, Q., Wang, Z. G., and Tsai, M. C. (2019). A blind thrust and overlying folding earthquake of the 2016 Mw 6.0 hutubi earthquake in the Northern Tien Shan fold-and-thrust belts, China. *Bulletin of the Seismological Society of America*, 109(2):770–779.

Yang, Z. X., Zhao, J. R., Zhang, X. K., Zhang, C. K., Cheng, S. X., Duan, Y. L., Zhang, J. S., and Wang, S. J. (2002). Tomographic determination of the upper crustal structure in the Jiashi strong earthquake swarm region. *Acta Seismologica Sinica English Edition*, 15(2):162–170.

Yao, Q., Yang, W., Jiang, X., Guo, Y., Liu, J., Zhang, Y., Wang, H., Ren, J., Yu, C., Yue, C., and Zhao, J. (2021a). The 2020 M6.4 Jiashi Earthquake: An Event that Occurred Under the Décollement on the Kaping Fold-and-Thrust Belt in the Southwestern Tien Shan Mountains, China. *Frontiers in Earth Science*, 9(May):1–14.

Yao, Y., Wen, S., Li, T., and Wang, C. (2021b). The 2020 Mw6.0 Jiashi earthquake: A fold earthquake event in the southern Tian Shan, northwest China. *Seismological Research Letters*, 92(2):859–869.

Yin, A., Craig, P., Harrison, T. M., Ryerson, F. J., Qian, X., and Yang, G. (1998). Late Cenozoic tectonic evolution of the southern Chinese Tian Shan. *Tectonics*, 17(1):1–27.

Yin, A. and Harrison, T. M. (2000). Geologic evolution of the himalayan-tibetan orogen. *Annual review of earth and planetary sciences*, 28(1):211–280.

Yin, J., Chen, W., Hodges, K. V., Xiao, W., Cai, K., Yuan, C., Sun, M., Liu, L.-P., and van Soest, M. C. (2018). The thermal evolution of chinese central tianshan and its implications: Insights from multi-method chronometry. *Tectonophysics*, 722:536–548.

Yu, C., Li, Z., and Penna, N. T. (2018). Interferometric synthetic aperture radar atmospheric correction using a GPS-based iterative tropospheric decomposition model. *Remote Sensing of Environment*, 204(August 2017):109–121.

Yu, J., Zheng, D., Zhang, H., Wang, Y., Hao, Y., and Li, C. (2022). Initial cenozoic exhumation of the northern chinese tian shan deduced from apatite (u-th)/he thermochronological data. *Lithosphere*, 2022(1):8099539.

Yu, P., Qiao, X., Xiong, W., Chen, W., Nie, Z., Wang, D., Jia, Z., and Li, J. (2020). Source model for the M w 6.0 earthquake in Jiashi, China on 19 January 2020 from Sentinel-1A InSAR data. *Earth, Planets and Space*, 72(1).

Yu, S., Chen, W., Evans, N. J., McInnes, B. I., Yin, J., Sun, J., Li, J., and Zhang, B. (2014). Cenozoic uplift, exhumation and deformation in the north kuqa depression, china as constrained by (u–th)/he thermochronometry. *Tectonophysics*, 630:166–182.

Yuan, D.-Y., Champagnac, J.-D., Ge, W.-P., Molnar, P., Zhang, P.-Z., Zheng, W.-J., Zhang, H.-P., and Liu, X.-W. (2011). Late quaternary right-lateral slip rates of faults adjacent to the lake qinghai, northeastern margin of the tibetan plateau. *Bulletin*, 123(9-10):2016–2030.

Yuan, W., Dong, J., Shicheng, W., and Carter, A. (2006). Apatite fission track evidence for neogene uplift in the eastern kunlun mountains, northern qinghai–tibet plateau, china. *Journal of Asian Earth Sciences*, 27(6):847–856.

Yue, L.-F., Suppe, J., and Hung, J.-H. (2005). Structural geology of a classic thrust belt earthquake: the 1999 chi-chi earthquake taiwan (mw= 7.6). *Journal of Structural Geology*, 27(11):2058–2083.

Yue, Y., Ritts, B. D., Graham, S. A., Wooden, J. L., Gehrels, G. E., and Zhang, Z. (2004). Slowing extrusion tectonics: lowered estimate of post-early miocene slip rate for the altyn tagh fault. *Earth and Planetary Science Letters*, 217(1-2):111–122.

Zachos, J., Pagani, M., Sloan, L., Thomas, E., and Billups, K. (2001). Trends, rhythms, and aberrations in global climate 65 ma to present. *science*, 292(5517):686–693.

Zhang, B., Chen, W., Liu, J., Yin, J., and Sun, J. (2020). Thermochronological insights into the intracontinental orogeny of the chinese western tianshan orogen. *Journal of Asian Earth Sciences*, 194:103927.

Zhang, G., Zhu, L., Song, X., Li, Z., Yang, M., Su, N., and Chen, X. (1999). Predictions of the 1997 strong earthquakes in Jiashi, Xinjiang, China. *Bulletin of the Seismological Society of America*, 89(5):1171–1183.

Zhang, Z., Guo, Z., Wu, C., and Fang, S. (2007a). Thermal history of the Jurassic Strata in the Northern Tianshan and its geological significance, revealed by apitite fission-track and vitrinite-reflectance analysis. *Acta Petrologica Sinica*, 023(07):1683–1695.

Zhang, Z., Wang, Huijun and, G. Z., and Jiang, D. (2007b). Impacts of tectonic changes on the reorganization of the cenozoic paleoclimatic patterns in china. *Earth and Planetary Science Letters*, 257(3):622–634.

Zhang, Z., Zhu, W., Shu, L., Wan, J., Yang, W., Su, J., and Zheng, B. (2009). Apatite fission track thermochronology of the precambrian aksu blueschist, nw china: Implications for thermo–tectonic evolution of the north tarim basement. *Gondwana Research*, 16(2):182–188.

Zhang, Z., Zhu, W., Shu, L., Wan, J., Yang, W., Zheng, B., and Su, J. (2011). Multi-stage exhumation of the ne tarim precambrian bedrock, nw china: constraints from apatite fission track thermochronology in the kuluketage area. *Terra Nova*, 23(5):324–332.

Zhang, Z., Zhu, W., Zheng, D., Zheng, B., and Yang, W. (2016). Apatite fission track thermochronology in the kuluketage and aksu areas, nw china: Implication for tectonic evolution of the northern tarim. *Geoscience Frontiers*, 7(2):171–180.

Zhang, Z. Q., Chen, J. Y. S., and Lin, J. (2008). Stress interactions between normal faults and adjacent strike-slip faults of 1997 Jiashi earthquake swarm. *Science in China, Series D: Earth Sciences*, 51(3):431–440.

Zheng, D., Clark, M. K., Zhang, P., Zheng, W., and Farley, K. A. (2010). Erosion, fault initiation and topographic growth of the north qilian shan (northern tibetan plateau). *Geosphere*, 6(6):937–941.

Zheng, D., Wang, W., Wan, J., Yuan, D., Liu, C., Zheng, W., Zhang, H., Pang, J., and Zhang, P. (2017). Progressive northward growth of the northern qilian shan–hexi corridor (northeastern tibet) during the cenozoic. *Lithosphere*, 9(3):408–416.

Zhengle, C., Li, L., Jian, L., Hongliang, G., Rongbao, J., Shengxiang, L., Enjiu, Z., Xiaozhong, H., Xigeng, L., Cheng, W., et al. (2008). Preliminary study on the uplifting-exhumation process of the western tianshan range, northwestern china. *Acta Petrologica Sinica*, 24(4):625–636.

Zhou, S. Y. and Xu, Z. H. (2000). Fracture characteristics of the 1997 Jiashi, Xinjiang, China, earthquake swarm inferred from source spectra. *Acta Seismologica Sinica English Edition*, 13(2):125–135.

Zhou, Z., Kusky, T. M., and Tang, C.-C. (2019). Coulomb stress change pattern and aftershock distributions associated with a blind low-angle megathrust fault, Nepalese Himalaya. *Tectonophysics*, 767:228161.

Zhu, W., Zhang, Z., Shu, L., Wan, J., Lu, H., Wang, S., Yang, W., and Su, J. (2007). Uplift and exhumation history of the Precambrian basement, northern Tarim: Evidence from apatite fission track data. *Acta Petrologica Sinica*, 23(7):1671–1682.

Zhu, W., Zhang, Z., Shu, L., Wan, J., Lu, H., Wang, S., Yang, W., and Su, J. (2009). Thermotectonic evolution of precambrian basement rocks of the kuruktag uplift, ne tarim craton, china: evidence from apatite fission-track data. *International Geology Review*, 52(9):941–954.

Zubker, H. and Goldstein, R. (1986). Topographic mapping from interferometric sar observations. *J. Geophys. Res*, 91(B5).

Zubovich, A. V., Wang, X. Q., Scherba, Y. G., Schelochkov, G. G., Reilinger, R., Reigber, C., Mosienko, O. I., Molnar, P., Michajljow, W., Makarov, V. I., Li, J., Kuzikov, S. I., Herring, T. A., Hamburger, M. W., Hager, B. H., Dang, Y. M., Bragin, V. D., and Beisenbaev, R. T. (2010). GPS velocity field for the Tien Shan and surrounding regions. *Tectonics*, 29(6):1–23.